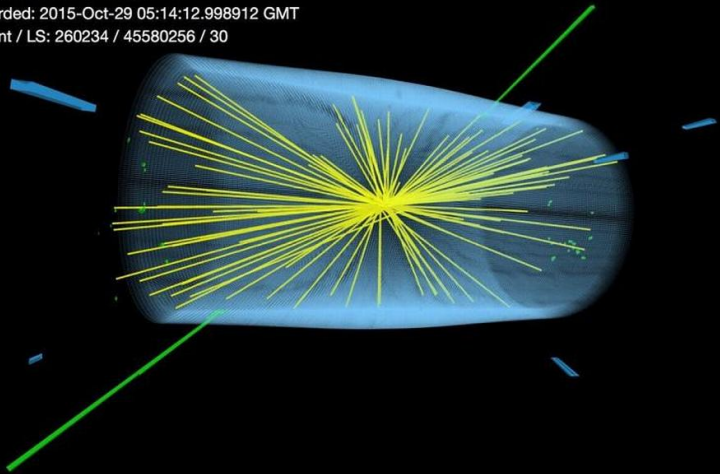# Introduction to Particle Physics

Dezső Horváth and Zoltán Trócsányi

CMS Experiment at the LHC, CERN
Data recorded: 2015-Oct-29 05:14:12.998912 GMT
Run / Event / LS: 260234 / 45580256 / 30

Introduction to Particle Physics

Introduction to Particle Physics

By

Dezső Horváth and Zoltán Trócsányi

Contents

Foreword

One of the methods of studying Nature is to penetrate deeper and deeper in the structure of matter ever increasing the spatial resolution, i.e., studying smaller and smaller objects. In the history of natural sciences new and new particles appeared which were thought to be *elementary*: the four atoms (a-tom = not divisible) of Anaximenes and Democritus, the elements/atoms of Dalton and Mendeleev, the atomic nucleus of Rutherford and the so-called *elementary* particles of which the proton, the neutron, the electron and the neutrino are the most well-known. Between 1930 and 1960 hundreds of such particles were discovered, thus a new level of elementariness was needed and the quark model appeared. We will see that, in fact, the proton and the neutron are also composite particles although the electron stays elementary. This development was crowned by the standard model (SM) in the late sixties and it is still the uncontested global theory of matter, supported by all available theoretical and experimental evidence.

In this textbook we summarize the present knowledge of particle physics at an introductory level. Particle physics is a very broad subject including many different sub-fields. While we mention many of these, a detailed account on all is impossible. Our clear focus is on high energy collider physics that is among the most widely pursued subfields where the threshold of current research is high. With the Large Hadron Collider in operation new results appear regularly. Our goal here is to keep the level introductory, yet help students reach this high threshold making them acquainted with both the experimental and theoretical minimum needed to comprehend current research at colliders. Our treatise is detailed on established results of collider physics while mostly marginal on current developments with the exception of the discovery of the Higgs particle due to its utmost importance.

The first part (written by D. Horváth) is planned to be accessible for advanced BSc or freshmen MSc students, while the second part (written by Z. Trócsányi) on the theory is intended for advanced MSc or freshmen PhD students in particle physics, with some attempt to go into the rather complex mathematical formalism of the field. Our aim is to provide concise but hopefully comprehensive account on the subject and also try to help students in their decision whether to orient themselves towards experiment or theory. We assume that the book can be covered during a full academic year with about 10 hours of serious effort per week. Although the reader may be confused on several occasions when not all details are given, the theory is very precisely elaborated and its predictions beautifully agree with the experimental observations. All present day experimental evidence is

summarized in the biennial *Particle Physics Review* of the Particle Data Group [Beringer et al., 2012]; for a theoretical introduction we recommend the textbooks of Halzen and Martin [Halzen and Martin, 1984], Collins, Martin and Squires [Collins et al., 1989], and Perkins [Perkins, 1982]. The theory provides a nice glance at the key experiments as well.

Experimental particle physics is also called high-energy physics, because of its basic method of study. Energy is measured in units of electroplate, eV, the energy gained by a particle of unit charge (e.g. an electron or proton) when crossing a gap of 1 V voltage. One of the earliest means of structural studies was the optical microscope. Its resolution is limited by the wavelength of visible light (corresponding to an energy of ~ 1 eV) to the size of bacteria, 10^{-5} m. The smaller a detail, the shorter wavelength is needed to see it. For the atoms (10^{-10} m) we need X-rays or electron beams of keV (1 keV = 1000 eV) energies, for the atomic nucleus of 10^{-14} m electrons or protons between MeV (10^6 eV) and GeV (10^9 eV) energies, and for the quarks (below 10^{-18} m) up in the TeV (10^{12} eV) region. Higher energy means smaller distances and so studying finer details of the structure of matter. As far as we know at present, the basic particles of the standard model are really elementary: point-like and structureless.

Throughout this book we use the *natural* units of particle physics where the speed of light c and Planck's reduced constant $\hbar = h/(2\pi)$ are both equal to unity and thus both distance and time can be expressed in inverse energy units, i.e. in GeV^{-1} (see Table 1).

We shall quote only selected, but not all original publications as this is intended to be an introductory textbook, not a monograph and we do not want to overwhelm students. Yet we encourage the reader to consult some trustworthy sites on the Web (like Wikipedia *http://en.wikipedia.org/*, Hyperphysics *http://hyperphysics.phy-astr.gsu.edu/hbase/hph.html* and Google Scholar *http://scholar.google.com/*) for simple explanations and the inSpire (*http://inspirehep.net/*) publication data base for reviews and original publications. Typing in the author's name and the date will produce all kind of information at any depth for the reader. We consider especially useful the web version of Particle Physics Review by the Particle Data Group (*http://pdg.web.cern.ch/pdg/*) which provides reliable and comprehensive reviews. Reliability is important in high energy physics as it is in the very front of knowledge and as such it is full of speculations, untested ideas and unconfirmed experimental findings. At some points we shall only mention some examples of those: Earth-absorbing black holes produced in high-energy particle collisions, faster-than-light neutrinos and pentaquarks.

The authors acknowledge the support of the Hungarian Scientific Re-

Quantity	MKS	particle physics	natural unit	$\hbar = c = 1$
Energy	1 J	$6.24 \cdot 10^9$ GeV	GeV	GeV
Momentum	1 kg m/s	$5.61 \cdot 10^{26}$ GeV/c	GeV/c	GeV
Mass	1 kg	$5.61 \cdot 10^{26}$ GeV	GeV/c^2	GeV
Distance	1 m	$5.07 \cdot 10^{15}$ GeV^{-1}	$\hbar c$/GeV	1/GeV
Time	1 s	$1.52 \cdot 10^{24}$ GeV^{-1}	$\hbar$/GeV	1/GeV
Electric charge (e)	0.16 aC	$\sqrt{4\pi\epsilon_0 \alpha \hbar c}$	$\sqrt{4\pi\epsilon_0 \hbar c \alpha}$	$\sqrt{4\pi\epsilon_0 \alpha}$

Table 1: Natural units of particle physics. $\alpha = 1/137$ is the fine structure constant, $\epsilon_0 = 8.8 \cdot 10^{-12}$ F/m is the electric permittivity of vacuum. In the last column only energy units appear, which permits the use of the power of GeV to characterize the unit as "mass dimension", e.g., the unit of length, GeV^{-1} is referred to as mass dimension minus one. *In this book we use the units of the last column, except for two cases.* One is momentum, which has natural units GeV/c, to become GeV if $c = 1$. However, in order not to confuse it with energy, we keep the natural unit for momentum. The other exception is the electric charge, for which we use the conventional notation $\sqrt{4\pi\alpha}$, i.e., we use $\epsilon_0 = 1$, which should not cause any confusion.

Part I

Particle phenomenology

Chapter 1

Particles and symmetries

MOTTO:

Central to that theory is the concept of sponta-
neously broken gauge symmetry. According
to this concept, the fundamental equations of
physics have more symmetry than the actual
physical world does.

(Frank Wilczek)

1.1   Symmetries in particle physics

Symmetries in particle physics are even more important than in chemistry or
solid state physics. Just like in any theory of matter, the inner structures of
the composite particles are described by symmetries, but in particle physics
everything is deduced from the symmetries (or invariance properties) of
the physical phenomena, or from their violation: the conservation laws, the
interactions and even the masses of the particles. Symmetries that are not
connected to space and time are called *internal* symmetries. Continuous
symmetries can be *global*, i.e. independent of the space-time coordinates, or
local. The latter means that we can choose the orientation of the (external or
internal) coordinate axes freely at any space-time point. These symmetries
are also called *gauge symmetries* or *gauge invariance* laws.

3

In field theory, according to the theorem of *Emmy Noether* any continuous global symmetry leads to a conservation law. Thus the freedom to choose the origin and orientation of our coordinate system leads to the conservation of momentum and angular momentum, that of the origin of time measurement to the conservation of energy. The conserved quantities due to continuous global internal symmetries are called conserved charges. An example is the free choice of the phase of the electron wave function as it is not measurable experimentally. This global phase invariance is also a continuous symmetry and the emerging conservation law is the conservation of the fermion charge in general. The global gauge invariance of electrodynamics leads to the conservation of the electric charge.

Gauge symmetries have far reaching consequences as they lead to interactions between particles. In the theory part (Part IV) of this book we formulate gauge symmetries in a precise mathematical sense to *discover* the three fundamental interactions of particles (the strong, weak and electromagnetic forces). Local symmetry always implies the existence of a related global symmetry as well, but a global symmetry may not necessarily imply a local symmetry, hence an interaction.

1.2   Symmetry groups and spin

The characteristic features of particles are described in terms of *symmetry groups*. The language of physics is mathematics: the mathematical formulation makes the difference between theory and speculation in physics as that allows for making quantitative predictions, which then can be checked experimentally. A new physical theory is accepted if the predictions agree with *all* available experimental information.

As symmetries usually appear at transformations of our coordinate systems the mathematical apparatus is chosen accordingly. A trivial example is the rotation of a 2-dimensional coordinate system around its origin by an angle Θ. As shown by Fig. 1.1 the new (x', y') coordinates of point P are obtained in the rotated system from the old (x, y) coordinates by the transformation

$$x' = a + b = x \cos \Theta + y \sin \Theta,$$
$$y' = y'' - c = y \cos \Theta - x \sin \Theta.$$

The point P, just as any two-dimensional vector, undergoes the following
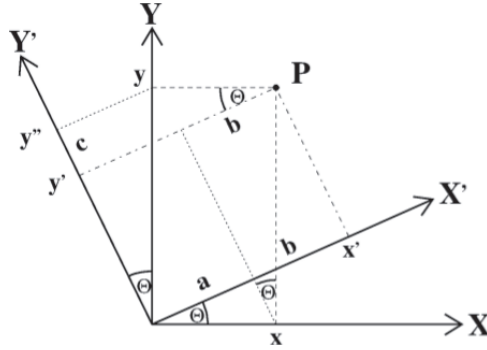
Figure 1.1: Rotation of a coordinate system in two dimensions: coordinate system $[X', Y']$ is obtained by rotating system $[X, Y]$ by an angle Θ.

coordinate transformation:

$$
\begin{pmatrix} x' \\ y' \end{pmatrix} = \begin{pmatrix} \cos\Theta \cdot x + \sin\Theta \cdot y \\ -\sin\Theta \cdot x + \cos\Theta \cdot y \end{pmatrix} = \begin{pmatrix} \cos\Theta & \sin\Theta \\ -\sin\Theta & \cos\Theta \end{pmatrix} \cdot \begin{pmatrix} x \\ y \end{pmatrix}.
$$

This means that the vector $\begin{pmatrix} x' \\ y' \end{pmatrix}$ is obtained by multiplying the vector $\begin{pmatrix} x \\ y \end{pmatrix}$ with the matrix in front of it. An important property of these rotation transformations is that they do not change the length of the vector pointing to P (its absolute value) as

$$
x'^2 + y'^2 = (x^2 + y^2) \cdot \left(\cos^2\Theta + \sin^2\Theta \right) = x^2 + y^2.
$$

The condition that the length of the vector remains unchanged demands that the complex transformation matrix be unitary:

$$
U^\dagger U = \begin{pmatrix} U_{11}^* & U_{21}^* \\ U_{12}^* & U_{22}^* \end{pmatrix} \cdot \begin{pmatrix} U_{11} & U_{12} \\ U_{21} & U_{22} \end{pmatrix} =
$$
$$
\begin{pmatrix} U_{11}^2 + U_{21}^2 & U_{11}^* U_{12} + U_{21}^* U_{22} \\ U_{12}^* U_{11} + U_{22}^* U_{21} & U_{12}^2 + U_{22}^2 \end{pmatrix} = \begin{pmatrix} 1 & 0 \\ 0 & 1 \end{pmatrix}
$$

Rotations of this type have the following mathematical properties:

- they are additive: rotation by Θ_1 and then by Θ_2 is equivalent to a rotation by $\Theta = \Theta_1 + \Theta_2$;

- their addition is associative: $(\Theta_1 + \Theta_2) + \Theta_3 = \Theta_1 + (\Theta_2 + \Theta_3)$;

- they have a unit element: rotation by $\Theta = 0$ which does not do anything;

- the rotations can be inverted ($\Theta - \Theta = 0$ and the inverse elements are also members of the set.

Sets with operation among its elements obeying these properties are called *groups*. Spin is a three-dimensional quantity with the properties of the rotation group and its mathematical description (*representation*) is called the $SU(2)$ group of special (determinant = 1) unitary complex 2×2 matrices. $SU(2)$ can be applied not only for spin, but for any physical quantity with similar symmetry properties, like for example the *isospin* to be introduced later.

When we increase the degrees of freedom we get higher symmetry groups of similar properties. The next step, $SU(3)$, which is also used in particle physics, is the symmetry group of special unitary complex 3×3 matrices. It has three possible *eigenstates* which can be interpreted as three corners of a triangle with an $SU(2)$ symmetry between any two of its corners (see Chapter 3).

In case of complex quantities we can also decrease the degrees of freedom of rotations, then we get the $U(1)$ group of 1×1 unitary matrices, i.e. $e^{i\phi}$ complex phases. That is the symmetry group of the *gauge transformations* of the electromagnetic interaction. The simplest manifestation of the gauge symmetry of electromagnetism is that we can freely choose the zero point of the electrostatic potential as demonstrated by the birds sitting on high-voltage wires. The global $U(1)$ symmetry of Maxwell's equations leads to the conservation of the electric charge. In the more general case, the $U(1)$ symmetry of the Dirac equation [Dirac, 1931], the general equation describing the motion of a fermion, causes the conservation of the number of fermions or *fermion charge* [Halzen and Martin, 1984].

1.3   Fermions and bosons

Particles are categorized according to various properties. The most important one is spin, the intrinsic angular momentum. Spin cannot be interpreted as related to actual rotation, but it is added to the orbital momentum. Its natural unit is the reduced Planck constant $\hbar = h/(2\pi)$. Spin is strange: the spin of the electron is added to its orbital momentum, but it has two eigenstates only: it is either left or right polarized as compared to its momentum (or points either up or down in a vertical magnetic field) in any coordinate system. Thus

spin is characterized by two independent quantities in three dimensions: by its length and one of its vector components.

The particles with half-integer spin ($S = \frac{1}{2}, \frac{3}{2}, \frac{5}{2}$...) follow the Fermi–Dirac statistics and they are called *fermions*, whereas those with integer spin ($S = 0, 1, 2$ ...) follow the Bose–Einstein statistics and called *bosons*. They have very different symmetry and other properties. The wave function describing a system of fermions changes sign when two fermions switch quantum states whereas in the case of bosons there is no change; all other differences can be deduced from this property. Fermion number is conserved whereas one can create and absorb bosons: a lamp can irradiate any number of photons ($S = 1$) and an antenna can absorb them, assuming that the energy and momentum are conserved. At the same time the electrons ($S = \frac{1}{2}$) in order to illuminate a lamp or a cathode tube of an old-fashioned TV set have to be brought there and then conducted away. Another very important difference is that any number of bosons can be put in any particular quantum state, but only one fermion: this is *Pauli's exclusion principle*. That is why the electrons of the atom fill discrete energy levels and this is the force which prevents the atoms of matter and the nucleons in the nucleus from penetrating each other; it provides macroscopic forms for our material objects.

Actually, the mathematics behind Pauli's exclusion principle is extremely simple. The state function for a two-fermion system changes sign when you exchange its particle states, $\psi_F(1, 2) = -\psi_F(2, 1)$, while that of a bosonic system does not, $\psi_B(1, 2) = +\psi_B(2, 1)$. Thus if the two fermions would have exactly the same quantum numbers, their state function should be zero as that is the only function which does not change at changing its sign.

Some basic properties of fermions and bosons are compared in Table 1.1. The elementary fermions of the standard model are the six leptons and six quarks, the elementary bosons are the mediators of the three particle interactions and the Higgs boson.

The standard model assumes that our world is constructed of three fermion families, each consisting of a pair of quarks and a pair of leptons, and their interactions, deduced on the basis of symmetry principles, are mediated by vector bosons of spin 1. All fermions have *antiparticles* with opposite charges and otherwise the same properties. The interaction of a particle with its antiparticle leads to their annihilation. When an electron and its antiparticle, the *positron* annihilate they produce two or three photons, whereas the annihilation of a proton with an antiproton releases so much energy, almost 2 GeV, that half a dozen particles (mostly pions, the lightest mesons) could be emitted.

The lack of antimatter in the Universe [Cohen et al., 1998] implies a
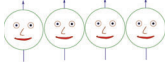
Property	fermion	boson
Spin	half-integer ($\frac{1}{2}$, $\frac{3}{2}$ ...)	integer (0, 1, 2, ...)
$\psi(1, 2) = \pm\psi(2, 1)$	−	+
Pauli exclusion	yes	no
Particle number conserved	yes	no
Condensation	no	yes
Statistics	Fermi-Dirac	Bose-Einstein

Table 1.1: Comparison of the properties of fermions and bosons

possible asymmetry between particle and its antiparticle, and that is one of the great mysteries of physics. Were there antimatter galaxies, they would emit antiparticles and they would be encircled by a halo of annihilation when meeting the particles emitted by neighbouring galaxies of ordinary matter, but the astronomers do not see such phenomena anywhere.

1.4   Mirror reflection: parity

Changing signs of all three coordinates, i.e. changing the directions of all three axes of a rectangular (Cartesian) coordinate system is equivalent to changing just one sign: we call it going from the usual right-handed coordinates to left-handed ones as in the usual coordinate system rotating the x-axis to y defines the direction of z according to a right-handed screw. This is explained in Fig. 1.2.

Parity is a general property of the mathematical functions of physics. Any function $f(x)$ can be written as a sum of two functions of odd and even parities, e.g. by separating even and odd terms in its Taylor or trigonometric expansion or simply by writing $f(x) = \frac{1}{2}[f(x) + f(-x)] + \frac{1}{2}[f(x) - f(-x)]$. The parity operator is of course unitary,

$$P\psi(r, t) = \psi(-r, t); \quad P^2 = 1 .$$

Any interaction with a spherically symmetric potential, e.g. the Coulomb
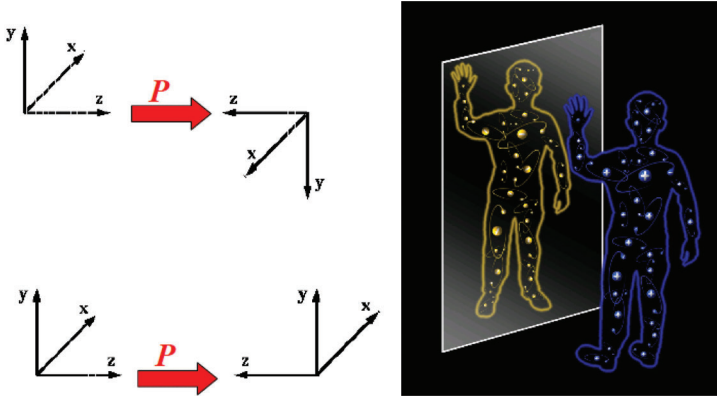
Figure 1.2: Mirror reflection and parity change (after D. Kirkby, APS, 2003) from right-handed to left-handed coordinates.

potential of a point-like electric charge, conserves parity:

$$V(r) = V(-r) \Rightarrow H(r) = H(-r) \Rightarrow [P, H] \equiv PH - HP = 0\,.$$

As a result, parity is a good quantum number[1] of particles. For instance, the wave function of the hydrogen atom is a parity eigenstate:

$$PY_{\ell m}(\Theta, \phi) = Y_{lm}(\pi - \Theta, \pi + \phi) = (-1)^{\ell} Y_{\ell m}(\Theta, \phi)$$

with an eigenvalue of $P_{em} = (-1)^{\ell}$ where ℓ is the orbital momentum. As the minimal electromagnetic transition, $E1$ means a change of orbital momentum $\Delta \ell = \pm 1$, the photon emitted in electromagnetic reactions should have at least $P_\gamma = -1$, the photon has a negative intrinsic parity (it can have an orbital momentum as well, of course). Anti-fermions have the opposite parities as fermions, whereas particles and antiparticles of composite bosons[2] have the same parity determined by the parity and angular momentum of its constituents.

Parity quantum numbers are multiplicative, e.g. for a system of three particles: $P(123) = P_1 \cdot P_2 \cdot P_3$. As mesons are bound states of quarks and

---

[1]Quantum number: such a physical quantity which can change in definite quanta only, like charge or angular momentum, and a set of which can uniquely characterize a physical state.

[2]Fundamental bosons do not have antiparticles as the existence of antiparticles is related to the Dirac equation of the fermions.

anti quarks, their ground state ($\ell = 0$) parity is $P(q\overline{q}) = P(q) \cdot P(\overline{q}) = -1$. By definition for the nucleons $P_p = P_n = +1$, thus the parities of quarks are +1, and of anti-quarks –1. For the particles spin J and parity P are denoted as J^P, e.g. for charged pions $\pi^{\pm} : 0^-$.

We shall see later that parity is not conserved by the weak interaction, it is a broken symmetry. Stephen Weinberg calls such symmetries *accidental symmetries*.

1.5 Charge conjugation

Charge conjugation converts a particle into its antiparticle, $C|p\rangle = \pm|\overline{p}\rangle$. It is also a unitary operator, $C^2 = 1$. It changes the signs of all kinds of charges: electric, baryon, lepton charges, but not the spin. Only neutral particles could be C-eigenstates, the eigenvalue is the C-parity. Strong and electromagnetic interactions conserve it. For instance, in the electromagnetic decay of the neutral pion 2 photons are emitted, $\pi^0 \rightarrow \gamma\gamma$ and $C|\pi^0\rangle = C|\gamma\gamma\rangle = |\gamma\gamma\rangle = |\pi^0\rangle$, thus $C_{\pi^0} = +1$. As $C|\gamma\rangle = -1$, the π^0 cannot decay to three photons, $\pi^0 \nrightarrow \gamma\gamma\gamma$.

1.6 *CPT* symmetry

Antiparticles can mathematically be treated as particles of the same properties *going backward in space and time*. This is a very important symmetry of Nature: the physical laws do not change when charge (C), space (P) and time (T) are simultaneously inverted:

- charge conjugation (i.e. changing particles into antiparticles), $C\psi(r,t) = \overline{\psi}(r,t)$;

- parity change (i.e. mirror reflection), $P\psi(r,t) = \psi(-r,t)$, and

- time reversal, $T\psi(r,t) = \psi(r,-t)K$ where K denotes complex conjugation.

This is called *CPT* invariance. As time reversal is an *anti-unitary* operation, *CPT* is also anti-unitary, it *conjugates the phase of the system*, but does not change any measurable properties. The electron-positron annihilation can be mathematically described as if an electron arrived, irradiated two or three photons and left backward in space and time. Using an analogy with

the electric current we call this *particle current*; in the above example the incoming electron and positron constitute a lepton current.

In the simplest case of particle collision two such particle currents exchange a boson. This is made possible by the *uncertainty principle* of Heisenberg, as it allows a violation of energy and momentum conservation for very small time and space intervals: $\Delta E \cdot \Delta t \geq \hbar/2$ and $\Delta p \Delta x \geq \hbar/2$, where Δ indicates a very small change in the quantity behind it and E, p, t, x the energy, momentum, time and space position. The very small value of the reduced Planck constant ($\hbar \simeq 1.055 \cdot 10^{-34}$ J·s) ensures that the conservation laws are fulfilled in the macro-world. The boson mediating the interaction can be *real* or *virtual* depending on whether or not it satisfies the on-shell condition $E^2 = m^2 c^4 + \vec{p}^2 c^2$. Effects of virtual particles can be detected experimentally: in the inelastic scattering of high energy electrons on each other quark pairs could be produced when a virtual photon emitted by one of the electrons is absorbed by a quark of a virtual quark-antiquark pair produced momentarily by another photon emitted by the other electron.

CPT invariance is supported by ample experimental evidence. Its role is so important in quantum field theory that according to some theorists it is impossible to test experimentally: in the case of observing a small deviation one should rather suspect the violation of a conservation law than *CPT* violation. In spite of this, there are considerable efforts to test it experimentally. The most precise of those tests is the very small possible relative mass difference between neutral kaon and anti-kaon which is less than 10^{-18}. The European Particle Physics Laboratory, CERN has built the *Antiproton Decelerator* facility in 1999 with the aim to test *CPT* invariance using precision spectroscopy of antihydrogen, the bound state of an antiproton and a positron and also that of anti-protonic atoms where an electron is replaced by an antiproton. The latter measures the mass and charge of the antiproton (*antimatter physics*).

If *CPT* invariance is indeed a fundamental symmetry of nature, then the violation of time reversal is equivalent to the violation of the combined *CP* symmetry. We shall see later the weak interaction breaks not only *P* (maximally), but also *CP* (a little). As a result, time invariance is also violated by the weak interaction, in contrast to classical mechanics.

1.7 Isospin and strangeness

One of the earliest observations implying an inner structure of particles thought to be elementary is the similarity of the proton and the neutron:

these have almost the same mass and apart from a charge effect the strong interaction within the atomic nucleus affects them identically. *Heisenberg* introduced the concept of the *nucleon* which has two eigenstates, the proton and the neutron. This needed a new quantum number characterizing it; as its symmetry properties are identical to those of the spin he called it the *isospin I* from isotopic spin (isobaric would be more precise as isotopes have different numbers of nucleons whereas isobaric nuclei have the same numbers of nucleons). The nucleon has an isospin $I = \frac{1}{2}$, the proton is the nucleon state with $I_3 = +\frac{1}{2}$ and the neutron[3] is that of $I_3 = -\frac{1}{2}$.

With the development of experimental methods many strongly interacting particles, *hadrons* were observed and all had characteristic isospins, i.e. all could be arranged in groups of particles of similar properties but different charges according to their isospins. The nucleon has an isospin $I = \frac{1}{2}$ and two similar states, with $I_3 = \pm\frac{1}{2}$. The lightest hadron, the π-*meson* or *pion* has $I = 1$ with three eigenstates (I_3 = -1, 0 and +1) and three charge states π^+, π^0 and π^-. The Δ hyperon has $I = \frac{3}{2}$:

$$\Delta^-(I_3 = -\frac{3}{2}), \ \Delta^0(I_3 = -\frac{1}{2}), \ \Delta^+(I_3 = +\frac{1}{2}), \ \Delta^{++}(I_3 = +\frac{3}{2}).$$

A unit change of I_3 involves a corresponding unit change in charge.

Then a third quantum number, *strangeness S* was discovered. Pairs of particles were produced in collisions of energetic protons with probabilities characteristic of the strong interaction and lived long enough that they must have decayed via weak interactions. They were called V-particles as their tracks curved in the magnetic field of the detectors in opposite directions. To explain this *Murray Gell-Mann*, *Abraham Pais* and *Kazuhiko Nishijima* introduced *strangeness S* as a new additive quantum number which is conserved in strong interactions but not in weak reactions. For instance, the Σ^- hyperon ($S = -1$, $I = 1$) created in π^-p$\rightarrow$ K$^+\Sigma^-$ decays via $\Sigma^- \rightarrow$ nπ^- with a lifetime of $\tau \sim 10^{-10}$ s whereas the Δ^+ hyperon ($S = 0$) decays in $\Delta^+ \rightarrow$ nπ^+ with a lifetime of $\tau \sim 10^{-23}$ s. It was postulated that only the weak interaction can change the new quantum number.

Strangeness and isospin made together an $SU(3)$ group which made it possible to construct a unique frame for all known particles. In order to explain this, *Murray Gell-Mann* and *George Zweig* suggested the *quark* model of hadrons. Using three new elementary fermions, three quarks (Table 1.2), all observed hadrons could be described. Isospin became the

---

[3]In nuclear physics often a converse convention is used and $I_3 = +\frac{1}{2}$ is associated with the neutron.

quantum number of the two lightest quarks and because of the analogy to the spin the $I_3 = +\frac{1}{2}$ state was named *up quark* with the sign u and the $I_3 = -\frac{1}{2}$ state *down quark*, d. The third quark's quantum number is the strangeness, so that is the *strange* (s) quark. The isospin and strangeness, characterizing the various kinds of quarks are called *flavour* quantum numbers.

The quark model postulates that quarks can bind together only in two ways: in quark-antiquark pairs, those are called *mesons*, and three-quark states, those are the *baryons*. As the quarks have spin $\frac{1}{2}$, naively we expect that mesons are bosons and baryons are fermions. Quarks have baryon number $\frac{1}{3}$ and fractional electric charges: in units of elementary charge e the u quark has charge $+\frac{2}{3}$ while the d and s quarks $-\frac{1}{3}$. This of course gives the proper charges to the proton p = [uud] and the neutron n = [udd] or the pions: $\pi^+ = [u\bar{d}]$, $\pi^0 = \frac{1}{\sqrt{2}}[u\bar{u} + d\bar{d}]$, $\pi^- = [\bar{u}d]$. Thus the third component of the isospin is directly connected to the charge, as its unit increase means replacing a d by a u quark, i.e. increasing the total charge by $+\frac{2}{3} - (-\frac{1}{3}) = 1$.

quark	J	e_q	B	I_3	S	$Y = B + S$
u	$\frac{1}{2}$	$+\frac{2}{3}$	$\frac{1}{3}$	$\frac{1}{2}$	0	$+\frac{1}{3}$
d	$\frac{1}{2}$	$-\frac{1}{3}$	$\frac{1}{3}$	$-\frac{1}{2}$	0	$+\frac{1}{3}$
s	$\frac{1}{2}$	$-\frac{1}{3}$	$\frac{1}{3}$	0	-1	$-\frac{2}{3}$

Table 1.2: The first three quarks (up, down and strange): their spin J, electric charge e_q, baryon number B, isospin third component I_3, strangeness S and hypercharge $Y = B + S$.

Strangeness and isospin constitute together an $SU(3)$ group which made it possible to construct a unique frame for all known particles. Gell-Mann and Zweig proposed in 1964 the quark model with the first three quarks (Table 1.2). The quark model postulated that quarks cannot exist free, only in bound states of two combinations: the three-quark bound states make baryons and the quark+antiquark states mesons. As the quarks are fermions ($J = \frac{1}{2}$), the baryons are also fermions with baryon number $B = 1$ while the mesons are bosons with $B = 0$. The proton is a [uud], the neutron a [udd] ground state (i.e. $J = \frac{1}{2}$ with zero orbital momentum) whereas the pions are the lightest $[q\bar{q}']$ (q, q' = u, d) combinations.

Exercise 1.1
What invariance principles are violated by the weak, electromagnetic and colour interactions?

Exercise 1.2
What are the analogies and differences between spin and isospin?

Exercise 1.3
How can the three-dimensional spin be characterised by two independent quantities?

Exercise 1.4
What gauge symmetry facilitates the conservation of electric charge and fermion number?

Chapter 2

What is measured in experiment?

MOTTO:

I was brought up to look at the atom as a nice hard fellow, red or grey in colour, according to taste.

(Ernest Rutherford)

Physics is experimental science, in particle physics every single statement has to be based on experimental observations. In high energy physics the two most important experimentally measurable quantities are the cross section and the resonance with its invariant mass and width.

2.1   Cross section

The probability of an interaction in accelerator experiments of nuclear and particle physics is usually characterized by the ratio of the measured transition probability of the reaction in unit time, and the intensity of the bombarding beam, the *flux*:

$$\sigma = W/\Phi,$$

15

measured in units of *cross section* (see Fig. 2.1).

The flux of a beam, $\Phi = n_b \cdot v_b$ is the number density times velocity of the particles in a beam, number of particles divided by cross section and time. The σ cross section of a reaction is measured in units of *barn* (1 barn = 10^{-28} m^2). That unit comes from atomic physics and it is very large in particle physics (that is how it got its name), so large

Figure 2.1: Cross section characterizing interaction in particle scattering

that in high energy physics we most often express our measured cross sections in pico-barn (1 pb = 10^{-12} barn) or femto-barn (1 fb = 10^{-15} barn).

When the interaction is perturbative, i.e. the Hamilton operator can be written in the form $H = H_0 + H'$ with eigenvalues $E' \ll E_0$, the transition probability between an initial and a final state can be written as

$$W(i \rightarrow f) = \frac{2\pi}{\hbar} |M_{if}|^2 \rho_f$$

where $\rho_f = \frac{dn}{dE_{CM}}$ is the density of final states in unit centre-of-mass energy and $M_{if} \approx \int \psi_f^* H' \psi_i d\tau$ is the transition matrix element, the overlap between the two approximate wave functions. As the strong and electromagnetic interactions are invariant under CP (charge and parity) reflection, CPT invariance, which is supposed to be valid in field theory, demands that they should also be invariant against time reflection T, and so $|M_{if}|^2 = |M_{fi}|^2$ (the principle of *detailed balance*).

In a centre-of-mass system a non-relativistic $a + b \rightarrow c + d$ particle scattering reaction will have the cross section

$$\sigma = \frac{W}{n_a v_i} = \frac{1}{\pi \hbar^4} |M_{if}|^2 \frac{(2S_c + 1)(2S_d + 1)}{v_i v_f} p_f^2$$

where $p_f = |\vec{p}_c| = |\vec{p}_d|$ is the final state momentum, $n_a = 1$ is the number of scattered particles, $v_i = |\vec{v}_a - \vec{v}_b|$ and $v_f = |\vec{v}_c - \vec{v}_d|$ are the relative velocities. The density of available final states will be

$$\frac{dp_f}{dE_0} = \frac{E_c E_d}{p_f E_0} \approx \frac{1}{v_f} .$$

2.2 Resonance

A simple, structureless, unstable system will have an exponential decay law

$$|\psi(t)|^2 = |\psi(0)|^2 e^{-\Gamma t} \tag{2.1}$$

with a lifetime $\tau = \Gamma^{-1}$ where Γ is the decay rate. The state function of the system will have a time evolution $\psi(t) \sim \psi(0)e^{-iMt}e^{-\Gamma t/2}$. Here we use the natural units of particle physics . In SI units $\tau = \hbar/\Gamma \simeq 6.582 \cdot 10^{-22}/\Gamma$ s where the Γ energy is measured in MeV. The time development of the system (assuming a plain wave initial state) is $\psi(t) = \psi(0)e^{-iMt}e^{-\Gamma t/2}$, and its energy amplitude will be the Fourier transform of the time amplitude:

$$\chi(E) = \int_0^\infty \psi(t)e^{iEt}\,dt = \int_0^\infty e^{i(E-M)t}e^{-\Gamma t/2}\,dt = \frac{1}{i(E-M)-\Gamma/2}$$

The result of the Fourier transformation is a probability distribution, which appears in the measurement as a *Lorentz curve*:

$$|\chi(E)|^2 = \frac{1}{(E-M)^2 + \Gamma^2/4} \tag{2.2}$$

This is the *Breit-Wigner* resonance (Fig. 17.2, left): an energy distribution with a maximum at the M mass of the decaying particle and a Γ width corresponding to its decay probability. New particles can be discovered by observing the Breit-Wigner resonances of their decays, those of course have to be at the same (so-called *invariant*) mass in the different decay channels.

One of the most important resonances in high energy physics is the Z peak in electron-positron collisions (Fig. 17.2). Two colliding beam accelerators, LEP at CERN and SLC at Stanford were especially built to study it, and they provided an incredible wealth of information for testing and confirming the standard model, the theory of particle physics.

We have shown above how the lifetime of a decaying particle is connected to its energy spectrum. In low-energy physics exponential decay curves of the type (2.1) can be directly measured by measuring the time difference between the birth and decay of a system. In high energy physics the reactions are usually much too fast for that, so the lifetimes have to be estimated by measuring the width of the mass resonance of the decaying particle.

Exercise 2.1
Why can we use cross sections to characterize interactions in particle scattering?

Exercise 2.2
How can we discover a new particle by measuring energy in particle scattering?

Exercise 2.3
How can one estimate the lifetime of a decaying particle by measuring the energy of its decay products?

Chapter 3

Quark model

3.1 Coloured quarks

The quark model, although very successful in explaining particle properties, had serious inconsistencies. Nobody understood, for instance, why only those postulated two kinds of bound states (3-quark and quark + antiquark combinations) exist, why there are no free quarks in Nature and why there could be several quarks in a particle in exactly the same quantum state in spite of the Pauli principle. An excellent example for the latter is the Δ^{++} particle: it has double charge and spin $\frac{3}{2}$ and so it consists of three u quarks in the same spin state.

In the course of the history of particle physics, whenever some new unexplained behaviour was observed, often new quantum numbers were introduced. Good examples for those are isospin and strangeness. In order to explain the magic combination of three identical quarks, a new quantum number was suggested: *colour charge*, in analogy with the three basic colours seen by our eye, with three possible values, red (R), green (G) and blue (B).
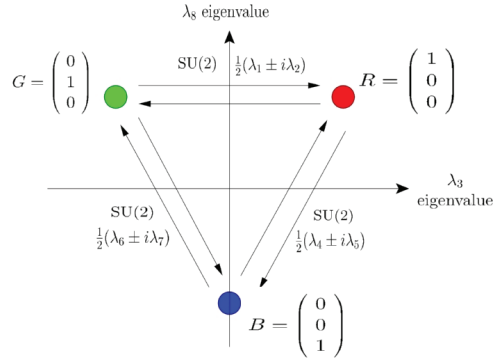
Figure 3.1:
Colour-SU(3) with its three eigenstates and SU(2)-type stepping operators

The quarks have colour charges whereas anti-quarks have anti-colour ones. Colour solved all those problems: the new quantum number made each quark state in the observed particles specific and so the Pauli principle was fulfilled. Moreover, colour is considered to play the same role for the strong quark–quark interaction as the electric charge in electrodynamics: it is the strong charge. The existence of all observed particles is consistent with the condition that only *colourless* (white) states are allowed in Nature. This condition accounts for the non-existence of free quarks (*quark confinement*), as only the combinations of colour+anti-colour (those bound states are the mesons) or that of all three colours (baryons) can exist. This is an algebraic explanation for quark confinement. The dynamical understanding is far more complex.

Thus there is a good analogy between the strong colour charge of quarks and colour vision in humans. The three eigenstates of the quark charges correspond to the three basic colours and strong anti-charge is the analogy of the complementary colour. The equilibrium mixture of the three charges or the mixture of charge + anti-charge will be neutral, colourless in colour vision.

In order to get free particles we have to construct colourless states. According to the experimental observations colour makes the state functions of the composite bosons, the mesons symmetric and of the baryons, as required for fermions, antisymmetric. For the mesons it is of the form $\frac{1}{\sqrt{3}}(R\overline{R} + G\overline{G} + B\overline{B})$ and for the baryons $\frac{1}{\sqrt{6}}(RGB - RBG + BRG - BGR + GBR - GRB)$. Anti-baryons have the colour arrangement $\frac{1}{\sqrt{6}}(\overline{RGB} - \overline{RBG} +$

$\overline{BRG} - \overline{BGR} + \overline{GBR} - \overline{GRB}$). Thus when building the state function of a mesonic or baryonic system, we just have to construct a symmetric (space ⊗ spin ⊗ flavour) function and let the colour part make it symmetric or asymmetric as needed.

The quark model was very successful: it explained all observed hadrons and correctly predicted the existence of new hadronic states. There are no exceptions, like e.g., states with charges $Q > 2$ or isospin $I > 3/2$.

3.2 Colour interaction, QCD

The strong interaction is interpreted as an interaction of colour charges. As this means an exchange of colour between quarks, its mediators should have the form colour+anti-colour. There are 9 such combinations, but one of them does not exchange colour, drop out as colourless, so there are eight independent ones, called *gluons*. The existence of 8 gluons corresponds to the 8 generators (denoted as $\lambda_1 \ldots \lambda_8$ in Fig. 3.1) of the related $SU(3)$ group. Comparison of the colour interaction with electromagnetism shows similarities and differences as well. The gluons and the photon are similar as they carry neither electric charge nor isospin, have zero mass and their spin-parity is $J^P = 1^-$. However, while the photon does not carry the charge of its mediated electromagnetic interaction, the gluon carries the strong charge, colour. As a result, there is a strong gluon-gluon interaction. Photons can freely propagate whereas gluons cannot: they must convert into colourless free hadrons. When we try to separate two coloured objects, quarks or gluons, more and more energy is consumed and more and more gluons are produced until the energy is sufficient to break up and unite all coloured particles into hadrons. This *fragmentation* or *hadronization* goes on until no free colour remains. An electric charge when watched from a large distance is partially screened due to vacuum polarization as different charges attract and identical ones repulse each other, whereas the colour grows with distance as all colours attract each other the same way. Colour interaction strengthens with increasing distance while the electromagnetic one weakens.

3.3 Reminder: summing up spins

When constructing a meson we add up $\frac{1}{2}$ spins: $S_1 = S_2 = \frac{1}{2}$; $S = S_1 + S_2 = 0$ or 1: $2 \otimes 2 = 3 \oplus 1$, thus the result is 4 states, a triplet and a singlet. The eigenstates of the angular momentum operator $\vec{J} = (J_1, J_2, J_3)$ are of the form $|S, M >$ where S is the spin and M is its projection.

Triplet states:

$$\left.\begin{array}{l}|S = 1, M = +1 >= \uparrow\uparrow \\ |S = 1, M = \ 0 >= \frac{1}{\sqrt{2}}(\uparrow\downarrow + \downarrow\uparrow) \\ |S = 1, M = -1 >= \downarrow\downarrow\end{array}\right\} \qquad (3.1)$$

Singlet state:

$$|S = 0, M = \ 0 >= \frac{1}{\sqrt{2}}(\uparrow\downarrow - \downarrow\uparrow) \qquad (3.2)$$

The conserved quantities and eigenvalues of angular momentum are: $J^2|S, M >= S(S + 1)|S, M >$ and $J_3|S, M >= M|S, M >$.

The projections are increased and decreased with the stepping operators: $J_\pm = J_1 \pm i J_2$ such that $J_\pm|j, m >= \sqrt{j(j + 1) - m(m \pm 1)}|j, m \pm 1 >$.

3.4   Lightest mesons

From the two light quarks, u and d one can construct 4 $J^P = 0^-$ *pseudo-scalar* (zero spin, negative parity) mesons ($2 \otimes 2 \Rightarrow 3 \oplus 1$): $I = I_1 + I_2 = \frac{1}{2} + \frac{1}{2} = (0, \ 1)$ (Table 3.1).

I	I_3	meson state	charge	mass (MeV
1	+1	$u\bar{d} = \pi^+$	+1	139.6
1	-1	$-\bar{u}d = \pi^-$	−1	139.6
1	0	$\sqrt{\frac{1}{2}}(u\bar{u} - d\bar{d}) = \pi^0$	0	135.0
0	0	$\sqrt{\frac{1}{2}}(u\bar{u} + d\bar{d}) = \eta^0$	0	547.9

Table 3.1: The lightest mesons: the three pions, and the η^0.

3.5   Meson nonet (flavour $SU(3)$)

Figure 3.2 shows how the three lightest quarks can combine into the pseudo-scalar mesons. $\bar{u}u$, $\bar{d}d$ and $\bar{s}s$ can be combined in three different ways to get symmetric bound states as shown in Table 3.2. This scheme also shows that the Y hypercharge is a real charge as it changes sign when going from K^0 to $\overline{K^0}$, i.e. between a neutral particle and its antiparticle.
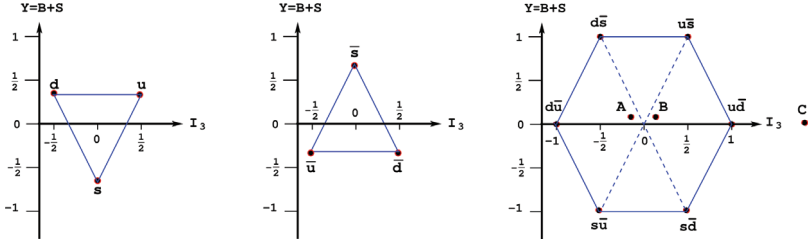
Figure 3.2: Construction of the meson nonet of the three light quarks ($3 \otimes 3 = 8 \oplus 1$). A, B and C are the three possible symmetric combinations of $\bar{u}u$, $\bar{d}d$ and $\bar{s}s$.

$(I = 0, I_3 = 0)$	$C = \frac{1}{\sqrt{3}}(u\bar{u} + d\bar{d} + s\bar{s})$	(singlet: η_1)
$(I = 1, I_3 = 0)$	$A = \frac{1}{\sqrt{2}}(u\bar{u} - d\bar{d})$	(triplet: π^0)
$(B \perp A, B \perp C)$	$B = \frac{1}{\sqrt{6}}(u\bar{u} + d\bar{d} - 2s\bar{s})$	(rest: η_8)

Table 3.2: Symmetric combinations of $\bar{u}u$, $\bar{d}d$ and $\bar{s}s$.

The quark flavour states of the meson nonet have to be combined with spin states. If the spins of the quarks are anti-parallel they will make $J^P = 0^-$ pseudo-scalar mesons, parallel spins make $J^P = 1^-$ vector mesons. Orbital momentum L between the quarks will change the state parity $P = -(-1)^L$.

The lightest, ground-state, neutral pseudo-scalar mesons are listed in Table 3.2. States B and C have the same quantum numbers ($I = 0$), they will mix and create two mass eigenstates: $\eta_1, \eta_8 \Rightarrow \eta, \eta'$ and the latter can be observed in experiment:

$$\left. \begin{array}{l} \eta = \eta_8 \cos \Theta_p - \eta_1 \sin \Theta_p \\ \eta' = \eta_8 \sin \Theta_p + \eta_1 \cos \Theta_p \end{array} \right\}$$

where $\Theta_p \approx 10°$ is the mixing angle. In particle physics all states that may mix happen to mix with mixing angles to be determined experimentally. We shall see more such cases later.

As the $SU(3)$ group corresponds to 3 $SU(2)$ subgroups, in the scheme drawn in Fig. 3.2 in addition to the usual $SU(2)$ isospin connected to the u↔d exchange one can define similar symmetries for u↔s and d↔s; historically, the u↔d $SU(2)$ was called I−spin, the d↔s $SU(2)$ U−spin and the u↔s $SU(2)$ V−spin, but these obsolete quantities are not used any more.
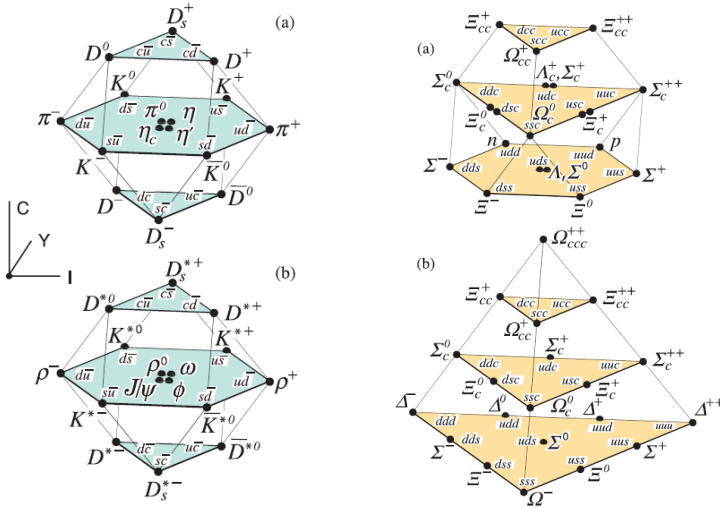
Figure 3.3: Construction of the lightest hadrons using the first four quarks. Left: pseudo-scalar (a) and vector (b) mesons ; right: baryons of octet (a) and decuplet (b) structure [Beringer et al., 2012]). Note the nucleons at the back of the baryon octet.

Adding the fourth quark, charm to the set we get an $SU(4)$ scheme. In the left panel of Fig. 3.3 each horizontal plane corresponds to the Y vs. I_3 $SU(3)$ plane of Fig. 3.2, the vertical axis shows the charm quark content. In addition to the quark compositions also the historic names[1] of the mesons are noted. The u+d $SU(2)$ is quite good symmetry as those quarks have very little mass, of the order of 5 MeV. Flavour $SU(3)$ for u+d+s is already broken as the s quark is much heavier, around 100 MeV. The c quark is even heavier, $M_c \simeq 1275$ MeV, so flavour-$SU(4)$ cannot really be used for quantitative predictions. We have to point out here that the mass of our macroscopic world is predominantly due to the energy content of the nucleons, the masses of the u and d quarks contribute very little.

There are quite a few meson nonets observed (Table 3.3). Generally, when we speak of a particle, we always write down its mass to make the situation unambiguous. For instance, the ground-state vector mesons ($J^P = 1^-$) are $\rho(770)$, $K^*(892)$, $\omega(782)$ and $\phi(1020)$ (in Table 3.3 average mass values are listed).

_____

[1]Enrico Fermi: *Young man, if I could remember the names of these particles I would have been a botanist.*

L ($q\bar{q}$)	Spin ($q\bar{q}$)	J^{PC}	Nonet			$<$mass$>$
			$I = 1$	$I = \frac{1}{2}$	$I = 0$	MeV
0	0	0^{-+}	π	K	η, η'	500
	1	1^{--}	ρ	K*	ω, ϕ	900
1	0	1^{+-}	b_1	K_{1B}	h_1, h_1'	1250
	1	0^{++}	a_0	K_0^*	f_0, f_0'	1150
	1	1^{++}	a_1	K_{1A}	f_1, f_1'	1300
	1	2^{++}	a_2	K_2^*	f_2, f_2'	1400
2	..	..	..	..	..	..
	..	..	..	..	..	..

Table 3.3: Some of the observed meson nonets. $\omega \approx \frac{1}{\sqrt{2}}(u\bar{u} - d\bar{d})$ and $\phi \approx s\bar{s}$

flavour$-SU(3)$	$\otimes$	spin$-SU(2)$
(qqq)		$\frac{1}{2} + \frac{1}{2} + \frac{1}{2}$ $(L = 0)$
$3 \otimes 3 \otimes 3$		$2 \otimes 2 \otimes 2$
$(10 \oplus 8 \oplus 8 \oplus 1)$	$\otimes$	$(4 \oplus 2 \oplus 2)$
TS MS MA TA		TS MS MA

Table 3.4: Three-quark combinations to create ground-state baryons.

3.6 Ground-state baryons

The construction of baryons is similar to that of the mesons, but using three quarks. They can be composed of symmetric flavour-$SU(3) \otimes$ spin$-SU(2)$ combinations (see Table 3.4).

When we switch the positions of the first two quarks in the bound states of three, we shall have the following symmetry situations:

Total symmetry (TS) $(123) = (213) = (132)$
Mixed symmetry (MS) $(123) = (213) = -(132)$
Mixed antisymmetry (MA) $(123) = -(213) = (132)$
Total antisymmetry (TA) $(123) = -(213) = -(132)$

As colour makes the baryon states antisymmetric, we have to choose symmetric flavour $\otimes$ spin states:

$$\text{TS} \otimes \text{TS} = (10 \otimes 4): \text{ 4 decuplets, } J = \tfrac{3}{2}$$
$$\tfrac{1}{\sqrt{2}}(\text{MS} \otimes \text{MS} + \text{MA} \otimes \text{MA}) = (8 \otimes 2): \text{ 2 octets, } J = \tfrac{1}{2}$$

3.7   Baryon multiplets

Figure 3.3 (right) shows the construction of the lightest baryons of the first four quarks [Patrignani et al., 2016] for the cases of an octet and a decuplet. Generally, as a rule, we denote mesons with lower-case, baryons with upper-case Greek letters (except the first observed ones). The masses of baryons increase by about 200 MeV when adding an s quark, and that is an indication of the mass of the s quark. Changing the spin of a baryon from $\tfrac{1}{2}$ to $\tfrac{3}{2}$ i.e. making the quark spins all parallel adds $\Delta m \sim +300$ MeV to the mass. Baryons, of course, can be excited. Spin states up to $J = L + S = \tfrac{9}{2}$ were observed.

3.8   Three families of fermions

A big step from the simple quark model to the standard model of particle physics was made by *Sheldon Glashow*, *Jon Iliopoulos* and *Luciano Maiani* in 1970 [Glashow et al., 1970] by introducing what became known as the *GIM mechanism*. On the basis of various experimental observations they postulated that the weak interaction arranges the quarks and leptons in pairs, *weak isospin doublets* and they predicted the existence of a fourth quark, the *charm* (c) quark (Table 3.5), with a charge of $+\tfrac{2}{3}$. In 1974 two groups, [Augustin et al., 1974] and [Aubert et al., 1974], succeeded at the same time in discovering the (c$\overline{\text{c}}$) bound state (they named it differently so it is now called J/ψ meson) and for that *Burton Richter* and *Samuel Ting* received the Nobel Prize in 1976.

According to the GIM mechanism there should be as many lepton pairs as quark pairs (these groups are called *families*), because in order to prevent the theory from having anomalies[2] the sum of electric charges of all particles has to be zero. This is fulfilled for each family (see Table 3.5) as the charge sum from the top down is $0 - 1 + 3 \cdot (\tfrac{2}{3} - \tfrac{1}{3}) = 0$, where the factor 3 stands for the number of quark colours. Of course, as soon as *Martin Perl's* group observed a third lepton, the τ (discovery in 1976, Nobel Prize in 1995) another pair of quarks were immediately predicted and much later discovered. Thus we have the menagerie of basic fermions listed in Table 3.5. The place of a fermion

---

[2]Their definition is given in Section 22.9.

	Family 1	Family 2	Family 3	charge	T_3
Leptons	$\begin{pmatrix} \nu_e \\ e \end{pmatrix}_L$	$\begin{pmatrix} \nu_\mu \\ \mu \end{pmatrix}_L$	$\begin{pmatrix} \nu_\tau \\ \tau \end{pmatrix}_L$	0 -1	$+\frac{1}{2}$ $-\frac{1}{2}$
Quarks	$\begin{pmatrix} u \\ d' \end{pmatrix}_L$	$\begin{pmatrix} c \\ s' \end{pmatrix}_L$	$\begin{pmatrix} t \\ b' \end{pmatrix}_L$	$+\frac{2}{3}$ $-\frac{1}{3}$	$+\frac{1}{2}$ $-\frac{1}{2}$

Table 3.5: Leptons and quarks, the three families of basic fermions. T_3 is the third component of the weak isospin, the rest of the notation is explained in the text step by step.

in the table is determined by its *weak isospin* (T) introduced in analogy of the isospin: for the upper particles its third component has an eigenvalue of $T_3 = +\frac{1}{2}$, for the lower ones it is $T_3 = -\frac{1}{2}$. Thus the pairs are *weak isospin doublets*. Note that the weak isospin is quite different from isospin: the latter is a property of the two lightest quarks only, whereas all fermions have a weak isospin. Moreover, isospin is a quantum number of the strong interaction whereas weak isospin is related to the weak interaction.

At this point one could ask how many more such families are hidden by Nature at higher energies. The answer was given by experiments performed on LEP of CERN: none, there are three families only. The proof is that the Z-boson produced in those high-energy collisions can decay in various ways and the standard model quantitatively describes all of them; detecting all products the only unknown is the number of different neutrinos which cannot be seen there. By comparing the total decay width with those of the detected modes one can deduce the contribution of the invisible ones and it turned out that we have just three types of light neutrinos (with masses lower than half of the mass of the Z-boson) and so three families only (a possible, unobservable heavy neutrino would not carry a charged lepton and quarks, because those should have been observed already from their low–energy effects). The number of light neutrino flavours is limited to three by cosmology as well.

Only the fermions of the first family are stable and therefore those build our observable world; the heavier leptons and quarks of the second and third

families decay quickly to lighter ones. For the quarks the eigenstates of
weak and strong interactions are different. The bound states of quarks, the
hadrons are produced in strong interaction. These particles are identified by
their masses, so if we speak of a given quark, we mean their mass eigen-
states. However, the weak isospin doublets should contain weak eigenstates,
mixtures of mass eigenstates, symbolized by the prime behind their symbols
in Table 3.5. It was shown by *Makoto Kobayashi* and *Toshihide Maskawa*
(discovery in 1973, Nobel Prize in 2008) that in order to explain CP-violation
(see Section 12.4) there have to be at least 3 families of quarks. It is sufficient
to mix one row of quarks, the lower ones are chosen.

According to our present knowledge Table 3.5 contains all of the basic
fermions of the standard model. The reader should not be frightened by the
extraordinary caution of the above statement. Theoretically, the standard
model was extended in many-many ways and all those extensions predicted
numerous hypothetical new basic particles [Collins et al., 1989]. Although
till now no real evidence was found against the standard model, there are
many possible extensions that do not contradict to the present experimental
data, and so one cannot *a priori* exclude their validity.

Exercise 3.1
*How many different quarks are in the standard model? Explain in what
sense 3, 6, 12, 18 and 36 could be all correct answers.*

Exercise 3.2
*How could electromagnetic interaction explain the fractional charges of the
quarks?*

Exercise 3.3
How can the bound state of 3 spin-$\frac{1}{2}$ quarks have a spin $\frac{9}{2}$?

Exercise 3.4
Is there any direct evidence for the 3 quark colours?

Exercise 3.5
*Quark confinement is explained by gluon exchange. How could the 983 MeV
proton mass created by three quarks of 5–15 MeV masses?*

Exercise 3.6
*The existence of gluons is shown by detecting 3-jet events in lepton collisions.
Why must the 3 jets be in the same plane?*

Exercise 3.7
Compare and explain the signs of the terms in Eqs. (3.1, 3.2) *and Table* 3.1.
Hint: *consider symmetries.*

Exercise 3.8
How can the quark model explain the non-zero magnetic moment of the neutron?

Chapter 4

Dirac equation

4.1 Covariant formalism

Paul Dirac composed his famous equation for fermions when he tried to find a linear equation of motion for the electron. The Dirac equation is based on the *covariant formalism*: it works with covariant and contravariant 4-vectors where component 0 is related to time and energy and the other three components make the usual three-dimensional vectors of space and momentum. The covariant 4-vectors have their indices as subscripts $A_\mu = (A^0, -\vec{A})$, whereas the contravariant ones as superscripts: $A^\mu = (A^0, +\vec{A})$. The symbol of derivation has the opposite rule: $\partial_\mu = (\frac{\partial}{\partial t}, +\vec{\nabla})$ and $\partial^\mu = (\frac{\partial}{\partial t}, -\vec{\nabla})$ where $\vec{\nabla} = (\partial_1, \partial_2, \partial_3)$ is the vector operator of spatial derivation in

three space dimensions.

The same Greek index repeated as super- and subscript means a scalar product of two 4-vectors (with an implied sum $\sum_{\mu=0}^{3}$) and it can be written in different ways: $A \cdot B = A^0 B^0 - \vec{A} \cdot \vec{B} = A_\mu B^\mu = A^\mu B_\mu = g_{\mu\nu} A^\mu B^\nu = g^{\mu\nu} A_\mu B_\nu$ where

$$g_{\mu\nu} = g^{\mu\nu} = \begin{pmatrix} 1 & 0 & 0 & 0 \\ 0 & -1 & 0 & 0 \\ 0 & 0 & -1 & 0 \\ 0 & 0 & 0 & -1 \end{pmatrix} \qquad (4.1)$$

is the *metric tensor* that converts contravariant and covariant vectors into each other and defines the length of a vector in Minkowski space-time.

The eigenfunctions of the Dirac equation are four-component *spinors* ψ. The components are in the sequence: particle with spin up, particle with spin down, antiparticle with spin up, antiparticle with spin down[1]. Antiparticles have negative rest energies (masses). As the concept of spinors was originally connected to the SU(2) eigenvectors of spin, the Dirac spinors are often called *bispinors*.

$$\begin{pmatrix} 1 \\ 0 \\ 0 \\ 0 \end{pmatrix} \begin{pmatrix} 0 \\ 1 \\ 0 \\ 0 \end{pmatrix} \begin{pmatrix} 0 \\ 0 \\ 1 \\ 0 \end{pmatrix} \begin{pmatrix} 0 \\ 0 \\ 0 \\ 1 \end{pmatrix} \quad \begin{matrix} \uparrow \\ \downarrow \\ \uparrow \\ \downarrow \end{matrix} \quad \begin{matrix} m \\ m \\ -m \\ -m \end{matrix}$$

4.2　Gamma matrices

The Dirac–Pauli formalism builds the Dirac equation using the 4×4 γ-matrices. They are defined as $\gamma_\mu = (\beta, \beta\vec{\alpha})$ where $\beta = \begin{pmatrix} I & 0 \\ 0 & -I \end{pmatrix}$ and $\vec{\alpha} = \begin{pmatrix} 0 & \vec{\sigma} \\ \vec{\sigma} & 0 \end{pmatrix}$. Here $I = \begin{pmatrix} 1 & 0 \\ 0 & 1 \end{pmatrix}$ is the 2×2 unit matrix and σ_i are Pauli's spin matrices:

$$\sigma_1 = \begin{pmatrix} 0 & 1 \\ 1 & 0 \end{pmatrix} \quad \sigma_2 = \begin{pmatrix} 0 & -i \\ i & 0 \end{pmatrix} \quad \sigma_3 = \begin{pmatrix} 1 & 0 \\ 0 & -1 \end{pmatrix}.$$

$\gamma_\mu (\mu = 0 \ldots 3)$ is treated as a space-time 4-vector. There is an additional gamma matrix which plays a key role in this formalism: $\gamma^5 \equiv i\gamma^0\gamma^1\gamma^2\gamma^3 = \begin{pmatrix} 0 & I \\ I & 0 \end{pmatrix}$. γ^4 is not used here; it replaces γ^0 in other notation systems.

---

[1]The four components of the spinor have absolutely no relation to the four-vector of space-time.

4.3 Bilinear products of spinors

In the physical quantities the following bilinear products of spinors can take place (Table 4.1):

Type	form	components	effect of P reflection
Scalar	$\overline{\psi}\psi$	1	sign +
Vector	$\overline{\psi}\gamma^{\mu}\psi$	4	spatial comp. −
Tensor	$\overline{\psi}\sigma^{\mu\nu}\psi$	6	
Axial vector	$\overline{\psi}\gamma^{\mu}\gamma^{5}\psi$	4	spatial comp. +
Pseudo-scalar	$\overline{\psi}\gamma^{5}\psi$	1	sign −

Table 4.1: Bilinear products of spinors, component numbers and the effect of coordinate reflection.

In Table 4.1 $\overline{\psi} = \psi^{\dagger}\gamma^0$ is Dirac's *adjoint spinor* and in the definition of the tensor $\sigma^{\mu\nu} = \frac{i}{2}(\gamma^{\mu}\gamma^{\nu} - \gamma^{\nu}\gamma^{\mu})$.

The theory of weak interactions is called V-A (vector minus axial-vector) theory as the weak charged current has the form $\overline{\psi}\gamma^{\mu}(1 - \gamma^{5})\psi$.

4.4 Free fermions

The standard model uses the Lagrange-Hamilton formalism of field theory. The Lagrangian is $L = T - V$ where T and V are the kinetic and potential energy densities of the particle. The classical Lagrangian depends on the general coordinates of the particle, $L(q, \dot{q}, t)$ whereas in field theory it becomes a Lagrangian energy density $L(\Phi, \frac{\partial \Phi}{\partial x_{\mu}}, x_{\mu})$ with the $\Phi(x_{\mu})$ field depending on space-time four-vector x_{μ} and on $\partial_{\mu}\Phi \equiv \frac{\partial \Phi}{\partial x^{\mu}}$.

The Lagrangian is completely equivalent to the equation of motion, but it shows the symmetry properties of the system better. The Dirac Lagrangian of the free fermion is

$$L = i\overline{\psi}\gamma^{\mu}\partial_{\mu}\psi - m\overline{\psi}\psi \tag{4.2}$$

where $\overline{\psi} \equiv \psi^{\dagger}\gamma^0$ is the *Dirac-adjoint spinor*. Applying the Euler-Lagrange equation,

$$\delta L = \partial_{\mu}\left[\frac{\partial L}{\partial(\partial_{\mu}\psi)}\right] - \frac{\partial L}{\partial\psi} = 0, \tag{4.3}$$

to Lagrangian (4.2) one immediately obtains the Dirac equation for the adjoint spinor:

$$i\partial_\mu \overline{\psi} \gamma^\mu + m\overline{\psi} = 0 \,.$$

Hermitian conjugation transforms it into the Dirac equation in its usual, covariant form:

$$[i\partial_\mu \overline{\psi} \gamma^\mu + m\overline{\psi}]^\dagger = -i\gamma^{\mu\dagger} \gamma^{0\dagger} \partial_\mu \psi + m\gamma^{0\dagger} \psi = -i\gamma^0 \gamma^\mu \partial_\mu \psi + m\gamma^0 \psi$$
$$= -\gamma^0 (i\gamma^\mu \partial_\mu \psi - m\psi) = 0 \,. \tag{4.4}$$

Thus the Dirac equation of the free fermion in its final form is

$$\boxed{(i\gamma^\mu \partial_\mu - m)\psi \equiv (i\slashed{\partial} - m)\psi = 0} \tag{4.5}$$

where we introduced the popular notation $\slashed{\partial} \equiv \gamma^\mu \partial_\mu$.

4.5 Lagrangians and equations of motion

In particle physics all equations of motion can be written in terms of the Lagrange formalism.

- A spinless, massive ($J = 0$, $m > 0$) real scalar particle has the Lagrangian $L = \frac{1}{2}(\partial_\mu \phi)(\partial^\mu \phi) - \frac{1}{2}m^2\phi^2$ which gives the Klein-Gordon equation: $\partial_\mu \partial^\mu \phi + m^2\phi = 0$.

- The Lagrangian of quantum electrodynamics for a j_μ current in interaction with a zero-mass A^μ vector field ($m_A = 0$, $J_A = 1$ spin) is

$$L = E_{\text{field}} - \text{current} \times \text{field} = -\frac{1}{4}F_{\mu\nu}F^{\mu\nu} - j_\mu A^\mu$$

  which yields Maxwell's equation in its covariant form: $\partial_\mu F^{\mu\nu} = j_\nu$ where $F_{\mu\nu} = \partial_\mu A_\nu - \partial_\nu A_\mu$ is the field strength tensor of the vector field.

- The Lagrangian of a vector field A^μ of non-zero mass $m_A > 0$ and spin $J = 1$ would be $L = -\frac{1}{4}F_{\mu\nu}F^{\mu\nu} - j_\mu A^\mu - \frac{1}{2}m^2 A_\mu A^\mu$, but such a field was never observed.

4.6   Conservation of fermion current

Let us add Dirac's equation multiplied from left by $\overline{\psi}$ and its adjoint equation multiplied from right by ψ:

$$\overline{\psi}[i\gamma^\mu \partial_\mu \psi - m\psi] + [i\partial_\mu \overline{\psi}\gamma^\mu + m\overline{\psi}]\psi = 0\,.$$

Using the rules of derivation we find $\partial_\mu(\overline{\psi}\gamma^\mu\psi) = 0$ which states that the total derivative of the four-vector $j^\mu = \overline{\psi}\gamma^\mu\psi$ is zero, i.e. it is a conserved quantity. In 3-vector notation it has the form $\frac{\partial j_0}{\partial t} - \sum_i \frac{\partial j_i}{\partial x_i} = \frac{\partial\rho}{\partial t} - \operatorname{div}j = 0$. Thus it is a continuity equation. We saw earlier that $\overline{\psi}\gamma^\mu\psi$ is the only vector constructed from the ψ spinor of the Dirac fermion, so that must be the fermion current that is conserved. The matter density of the fermion is $j^0 = \overline{\psi}\gamma^0\psi = \psi^\dagger\gamma^{0^2}\psi = \psi^\dagger I\psi = \sum_{i=1}^4 |\psi_i|^2$ and continuity means the change in matter density balances the current.

It can be shown that the same law can be deduced from the fact that the Dirac Lagrangian of the free fermion has a global $U(1)$ gauge invariance. $U(1)$ is the group of unitary ($U^\dagger U = 1$) 1×1 matrices i.e. of $U = e^{i\alpha}$ scalars. Indeed, the Dirac Lagrangian is invariant to the transformation $\psi \to e^{i\alpha}\psi$ where α is a real number. This is, of course, in accordance with Noether's theorem that any invariance of a Lagrangian with respect to a global continuous transformation leads to a conserved current. Thus the fermion charge is conserved. For instance, a lamp can emit any number of bosons (photons), but for that one has to bring fermions (electrons) there and carry them away. Neutron decay is a good example as well: $n \to p + e^- + \overline{\nu}_e$, where both the baryon and the lepton currents are separately conserved.

4.7   Isospin algebra and conservation

Isospin helps to perform two-nucleon calculations. As we saw before, the $SU(2)$ symmetry of isospin makes a triplet and a singlet isospin states of two nucleons, $(I = \frac{1}{2}) + (I = \frac{1}{2})$; $2 \otimes 2 = 3 \oplus 1$ (Table 4.2).

Figure 4.1 illustrates how isospin helps to calculate two-nucleon correlations. When corrected for the Coulomb-interaction differences between proton and neutron, the $^4\mathrm{He} + 2N$ systems have very similar masses. However, the whole isospin is also a good quantum number. Let us compare the production rates of deuterons and pions in the inelastic scattering of protons and neutrons on protons:

$$R = \frac{\sigma(\mathrm{pp} \to \pi^+\mathrm{d})}{\sigma(\mathrm{np} \to \pi^0\mathrm{d})} = ?$$

$$|I = 1, I_3 = +1 >= \text{pp}$$
$$|I = 1, I_3 = 0 >= \tfrac{1}{\sqrt{2}}(\text{pn} + \text{np}) \left.\right\} \quad \text{triplet states}$$
$$|I = 1, I_3 = -1 >= \text{nn}$$

$$|I = 0, I_3 = 0 >= \tfrac{1}{\sqrt{2}}(\text{pn} - \text{np}) \left.\right\} \quad \text{singlet state}$$

Table 4.2: Isospin eigenstates in two-nucleon systems
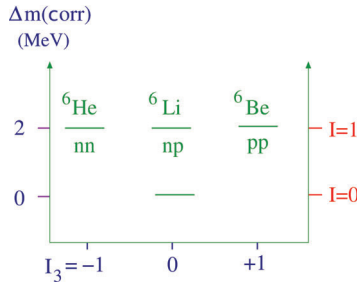
Figure 4.1: Nuclear masses of ^{4}He + NN isotopes as a function of isospin. The values are corrected for the proton-neutron differences.

where the σ cross sections[2] of the reactions are similar:

$$\sigma \propto \sum_I | < I', I_3'|A|I, I_3 > |^2 .$$

Here I, I_3 and I', I_3' are the whole isospin and its 3rd component in the initial and final states. Conservation laws dictate that $I' = I$; $I_3' = I_3$. We know the measured values $I_\pi = 1$ and $I_d = 0$. The first reaction:

$$\text{pp} \rightarrow \pi^+\text{d} : \quad |I = 1, I_3 = 1 > \rightarrow |I = 1, I_3 = 1 >$$

and the second one (see Table 4.2):

$$\text{np} \rightarrow \pi^0\text{d} : \quad \frac{1}{\sqrt{2}}(|I = 1, I_3 = 0 > - |I = 0, I_3 = 0 >) \rightarrow |I = 1, I_3 = 0 >$$

and thus $R = 1^2/(1/\sqrt{2})^2 = 2$ in agreement with the experimental data.

Similar considerations can explain that the deuteron, the bound state of a neutron and a proton exists whereas that of two neutrons does not.

---

[2]In high-energy physics the probability of a reaction is characterized by the effective cross section of the involved collision process, see in detail in Ch. 2

4.8 Nucleon as quark atom

How could the neutral neutron have a non-zero magnetic moment? Let us calculate the magnetic moments of the nucleons assuming that they consist of three quarks only and nothing else (we shall see later that this is a very rough approximation). We have to construct a symmetric spatial distribution function as colour will make it antisymmetric and that has no role in the magnetic moments. To make the state function symmetric we have to couple wave functions with symmetric flavour (p_S) to symmetric spin parts (M_S), or those with antisymmetric flavour (p_A) to antisymmetric spin ones (M_A). Here symmetry and antisymmetry are related to the exchange of the first two quarks:

$$|p> = \frac{1}{\sqrt{2}}[p_S \cdot \chi(M_S) + p_A \cdot \chi(M_A)].$$

Flavour ($I - SU(2)$): $\left\{ \begin{array}{l} p_S = \frac{1}{\sqrt{6}}[(ud + du)u - 2uud] \\ p_A = \frac{1}{\sqrt{2}}(ud - du)u \end{array} \right\}$

Spin ($J - SU(2)$): $\left\{ \begin{array}{l} \chi(M_S) = \frac{1}{\sqrt{6}}[(\uparrow\downarrow + \downarrow\uparrow)\uparrow - 2\uparrow\uparrow\downarrow] \\ \chi(M_A) = \frac{1}{\sqrt{2}}(\uparrow\downarrow - \downarrow\uparrow)\uparrow \end{array} \right\}$

where the arrows stand for spin-up and spin-down states.

After some cancellations we get for the state function of the proton three permutations:

$$|p\uparrow> = -\frac{1}{\sqrt{18}}(u\uparrow u\downarrow d\uparrow + u\downarrow u\uparrow d\uparrow - 2u\uparrow u\uparrow d\downarrow +$$
$$d\uparrow u\uparrow u\downarrow + d\uparrow u\downarrow u\uparrow - 2d\downarrow u\uparrow u\uparrow +$$
$$u\downarrow d\uparrow u\uparrow + u\uparrow d\uparrow u\downarrow - 2u\uparrow d\downarrow u\uparrow).$$

Let us try to estimate the magnetic moments of the nucleons considering the three *valence quarks* only. The magnetic moment of a quark is $\mu_q = \frac{e_q}{2m_q}$ where e_q and m_q are the charge and mass of quark q. Assuming that the two valence quarks have approximately the same mass,

$$\frac{\mu_u}{\mu_d} \approx \frac{e_u}{e_d} = \frac{2/3}{-1/3} = -2.$$

The magnetic moment of the proton is roughly

$$\mu_p = \sum \mu_q = \sum_{i=1}^{3} <p\uparrow|\mu_i\sigma_3|p\uparrow>$$

where $\sigma_3 = \begin{pmatrix} 1 & 0 \\ 0 & -1 \end{pmatrix}$, $\text{u} = \begin{pmatrix} 1 \\ 0 \end{pmatrix}$, $\text{d} = \begin{pmatrix} 0 \\ 1 \end{pmatrix}$.

$$\mu_p = \frac{1}{18}[(\mu_u - \mu_u + \mu_d) + (-\mu_u + \mu_u + \mu_d) + 4(2\mu_u - \mu_d)] \times 3 = \frac{1}{3}(4\mu_u - \mu_d).$$

By switching u and d in the formula we get the magnetic moment of the neutron, neutron = proton (u ↔ d): $\mu_n = \frac{1}{3}(4\mu_d - \mu_u)$. Their ratio is

$$\frac{\mu_n}{\mu_p} = \frac{4 - \mu_u/\mu_d}{4\mu_u/\mu_d - 1} \simeq -\frac{2}{3}.$$

The experimental observation $\frac{\mu_n}{\mu_p} = -0.68497934(16)$ (with the experimental uncertainty of the last digits in parentheses) [Mohr et al., 2016] agrees very well with this rough estimation in spite of the fact that the mass of the nucleon is mostly energy (in the form of gluons and virtual quark-antiquark pairs), the valence quarks contribute very little to its mass. This agreement is a supporting argument for the validity of the quark model.

Exercise 4.1
Considering the Dirac equation in what sense can we speak of anti-bosons?

Exercise 4.2
What property of the Dirac equation leads to the conservation of the lepton and baryon numbers?

Exercise 4.3
Prove Eq. (4.4) using $\gamma^{0^2} = I$, $\gamma^{0\dagger} = \gamma^0$ and $\gamma^{\mu\dagger} = \gamma^0\gamma^\mu\gamma^0$).

Exercise 4.4
Explain the signs of the terms when summing up the isospins in Table 4.2. Hint: consider symmetries.

Exercise 4.5
Why is it a rough approximation to consider the three quarks only for calculating the magnetic moment of the nucleon?

Chapter 5

Interactions

5.1   Three interactions of particle physics

As mentioned before, ignoring gravity (which is many orders of magnitude weaker than the others), there are three fundamental interactions in nature. Their basic properties are summarized in Table 5.1.

According to the standard model the interactions are deducible from local gauge symmetries, their source is some charge and they are mediated by bosons characteristic for the given interaction. These bosons are real particles in the sense that they exist not only as virtual particles mediating interactions, but they can also be emitted and observed experimentally. A fermion enters into an interaction if it possesses the corresponding charge; the weak interaction operates on all fermions, the electromagnetic one on those having electric charges or magnetic moments and the strong interaction on the coloured fermions, i.e., on the quarks.

The photon (γ) mediates the electromagnetic interaction, and the three weak bosons (W^+, W^- and Z^0) the weak interaction. In the strong interaction

Interaction	relative strength	potential	lifetime	med. boson	mass GeV
Strong	1	$\propto r$	10^{-23} s $(\Delta \to p\pi)$	8 gluons	0
Electro-magnetic	10^{-2}	$\propto \frac{1}{r}$	$10^{-20} - 10^{-16}$ s $(\pi^0 \to \gamma\gamma)$	photon	0
Weak	10^{-7}	$\propto \frac{1}{r}e^{-\frac{r}{R}}$ $R \sim \frac{\hbar}{M_W c}$	$> 10^{-12}$ s $(\pi^- \to \mu^- \overline{\nu})$	$W^\pm$ Z^0	80 91

Table 5.1: Three fundamental interactions: strength, potential, lifetime, mediating boson and its mass. In column 3 r is the distance from the source and R is the range of interaction. In column 4 under the typical lifetime a characteristic reaction is presented in parentheses

two quarks exchange colour so the mediating boson, the *gluon* (from glue) should carry a colour and an anti-colour. This means 8 different gluons: the $3 \times 3 = 9$ combinations have one less degree of freedom as the combination $R\overline{R} + G\overline{G} + B\overline{B}$ changes white to white and so does not carry any colour.

Pion decay provides an excellent example to compare the strengths of the electromagnetic and weak interactions. The decay of the neutral pion to two photons, $\pi^0 \to \gamma\gamma$, is a typical electromagnetic reaction with a lifetime of $8 \cdot 10^{-17}$ s. The charged pion can decay via weak interaction only to a muon and its neutrino: $\pi^- \to \mu^- + \overline{\nu}_\mu$ and its lifetime is 26 ns = $2.6 \cdot 10^{-8}$ s, 8 orders of magnitude longer than that of its neutral brother. Please note that in the above reaction a boson disappeared and a lepton was created together with an anti-lepton: the fermion number is conserved, whereas the boson number is not.

5.2   Electromagnetic interaction

5.2.1   Local $U(1)$ invariance

The properties of the electromagnetic interaction have been well known for a long time: its source is the electric charge, its mediator is the photon and it is

described by Maxwell's equations. The Lagrangian of the latter in covariant form is $\mathcal{L} = E_{\text{field}} + \text{current} \times \text{field} = -\frac{1}{4} F_{\mu\nu} F^{\mu\nu} - j_\mu A^\mu$. The Maxwell equations themselves are of the form $\partial_\mu F^{\mu\nu} = j_\nu$, where $F^{\mu\nu} = \partial^\mu A^\nu - \partial^\nu A^\mu$.

The standard model derives electromagnetism from the local version of the $U(1)$ invariance of the Dirac equation. The requirement of local symmetry (also called *gauge invariance*) means that the equation of motion has to be invariant under a gauge transformation with space-time variation, i.e. choosing the phase of the electron-field freely at any point in space and time. For a free $\psi(x)$ particle field the global $U(1)$ symmetry that provides the conversation of fermion charge is trivial: $\mathcal{L}(e^{i\alpha}\psi) = \mathcal{L}(\psi)$ for any real constant α as $\mathcal{L}$ contains both ψ and its adjoint spinor, $\overline{\psi} \equiv \psi^\dagger \gamma^0$ with the complex conjugate. On the other hand, the gauge transformation will be $\psi'(x) = e^{i\alpha(x)}\psi(x)$, where $\alpha(x)$ is an arbitrary space-time function.

In the case of the classical Maxwell equation the electromagnetic vector potential A can be included in the *general momentum*: $p \rightarrow p + Q_f A$, where p is the momentum and Q_f is the particle charge. In transition from classical to quantum treatment the momentum is replaced by derivation, thus electromagnetism should involve a general derivative $i\partial_\mu \rightarrow iD_\mu = i\partial_\mu + Q_f A_\mu$.

Let us define a covariant derivation for the local $U(1)$ gauge symmetry where the A vector field transforms according to the $\alpha(x)$ function: $A_\mu \rightarrow A_\mu + \frac{1}{e}\partial_\mu\alpha$, with the e electric charge unit (we assume to have a charged lepton). The new Lagrangian,

$$\mathcal{L}' = i\,\overline{\psi}\,\gamma^\mu D_\mu \psi - m\overline{\psi}\psi$$

can be brought to the following form:

$$\overline{\psi}(i\,\gamma^\mu\partial_\mu - m)\psi + e\overline{\psi}\,\gamma^\mu\psi A_\mu = \mathcal{L} - j^\mu A_\mu.$$

We saw previously that the vector $j^\mu = Q_f\,\overline{\psi}\,\gamma^\mu\psi$ is a conserved current density of particle f and that should be multiplied by the new A field of the interaction. We have to account for the energy density of the field itself and with that we complete the Lagrangian of electromagnetism:

$$\mathcal{L}'' = \overline{\psi}(i\,\gamma^\mu\partial_\mu - m)\psi + e\overline{\psi}\,\gamma^\mu\psi A_\mu - \frac{1}{4}F^{\mu\nu}F_{\mu\nu}$$

Thus we have an interaction of a massive fermion with a field of zero-mass field. Local $U(1)$ gauge symmetry does not allow for a massive gauge field , adding a mass term of $\frac{1}{2}m_\gamma^2 A^\mu A_\mu$ should violate the symmetry. In order to create the massive vector fields of the weak interaction the related $SU(2)$ gauge symmetry has to be violated (see below in Section 5.5.1 and in the Theory part).

5.2.2   Quantum electrodynamics (QED)

The free phase gives rise to the electromagnetic field with zero mass of the mediating boson after some mathematical manipulations. As the photon has zero rest mass, the electromagnetic interaction has an infinite range and its *Coulomb* potential is inversely proportional to the distance. Freely propagating photons are detected by our eyes (visible light) or by our TV sets (radio waves) and so their real existence is evident.

Let us consider the interaction of spinless point charges. The *Klein-Gordon equation* describes them as free particles: $(\partial_\mu \partial^\mu + m^2)\phi = 0$. Introducing the $U(1)$ covariant derivation one gets

$$D_\mu D^\mu \phi = (\partial_\mu - ieA_\mu)(\partial^\mu - ieA^\mu)\phi =$$

$$\partial_\mu \partial^\mu \phi - ie(\partial_\mu A^\mu + A_\mu \partial^\mu)\phi - e^2 A^\mu A_\mu \phi = \partial_\mu \partial^\mu \phi + V\phi$$

where $V = -ie(\partial_\mu A^\mu + A_\mu \partial^\mu) - e^2 A^\mu A_\mu$ is the scalar potential of the interaction derived from the A^μ vector potential.

The transition probability from an i initial to an f final state is proportional to the overlap of their state functions in space-time, the *matrix element*, when embracing the V potential: $M_{fi} = -i \int \phi_f^* V \phi_i d^4x$. As the coupling $\alpha \equiv \frac{e^2}{4\pi} \simeq \frac{1}{137}$ is small, the $e^2 A^\mu A_\mu$ term can be neglected in first approximation (*first order perturbation calculation*), and then $V \approx -ie(\partial_\mu A^\mu + A_\mu \partial^\mu)$. Assuming that the potential disappears at infinity, i.e. in the initial and final states,

$$\int \partial_\mu (\phi_f^* A^\mu \phi_i) d^4x = [\phi_f^* A^\mu \phi_i]_{(0,-\infty)}^{+\infty} = 0,$$

after an integration by parts, the matrix element becomes

$$M_{fi} = -i \int (-ie)[\phi_f^*(\partial_\mu \phi_i) - (\partial_\mu \phi_f^*)\phi_i] A^\mu d^4x = -i \int j_\mu^{if} A^\mu d^4x.$$

5.2.3   Current-current interaction

Before and after the interaction we have free particles with plain wave state functions of the form $\phi(x) = Ne^{-ip\cdot x}$ where N is a normalization factor. The current is $j_\mu^{fi} = -eN_i N_f(p_i + p_f)_\mu \exp\{i(p_f - p_i)\cdot x\}$.

We see that in the QED Lagrangian a term of *current×field strength* accounts for the interaction of the fermion with the field. In the following we shall show in a simple example that interaction between two charged particles will be similar: the field raised by the current of one particle interacts with
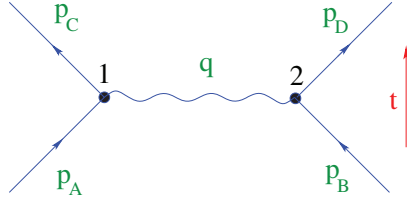
Figure 5.1: Scattering of point charges, A + B → C + D (A≠B)

the charge of the other one. Thus, it can be treated as a current-current interaction. The probability amplitude for the transition is proportional to

$$\mathcal{M}_{fi} = -i \int \phi_f^*(x)V(x)\phi_i(x)\mathrm{d}^4x = -i \int j_\mu^{fi} A^\mu \mathrm{d}^4x$$

where $j_\mu^{fi} = -ie[\phi_f^*(\partial_\mu\phi_i)-(\partial_\mu\phi_f^*)\phi_i]$ is the electromagnetic current density.

5.2.4 Photon

The scattering of point charges A + B → C + D (A≠B) involves a momentum exchange $q \equiv p_D - p_B = p_A - p_C$ and the matrix element determining the reaction probability will have the form $\mathcal{M}_{fi}^{(1)} = -i \int j_\mu^{(1)} A_{(2)}^\mu \, \mathrm{d}^4x$. The potential is the solution of D'Alembert's equation: $\Box^2 A_{(2)}^\mu = j_{(2)}^\mu$ with $j_{(2)}^\mu = -eN_B N_D (p_D + p_B)^\mu e^{-iqx}$, giving $A_{(2)}^\mu = -\frac{1}{q^2} j_{(2)}^\mu$. Thus we have for the transition matrix element

$$\mathcal{M}_{fi} = -i \int j_\mu^{(1)}(-\frac{1}{q^2})j_{(2)}^\mu \, \mathrm{d}^4x$$

and in the given case $-i\mathcal{M} = [ie(p_A + p_C)^\mu][-i\frac{g_{\mu\nu}}{q^2}][ie(p_B + p_D)^\nu]$ where $g_{\mu\nu}$ is the metric tensor (4.1).

Thus the interaction is described in a symmetric current × current form. It is mediated by the photon which is obviously virtual as it transfers energy and momentum and so it has a finite mass, $q^2 > 0$. That, however, is allowed by Heisenberg's uncertainty principle. The photon appears between the two currents as $1/q^2$: that corresponds to the *photon propagator*. It has finite mass and lifetime and is denoted by a wavy line in the Feynman diagrams (Fig. 5.1).

5.3   Mandelstam variables

Particle physics widely uses the Lorentz-invariant variables introduced by *Stanley Mandelstam* in 1958:

$$s = (p_A + p_B)^2,$$
$$t = (p_A - p_C)^2,$$
$$u = (p_A - p_D)^2.$$

The use of these variables makes the handling of the Feynman diagrams extremely simple as it facilitates the interrelation of different reactions via *diagram rotations*, i.e. space-time reflections, called *crossing*. The scattering reaction of Fig. 5.1 the original $AB{\rightarrow}CD$ reaction is called *s channel*, a $(s{\leftrightarrow}-t)$ rotation gives the $\overline{DB}{\rightarrow}C\overline{A}$ *t channel*, and $(s{\leftrightarrow}-u)$ the *u channel*. There are many sum rules for the Mandelstam variables, some of them are tested in the Exercises.

As the simplest possible case, let us consider electron-positron collisions. The momentum is $p = (E, \vec{k})$ and its square is $p^2 \equiv m^2 = E^2 - \vec{k}^2$ where m is the electron mass. In the centre-of-mass system (like at the LEP collider, CERN, 1989-2000) $p_A = (E, \vec{k}_i)$, $p_B = (E, -\vec{k}_i)$, $p_C = (E, \vec{k}_f)$, and $p_D = (E, -\vec{k}_f)$. Then $s = E_{\text{CM}}^2$ ($E_{\text{CM}} = 2E$ is the total collision energy), $t = -2\vec{k}^2(1 - \cos\theta)$ and $u = -2\vec{k}^2(1 + \cos\theta)$, where θ is the scattering angle between the incoming and outgoing particles.

Without going into details, let us list a few examples for diagram rotation, or crossing. The square of invariant amplitudes averaged for initial and summed over final state spins for the $e^-e^-{\rightarrow}e^-e^-$ Møller scattering is

$$\overline{|\mathcal{M}|^2} = \frac{e^4}{2}\left(\frac{s^2 + u^2}{t^2} + \frac{s^2 + t^2}{u^2} + \frac{2s^2}{tu}\right)$$

where the terms describe the forward and the backward scattering, and their interference. This interference term has a negative sign from direct computation, but there is a subtle point in computing the square of the amplitude: as there are identical fermions in the final state and under particle interchange fermionic systems are odd, we have to square the *difference* of the two contributions shown in the left panel of Fig. 5.2, which turns the sign of the interference term positive. If we want to obtain the squared amplitude for the $e^+e^- \rightarrow e^+e^-$ Bhabha scattering via an $s{\leftrightarrow}-u$ crossing, we should use the *sum* of the two diagrams, i.e. the Møller formula with minus sign for the interference term as this time the fermions are different in the final state.

Thus, we find

$$\overline{|\mathcal{M}|^2} = \frac{e^4}{2} \left(\frac{s^2 + u^2}{t^2} + \frac{u^2 + t^2}{s^2} + \frac{2u^2}{ts} \right).$$

Another example is the connection between the $\gamma e \rightarrow \gamma e$ Compton scattering and positron annihilation. From the invariant amplitude of the former,

$$\overline{|\mathcal{M}|^2} = \frac{e^4}{2} \left(-\frac{u}{s} - \frac{s}{u} \right)$$

(there is no interference term in this case), one obtains that of annihilation (shown in Fig. 5.3):

$$\overline{|\mathcal{M}|^2} = \frac{e^4}{2} \left(\frac{u}{t} + \frac{t}{u} \right)$$

by an $s \leftrightarrow -t$ crossing.

Another interesting case is electron scattering on muon, described with a photon exchange (shown in Fig. 5.4 left). Its invariant amplitude is

$$\overline{|\mathcal{M}|^2} = \frac{e^4}{2} \left(\frac{s^2 + u^2}{t^2} \right),$$

which gives after an $s \leftrightarrow -t$ crossing the amplitude for the creation of a muon pair in an electron-positron annihilation. At high energies the lepton masses can be neglected as compared to their energies and we obtain

$$\overline{|\mathcal{M}|^2} = \frac{e^4}{2} \left(\frac{u^2 + t^2}{s^2} \right) = \frac{e^4}{2} \frac{8k^4(1 + \cos^2 \theta)}{(4k^2)^2} = \frac{e^4}{4}(1 + \cos^2 \theta)$$

for the invariant squared amplitude of the process $e^- e^+ \rightarrow \mu^- \mu^+$. Its differential cross section in the centre-of-mass system is $\frac{d\sigma}{d\Omega}\big|_{CM} = \frac{\alpha^2}{4s}(1 + \cos^2 \theta)$ where α is the fine structure constant. Integrating over the polar and azimuth angles, we find its total cross section $\sigma(e^+ e^- \rightarrow \mu^+ \mu^-) = \frac{4\pi\alpha^2}{3s}$ in very good agreement with the experimental result.

In experimental papers very frequently $\sqrt{s}$ is used to denote the centre-of-mass energy of particle collisions.

5.4   Strong interaction

5.4.1   Colour charges

The source of the strong interaction is the *colour charge*. It is mediated by the 8 gluons and according to the three colours, its origin is the local
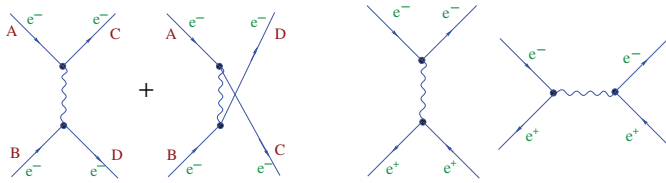
Figure 5.2: From Møller scattering on the left we get via $s \leftrightarrow -u$ crossing (diagram rotation) Bhabha scattering
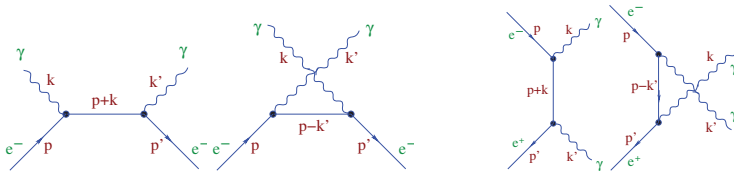
Figure 5.3: From Compton scattering (left) $s \leftrightarrow -t$ crossing we get electron-positron annihilation (diagram rotation)
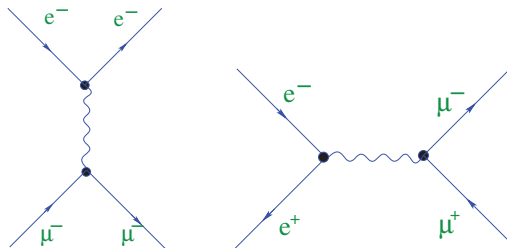
Figure 5.4: From electron-muon scattering (left) one gets by $s \leftrightarrow -t$ crossing the production of muon pairs in electron-positron scattering (diagram rotation)

$SU(3)$ symmetry. The usual representation of $SU(3)$ transformations is $U = \exp(i\vec{\alpha} \cdot \vec{T}) \equiv \exp(i \sum_{a=1}^{8} \alpha_a T_a)$ where α_a are real constants for a global $SU(3)$ symmetry and real space-time functions for the local one. The eight generators have the commutation rule $[T_a, T_b] = i \sum_{c=1}^{8} f_{abc} T_c$. The structure constants are the following: $f_{123} = 1$; $f_{458} = f_{678} = \frac{\sqrt{3}}{2}$; $f_{147} = f_{165} = f_{246} = f_{257} = f_{345} = f_{376} = \frac{1}{2}$ with the permutations $f_{abc} = -f_{acb} = -f_{bac} = -f_{cba}$. The rest with the possible indices are zero. The generators can be realized as $T_a \equiv \lambda_a/2$ with the λ_a 3×3 Gell-Mann matrices built via extending the 2×2 Pauli matrices of $SU(2)$ with zeroes:

$$\lambda_i = \begin{pmatrix} \sigma_i & \\ & 0 \end{pmatrix} \quad (i = 1, 2, 3).$$

$$\lambda_4 = \begin{pmatrix} 0 & 0 & 1 \\ 0 & 0 & 0 \\ 1 & 0 & 0 \end{pmatrix} \quad \lambda_5 = \begin{pmatrix} 0 & 0 & -i \\ 0 & 0 & 0 \\ i & 0 & 0 \end{pmatrix} \quad \lambda_6 = \begin{pmatrix} 0 & 0 & 0 \\ 0 & 0 & 1 \\ 0 & 1 & 0 \end{pmatrix}$$

$$\lambda_7 = \begin{pmatrix} 0 & 0 & 0 \\ 0 & 0 & -i \\ 0 & i & 0 \end{pmatrix} \quad \lambda_8 = \frac{1}{\sqrt{3}} \begin{pmatrix} 1 & 0 & 0 \\ 0 & 1 & 0 \\ 0 & 0 & -2 \end{pmatrix}.$$

Note that λ_3 and λ_8 are diagonal. As mentioned before in some sense $SU(3) \sim 3 \times SU(2)$, see Fig. 3.1 and the stepping operator between any two, k and ℓ of the three $SU(3)$ states are $\frac{1}{2}(\lambda_k \pm i\lambda_\ell)$.

5.4.2 Nuclear forces

Before the colour charge was invented and quantum chromodynamics (QCD) developed, *Hideki Yukawa* interpreted the short range of nuclear forces as a sign of a massive mediator and introduced the *Yukawa potential* in the form of $V(r) = -g^2 e^{-Mr}/r$ (in energy units).[1] In $V(r)$ g is the coupling, r is the distance to the source, and M is the mass of the mediating particle. Assuming that the proton radius (0.8 fm) should be close to the range of the interaction, in 1935 Yukawa predicted the existence of the *meson* with a mass of $M \sim 100 - 300$ MeV. In cosmic rays *C. D. Anderson* found the muon of the mass in the right range (first called μ-meson) in 1936, but that turned out to be a lepton, the heavy brother of the electron. However, in 1947 *C. Powell* observed the π-meson at $M \simeq 140$ MeV and it seemed to be already correct for mediating the strong interaction. Pion exchange is a good approximation for the nuclear forces at low energies even today. All three received Nobel Prizes in physics: Anderson in 1936 (for the positron),

---

[1]In atomic and sub-atomic physics, the term 'potential' is often used sloppily instead of the correct term 'potential energy'.

Yukawa in 1949 and Powell in 1950.

5.4.3   Local $SU(3)$ invariance

A *free quark* (please note that it cannot exist) should move according to the Dirac equation $L_0 = \sum_{j=1}^{3} \overline{q}_j(i\gamma^\mu \partial_\mu - m)q_j$ where the summation is performed over the colour degrees of freedom, which is usually not shown, but meant implicitly (over repeating indices).

Global $SU(3)$ gauge invariance of the Dirac Lagrangian is trivial. Local $SU(3)$ requires invariance under the transformation

$$q(x) \rightarrow U q(x) = e^{i\alpha_a(x)T_a} q(x)$$

(this time the summation over the repeating indices is over the 8 generators). Here, similarly to the QED case, $\alpha_a(x)$ are real space-time functions. The $SU(3)$ gauge field is introduced via the covariant derivation

$$D_\mu = \partial_\mu + i g_s T_a G_\mu^a$$

with the transformation rule

$$G_\mu^a \rightarrow G_\mu^a - \frac{1}{g}\partial_\mu \alpha_a - f_{abc}\alpha_b G_\mu^c.$$

The field strength will be

$$G_{\mu\nu}^a = \partial_\mu G_\nu^a - \partial_\nu G_\mu^a - g_s f_{abc} G_\mu^b G_\nu^c$$

with a coupling g_s. Note that the first two terms are exact analogies of the QED field. Similarly to QED the QCD Lagrangian is

$$L_{QCD} = \overline{q}_j(i\gamma^\mu \partial_\mu - m)q_j - g_s(\overline{q}_j\gamma^\mu T_a q_j)G_\mu^a - \frac{1}{4}G_{\mu\nu}^a G_a^{\mu\nu}.$$

The QCD Lagrangian in its expanded form (Fig. 17.1), in addition to a linear term similar to that in the QED case, has terms of higher order interactions.

5.4.4   Running coupling

The colour interaction is mediated by eight gluons. As local gauge invariance cannot include masses for the mediating bosons, the mass of the gluons is also zero and so the range of the colour interaction is also infinite; its potential at short distances is of the Coulomb form, but at long distances it is roughly

	QED	QCD
Elementary fermions	leptons	quarks
Charge	electric	colour
Gauge boson	photon (γ) no charge	8 gluons (g) have colours
Coupling Q^2 dependence	$\alpha(Q^2 = 0) = \frac{1}{137}$ weak	$\alpha_s(Q^2 = m_Z^2) = 0.12$ strong
Free particles	leptons	hadrons
Calculation precision	$< 10^{-8}$	$5 - 20\%$

Table 5.2: Comparison of the basic properties of quantum electrodynamics (QED) and quantum chromodynamics (QCD)

proportional to the distance of the coloured objects. This the consequence of the fact that–as opposed to the photons–the gluons themselves also carry colour, the charge of the interaction, and so they interact with each other. When we try to separate two quarks, the energy of the field will grow with the distance as the gluons will produce more gluons and quark–antiquark pairs, and the quarks will combine into hadrons so that we see colourless objects only: that is *quark confinement*. Presently it is not known how this *hadronization* can be deduced from first principles and it is one of the main sources of uncertainty of simulations in particle physics.

The strengths of interactions as reflected by their coupling depend on the distance of the charges involved. This dependence is weak for electromagnetism: the fine structure constant at low energies is $\alpha(E = 0) \simeq 1/137$, whereas at the energy corresponding to the mass of the Z boson it is $\alpha(E = 91\,\text{GeV}) \simeq 1/128$. The strong coupling is close to unity at low energies (as manifested by quark confinement) and converges to zero at extreme high energies (asymptotic freedom). Table 5.2 compares the basic properties of the two interactions.

Because of quark confinement the characteristic particles of strong interaction do not appear free in Nature, but can be studied via their particular decay properties. The most convincing proof for the existence of quarks is the detection of events with two hadron showers, jets, in high-energy electron-positron collisions . In electromagnetic or weak processes the production of an additional particle in scattering or decay reactions involves one more coupling, decreasing the reaction probability by at least an order of magnitude. In the electron+positron atomic bound state, the positronium

the two particles can have parallel or opposite spins; the former state, with spin $S = 1$ called ortho-positronium decays by emitting three photons because of parity conservation and has a lifetime of 140 ns, whereas the other one, the $S = 0$ para-positronium, decays to two photons with a lifetime of 125 ps. A high-energy hadron jet contains dozens of particles and so cannot be produced by other interactions, just hadronization.

5.4.5 Gluons

Gluons are produced most frequently in hadron-hadron collisions. In the proton-proton collisions of the Large Hadron Collider that is the most frequent phenomenon. Higgs bosons are produced most frequently in gluon-gluon collisions (*gluon fusion*). Gluon production is manifested best in 3-jet events (Fig. 17.25); at the production of quark pairs in electron-positron collisions, the quarks can interact with each other emitting a gluon and we see an event of three jets in a common plane. The third jet must be from a boson because of the conservation of fermion charge and that boson must be coloured to be able to form a third jet.

   The properties of gluons were established via studying such 3-jet events in electron-positron collisions where two of the jets were identified as b quarks (due to its longer lifetime and increased lepton emission), so that the third jet had to be a gluon. The unit spin and zero mass of the gluons were this way confirmed experimentally.

5.5   Electroweak interaction

The weak interaction is weak not because of a small coupling, but because of its very heavy mediating bosons. When the neutron decays,

$$n \rightarrow p + W^- \rightarrow p + e^- + \overline{\nu}_e \,,$$

the 1.3 MeV mass difference have to be transferred by the $M_W = 80$ GeV gauge boson, which is possible due to the uncertainty relation allowing for a low decay probability and a relatively long lifetime for the neutron.

   The birth of the standard model is usually dated to the early seventies, the time when the theory of the *electroweak interaction* was developed, for which *Sheldon Lee Glashow*, *Abdus Salam* and *Steven Weinberg* was awarded the Nobel Prize in physics in 1979. The theory had to solve two problems:

- One had to introduce the masses of elementary particles, those for the weak bosons and the elementary fermion, the quarks and leptons. As gauge invariance prohibited that, it had to be somehow violated.

- The equations of electromagnetic and weak scattering had infinite terms. In order to help to eliminate them a scalar boson (having zero quantum numbers) was needed.

5.5.1 Spontaneous symmetry breaking

As we could see, the electromagnetic and strong interactions are successfully described by local gauge symmetries with massless mediating bosons. For the weak interaction local $SU(2)$ symmetry seems to be adequate except for the masses: we have to introduce a violation to get finite masses for the gauge bosons. How can one violate local $SU(2)$ without violating the other two invariances, to keep zero masses for the gluons and the photon?

The Brout–Englert–Higgs (BEH) mechanism solves this problem the following way. It unites the electromagnetic $U(1)$ and weak-like $SU(2)$ gauge symmetries in a vacuum filled with the four-component, scalar $SU(2)$ BEH field:

$$\phi = \begin{pmatrix} \phi_\alpha \\ \phi_\beta \end{pmatrix} = \sqrt{\tfrac{1}{2}} \begin{pmatrix} \phi_1 + i\phi_2 \\ \phi_3 + i\phi_4 \end{pmatrix}$$

with the corresponding Lagrangian

$$L = (\partial_\nu \phi)^\dagger (\partial^\nu \phi) - \mu^2 \phi^\dagger \phi - \lambda (\phi^\dagger \phi)^2$$

where $(\lambda > 0)$ is a real constant. If $\mu^2 > 0$ this is a scalar field with a finite mass; however, if $\mu^2 < 0$ its stable vacuum state is not at $\phi = 0$, but at a different *vacuum expectation value*.

The Mexican hat illustrates the BEH potential in two dimensions: it has a perfect axial symmetry (Fig. 5.5) and that is not violated by putting a ball on the top of the potential at point (0,0). However, the symmetry will be spontaneously violated when the ball will roll down. In the valley it can move without spending energy, so we can put one axis of our coordinate system on the position of the ball. The new system will be characterized by one parameter, the distance of the minimum from zero, the vacuum expectation value (generally abbreviated as *vev*). Then we parametrize the BEH field around the displaced minimum and write it in the form $\phi(x) = \sqrt{\tfrac{1}{2}} \begin{pmatrix} 0 \\ v + h(x) \end{pmatrix}$.
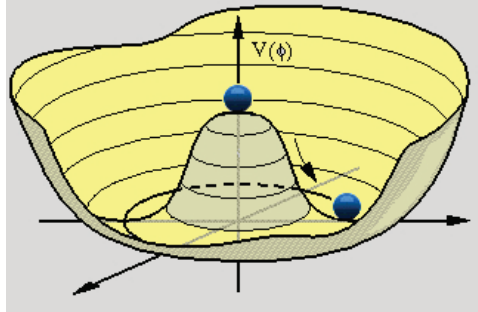
Figure 5.5: Spontaneous symmetry breaking. The perfect axial symmetry of the BEH potential is violated when we place the ball on top, because its stable state is somewhere in the valley; as it is indifferent where, we can adjust our coordinate system accordingly.

5.5.2 BEH mechanism

The $U(1)_Y$ local gauge invariance, related to the Y *hypercharge* generates a B field and the $SU(2)_L$ (the L index means that it acts on left-handed fermion currents only) a 3-component $\vec{W} = (W^1, W^2, W^3)$ field. Together they correspond to a $U(1) \otimes SU(2)$ 4-component local gauge invariance field which is then violated by the 4-component (complex doublet) BEH field . We know that the photon is massless, so we have to restore the $U(1)$ local gauge invariance, i.e. to separate an electromagnetic vector potential A from a mixture of the B field with the neutral component of $\vec{W}$, W_3. The charged currents will be $W^\pm = \frac{1}{\sqrt{2}}(W_1 \pm W_2)$ and the rest of the neutral part of $U(1) \otimes SU(2)$ will give the neutral current with the Z^0 boson of mass $m_Z \simeq 91\,\text{GeV}$ as mediator.

To calculate the electromagnetic current we use the definition of the hypercharge as $Y = 2(Q - T^3)$ where Q is the electric charge and T^3 is the third component of the *weak isospin* related to the $SU(2)$ doublets. The current of the hypercharge is connected to $U(1)_Y$ as $j_\mu^Y = \bar{\psi}\gamma_\mu Y \psi$ and the electromagnetic current will be $j_\mu^{em} = J_\mu^3 + \frac{1}{2}j_\mu^Y$ (in units of the electric charge unit). Identifying the coupling of the electromagnetic current with the charge one immediately gets the coupling for electromagnetism as the mixing of $U(1)$ with the neutral part of $SU(2)$ and it is characterized–as usual in particle physics–with the *weak* or *Weinberg mixing angle* $\theta_W \simeq 28.2^0$. In the measurable quantities it generally appears as $\sin^2 \theta_W$ with a slightly energy-dependent value: 0.221 at low energies and 0.231 at $E = m_Z c^2 \simeq 91.2\,\text{GeV}$.

The BEH field introduces four new degrees of freedom in the system, three of them will give masses to the weak bosons and the fourth one the Higgs boson, a heavy particle with all quantum numbers zero. From the known couplings one can calculate the masses of the weak bosons and the vacuum expectation value of the BEH field, $v \simeq 246$ GeV.

The BEH mechanism was independently published in 1964 by *Peter Higgs* and two research groups, but at that time it was received by a great deal of scepticism. It actually introduces an artificial new field, a force field with no source, which fills vacuum and creates a new scalar particle with all zero quantum numbers except its mass which is not predicted by the theory. It is very hard to detect such a particle. It was clarified in the early seventies only that the BEH mechanism, in addition to the production of masses for the weak bosons, solves a whole bunch of other problems: facilitates to introduce the fermion masses and creates the badly needed scalar boson to eliminate some mathematical difficulties. As the theory and experiment of particle physics developed, the belief of physicists increased that the BEH mechanism should be correct: the predicted neutral currents were observed, the properties of the weak bosons determined, and all experimental data seemed to agree with the calculations of the standard model. Finally, 48 years after its prediction, the Higgs boson was observed at the LHC in 2012.

5.6 Basic bosons

Thus the interactions are derived from local gauge symmetries: exact $SU(3)$ symmetry in the case of QCD and a spontaneously broken $U(1)_Y \otimes SU(2)_L$ symmetry in the case of the electroweak interaction. The strong and the electromagnetic interactions are mediated by zero-mass *gauge bosons*, the 8 gluons and the photon. The gauge bosons of the weak interaction are heavy: $M_W = (80.385 \pm 0.015)$ GeV and $M_Z = (91.1876 \pm 0.0021)$ GeV [Patrignani et al., 2016]. The Higgs boson was the last particle of the standard model discovered, it was observed in 2012 only by the ATLAS and CMS experiments at the Large Hadron Collider of CERN at the mass $M_H = (125.09 \pm 0.24)$ GeV [Patrignani et al., 2016] where the uncertainty includes both statistical and systematic ones.

With the observation of the Higgs boson the standard model became complete: all of its predicted particles were found experimentally, all measurements agree with its predictions and no exception or deviation was observed. Of course, since its foundation in the early seventies, many experiments gave results seemingly contradicting the standard model, but those
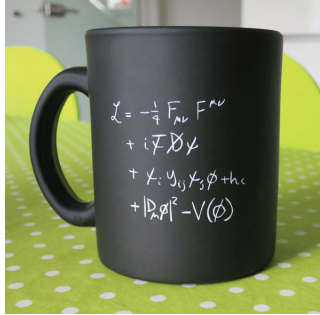
Figure 5.6: CERN coffee mug with the electroweak Lagrangian

were either refuted later or stayed unconfirmed by independent new data. Thus at the moment we have to accept the standard model as the theory of matter, of particle physics.

5.7 Electroweak Lagrangian with interactions

The rather complicated electroweak Lagrangian of the standard model including the interactions and the BEH mechanism (derived and explained in detail in Section 22.2 of this book) can be written in an extremely concise form which is widely distributed on T-shirts and coffee mugs (Fig. 5.6) at CERN:

$$\mathcal{L} = -\frac{1}{4} F^{\mu\nu} F_{\mu\nu} + i\overline{\psi} \slashed{D} \psi + \psi_i y_{ij} \psi_j \phi + \text{h.c.} + (D_\mu \phi)^2 - V(\phi)$$

The first two terms are similar to those of QED: the first one is the field energy density, the second term stands for the interaction of the fermion, $\slashed{D} = \gamma^\mu D_\mu$ where D denotes the covariant derivation. The third term is a possible gauge-invariant coupling between the fermions and the ϕ BEH field that leads to fermion masses, the term $(D_\mu \phi)^2$ generates the masses of the gauge bosons and the last term is the self-interacting BEH-potential. The fermion interaction terms need to be complemented by their Hermitian conjugates. This equation is nicely explained in a generally comprehensible way in [Woithe et al., 2017].

Exercise 5.1

What is common in the three interactions described by the Standard Model? Why is gravity different from them?

Exercise 5.2

To what extent does the magic number 3 connect the 3 fermion families with the 3 quark colours and 1/3 quark charges?

Exercise 5.3

Conservation of the electric charge and colour charge is connected to which Noether theorem? What are the two physical quantities whose conservation is violated by the weak interaction?

Exercise 5.4

Why do quark states mix in ground state? Why is the number of families limited to 3 in the standard model?

Exercise 5.5

Why does the number of quarks equal that of the leptons?

Exercise 5.6

Explain in what sense it is correct to consider for the numbers of different quarks 3, 6, 9, 12, 18 and 36.

Exercise 5.7

Explain in what sense it is correct to consider in the standard model for the numbers of different elementary particles (i.e. of the basic fermions and bosons) 17, 21, 44, 52, 61 and 109.

Exercise 5.8

How did we determine the number of fermion families? Why cannot quarks heavier than the top quark exist within the standard model?

Exercise 5.9

Why are the masses of the charged and neutral weak bosons different?

Part II

Experimental methodology

Chapter 6

Accelerators

One needs higher and higher energies to get deeper and deeper in the structure of matter. Cosmic rays can have very high energies, but at extremely low intensity and with no choice of parameters. At the times of Columbus the front line of discovery in Europe was the shore of the Atlantic Ocean: he used ships to reach India and found America. Nowadays on the front line of physics we see the Higgs boson and the quark-gluon plasma, the state of matter right after the Big Bang. We use particle accelerators, now the Large Hadron Collider (LHC) of CERN to study them, and in the 21st century after many decades of hard work we see them both. Of course, the devil is in the details, one needs more and more precise measurements as that is the only way to find deviations from the predictions of the standard model, i.e. new physics.

The word *accelerator* is a bit confusing in contemporary particle physics as all machines produce particles with velocities extremely close to c, the
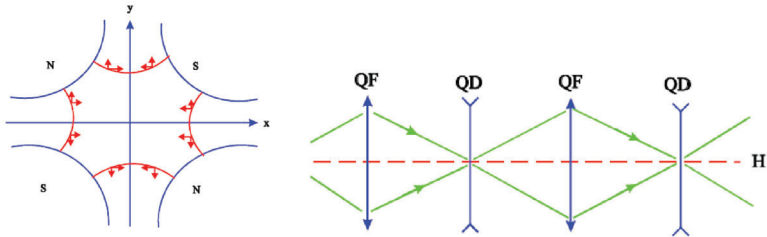
Figure 6.1: Left: forces in a quadrupolar magnetic field. Right: focusing charged particles in a quadrupole triplet: each magnet focuses in its focusing plane to the centre of the defocusing plane of the next magnet.

speed of light in vacuum. We increase rather energies than velocities. For instance, in 2012 the protons in the LHC ring moved at velocities $v \simeq 0.99998c$.

The electromagnetic field in an accelerator has to serve both to increase the energy of the particles and to keep them together on the required orbit. As a general rule, an electric field accelerates and a magnetic fields bends the trajectories of charged particles. Using potentials one can write for the magnetic field strength $\vec{B} = \vec{\nabla} \times \vec{A}$ and for that of the electric field $\vec{E} = -\vec{\nabla}\Phi - \partial\vec{A}/\partial t$. Here $\vec{\nabla} = (\partial x, \partial y, \partial z)$ is the 3-dimensional derivation vector, $\vec{A}$ is the vector potential and Φ is the scalar potential.

6.1 Magnets: bending and focusing

The bending strength of a magnetic field B on a particle of charge e and velocity $\vec{v}$ is $\vec{F} = e\vec{v} \times \vec{B}$; $|\vec{F}| = mv^2/r$ where r is the bending radius. The *magnetic rigidity* is $Br = p/e \approx 3.34p$ for a particle with momentum $\vec{p}$ orthogonal to $\vec{B}$ in units of $[p] = \text{GeV}/c$, $[B] = \text{T}$ and $[r] = \text{m}$. In length L the bending angle (Fig. 17.3) is $\sin\frac{\Theta}{2} = \frac{L}{2r} = \frac{LB}{2(Br)}$. At high energies the bending angle is small, so $\sin\Theta \simeq \Theta$ and $\Theta \simeq \frac{LB}{(Br)}$.

As shown in Fig. 6.1 a quadrupole magnet focuses in one plane and defocuses in the other one, while it does not affect the particles in its centre. They are set in doublets and triplets and tuned so that the first magnet focuses the particles to the centre of the defocusing plane of the second one, which ensures an overall focusing effect.

The high-energy accelerators use superconducting technologies. Fig-
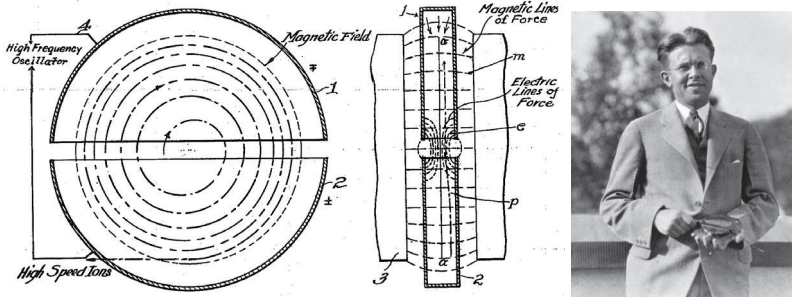
Figure 6.2: Left: The original drawing of Lawrence's cyclotron patent. Right: Lawrence with his first cyclotron in hand

ure 17.4 shows the cross section of a dipole magnet of the Large Hadron Collider. The LHC keeps two proton beams in orbit in opposite directions, and so it has two storage rings with two sets of dipole magnets.

6.2 Acceleration

At low energies sufficient particle acceleration was achieved using electrostatic fields. The largest electrostatic accelerators are the Van de Graaff generators which can provide about 35 MeV energies. The contemporary accelerators use resonance acceleration in microwave cavities rather than electrostatic fields: $\vec{E} = -\partial \vec{A}/\partial t$. The modern accelerator cavities can provide as high as 45 MeV/m acceleration. Figure 17.4 shows such a resonator cavity built for the TESLA project at DESY, Hamburg.

The first *cyclotron* was built by E. Lawrence in Berkeley in 1929. He spent 20 $ on it and was awarded the Nobel Prize for it in 1939. It is a circular machine (Fig. 6.2) consisting of two half-cylinders (D's): the particles circulate in orbits of increasing radii as gaining energy in the gaps between the D's where the direction of the field changes in phase with the circulation of the particles. In the *synchrotron* the radius of the particles is fixed and the magnetic fields are tuned to keep the particles in the same orbit. At CERN all circular machines are synchrotrons.

The linear accelerator (nicknamed *linac*) developed parallel with the circular ones. It was first built by Rolf Widerøe in 1928; now usually the first stage of any accelerator system is a linear one. The accelerator cavity is in principle similar in the circular and linear accelerators, but in the circular

ones the same cavities are used again and again in every turn of the beam, whereas in the linear accelerators they are passed only once.

6.3   Colliders

In an ordinary accelerator the beam hits a fixed target. For the collision of identical particles the centre-of-mass energy is $E_{\text{CM}}^2 = s \equiv (p_1 + p_2)^2 = 2M_X E_b + 2M_X^2$, i.e. $E_{\text{CM}} \sim \sqrt{E_b}$. With increasing beam energy E_{CM}, the useful energy of the collision that can produce new particles grows with the square root of the beam energy. If both particles are accelerated, the energy released in the collision is the sum of the beam energies in the CM system.

Another advantage of the colliders with identical particles is the centre-of-mass system in the laboratory. This means not only an easier interpretation of the data, but also the possibility to encircle the interaction point by a completely symmetric detector system with which one can detect all produced particles.

6.4   Flux and luminosity

Flux is defined as the number density of particles hitting a unit surface of the target in unit time. It is naturally connected to the cross section, and so physicists like to give it in units of 1/(barn s).

Luminosity is the rate of collecting data for colliders, similar to the flux of fixed-target experiments. It is defined as $L = fn\frac{N_1 N_2}{A}$ where f is the circulation frequency of the colliding beams; n is the number of particle bunches in the ring; N_1, N_2 are the numbers of particles in the two kinds of bunches; A is the spatial overlap of the colliding bunches. The total number of collisions is characterized by the integrated luminosity: $\int_{t_1}^{t_2} L \mathrm{d}t$ which is usually measured in units of inverse cross section, at LHC in [pb^{-1}, fb^{-1}]. The expected detection rate of a reaction with cross section σ at ϵ detection efficiency is $R = \epsilon \sigma L$.

6.5   Beam cooling

In order to store particles in storage ring, they have to be focused, both in space and in momentum. The trajectories of particles are focused with magnets, and in momentum space by stochastic and electron cooling. It is

called cooling in analogy to gases where higher temperature means larger momentum spread among the molecules.

Stochastic cooling was invented together with many other things in accelerator physics by Simon van der Meer (Nobel Prize, 1984). It is used to reduce the transverse momentum spread within a bunch of charged particles in a storage ring by detecting fluctuations in the momentum of the bunches and applying corrections to reduce them. While acceleration (or in some cases, deceleration) is done to particles in small, dense bunches, cooling is most efficient when they are stretched out, *debunched*. This is technically done via bridges of microwave conductors (Fig. 17.6) across the storage ring to time the correction *kick* to reach the same particle whose wayward momentum was detected.

Electron cooling, invented by *G. I. Budker* can be used to low-energy or slow particles (Fig. 17.6) to reduce their relative momenta. A dense beam of electrons having the same velocity as the average one of the beam to be cooled is mixed to the stored particles. The stored heavier particles loose their momentum spread via Coulomb scattering on the highly monochromatic electrons.

6.6   CERN's accelerator complex in the LEP era

For more than 10 years, from 1989 to 2000, two storage rings, the Large Electron Positron (LEP) collider at CERN and the Tevatron proton-antiproton collider at the American Fermilab dominated high energy physics. Tevatron observed the top quark first. Right at the beginning of its work LEP has shown that there are only three kinds of light neutrinos, and consequently, there are three fermion families only. After this an incredible amount of precise LEP measurements tested and confirmed the predictions of the standard model of particle interactions. At the same time two other large colliders worked as well: the Stanford linear electron-positron collider at the American SLAC laboratory and the Hadron-Electron Ring Accelerator (HERA) at the DESY laboratory in Hamburg. The former–similarly to LEP–studied the production and decay of the Z boson, while HERA delivered extremely important information on the quark structure of the proton. At present there is just one large collider, the LHC.

The scheme of the accelerator complex of CERN in the LEP era is shown in Fig. 17.5. It was based on the old (but apparently forever living) Proton Synchrotron (PS) which in every repetition cycle of 14.5 s duration went through the following phases: proton acceleration for antiproton production,

Year	$E(e^+e^-)$, GeV	$\int L dt/4$, pb^{-1}	main study
1989–94	$\simeq 91$	140	properties of Z
1995	130–136	5	
1996	161–172	20	properties of W$^\pm$
1997	184	60	W$^+$W$^-$, ZZ production
1998	189	190	W$^+$W$^-$, ZZ production
1999	192–202	220	search for the Higgs boson
2000	204–209	220	search for the Higgs boson

Table 6.1: The Large Electron-Positron (LEP) collider: energies, integral luminosities for each experiment and main goal of study.

proton and heavy ion acceleration for the Super Proton Synchrotron (SPS), electron and positron acceleration for LEP and antiproton deceleration for LEAR, the Low Energy Antiproton Ring. Let us study these phases.

6.6.1 Electrons and positrons

Electrons of 180 MeV energy from a linac were injected into a tungsten target to produce positrons via pair production. Both the electrons and positrons were accelerated in another linac to 500 MeV and then stored in EPA, the Electron-Positron Accumulator. When the luminosity of LEP was already low, they were accelerated by the PS to 3.5 GeV and transferred to the SPS for further acceleration and finally fed into the LEP ring. The electrons and positrons collided at four interaction points of LEP equipped with huge experimental detector systems called ALEPH, DELPHI, L3 and OPAL. The collision energies and luminosities of LEP are summarized in Table 6.1. In its last two years of study, while searching for the Higgs boson, LEP provided more data than in the previous 10 years together, in spite of the fact that its collision energy was well over the enormous yield of the Z peak (Fig. 17.2).

LEP was a very precise machine, its 27 km ring was sensitive to all kinds of macroscopic and regional factors such as the position of the Moon or seasonal changes of the rainfall in the area (tide effect of underground water). In 1995 a strange noise was registered in its magnets and champagne was promised to the person who finds its source. Somebody found a correlation with the schedule of the fast train between Geneva and Paris. A parasitic flow of electricity, originating from the trains, travelled along underground rivers to the grounding cable and the vacuum chamber of LEP, disturbing the current of the bending magnets.

LEP energy was severely limited by synchrotron radiation. A relativistic particle of charge e_p in a circular machine of radius r loses its energy due to synchrotron radiation. The energy loss is

$$\Delta E = -\frac{4\pi}{3}\frac{e_p^2\beta^2\gamma^4}{r} \tag{6.1}$$

per turn where $\beta = v/c$ is its relative velocity and $\gamma = 1/\sqrt{1-\beta^2}$ is the relativistic factor. This means that the energy loss from synchrotron radiation sensitively depends on the mass of the charged particle, roughly proportional to the negative fourth power of its mass. It prevented LEP's further energy increase, while for the much heavier proton it is negligible at LHC energies.

In the last two years of LEP running workers started to dig the huge caves for ATLAS and CMS, the two LHC experiments too large to fit in the place of a former LEP detector. Simulations predicted that the LEP tunnel will relax, elevate by several millimetres during this work because of the removal of the thousands of tons of earth, possibly ruin the extremely precise alignment of the LEP magnets. The accelerator experts at CERN solved this problem by continuously correcting the LEP magnets so that the work of LEP was not disturbed by the underground work.

6.6.2 Protons

The protons started from a duo-plasmotron ion source where the electrons were shaken off from hydrogen molecules, then accelerated in a proton linac up to 50 MeV. They were injected into the PS Booster where they got to 1 GeV and injected into the PS. The PS provided:

- proton beams up to 25 GeV/c momentum to the PS experiments in a continuous extraction mode;

- injected bunches of protons into the Super Proton Synchrotron (SPS) for further acceleration to 450 GeV/c;

- shot bunches of protons onto an antiproton production target for the Antiproton Accumulator / Collector storage ring.

The PS Booster also provided 1 GeV protons for the ISOLDE radioactive beam facility of CERN to prepare radioactive atomic beams.

6.6.3   Heavy ions

The SPS accelerated also ions with atomic mass up to that of lead for heavy ion physics. Lead ions, Pb^{53+} are accelerated in a dedicated linac, in the PS Booster, in the PS and injected into SPS where they are completely *stripped* to Pb^{82+} and after further acceleration ejected for the SPS experiments. The SPS remains in operation in the regime even in the LHC era.

6.6.4   Antiprotons

25 GeV protons from PS were injected into an iridium target to produce proton-antiproton pairs; antiprotons of momentum 3.75 GeV/c were collected in the AA-AC (antiproton accumulator - antiproton collector) double ring to be cooled and stored until the SPS in its Sp$\bar{p}$S collider regime or later LEAR, the Low Energy Antiproton Ring received them. The PS decelerated the antiprotons to 600 MeV/c before ejecting them into LEAR that further accelerated or decelerated them for the LEAR experiments.

6.7   Other accelerators

In addition to CERN there are several particle-physics oriented accelerator laboratories on Earth, most of them are in the USA, Germany, Japan and Russia. Here we shall mention only a few of them. Particle and nuclear physics uses about a hundred accelerators whereas medicine and solid-state technology uses a hundred times more, of course, at much lower energies. Later we shall mostly concentrate on CERN experiments, but here we mention some of others.

6.7.1   Tevatron at Fermilab

Before LHC Tevatron at Fermilab, the Fermi National Accelerator Laboratory (Batavia near Chicago, USA) was the highest energy accelerator on Earth. It collided accelerated protons and antiprotons at almost 2 TeV energy. It had two major experiments, CDF and D0. The last quark with the highest mass, the t quark was discovered at the Tevatron, although its mass was estimated much earlier from radiative corrections. The Tevatron was stopped when LHC started to collect p-p collision data at 7 TeV, later in 2012 at 8 TeV, at orders of magnitude higher luminosities.

6.7.2   HERA at DESY

The DESY (Deutsches Elektronen-Synchrotron) laboratory is located in Hamburg, Germany. It operated several accelerators, including HERA, the first accelerator using superconducting magnets. HERA was the only accelerator in the world that was able to collide protons with either electrons or positrons. It operated between 1990 and 2007. HERA's tunnels run 10 to 25 meters below ground level and contained two accelerator rings. Its two major experiments, ZEUS and H1 watched the collisions of 27.5 GeV electrons or positrons with protons of 920 GeV, they increased the available information on the structure of the proton by an order of magnitude.

6.7.3   RHIC at Brookhaven NL

The accelerator physicists at Brookhaven National Laboratory played a pioneering role by designing and building AGS, the Alternating Gradient Synchrotron. The Proton Synchrotron at CERN was built along the line laid by the AGS. BNL is a general research laboratory, not only for particle physics, but also for solid state physics, chemistry and material sciences. Among other facilities BNL built another ground-breaking machine, the Relativistic Heavy Ion Collider (RHIC) where ions are collided inside the detectors of several experiments, the largest ones being STAR and PHENIX. The types of colliding particles are p + p, d + Au, Cu + Cu, Cu + Au, Au + Au and U + U. The typical Au+Au collision energy is 200 GeV/nucleon pair (that is the usual energy unit of heavy ion collisions) at a luminosity of $3 \times 10^{27} \mathrm{cm}^{-2}\mathrm{s}^{-1}$.

6.8   CERN's facilities in the LHC era

CERN's accelerator complex after 2008 is shown in Fig. 17.7. The complexity of the system decreased by eliminating EPA, the electron-positron ring, but made more complicated by several additions, the greatest ones are the proton injectors from two sides and the neutrino beam.

6.8.1   LHC, the Large Hadron Collider

We shall devote special emphasis on the description of the LHC, today's flagship of high energy physics .

Using protons means two advantages against electrons in a collider. In addition to the much less energy loss due to synchrotron radiation, a proton

machine has much larger discovery potential. As the proton is a composite particle with quarks and gluons inside, a high-energy p-p collision means many different possible collisions among quarks and gluons. We shall see later that the 125 GeV Higgs boson was discovered at LHC in 8 TeV p-p collisions where the predominant production mechanism was gluon fusion.

When LEP was stopped, the electron-positron system was also dismounted. The LEP tunnel was filled with 9300 superconducting magnets, the most important ones being the 1232 double dipoles (Fig. 17.8, left) keeping the two circulating beams in orbit opposite to each other. Figure 17.8 (right) shows the radio-frequency cavities accelerating the particles in the LHC ring.

Protons in LHC

The Large Hadron Collider operates two counter-propagating proton beams, so it contains two accelerator systems and two storage rings. The fact that it collides protons instead of protons with antiprotons like the Tevatron increased its luminosity by many orders of magnitude. As gluon fusion is the dominant process of new particle production (like that of the Higgs boson), this did not reduce the discovery potential.

The work of LHC is well illustrated by the official beam diagnostics page of CERN (Fig. 17.9) taken by one of authors on 12 June 2016 at 18:28 hours while supervising data collection by the CMS detector. The previous evening at 18:00 the LHC beam was dumped, as the proton intensities in the two beams (red and blue curves) went already down to 6×10^{13} protons. The magnet currents were brought to zero at 19:00 hours for a short time (as shown by the black curve corresponding to the right axis) and shortly later brought back to 450 GeV SPS energy. Around 22:30 the two LHC beam pipes were refilled by protons in an hour (in 24 steps by 96 bunches in each) by 2.4×10^{14} protons in each direction. After cooling and focusing, while the magnet currents were increased step-by-step, in about a quarter hour the two beams were accelerated up to 6500 GeV. After further cooling and squeezing the beams and adjusting them to collide in the geometric centres of the detectors, stable collisions were reached at about midnight and the detectors could be turned on fully. At the moment of taking the snapshot the LHC data were collected already since 18 hours in stable collision regime, but the beam intensities were down at 70% of the initial values. All five experiments, the huge ATLAS and CMS, the somewhat smaller ALICE and LHCb and the much smaller TOTEM were working in their stable *PHYSICS* mode.

The LHC detectors are quite different from each other. ATLAS and CMS can handle 15 times higher luminosities than LHCb, and 1500 times higher than ALICE. Depending on the circumstances the LHC could deliver stable collisions for several days with one fill, although they were frequently interrupted by glitches in the electric network. The accelerator has many information pages, for instance we could learn that at the time of taking Fig. 17.9 the two proton beams met at the collision points at an angle of 170 μrad different from the head-on 180 degrees, their overlap was 25 mm along the beam direction and $20 \times 16\,\mu$m in the $x - y$ plane orthogonal to the beam. The proton bunches followed each other by 25 ns and each ring contained 2220 proton bunches. In ATLAS and CMS there were 2208 bunch crossings, in LHCb 2036, and in ALICE 1940.

LHC was started with protons in 2009 and went through an incredible development. During 2010, its first full data taking year, the luminosity went through a gradual increase of 8 orders of magnitude in 8 months, it delivered 46 pb^{-1} integrated luminosity of proton-proton collisions at 7 TeV energy. In 2011 it worked at 7 TeV and provided 4.5 fb^{-1}. In 2012 the integrated luminosity was 23 fb^{-1} at 8 TeV. That was the time of observation of the Higgs boson. After a long shutdown in 2015, the LHC restarted with 6.5 + 6.5 GeV p-p collisions: it provided 4 fb^{-1} in 2015, 40 fb^{-1} in 2016 and 51 fb^{-1} integrated luminosity in 2017. Of course, there are always inefficiencies, things sometimes break down and the inner detector part of the detector is always delayed a bit behind the announcement of "Stable beams". Nevertheless, the experiments did very well, with beam usage efficiencies well above 90%.

Heavy ions in LHC

Lead ions are prepared and stored in LEIR, the Low Energy Ion Ring that was built using the elements of LEAR (Fig. 17.6). The lead ions are then injected to PSB, PS, SPS and LHC for acceleration. At the end of 2010 and 2011 LHC worked a few weeks with Pb-Pb collisions, and after its 2012 proton run, it collided Pb ions with protons. The beam energy of the LHC in its heavy ion regime was 2.76 TeV / nucleon, so for reference LHC was also running for a short while colliding protons at 2.76 TeV. For the same reason, after the 13 TeV proton runs similarly reduced collision energies were also studied: 5.02 and 8.16 TeV/nucleon p-Pb collisions in 2016, and 5.02 TeV p-p collisions in 2017. Heavy ion physics will be treated in Chapter 15.

6.8.2   Neutrinos

SPS has a special facility that provides a neutrino beam to study neutrino oscillations: CERN Neutrinos to Gran Sasso (CNGS). The Italian *Laboratori Nazionali del Gran Sasso* (LNGS) is the largest underground laboratory on Earth devoted to particle and nuclear physics. It is located at 120 km from Rome near a highway tunnel through the Gran Sasso mountains, under 1.4 km of rock. It hosts 15 experiments of 900 scientists from 29 countries. We shall describe the neutrino beam in Chapter 13 devoted to neutrino experiments.

6.8.3   Antiprotons

CPT invariance, the equivalence of matter and antimatter is deeply embedded in particle physics. However, there are no antimatter galaxies in the Universe, although during the Big Bang particles and antiparticles should have been produced in identical quantities. There are also *CPT* violating extensions of the standard model. All this demands the precise check of *CPT* invariance.

LEAR, the Low Energy Antiproton Ring was built mostly for meson spectroscopy and it was stopped when the major LEAR experiments finished data taking. LEAR was converted into LEIR, but the *CPT* experiments asked for a low-energy antiproton source. Thus CERN built the Antiproton Decelerator facility using the space and elements of the dismounted Antiproton Accumulator / Collector rings (Fig. 17.10).

The Antiproton Decelerator (AD) works the following way. An extracted beam from the Proton Synchrotron of 1.5×10^{13} protons at $p = 26\,\text{GeV}/c$ momentum is produced in 5 pulses with a total duration of 500 ns. These protons hit an iridium target where they produce proton-antiproton pairs. Antiprotons of 3.57 GeV/c momentum are collected and focused using the magnetic horn technique developed by Simon van der Meer (Nobel Prize, 1984). The antiprotons are injected into the AD ring where they are decelerated to 100 MeV/c in four steps, in the first two steps with stochastic and then electron cooling (Fig. 6.3).

The AD delivers 3×10^7 antiprotons at 100 MeV/c momentum to several (seven in 2017) experiments, which trap them in electromagnetic fields and using slow positrons make antihydrogen ($\overline{\text{p}}\text{e}^+$) atoms. ALPHA and ATRAP prepares spectroscopy on trapped antihydrogen, ASACUSA and BASE compares the properties (mass, charge and magnetic moment) of protons and antiprotons at high precision, AEGIS and GBAR tries to measure the gravitational mass of antihydrogen, and ACE studies the effects of antiprotons on living tissue.
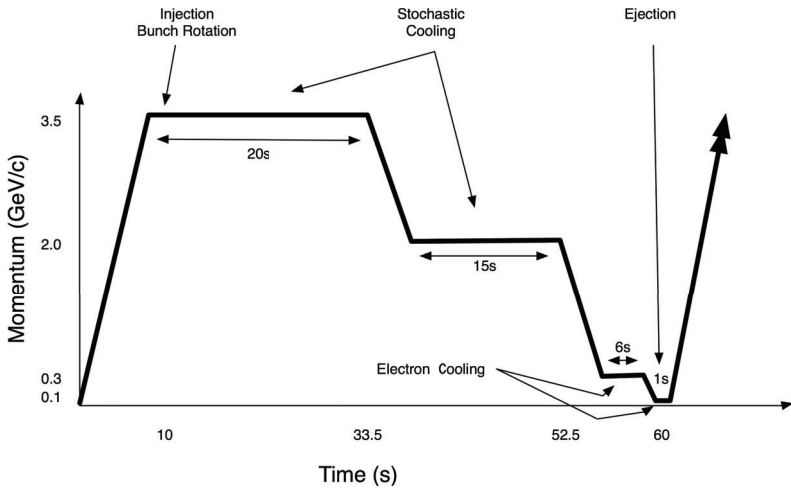
Figure 6.3: Deceleration and cooling of antiprotons in the Antiproton De-celerator.

Viewing the success of the AD experiments CERN decided to increase their efficiency by building a small storage ring ELENA (Extreme Low Energy Antiprotons) which will supply an order of magnitude higher number of slow antiprotons for trapping.

Exercise 6.1
What is the energy loss per turn of 100 GeV electrons and 7 TeV protons in the LEP/LHC tunnel of 27 km circumference due to synchrotron radiation?

Exercise 6.2
What is the energy limit one can reach with protons in a ring with a circumference of 27 km filled with 8 T magnets?

Exercise 6.3
Why is it impossible to keep the LHC detectors ready to take data during beam acceleration and adjustment?

Exercise 6.4
LHC was designed for 7 + 7 TeV collisions, but so far that was impossible to reach. According to Fig. 17.9 the 6.5 TeV beam energy could be reached

*very fast. What could be the reason why 7 TeV beams were not delivered in
2016-17?*

Exercise 6.5
*How do you get the 2.76 TeV / nucleon energy for the Pb + Pb run of LHC?
Hint: To what collision energy does it correpond for protons and lead ions?*

Chapter 7

Detectors, calorimetry

MOTTO:

Experimenter: A physicist who does experiments. Theorist: A physicist who does not do experiments.

(Leon M. Lederman)

7.1 Event registration

In high energy physics one tries to detect and identify as many of the particles produced in the beam collisions as possible. The main method is *event registration* (see Ch. 8). It means that after a suitable *trigger signal* we record all relevant information. The trigger may be physics or apparatus related. Physics triggers can be many things: observation of a muon or an isolated electron, large missing momentum (from a high-energy particle that escaped detection) or many particles in jets. In the high-energy experiments the various physics analysis groups define the triggers related to their interest, sometimes hundreds of different conditions. Other triggers could be apparatus-related, for instance laser pulses lighting up various parts of the detector for testing, or reading environmental measurements like the temperatures of the various parts of the equipment or the magnetic field strength. Of course, only those parts of the detector are read out that fired and are

related to the given trigger.

It is very important to collect and record all (but at least as much as possible) energy produced in the collisions. In analogy with thermal measurements that is called *calorimetry* and the detector elements involved are *calorimeters*. The high energy experiments generally have electromagnetic and hadron calorimeters, the former to catch electrons and photons, the latter for the hadrons.

In 2012 the LHC provided 20 million collision events per second, of which about 400 could be stored by CMS and ATLAS. With the development of the techniques in 2016-17 already 1000 were stored of the 40 million events per second of the LHC. Thus a very careful selection was made by the experiments to choose which events to store. That was done in two steps (two trigger levels) by CMS and three by ATLAS. For CMS the first level reduced the event rate to 100 kHz, while the second one to 1000 Hz. Of course, signals belonging to the same event are automatically in coincidence with each other. Every collision event contains many p-p collisions (called *pileup*, see Fig. 17.11). In 2016-17 that was already above 50 at average. This overwhelming amount of signals increases the discovery potential, but also the difficulties of data analysis. The detected signals in an event are automatically in coincidence, which is therefore unnecessary to prescribe in the analysis, but the particle tracks and calorimeter hits must originate from the same interaction point, called *vertex*, to belong to the same physical phenomenon. In low-rate experiments of nuclear studies one prescribed time coincidence for the events. In present-day high-energy experiments we have to demand precise space-time coincidence for the origins of particle tracks in the events.

7.2   Energy loss in matter

Fast particles lose their energy in collisions with the atoms of the medium. At lower energies, around 1 MeV Coulomb scattering dominates. Let us consider a particle of mass M and charge $z \times e$ moving at velocity $v = c\beta$ along the x axis in a medium of atomic number Z and atomic weight A. The forces along its trajectory compensate each other, there will be no exchange of momentum along x, $p_x = \int F_x(t)\mathrm{d}t \approx 0$. It applies a force $F_y = \frac{ze^2}{x^2+b^2}$ on an atomic electron (assumed to be at rest) located at longitudinal coordinate x in a cylinder at a radius b (Fig. 7.1) and thickness db. The momentum loss
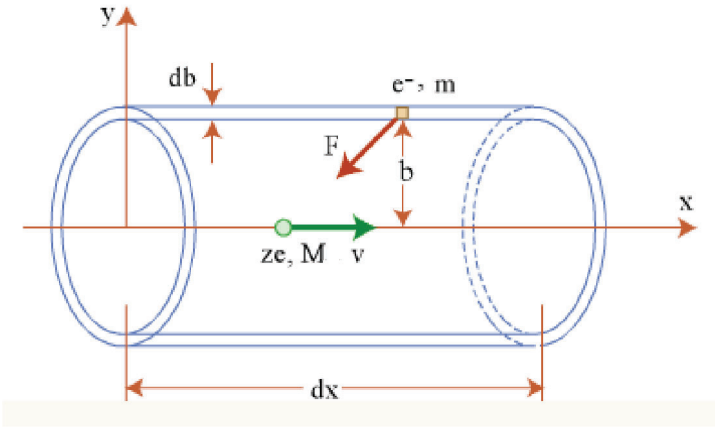
Figure 7.1: Derivation of the Bethe equation: a particle of mass M and charge ze moving at velocity v interacts with the atomic electrons in a cylinder of radius b of a medium

of the particle along an infinitesimal distance dx will be

$$p_y = \int F_y(t)dt =$$

$$\int \frac{ze^2}{x^2 + b^2} \frac{b}{\sqrt{x^2 + b^2}} \frac{dx}{v} = \frac{ze^2 b}{v} \int \frac{dx}{(x^2 + b^2)^{3/2}} = \frac{2ze^2}{vb}$$

The energy transfer from the incoming particle to a single electron is

$$\frac{p_e^2}{2m_e} = \frac{2z^2 e^4}{m_e v^2 b^2}.$$

We have $nZ(2\pi b db dx)$ electrons in unit length of the cylinder, so in order to calculate the average energy loss per unit path length we have to integrate over all impact parameters b between its minimal and maximal values:

$$-\frac{dT}{dx} = \int_{b_{min}}^{b_{max}} nZ \, 2\pi b \, db \, \frac{2}{m_e} \left(\frac{ze^2}{vb} \right)^2 = \frac{4\pi (ze^2)^2 nZ}{m_e v^2} \ln \left(\frac{b_{max}}{b_{min}} \right)$$

The minimum distance cannot be shorter than the *de Broglie wavelength*, $b_{min} \approx \frac{h}{m_e v}$, whereas the maximal distance is limited by the ionization potential of the medium, ie. the minimal transferable energy: $b_{max} \approx \frac{\gamma h c \beta}{I}$.

Here $\gamma = 1/\sqrt{1 - v^2/c^2}$ and I is the average ionization potential of the medium, which can be roughly estimated by $I \approx 10Z$ eV. Thus $\frac{b_{\max}}{b_{\min}} \approx \frac{m_e v^2}{I}$ and the total energy loss with relativistic and atomic shell corrections is

$$-\frac{\mathrm{d}E}{\mathrm{d}x} = Kz^2\frac{Z}{A}\frac{1}{\beta^2}\left[\frac{1}{2}\ln\frac{2m_ec^2\beta^2\gamma^2T_{\max}}{I^2} - \beta^2 - \frac{\delta}{2} - \frac{C}{Z}\right] \qquad (7.1)$$

This is called the Bethe–Bloch equation. Here x is the thickness of the medium in units of g/cm^2, $K = 0,307$ MeV $\cdot$ cm^2/g a constant, and $T_{\max}$ is the maximal transferable energy to an electron. The Bethe–Bloch equation can be written in a simplified form using the approximation

$$T_{\max} = \frac{2m_ec^2\beta^2\gamma^2}{1 + 2\gamma m_e/M + (m_e/M)^2} \approx 2m_ec^2\beta^2\gamma^2 \quad (2\gamma m_e/M \ll 1)$$

as

$$-\frac{\mathrm{d}E}{\mathrm{d}x} = K\frac{z^2}{\beta^2}\frac{Z}{A}\left[\ln\frac{2m_ec^2\beta^2}{I(1 - \beta^2)} - \beta^2\right].$$

Note that here the energy loss does not depend on the mass m of the particle, only on its velocity. Figure 7.2 shows the energy loss of a muon in copper as a function of the muon momentum. There is a wide minimum-ionization region between 0.1 and 100 GeV/c momentum which practically encompasses the energy range of the muon in high-energy experiments and that is why the energetic muons cannot be contained in the detector volumes. Nuclear losses are negligible for muons, but they dominate for the strongly interacting particles. That is why pions and muons have so vastly different penetration depths in matter although they have quite similar masses.

For high-energy electrons radiation is the most important means of energy loss. The total loss is $\frac{\mathrm{d}E}{\mathrm{d}x} = \left(\frac{\mathrm{d}E}{\mathrm{d}x}\right)_{\text{ion}} + \left(\frac{\mathrm{d}E}{\mathrm{d}x}\right)_{\text{rad}}$. *Critical energy* is the energy at which the radiation energy loss becomes equal to the ionization one for an electron, $\left(\frac{\mathrm{d}E}{\mathrm{d}x}\right)_{\text{ion}} = \left(\frac{\mathrm{d}E}{\mathrm{d}x}\right)_{\text{rad}}$. In rough approximation it is $E_c \approx \frac{800\text{MeV}}{Z+1.2}$. *Radiation length* X_0 is defined as the thickness of matter at which $\left.\frac{\mathrm{d}E(e^-)}{\mathrm{d}x}\right|_{\text{rad}} = -\frac{E}{X_0}$.

For composite materials (element j is present at weight fraction w_j) we can use Bragg's rule

$$\overline{\left(\frac{\mathrm{d}E}{\mathrm{d}x}\right)} = \sum_j w_j\left.\frac{\mathrm{d}E}{\mathrm{d}x}\right|_j$$

and

$$\overline{\left(\frac{Z}{A}\right)} = \sum_j w_j\frac{Z_j}{A_j} = \frac{\sum_j n_j Z_j}{\sum_j n_j A_j}.$$
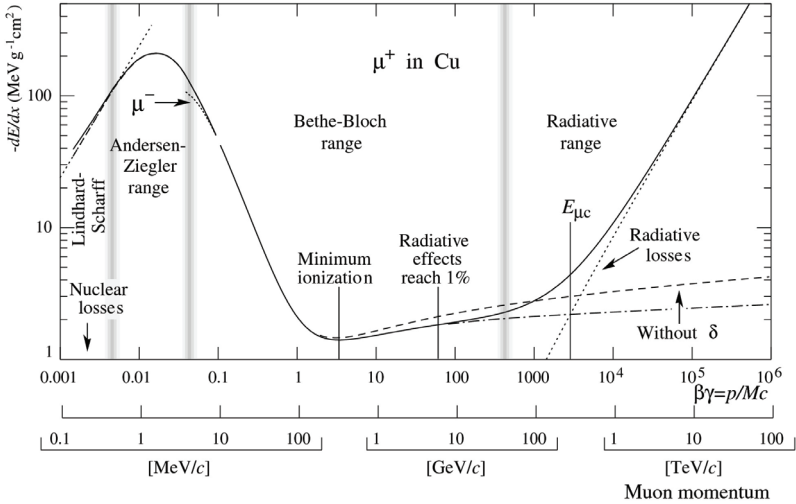
Figure 7.2: Energy loss of a positive muon in copper. Up to 500 GeV the Bethe-Bloch mechanism works well for muons. Below the minimal ionization region, 100 MeV/c, for different energy regions different approximative calculation methods are used. Above the Bethe-Bloch region radiative losses dominate for muons

Bragg's rule can be used for calculating the radiation length as well, but it overestimates the average ionization potential for molecules as the electrons have tighter bonds there than in the atoms.

Electrons lose energy via radiation and photons via bremsstrahlung[1] and pair creation. As a result, both produce electron-photon showers, and thus electrons and photons behave very similarly at high energies [Leo, 1987].

7.3 Particle identification

Practically all detectors of high-energy physics have strong magnetic fields inside. It is usually a solenoid, but ATLAS combines a solenoid encircled by a huge toroidal field (Fig. 17.12).

There are several methods to identify the particles in an event. From

---

[1]In English the original German word is used for the radiation emitted in the deceleration of charged particles in matter; other languages use the simple mirror translation of the German word: *braking radiation*

Det. type	space res., rms (μm)	time res.	dead time
Photo-emulsion	1		
Bubble chamber	$10 - 150$	1 ms	50 ms
Streamer chamber	300	2 μs	100 ms
Prop. chamber	$50 - 300$ ($d/\sqrt{12}$)	2 ns	200 ns
Drift chamber	$50 - 300$	2 ns	100 ns
Scintillator		100 ps/n	10 ns
LAr drift chamber	$\simeq 170 - 450$	$\simeq 200$ ns	$\simeq 2$ μs
Microstrip ch.	$30 - 40$	< 10 ns	
Resistive plate ch.	≤ 10	$1 - 2$ ns	
Silicon strip	$d/(3 - 7)$	readout	readout
Silicon pixel	2	readout	readout

Table 7.1: Detector types used in high-energy physics. The time resolution of the various scintillators depends on the material and size of the detectors. For the silicon detectors the read-out speed defines the timing

the trajectory of a charged particle in a magnetic field one can determine its charge and momentum. A mixed beam of different particles with a given momentum can be separated by their time of flight between two detectors. Different particles lose their energy in collisions with the atoms of a medium at different rates approximately at $dE/dx \sim z^2/\beta^2$ where x is the thickness of matter, z is the charge of the particle in units of the electron charge and $\beta = v/c$ is its relative velocity. Cherenkov radiation is also characteristic of a particle velocity: when a particle flies in a medium faster than the light, it emits Cherenkov light at an angle $\theta_c = \arccos \frac{1}{n\beta}$ where n is the refraction index of the medium.

7.4   Detector types

Some properties of the detector elements used in high-energy physics are summarized in Table 7.1

7.4.1   Multiwire chambers

The invention of multiwire chambers by *Georges Charpak* in the sixties revolutionized experimental particle physics. It made the visualization of the events electronic, the experiments fully automated and orders of magnitude faster than the previous method of bubble chambers with photographing events and later processing by hand. He published the method in 1968 and was awarded the Nobel Prize in 1992.

In a multiwire chamber the particles ionize a gas, the electrons are collected by anodes of very thin wires (typically gold-coated tungsten of 10-20 μm thickness) with cathodes of metal plates, semiconductor pads or thick steel wires. The gas should have an electron-collector quencher admixture in order to prevent a self-supporting long discharge. Typical such mixture is argon + isobutane with some freon added.

In the classical chambers there are many layers of wires placed in orthogonal directions with both ends read out: the position of the particle trajectory is determined by the position of the wire and the charge ratio at the two ends. This was changed as the detector volumes increased. The drift chambers gather one of the coordinates by the drift time of the electrons to the wire. The time projection chambers (TPC) combine the drift times with silicon pads on the bottom, which detect the mirror charges of the trajectories (Fig. 17.13). Drift chambers and TPC's sacrifice detection speed for spatial resolution: because of its TPC tracker, ALICE is better at particle identification, but it can take much less events than ATLAS or CMS that have semiconductor trackers. In the case of heavy ion collisions this is not a problem as they happen much less frequently than p-p collisions.

7.4.2   Scintillation counters

The scintillation detectors (called *counters* although they rarely count) are the most widely used detectors in nuclear and particle physics: they are fast and have an excellent energy resolution. Table 7.2 summarizes the most important types of scintillators. NaI(Tl) has the highest light yield, but it is highly hygroscopic, so hard to handle. Polystyrene is the fastest and PbWO$_4$ has the highest specific weight while almost as fast as polystyrene. That is why ALICE and CMS use PbWO$_4$ single crystal scintillators in their electromagnetic calorimeters (Fig. 17.15).

The light from scintillators is converted to electric pulses using photomultipliers or avalanche photo-diodes (APD). Photo-multipliers give higher gains than APD-s, but occupy more space and are sensitive to magnetic fields.

Scintillator	photon-yield	τ ns	$\lambda_{\max}$ nm	ρ g/cm^3	$\frac{\mathrm{d}E}{\mathrm{d}x}$ MeV/cm	X_0 cm
NaI(Tl)	1	250	410	3.7	4.8	2.59
polystyrene	0.12	3–5	360–480	0.9		$\simeq 12$
CsI(Tl)	0.4	1000	565	4.5	5.6	1.85
BGO	0.15	300	410	7.1	9.0	1.12
PbWO$_4$	0.01	5–15	420–440	8.3	10.2	0.9

Table 7.2: Basic properties of various scintillators: name, light yield relative to NaI(Tl), decay time of the signal, maximum of wavelength distribution, density, stopping power and radiation length.

7.4.3 Shower detectors

If the particles to be detected deposit little energy in unit volume they are forced to penetrate dense materials (some heavy metal) interleaved with scintillators or other active detector elements to detect secondary particles from the interaction of the primary particles with the dense medium. Very frequently the return yoke of the main magnet of the detector serves as the dense matter. The muon chambers of CMS are such shower detectors in between thick layers of steel.

In high energy calorimetry a special requirement is the complete coverage of the interaction point which leaves very little space for photon detectors. The solution is the scintillation tile: wavelength-shifting (green) fibres are embedded in the (blue) scintillators, which collect the light and transport it to the photon detectors (Fig. 17.16). This technique makes it possible to build walls of flat scintillators with no gap between them. The hadron calorimeter of CMS is a shower detector system, consisting of 4 mm thick scintillator tiles between 50 mm thick brass plates. For the latter over a million brass shell casements were melted, left behind by the Russian navy after World War II. (It was not enough, the USA added 1 million dollars worth of copper to finish them.)

7.4.4 Cherenkov detectors

Cherenkov detectors are widely used at LHC. Both ATLAS and CMS uses them to detect the forward scattered particles, which provides important information to measure the instantaneous luminosity of the experiment. Figure 17.17 shows the structure of the forward hadron calorimeter of CMS,

consisting of quartz fibres in steel to collect Cherenkov light from secondary electrons. Here the Cherenkov radiator is quartz, very resistant to radiation. The electromagnetic calorimeter of the OPAL detector at LEP consisted of large blocks of lead glass read by photo-multiplier tubes. The ATLAS forward detector is filled with freon gas (C_4F_{10}) as Cherenkov radiator just like the ring-imaging Cherenkov counters of LHCb (CF_4 and C_4F_{10}).

7.4.5 Transition radiation detectors

In a medium containing n_e quasi-free electrons in unit volume an electromagnetic radiation with ω frequency will have a phase velocity of

$$v_f = \frac{c}{n} = \frac{c}{\sqrt{1 - \frac{n_e e^2}{\varepsilon_0 m_e \omega^2}}} \tag{7.2}$$

where n is the refraction index. It can propagate if $v_f > 0$, i.e.

$$\omega > \omega_p = \sqrt{\frac{n_e e^2}{\varepsilon_0 m_e}} \tag{7.3}$$

where ω_p is the *plasma frequency* of the medium. Of course, in condensed matter the plasma frequency can deviate from Eq. 7.3 as there the electrons are not free.

Transition radiation is emitted when a fast charged particle passes the boundary of two media with different dielectric constants. It is caused by the continuous change of the electric displacement, $\vec{D} = \varepsilon \varepsilon_0 \vec{E}$ through a boundary while $\vec{E}$ jumps. When a charged particle approaches a boundary, with its mirror charge on the boundary they make a dipole which changes in time, that is why the radiation is emitted. This is significant for extreme relativistic particles only with $\gamma = 1/\sqrt{1 - \beta^2} \gg 1$.

When such a particle passes a thin absorber (foil) with plasma frequency ω_{p1} and enters a medium with ω_{p2}, it radiates photons of frequency $\omega \gg \omega_{p1}$ with a double differential energy distribution [Leo, 1987]

$$\frac{dE_{tr}}{d\omega d\Omega} = \frac{d_1 \omega}{2c} \left(\gamma^{-1} + \theta_c^2 + \frac{\omega_{p1}^2}{\omega^2} \right)^{-1} \tag{7.4}$$

where d_1 is the thickness of the foil and Ω is the solid angle. This is a radiation in the X–ray region, which is strongly forward peaked with a cone angle of $\theta_c \approx 1/\gamma$. The total energy radiated for $\omega_{p1} \gg \omega_{p2}$ is $E_t r = \alpha z^2 \gamma \hbar \omega_{p1}/3$.

A transition radiation detector (TRD) usually consists of hundreds of thin foils and a chamber to detect X-rays. ATLAS has a transition radiation tracker system made of *straw tubes*, small, thin multilayered tubes with proportional counter wires inside.

7.5   The CMS detector

All detector systems of high-energy collider experiments have similar structures. They consist of a barrel and two endcaps, both kinds are built of layers of different tasks. For the sake of presentation we consider the CMS (Compact Muon Solenoid) detector as a typical example (Fig. 17.14). The innermost layer, closest to the interaction point, right against the beam pipe is a 3-layer silicon pixel detector of high modularity, to make possible to identify the interaction point from which the given particle track originates. It is surrounded by many layers of silicon strip detectors, the *tracker* to trace the trajectories of charged particles curving in the magnetic field. The tracker is surrounded by the electromagnetic calorimeter, consisting of 75,848 $PbWO_4$ single crystal scintillators (Fig. 17.15), which absorbs all photons and electrons measuring their energies. The next layer is the hadron calorimeter for absorbing all energies carried by hadrons: pions, kaons, protons, neutrons, with its brass plates and scintillator tiles (Fig. 17.16).

All CMS calorimeters of the barrel are inside the largest superconducting solenoid on Earth: in its volume of 6 m inner diameter and 13 m length (Fig. 17.18) it can maintain a magnetic field of $B = 4$ Tesla, although it was up to now used at 3.8 T only to ensure its longevity. The outermost layer of the CMS detector around the magnet is the muon system: steel rings (return yoke) of the magnet interleaved with chambers to detect the muons emitted in high-energy collisions. The endcaps have a somewhat similar structure with elements close to the beam pipe to detect forward-scattered particles.

Exercise 7.1
What are the advantages and disadvantages of drift chambers against ordinary multiwire chambers and scintillation counters?

Exercise 7.2
Arrange the following particles according to their penetration depths in matter: *muons, pions, protons, electrons, photons, neutrinos.*

Exercise 7.3

Why does the muon has so much longer free flight path in matter than the pion that has almost the same mass?

Exercise 7.4

Arrange the following detectors in order of detection speed: scintillator, bubble chamber, emulsion, multiwire chamber, Cherenkov detector, drift chamber.

Exercise 7.5

Arrange the following detectors in order of energy resolution: scintillator, bubble chamber, multiwire chamber, Cherenkov detector, drift chamber.

Chapter 8

Event registration

MOTTO:

For those who want some proof that physicists are human, the proof is in the idiocy of all the different units which they use for measuring energy.

(Richard P. Feynman)

As mentioned in the previous chapter, the basic experimental method of high energy physics is event registration: particle collisions are received and studied one-by-one, and whenever a pre-defined trigger condition is fulfilled, the relevant parts of the detector (i.e. those which fired and/or related to the given trigger) are read out and the data are stored. There are physics and detector related events. In a *physics event* we have particle tracks in the tracking system and energy deposits in the calorimeters, and from all that one can reconstruct what happened in the detector.

Events are detected and simulated. The analysis of events is usually made by comparing the detected events with the results of simulations using the known processes. Events are simulated via creating particles with the Monte Carlo method and then letting them go through the detector simulation. This way we make sure that the simulated events are as close to detected ones as possible. New phenomena are searched for (and possibly observed) above the background of known processes when all possible reactions are taken

into account weighted by their cross sections. Of course one has to check first how well the simulation reproduces the known processes. At the end that has to be accounted for in the final uncertainty of the result.

Let us view a few typical event pictures recorded at LEP, Tevatron and LHC.

8.1 LEP events

OPAL (Omni-Purpose Apparatus for LEP, Fig. 17.19) was a typical high-energy calorimeter at LEP (the authors were its participants). Its main layers were from inside out: a vertex detector to identify the interaction point, a tracker made of multiwire drift chambers, the magnet, the electromagnetic calorimeter made of lead glass Cherenkov counters, the return yoke of the magnet instrumented with drift chambers serving as the hadron calorimeter, and the outermost layer, the muon chambers.

In the first years of LEP's operations (LEP1) the main goal was to study electron-photon processes at high-energy collisions (Fig. 17.20) and the properties of the Z-boson. It can decay to leptons (Fig. 17.21) and to quarks (Fig. 17.22).

Figures 17.20 and 17.21 show how electrons and photons are detected in the tracking system and in the electromagnetic calorimeter. The energy deposited in the calorimeter is characterized by the size of the yellow hit cluster. High energy electrons barely bend in the magnetic field and photons do not leave any trace in the tracker elements. They are both absorbed in the electromagnetic calorimeter, depositing all their energy there. Figure 17.20 shows electron-positron annihilation to two photons and a decay of a Z boson to two neutrinos accompanied by emission of a photon in the initial state by one of the charged particles. Neutrinos are not detected at all in accelerator calorimeters. Their creation and escape is observed by missing momentum only. In Fig. 17.21, middle and right the electron-positron collisions form Z bosons that subsequently decay to muon pairs or tau pairs. The tau lepton is very interesting as it can decay quite various ways: to its neutrino and electron + neutrino or muon + neutrino pairs and also to its neutrino and hadrons.

In electron-positron collisions at high energy quark production is very frequent and it is easy to identify by the presence of jets, sets of collimated particles (like a disperse beam). Fig. 17.22 shows events with two, three and four jets. The 2-jet events confirmed the existence of quarks, as without the requirement of fragmentation (colour neutrality of all detected particles), it
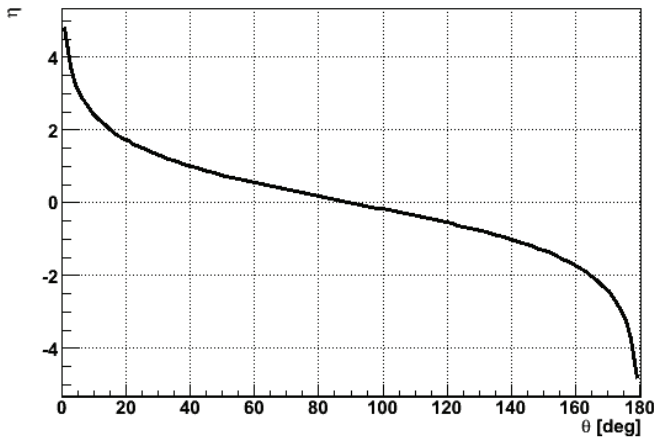
Figure 8.1: Dependence of pseudorapidity $\eta = -\ln\tan\frac{\theta}{2}$ on the polar angle

is impossible to explain the emission of dozens of charged particles. The existence of gluons was proven by the 3-jet events: fermions can be produced in pairs only and the third jet must belong to a boson with colour chargeThe 4-jet event demonstrates the pair production of W-bosons.

8.2 Transverse momentum, pseudorapidity

Hadron collisions are complicated because we collide composite systems with many constituent particles. In a proton-proton collision most of the constituents will scatter in the forward direction; as the decay fragments of new particles will be emitted in all directions, whatever is orthogonal to the beam direction is interesting. There are several quantities characterizing this feature, the most important ones being *transverse momentum* and *pseudorapidity*.

The transverse momentum is defined as the projection of the particle momentum on the plane orthogonal to the beam direction. As in accelerator experiments the beam is usually considered to be along the z axis, the transverse momentum is $p_T = p_x + p_y$.

As the initial state is cylindrically symmetric with respect to the beam axis, therefore the two direction coordinates are conveniently chosen as the

ϕ azimuthal and θ polar angles. Note that at beam crossing, where the collisions occur, the beams actually intersect each other at a very small angle different from zero (so the beams indeed cross each other), the transverse momentum corresponding to this can be neglected. While the transverse momentum and azimuthal angle are invariant under Lorentz boost along the z axis, the polar angle is not so. Thus instead of the polar angle we can use *rapidity* that is invariant under Lorentz-boost:

$$y = \tfrac{1}{2} \ln \left(\frac{E + p_{\mathrm{L}}}{E - p_{\mathrm{L}}} \right) \tag{8.1}$$

where E and p_{L} are the energy and longitudinal momentum of the particle. In high-energy collisions the mass of the detected particles (mostly leptons, pions and kaons) is negligibly small as compared to their energy and their rapidity is simplified to *pseudorapidity*, $\eta = -\ln \tan\frac{\theta}{2}$ (Fig. 8.1), which is much easier to calculate as for that one does not need to determine the energy of the particle. Furthermore, the kinematics of the events are such that most of the secondary particles fly out at small angles and pseudorapidity gives a more uniform scattering distribution than the polar angle.

Figure 8.1 shows the dependence of pseudorapidity on the polar angle. In the CMS experiment pseudorapidities $|\eta| < 2.1 - 2.5$ (the exact value depends on the subdetector) belong to the *barrel* region, outside that is the *forward* region.

At hadron colliders the number of events is frequently plotted on an $\eta - \phi$ picture which corresponds to the plane that you get if you cut the cylindrical part of the detector at a given radius along the z axis and fold it out. The angular distance of two tracks is expressed at hadron colliders in the rather peculiar angle-like quantity

$$\Delta R = \sqrt{\Delta\phi^2 + \Delta\eta^2} = \sqrt{(\phi_1 - \phi_2)^2 + (\eta_1 - \eta_2)^2}.$$

Another very important quantity is the *missing (transverse) momentum*, which means an imbalance in the momentum distribution of the event due to a neutrino or other undetected particle. In the case when leptons collide the total centre-of-mass energy is known, and adding up the momenta of the detected particles we get what is called *visible momentum (energy)*. The missing momentum (sometimes called *missing energy*) is the difference between the collisional and visible momenta (if particles of the same mass and energy collide, the collisional momentum is, of course, zero). Depending on how it is calculated, even at hadron colliders we use the quantities of missing energy or even *missing mass*, calculated from the missing transverse momentum.

8.3   Observation of the top quark

The t–often called top–quark is the heaviest among the quarks and after formation immediately decays to a b quark: t→bW$^+$. The b quark is easy to identify as it has a long lifetime, therefore if a reaction produces a b quark, the event may have a secondary vertex from such a "long-lived" particle. Another characteristic feature of the b quark is that it decays predominantly through two or three virtual W bosons and so together with jets several leptons could also be produced. Identifying the b quark is called *b-tagging* and it is quite important in high energy physics.

At the Tevatron the t quark was produced in the $\bar{p}p \to \bar{t}t$ reaction and the t quarks decayed to b quarks. The event reconstructed in Fig. 17.23 (left) is a t$\bar{t}$ created in $\bar{p}p$ collision: we required two identified b quarks from the t quark decays, 2 jets from one W-boson and muon + missing momentum from the other.

8.4   Mysterious events

There are several events which apparently contradict the standard model, but there are too few of them to draw conclusions. The most famous among them is the CDF event where a proton+antiproton collision produced an electron, a positron, two photons and some missing energy (Fig. 17.23, right). Thus all the coloured content–quarks and gluons–of the colliding hadrons simply disappeared. When this event was published by the CDF collaboration an avalanche of theoretical papers tried to interpret it in terms of various extensions of the standard model. Later the Tevatron experiments tried to find similar typhoon events for several years, in vain.

As we shall describe it in detail in Chapter 9 of data analysis, in particle physics we accept a new discovery, if (1) its signal is statistically significantly above background, (2) it is reliably and convincingly presented, and (3) confirmed by another, independent experiment. These conditions were all fulfilled when the observation of the Higgs boson was announced in 2012 at the LHC. ATLAS and CMS reported the observation of a new boson of the same mass, about 125 GeV, at more than five times the total experimental uncertainty above the background. That it had indeed been the Higgs boson as predicted by the standard model was confirmed only later, on the basis of a 4 times larger data set. The observation of this $\bar{p}p \to e^+e^-\gamma\gamma + E_{\text{miss}}$ event clearly does not fulfil the conditions of discovery.

Exercise 8.1

What is the expected number of events of a signal with the cross section of 2.5 pb at a detection efficiency of 20% if the collected luminosity is 10 fb^{-1}?

Exercise 8.2

Group the following data whether they must or may be written as part of the registered events: amplitude and timing of detector hits, temperatures of detector elements, temperatures of parts of the electronics, temperature of the counting room, atmospheric pressure, field strengths of the detector magnet, mains voltage, comments of the physicists on shift.

Exercise 8.3

How do multi-jet events like those in Fig. 17.22 prove the existence of quarks and gluons?

Exercise 8.4

Why do transverse momentum and pseudorapidity play more important roles at hadron collisions than at leptonic ones?

Exercise 8.5

In what conditions is pseudorapidity invariant under Lorentz boost?

Exercise 8.6

Why do we expect the t quark to decay predominantly to a b quark?

Chapter 9

Data analysis

MOTTO:

If you are receptive and humble, mathematics will lead you by the hand.

(Paul A. M. Dirac)

In high energy physics data analysis is very critical for several reasons.

- The experiments are extremely expensive in many senses: the accelerators and detectors are designed and built for decades, their operation needs the continuous works of thousands of physicists, engineers and technicians, and the accelerator time itself is extremely expensive. Thus one does not want to spare the effort to extract the maximum possible information from the data.

- The discovery potential of these experiments is very high and that makes it important to minimize the possibility of biased analysis, of hasty or even false discoveries.

- The huge collaborations (CMS and ATLAS each have more than 3000 participating researchers) can afford to let several groups analyse the same data, and that makes a strong competition for the best analysis that can make it to the paper at the end. The competing groups are the best testers for each others' work quality.

9.1 Statistical concepts of particle physicists

Those are as different from the *official* mathematical statistics as mechanical engineering from the Lagrangian or Hamiltonian formulation of theoretical mechanics. At the same time statistics is extremely important for data analysis in particle physics: every few years international workshops are organized by particle physicists working at the Large Hadron Collider to exchange ideas on the newest developments of the statistical methods, the last one in 2011 and its proceedings was published in [Prosper and Lyons, 2011]. In the Appendix of that thick volume *Eilam Gross* defines the aim of his paper entitled *LHC Statistics for Pedestrians* in a rather witty way: *"A pedestrian's guide . . . to help the confused physicist to understand the jargon and methods used by HEP phystatisticians. . . . A phystatistician is a physicist who knows his way in statistics and knows how Kendall's advanced theory of statistics book looks like."*

Every high-energy collaboration has phystatistician experts and they all have quite different ideas how to analyse data. In order to avoid confusion, the large LHC collaborations have Statistics Committees which maintain home pages of recommendations how to do things. The Statistics Committees of both CMS and ATLAS have several members who published text books of the type *Statistics for Physicists* and the two collaborations have a joint such committee as well.

In high energy physics the experimental data are events with many different variables as characteristics: tracking properties, energies deposited in various subdetectors, places and timing of detector hits. The results of event selection are counts collected in spectra, often equidistant intervals of a variable, called *bins* and the probability that we have n_i events collected in bin i follows the *Poisson distribution*

$$\mathcal{P}(n_i|\mu_i) = \frac{\mu_i^{n_i} e^{-\mu_i}}{n_i!},$$

with μ_i being the *average value* (or *mean value*) of n_i. There are many different ways of treating these spectra, we can build e.g., a *likelihood function* to be optimized in order to get the desired physics result, an optimal estimation of the physical parameters to be determined. On the basis of the Poisson distribution one can build a *Poisson likelihood*: $\mathcal{L} = \Pi_i \mathcal{P}(n_i|\mu_i)$ where the *expected number* of events is $\tilde{\mu}_i = \sum_j L\sigma_j\epsilon_{ji}$, L is the integral luminosity collected, σ_j is the cross section of source j and ϵ_{ji} is the efficiency (usually determined by Monte Carlo simulation) of detecting the contribution of source j in bin i. Note that $\tilde{\mu}_i$ is an estimation of μ_i.

According to the general convention in accelerator experiments a given new phenomenon is excluded if we can show it not appearing at a confidence level above 95 % and observed if it exceeds 5σ above background where now, for a change, σ is the experimental uncertainty of the excess according to the best honest guess of the experimentalist. These two conditions will be duly explained and refined later in this chapter.

Another important feature of high-energy data analysis is the *blind analysis*. According to [Klein and Roodman, 2005]: "A blind analysis is a measurement which is performed without looking at the answer. Blind analyses are the optimal way to reduce or eliminate experimenter's bias, the unintended biasing of a result in a particular direction." It came from medical research and in high-energy physics it means to optimize, prove and publish your analysis technique using simulations and earlier data only before touching new data in the critical region. For instance, in spring and early summer 2012, the new CMS data were blinded in the mass region $110 < m_H < 140\,\text{GeV}$ (where m_H is the simulated Higgs mass) because of the 3σ excess observed in 2011. The same procedure was used again in autumn 2012, after the announcement of the 5σ observation. The analysing methods had to be fixed, described in voluminous analysis notes and defended before the whole collaboration before the simultaneous *unblinding* for all analysis channels. These analysis notes, sometimes hundreds of pages long, are rarely read by other people, but frequently checked for certain plots and results.

9.2   Basic concepts of statistical analysis

Given a set of n data points y_i (e.g. event counts) as a function of a variable x_i, a *spectrum* is $\{x_i;\ y_i \pm \sigma_i\}_{i=1}^{n}$ where σ_i is the uncertainty of determination of y_i (sometimes misleadingly called *experimental error*). If y_i follow the Poisson distribution, i.e. $P(y) = e^{-a}\frac{a^y}{y!}$ with a mean value of $\overline{y} = a$, then the uncertainties can be estimated as $\sigma_i^2 = \overline{y_i} \approx y_i$.

A *model function* is a theoretical description of the data:

$$y = f(x; p_1, p_2, ...p_m) = f(x; \vec{p})$$

with the parameter vector $\vec{p}$. The aim of the analysis is to determine whether or not the model function describes the data well and to estimate its parameter values. When the values of $\vec{p}$ are determined on the basis of the data (via *fitting* the parameters of the model function to the data) we can also determine

the *covariance matrix* of the estimations for parameters $\vec{p}$ as

$$Q_{ik} = \langle \Delta p_i \Delta p_k \rangle = \langle (p_i - \overline{p_i})(p_k - \overline{p_k}) \rangle$$

where $\overline{x}$ and $\langle x \rangle$ both denote the estimations of the expectation values of x. The diagonal elements are the variances (the squares of the statistical uncertainties) and the off-diagonal ones the covariances:

$$Q = \begin{pmatrix} \sigma_{p_1}^2 & \langle \Delta p_1 \Delta p_2 \rangle & \cdots \\ \langle \Delta p_2 \Delta p_1 \rangle & \sigma_{p_2}^2 & \cdots \\ \cdots & \cdots & \cdots \end{pmatrix}$$

The *correlation matrix* is obtained by the normalization of the covariance matrix,

$$C_{ik} \equiv C(\tilde{p}_i, \tilde{p}_k) = \frac{Q_{ik}}{\sqrt{\sigma_{p_i}^2 \sigma_{p_k}^2}},$$

$$-1 \le C(\tilde{p}_i, \tilde{p}_k) \le +1$$

Figure 9.1: Uncorrelated and correlated coordinates for the same point.

so that its values fall in the range $[-1, +1]$.

The correlation between two parameters is $+1$ if they are proportional, and -1 if they are inversely proportional to each other. High correlation means that the model function is poor, or we have chosen the wrong parametrization. For instance in Fig. 9.1 the same point P can be described in the uncorrelated (x, y) and the highly correlated (x', y') coordinate systems. If P changes in the x direction, its y coordinate can remain the same, but if P changes in the x' direction, its y' coordinate must also change.

If a secondary variable $z = z(\vec{p})$ is calculated as a function of $\vec{p}$, its uncertainty according to the law of *error propagation* (here the misleading name *error* has stayed on) is

$$\sigma_z^2 = \sum_{i,k=1}^{m} \frac{\partial z}{\partial p_i} \frac{\partial z}{\partial p_k} \overline{\Delta p_i \Delta p_k} \,. \tag{9.1}$$

If the parameters are independent of each other (which never happens in practice except when orthogonal functions are fitted), then $Q_{ik} = \sigma_{p_i}^2 \delta_{ik}$ and

$$\sigma_z^2 = \sum_{i=1}^{m} \left(\frac{\partial z}{\partial p_i} \right)^2 \sigma_{p_i}^2.$$
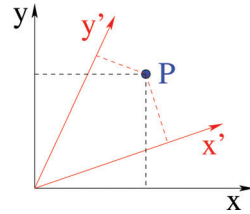
9.3 Fitting parameters

9.3.1 Goodness of fit

We have a model function $f(x; \vec{p})$ and a set of data $\{x_i; \ y_i \pm \sigma_i\}_{i=1}^n$. Once we have an estimation of the parameters, the question is how well the function fits the data. There are several ways to check that, the most common being the χ−*square* test. The χ−square function is defined as $\chi_k^2 = \sum_{i=1}^k X_i^2$ where X_i are independent variables following a Gaussian distribution

$$P(X) = \frac{1}{\sqrt{2\pi}} \exp(-\frac{X^2}{2})$$

with a mean value $\overline{X_i} = 0$ and variance $\sigma_{x_i}^2 = 1$. χ_k^2 follows the Γ distribution, thus it has a mean value of $\overline{\chi_k^2} = k$ and variance $\sigma^2(\chi_k^2) = 2k$ where k is its *degree of freedom*.

When fitting a spectrum by, e.g., the *least-squares fitting* method to a set of n independent data and m parameters, the χ_k^2 will have a degree of freedom $k = n - m - 1$:

$$\chi_{n-m-1}^2 = \sum_{i=1}^n \frac{1}{\sigma_i^2}[y_i - f(x_i; p_1 \cdots p_m)]^2 .$$

The relative or *reduced* χ_k^2 is defined as $\chi_r^2 = \frac{\chi_{n-m-1}^2}{n-m-1}$ with a mean $\overline{\chi_r^2} = 1$. $\chi_r^2 \ll 1$ means a too good fit, that is too little information in the data for the given model, whereas $\chi_r^2 \gg 1$ means a bad fit: a model function of poorly fitting parameters.

9.3.2 Confidence level

Let us assume that variable x follows a Gaussian distribution:

$$P(x) = \frac{1}{\sqrt{2\pi\sigma^2}} \exp(-\frac{(x - \mu)^2}{2\sigma^2})$$

and the estimation of the mean $\mu = \overline{x}$ is $\tilde{x} \pm \sigma$. The *confidence level* of $\overline{x}$ being in between a and b is $W(a \le x \le b) = \int_a^b P(x)\mathrm{d}x$. For instance, the confidence that $x > 0$ is $\int_0^\infty P(x)\mathrm{d}x$.

The full width at half maximum (FWHM) T is defined as $P(\tilde{x} \pm T/2) = P(\tilde{x})/2$. For a Gaussian distribution (Fig. 9.2) it is $T = 2\sqrt{2\ln 2}\,\sigma \approx 2.355\,\sigma$. In practice we use the standard library functions *erf* and *erfc* to calculate these values: $\mathrm{erf}(x) = \frac{2}{\sqrt{\pi}}\int_0^x e^{-t^2}\,\mathrm{d}t$, $\mathrm{erfc} = 1 - \mathrm{erf}$. Sometimes the value of erf is so close to unity that you better calculate erfc that omits the first term 1 from the expansion of erf.
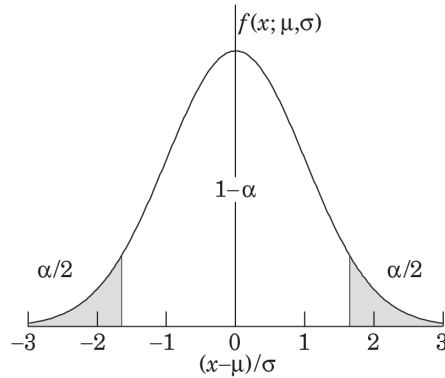

Figure 9.2: Gaussian distribution with mean $\overline{x}{=}0$ and width $\overline{\sigma}{=}1$. The confidence level of having $\tilde{x}$ within the unshaded region is $1 - \alpha$.

9.4 Estimating (fitting) parameters

We have a set of measured data and some model function with adjustable parameters. The final result will be the best estimation of some of the parameters. How can we get it?

9.4.1 Arithmetic mean and standard deviation

We shall now treat the various ways to estimate parameters in analysing data. For the examples we use the method of least squares, which for just one parameter means solving the following equation:

$$S(a) = \sum_{i=1}^{n} w_i(y_i - \tilde{y})^2 = \min, \tag{9.2}$$

with the weights $w_i = \frac{1}{\sigma_i^2}$ providing the minimal uncertainty σ_y for the arithmetic average $\tilde{y}$ of the n measured values $\{y_i \pm \sigma_i\}_{i=1}^n$. Then the *weighted average* is

$$\tilde{y} = \frac{\sum_i \frac{1}{\sigma_i^2} y_i}{\sum_i \frac{1}{\sigma_i^2}} \pm \sqrt{\frac{1}{\sum_i \frac{1}{\sigma_i^2}}}. \tag{9.3}$$

In some sense the real estimated uncertainty is the *standard deviation* (Fig 9.3):

$$\sigma_{SD} = \frac{S}{\sqrt{n-1}} \quad \text{with} \quad S^2 = \frac{1}{n}\sum_{i=1}^{n}(y_i - \tilde{y})^2$$

where $\tilde{y}$ is the estimated average. For large n this simplifies to $\sigma_{SD} \approx \frac{1}{n}\sqrt{\sum_{i=1}^{n}(y_i - \tilde{y})^2}$.

Of course, in all data analyses the most important factor is the reasonable mind of the experimentalist. There is a nice old tale about a committee which wanted to solve the problem of estimating the height of the Chinese Emperor by asking a million people (as measuring him was out of question). They reasoned that everybody can guess the

Figure 9.3: Gaussian (normal) distribution with its standard deviation regions around the centroid μ.

height of people by the uncertainty of ± 10 cm and thus the result will be as precise as $\sigma_{stat} = \pm\frac{10cm}{\sqrt{10^6}} = \pm 0.1$ mm $\approx \sigma_{SD}$. Of course, nobody asked had ever seen the Emperor standing!
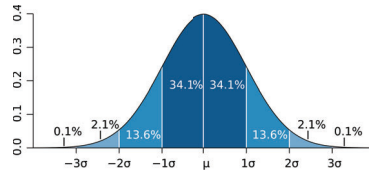
Let us estimate the average of the measurements $y_1 = 4 \pm 1$; $y_2 = 2 \pm 1$; $y_3 = 9 \pm 1$. The average is 5. Its *statistical uncertainty* $\sigma_{stat} = \sqrt{\frac{1}{3}} = 0.58$ is obviously too small, but correcting it with the reduced χ_r^2 is an overkill: $\sigma_{stat} \cdot \sqrt{\chi_r^2} = 0.58 \cdot \sqrt{26} = 3.0$. The standard deviation, however, gives a more reasonable error: $\sigma_{SD} \approx \sqrt{\frac{26}{6}} = 2.1$. If we are not sure about the statistical nature of the measurements, we should use the standard deviation for the estimation of the uncertainty.

9.4.2 Linear fitting

We call the model function $f(x; \vec{p})$ linear in parameters $\vec{p} = (p_1, p_2, \ldots p_m)$ if it can be written like

$$f(x; \vec{p}) = \sum_{k=1}^{m} p_k \frac{\partial f(x; \vec{p})}{\partial p_k} = \sum_{k=1}^{m} p_k \Phi_k(x),$$

where $\Phi_k(x)$ is independent of the parameters. Fitting parameters $\vec{p}$ using the least-squares method means solving the following minimization:

$$S(\vec{p}) = \sum_{i=1}^{n} \frac{1}{\sigma_i^2}(y_i - f(x_i; \vec{p}))^2 = \min,$$

i.e. the system of equations $\frac{\partial S(\vec{p})}{\partial p_k} = 0; \quad (k = 1, ...m)$. Using the notation $f_i \equiv f(x_i; \vec{p})$ we get

$$\sum_{l=1}^{m} p_l \sum_{i=1}^{n} \frac{1}{\sigma_i^2} \frac{\partial f_i}{\partial p_k} \frac{\partial f_i}{\partial p_l} = \sum_{i=1}^{n} \frac{1}{\sigma_i^2} y_i \frac{\partial f_i}{\partial p_k},$$

equivalent to $\sum_{l=1}^{m} p_l M_{kl} = b_k$. We can solve this if the matrix M_{kl} is symmetric and positive definite:

$$M\vec{p} = \vec{b} \quad \Rightarrow \quad \vec{p} = M^{-1}\vec{b} \equiv Q\vec{b}.$$

It can be easily shown that the covariance matrix of $\vec{p}$ will be just the inverse of the M_{kl} matrix.

For fitting a straight line $f(x; \vec{p}) = p_1 x + p_2$ to points $\{x_i; y_i \pm \sigma_i\}_{i=1}^{n}$:

$$M = \begin{bmatrix} \sum \frac{x_i^2}{\sigma_i^2} & \sum \frac{x_i}{\sigma_i^2} \\ \sum \frac{x_i}{\sigma_i^2} & \sum \frac{1}{\sigma_i^2} \end{bmatrix}; \quad \vec{b} = \begin{bmatrix} \sum \frac{x_i y_i}{\sigma_i^2} \\ \sum \frac{y_i}{\sigma_i^2} \end{bmatrix}.$$

The solution is $\begin{bmatrix} \tilde{p}_1 \\ \tilde{p}_2 \end{bmatrix} = M^{-1}\vec{b}$ with the covariance matrix $Q = M^{-1}$.

9.4.3 Non-linear fitting

If $\frac{\partial f}{\partial \vec{p}}$ depends on $\vec{p}$, then our model function $y = f(x; p_1, \ldots p_m)$ is non-linear in the parameters $\vec{p}$. Trivial example is $y = p_1 p_2 x$ which must be linearized to $y = ax$, with $a = p_1 p_2$. One could also linearize, say $y = p_1 \exp(-p_2 x)$ as $\ln y = \ln p_1 - p_2 x = a - bx$, but it is not worth it. Lineariza-tion in most of the practi-cal cases cannot be done and

Figure 9.4: Lorentzian functions

even it can be, it gives a biased estimation with distorted uncertainties.

The most frequent non-linear functions (with their usual parameter hand-ling) are the Gaussian function (or normal distribution): $p_1 \exp[-p_2(x-p_3)^2]$ (Fig. 9.2) and the Lorentzian (Cauchy or Breit-Wigner) function $p_1 [p_2^2 + (x - p_3)^2]^{-1}$ (Fig. 9.4). Non-linear functions can be fitted using least-squares, maximum likelihood or other methods. In the case of least-squares fitting as an example one looks for a local minimum of the function

$$S(\vec{P}) = \sum_{i=1}^{n} \frac{1}{\sigma_i^2} [y_i - f(x_i; \vec{p})]^2$$

but in all other methods one has to find a local minimum or maximum. In particle experiments the MINUIT program [James and Roos, 1975] has been the most popular for fitting for almost half a century.

The *Monte Carlo method* can be used if we have just a vague idea of the location of the minimum: one makes random probes in the given region and tries to find a minimal value of the function. It is extremely slow and inefficient.

The *simplex method* is very popular. The value of the function $S(\vec{p})$ to be minimized is calculated in $m + 1$ points in the m-dimensional space of the parameters $\vec{p}$ making a *simplex* of $m + 1$ edges $R_1 \ldots R_{m+1}$. Take the worst point (where e.g. $S(\vec{p})$ is maximal in the case of minimization) and send it to a point in the m-dimensional space on opposite side of centroid calculated from remaining m points (Fig. 9.5). The speed of convergence will depend on the distance you send the point away from the centroid: the usual value is
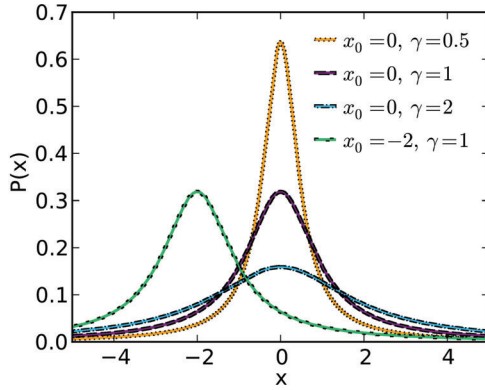
once or twice the original distance. This method is somewhat slow, but does not require calculating derivatives.

In particle physics the most popular minimization methods are the gradient ones. The *gradient* of $S(\vec{p})$ in the point of $\vec{p} = \vec{p}_0$ is

$$\vec{g} = \frac{\partial S}{\partial \vec{p}} = \left(\frac{\partial S(\vec{p})}{\partial p_1}, \ldots \frac{\partial S(\vec{p})}{\partial p_m} \right)^T_{\vec{p}=\vec{p}_0}$$

The gradient methods search for a minimum along the derivatives of the function, so its convergence is much faster than that of the simplex method. One can calculate the derivatives analytically or numerically, but the numerical derivatives are generally more reliable, stable and fast. Sometimes it is worth to start the minimization with the simplex method and when the minimum is close, change to the gradient methods.
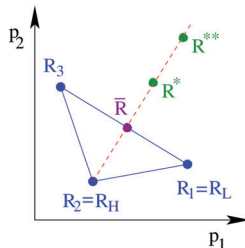

Figure 9.5: Simplex minimization for two parameters.

9.5   Uncertainties

The uncertainty of the estimated parameter value is usually obtained by changing the χ^2 of the fit by unity at the two sides of the minimum. This way one can get asymmetric uncertainty values. A quite popular method to gain error estimation of a single parameter is the MINOS method (Fig. 9.6). It changes the value of the given parameter and optimizes the rest of the parameters of the fitting so that $\chi^2_{new} = \chi^2_{min} + 1$. This will account for part of the correlations as well.

All uncertainties of the estimation which do not come from the number of detected events are considered to be *systematic*. They come from various sources, like Monte Carlo statistics and inputs, experimental calibration factors, detection efficiencies etc, with the common name *nuisance parameters*. They can be estimated
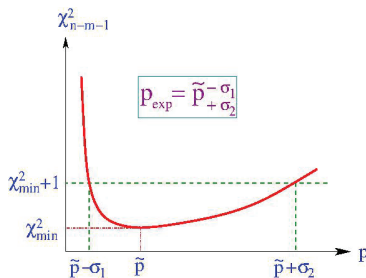

Figure 9.6: Estimating MINOS uncertainties by changing the parameter in question while optimizing the rest so that the χ^2 of the fit would increase by unity [James and Roos, 1975].

by changing the input information of the analysis by *reasonable* amounts. Most of the time this is just the experimental or theoretical uncertainty of the input parameters, but it could also be a different Monte Carlo algorithm or fit range. There are systematic uncertainties which can be corrected later on, like results of earlier measurements or theoretical calculations or some global calibration of the detector or accelerator beam. However, one cannot correct later the results of the simulations or uncertainties related to elements of the measuring apparatus, like the calibration of a subdetector. What amount of change is *reasonable* largely depends on the problem and has to be decided by the physicist. For instance, one can check the effect on the result of shifting a simulated spectrum by the amount of its deviation from data. Estimating the systematic uncertainties frequently takes much more effort than the pure data analysis itself.

One cannot just add statistical and systematic uncertainties to get a *total uncertainty* as one has to include the possible correlations, which is usually quite difficult. What is done at LHC is to eliminate the *nuisance parameters* Θ from the estimation of parameters P by marginalizing them (integrating out) [Cousins and Highland, 1992] from the analysis using the related $\mathcal{W}$ distributions:

$$\mathcal{L}(P; x) = \mathcal{W}(x|P) = \int \mathcal{W}(x|P, \Theta)\mathcal{W}(\Theta|P)\mathrm{d}\Theta\,.$$

One cannot be careful enough considering systematic uncertainties. The Particle Physics Review [Patrignani et al., 2016] analyses the time dependence of certain experimental data and the result is quite shocking: some data do not change for many years, different groups get similar results until somebody invents a more precise measuring method and the value undergoes a big change, sometimes much larger than the estimated total uncertainty of the previous measurements. A very difficult part of performing a measurement is to provide a correct estimation of the systematic uncertainties which should be neither too large nor underestimated.

9.6   Lower and upper limits

When searching for new physics one wants either to observe certain phenomena, or to exclude them in given parameter regions. According to the convention in accelerator particle physics an observation (*discovery*) has to have a significance of at least 5σ. Thus one can declare the observation of a new particle if one detects a mass peak at 5 times its uncertainty above the background. Still, it is not acknowledged by the community before another

n_0	0	1	2	3
$n_{max}(90\%)$	2.30	3.89	5.32	6.68
$n_{max}(95\%)$	3.00	4.74	6.30	7.75

Table 9.1: Numbers of excluded events at 90 % and 95 % confidence levels if we detected 0, 1, 2 or 3 events assuming a Poisson distribution

experiment reproduces the result. This convention is based on the experience that we do not know any such $> 5\sigma$ observation yet, that was later refuted by other experiments.

Exclusion needs a 95 % confidence level in accelerator particle physics. However, at certain areas where much less rates are detected, like in neutrino physics or astrophysics, 90 % exclusion is the accepted limit. For a Gaussian distribution, as shown in Fig. 9.2, the confidence limit that the real value of the estimated parameter is within the $\pm\delta$ region of the estimated μ value is

$$1 - \alpha = \int_{\mu-\delta}^{\mu+\delta} f(x; \mu, \sigma)\mathrm{d}x \ .$$

whereas the confidence that it is below or above that region is $\alpha/2$.

In the case of Poisson distribution if we detect n_0 events and we do not know the mean μ, what maximal event number can be excluded at a confidence of CL? In other words, at what μ will the probability of having more that n_0 events less than CL: $P(n > n_0) > CL = 1 - \alpha = \sum_{n=n_0+1}^{\infty} f(n; \mu)$? Table 9.1 shows what one can say of possible exclusion for various confidence levels and detected numbers of events. For instance, if we did not detect any event for a given phenomenon then at a 95 % confidence level we can say that we have less than 3.0 events.

In some cases we get non-physical measured data. In order to be able to state a limit in such cases one has to renormalize the obtained distribution to the physically meaningful region (Bayes-limit):

$$\int_{\text{phys. area}} f(x)\mathrm{d}x = 1$$

For instance, there was a case when a fitted mass-square was negative:

$$\pi^+ \rightarrow \mu^+ \nu_\mu \Rightarrow m(\nu_\mu)^2 = (-0.016 \pm 0.023)\text{MeV}^2,$$

which is of course non-physical. The distribution was renormalized and the limit $m(\nu_\mu) < 0.17$ MeV (90%CL) accepted.

9.7 Monte Carlo simulation

Any data analysis of high energy physics starts with simulations: that of the expected background and signal. It is done these days using the GEANT4 [Agostinelli et al., 2003] simulation package developed mostly at CERN. The basic idea is to produce simulated events which can be directly compared to the detected ones: the observed event features should not be manipulated. For that one simulates all possible physics processes which means using various algorithms for the various processes with cross checks and drives them all through the simulation of the whole detector system. The components of the background are summed up according to their cross sections and then the event selection is optimized to maximize the N_S signal at a minimal N_B background. The optimization means to maximize a *figure of merit* like in the simplest case $N_S/\sqrt{N_B} = \max$ or $N_S/\sqrt{N_B + N_S} = \max$ although these days we prefer the condition $2 \cdot (\sqrt{N_B + N_S} - \sqrt{N_B}) = \max$ [Bityukov and Krasnikov, 2000] or using the approximate formula of Ref. [Cowan et al., 2011].

9.8 Event selection

Both background and signal have to be checked against the previous measurements and the theoretical calculations for correctness. The steps of the event selection can be simple *cuts*, such as conditions on variables like $p_T > 20\,\mathrm{GeV}/c$ or complicated multi-variate procedures: likelihood or artificial neural network optimization.

A concrete example for event selection is the search for charged Higgs bosons in the four-jet decay channel ($e^+e^- \rightarrow H^+H^- \rightarrow c\bar{s}\,\bar{c}s$) from the practice of the authors in the OPAL experiment. Before likelihood optimization we applied a preselection with the following cuts (Fig 17.24):

(a) Eliminate those events where a Z-boson was emitted together with a photon (radiative return to Z). If an isolated photon is found, remove it from the total centre-of-mass energy $\sqrt{s}$ and apply a cut on the remaining energy $\sqrt{s'} > 170\,\mathrm{GeV}$.

(b) Cut on the total visible energy of the event by $E_{vis}/\sqrt{s} > 0.7$.

(c) Choose 4-jet events by cutting on the variable y_{34} of the Durham jet-determining algorithm, which is the threshold track distance where the event becomes 4-jet-like from 3-jet-like.

(d) Select those events where all jets have at least two charged tracks.

One can see that the simulation describes the data very well. We tried to apply cuts with maximum efficiency, i.e. eliminate much of the background and little of the signal. Of course the total number of events went down as we applied the cuts consecutively from (a) to (d).

   The next step was a likelihood optimization with the basic aim to reduce the main background of our searched signal $e^+e^- \to H^+H^- \to c\bar{s}\,\bar{c}s$. The only difference between $W^\pm$ and $H^\pm$ of the same mass is spin as the W is a $J = 1$ vector boson whereas the charged Higgs bosons are scalar with $J = 0$. That means we should try to find variables to select between them like angular distributions and jet structure. Using the simulations we created reference histograms for several such variables for signal and background and determined the probability of *signal likeness* for each event. The analysis was mass-dependent, i.e. for each assumed mass of the hypothetical charged Higgs boson a different optimization was made with different signal but the same background. As Fig. 17.24 shows the signal was obviously rejected for $M(H^\pm) = 60\,\text{GeV}$, but that cannot be told of a signal at 75 GeV. Actually, after collecting all information we obtained $M(H^\pm) > 75.5\,\text{GeV}$ at a 95% confidence level. We got close to the mass of $W^\pm$, but could not get over it.

Exercise 9.1
What are the main sources of the statistical and systematic uncertainties?

Exercise 9.2
What is the use of the covariance matrix in the interpretation of the analyzed data? How can it be used to estimate the statistical and systematic uncertainties of derived physical parameters?

Exercise 9.3
What is the meaning of χ^2? What shall we do if it is too high or too low?

Exercise 9.4
Deduce Eq. 9.3 for the weighted average from Eq. 9.2 using the error propagation law, Eq. 9.1.

Exercise 9.5
How can one include former results in the analysis of new data?

Exercise 9.6
How can one optimize the event selection for data analysis?

Part III

Basic experiments

Chapter 10

Experimental tests of the quark model

MOTTO:

If I could remember the names of all these particles, I'd be a botanist.

(Enrico Fermi)

10.1 Three fermion families

10.1.1 Z width

The Z boson can decay into particle-antiparticle pairs of leptons and quarks (it cannot decay into photons). In experiment the quark pair will appear as hadron showers, jets, and only the charged leptons will be detected, the neutrino pairs will escape the detector. Thus the total Z decay width will be

$$\Gamma_Z = \Gamma_{e^+e^-} + \Gamma_{\mu^+\mu^-} + \Gamma_{\tau^+\tau^-} + \Gamma_{had} + \Gamma_{inv} . \qquad (10.1)$$

According to the standard model the production of Z bosons in electron-positron collisions and its decay to fermion pairs should have the cross

section (the * superscript of Z means that it can be virtual as well):

$$\sigma(e^+e^- \to Z^{(*)} \to X) = \frac{12\pi M_Z^2}{E_{CM}^2} \frac{\Gamma(Z \to e^+e^-)\Gamma(Z \to X)}{(E_{CM}^2 - M_Z^2)^2 + M_Z^2\Gamma_Z^2} . \qquad (10.2)$$

The parameters of Eq. (10.2) were determined by fitting the peak shape of Fig. 17.2. The three charged leptons have the same cross section (*lepton universality* principle) with the average

$$\Gamma_{\ell^+\ell^-}/\Gamma_Z = 3.3658(23)\%$$

and that of the hadronic decays:

$$\Gamma_{hadr}/\Gamma_Z = 69.91(6)\%$$

where the numbers in parentheses mean uncertainties in the last digits of the results.

Thus the Z decay to quark pairs is 21 times more probable than that to a lepton pair. This much higher probability is not surprising as there are 3×5 pairs of quarks available for Z decay, three colours and 5 flavours.

10.1.2   Invisible width and the families

According to the standard model each fermion carries a *loop correction*, proportional to the charge of the fermion, and they appear as annoying *anomalies* (cf. Section 22.9) in the equations with no trace of them in experiment. However, they are cancelled if the sum of the electric charges of all fermions in a family is zero. That means that the number of quark pairs should be the same as that of leptons as the fractional charge of the quarks is evened out by the three colours.

The invisible decay of the Z boson is related to neutrinos and it constitutes

$$\Gamma_{inv}/\Gamma_Z = 1 - \Gamma_{hadr}/\Gamma_Z - 3 \times \Gamma_{\ell^+\ell^-}/\Gamma_Z = 20.0(6)\%$$

of the total. According to the standard model the contribution of neutrino decay to the total Z width is

$$\Gamma_{\nu\bar{\nu}} = \frac{2\Gamma_{\ell^+\ell^-}}{[1 + (1 - 4\sin^2\Theta_W)^2]} = 1.979\Gamma_{\ell^+\ell^-}$$

where Θ_W is the *weak mixing angle*, the mixing angle of $U(1)_Y$ and $SU(2)_L$ in the weak neutral current, $\sin^2\Theta_W = 0.23120(15)$. Thus the number of light neutrinos (neutrinos with masses less than half the Z mass)

$$N_\nu = \Gamma_{inv}/\Gamma_{\nu\bar{\nu}} = 2.9840(82),$$

meaning there are three fermion families (Fig. 10.1).

10.2   Hadron jets

The quark model, at its birth, was met by general doubts: the fractional charges and baryon number and the postulated non-existence of free quarks made the validity of the model very improbable. Even when some of the predictions calculated with the quark model were experimentally confirmed, the quarks could have thought to be mathematical tricks to explain things. The observation of jets however, started to make them real. Fig. 17.25 shows an event where an e^+e^- collision produces 75 charged particles in 4 jets due to the produc-

Figure 10.1: Z-width and three fermion families. Hadronic decay cross section against centre-of-mass energy of electron-positron collisions.

tion of a W^+W^- pair. As any additional particle production decreases the cross section of the reaction by several orders of magnitude, such an event can be explained by quark hadronization only.

Quarks are fermions, they can be produced in particle-antiparticle pairs only. Thus the 3-jet events copiously produced in high-energy electron-positron collisions have to contain at least one boson: in order to explain the jets all three have to be produced by coloured partons (coloured particles, quarks or gluons), and at least one of them has to be a gluon. Fig. 17.25 shows such an event. According to quantum chromodynamics, the theory of the strong interaction, the quarks interact with each other also via gluon exchange. As quarks exchange colours, gluons must carry colour and anti-colour and so they strongly interact with each other as well. As a gluon has a larger colour charge than a quark, they must have higher jet multiplicity. This was shown experimentally at LEP by studying 3-jet events where two jets were identified as belonging to b quarks due to their longer lifetimes, secondary vertices. Similarly, studying 3-jet events at LEP helped to identify the gluon's spin as 1.
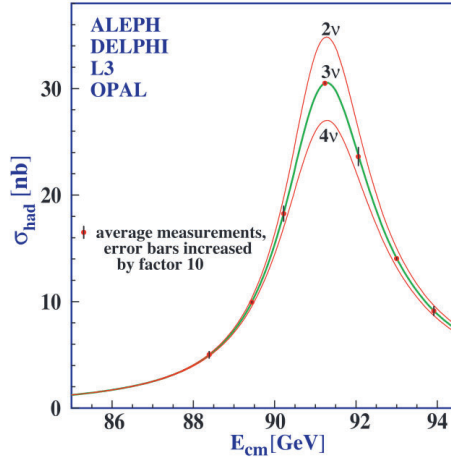
$\rho(770) = \frac{1}{\sqrt{2}}(u\bar{u} - d\bar{d})$
$\omega(782) = \frac{1}{\sqrt{2}}(u\bar{u} + d\bar{d})$

Table 10.1: Quark composition of the lightest neutral vector mesons

10.3   Fractional charges

As the electric charge is quantized, and the charges of the electron and proton compensate each other to the level of 10^{-22} judging from the neutrality of matter, it is hard to accept the fractional charges of the quarks. There are, however, many experimental proofs for the quark charges.

10.3.1   Neutral vector mesons

The neutral vector mesons[1] in ground state, $V^0 = (q\bar{q})$ $J^{PC} = 1^{--}$ can decay via electromagnetic interaction into lepton + anti-lepton pairs. The decay width will depend on the electric charges involved:

$$\Gamma(V^0 \rightarrow \ell^+\ell^-) \propto e_q^2 |\psi(0)|^2 / M_V^2 \,.$$

Two vector mesons, $\rho(770)$ and $\omega(782)$ have very similar masses, but due to their different quark charges $\rho(770)$ should decay to electrons with 9 times higher probability than $\omega(782)$ (Table 10.1): $\Gamma_e(\rho) : \Gamma_e(\omega) \simeq 9 : 1$. In spite of the very rough approximation when we neglected their different masses and state functions, the experimental observation is quite close to it, $[\Gamma_e(\rho) : \Gamma_e(\omega)]_{\exp} = \frac{7.02(11)}{0.60(2)} \simeq 12$. Of course, if the u and d quarks had different charges, the ratio would be quite different.

10.3.2   Pion scattering

The carbon-12 nucleus has 6 protons and 6 neutrons, that is 18 u and 18 d quarks. Let us study muon production in the scattering of positive and negative pions on ^{12}C. A negative pion has a d quark and a u anti-quark, $\pi^- = (\bar{u}d)$, its quark will scatter off the quarks of the nucleons, while the $\bar{u}$ can annihilate with one of the u quarks of the nucleons producing a $\mu^+\mu^-$ pair. The positive pion, $\pi^+ = (\bar{d}u)$, will do the same with the other kinds of

---

[1]Particles of unit spin are called vector bosons because of their 3 spin sub-states $J_3 = -1, 0, +1$
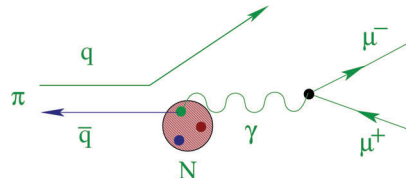
Figure 10.2: Pion scattering on nucleon.

quarks of the nucleons (Fig. 10.2). The reaction rates will be proportional to the charges of the annihilating quarks:

$$\pi^- = (\bar{u}d) \Rightarrow \sigma \propto 18 Q_u^2 = 18 \cdot \tfrac{4}{9}$$
$$\pi^+ = (u\bar{d}) \Rightarrow \sigma \propto 18 Q_d^2 = 18 \cdot \tfrac{1}{9}$$

The cross section ratio of the two reactions is

$$\frac{\sigma(\pi^- C \rightarrow \mu^+ \mu^- \ldots)}{\sigma(\pi^+ C \rightarrow \mu^+ \mu^- \ldots)} \simeq 4,$$

confirmed by experiment.

10.4   Colours

The quark model postulates that quarks come with three colour charges and colour makes the state function of baryon systems antisymmetric against baryon exchange. Of course, the three colours make possible the existence of such particles like the $\Delta^{++} = (u\uparrow u\uparrow u\uparrow)$: $J = 3/2$; $I_3 = 3/2$ hyperon. Also, the $J = 3/2$ ground state needs at least three quarks, and no impossible baryon state (like one having $I > 3/2$ isospin) was discovered. The simplest solution is a new $SU(3)$ quantum number, the three colours.

The standard model assumes that only 3-quark and quark + anti-quark states exist. The requirement of colourlessness of the free hadrons could also be fulfilled by e.g. bound states of 2 quarks + 2 anti-quarks (*tetra-quark*), of 4 quarks + 1 antiquark (*penta-quark*), or 3 + 3 quarks and/or anti-quarks (*hexa-quark* or *dibaryon*). Previously, all sightings of such states were subsequently refuted, but recently the LHCb Collaboration reported the observation of such states.

The existence of three colours were proven, e.g. by measuring the total cross section of hadron production as compared to that of muon pair emission.
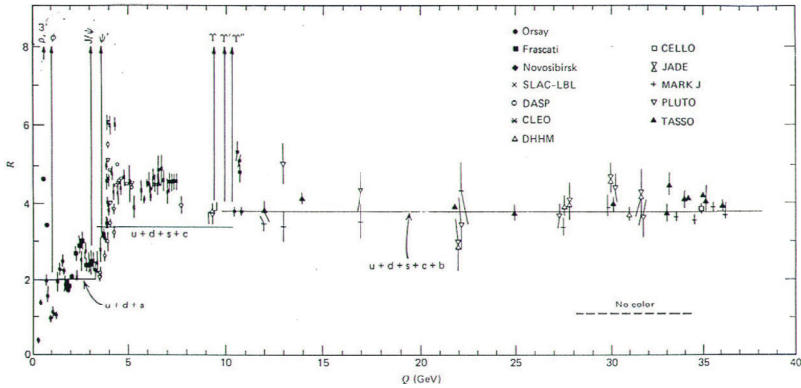
Figure 10.3: Hadron production cross section in electron-positron scattering divided by the cross section of muon emission. The high-energy results are well reproduced by assuming 3 quark colours and fractional charges

Again, those are electromagnetic reactions and their ratio is:

$$R = \frac{\sigma(e^+e^- \to \text{hadrons})}{\sigma(e^+e^- \to \mu^+\mu^-)} = \frac{\sum_i \sigma(e^+e^- \to q_i\bar{q}_i)}{\sigma(e^+e^- \to \mu^+\mu^-)} \propto \sum_i Q^2_{q_i}$$

If there is no colour, the ratio will be $R_0 = \sum_q Q^2_q$, the sum of charge-squared of the kinematically available quarks. In the case of three colours it will be $R_3 = 3R_0$. Depending on $E_{CM}(e^+e^-)$:

{u, d, s}: $R_0 = (2/3)^2 + 2 \cdot (1/3)^2 = 2/3$; $R_3 = 2$
{u, d, s, c}: $R_0 = 2 \cdot (2/3)^2 + 2 \cdot (1/3)^2 = 10/9$; $R_3 = 10/3$
{u, d, s, c, b}: $R_0 = 2 \cdot (2/3)^2 + 3 \cdot (1/3)^2 = 11/9$; $R_3 = 11/3$

As Fig. 10.3 shows the experimental results confirm the existence of three colours. The sharp peaks are meson resonances, the base lines show the hadron production rates related to the numbers of available quarks. This measurement also demonstrates the validity of fractional quark charges.

Exercise 10.1
How can we discover a new particle by measuring energy in particle scattering?

Exercise 10.2

What is the significance of having 3 kinds of light neutrinos for the rest of fermions? How is the number of lepton families connected to those of the quarks?

Exercise 10.3

How could the total Z-width be determined by studying the resonances of individual decay channels in electron-positron scattering?

Exercise 10.4

Why does the observation of hadron jets prove the existence of coloured particles? Why can 3 jets originate from gluons only?

Exercise 10.5

How was the idea of fractional charges of the quarks proven experimentally? And that of the three colours?

Exercise 10.6

Using the quark compositions of the lightest vector mesons, deduce the cross section ratio of electromagnetic decay widths $\Gamma_e(\rho) : \Gamma_e(\omega) \simeq 9 : 1$ (Hint: sum up the charges in Table 10.1).

Chapter 11

Parity violation, pions and muons

MOTTO:

I cannot believe God is a weak left-hander.

(Wolfgang Pauli)

11.1 Parity violation

11.1.1 $\tau - \theta$ **paradox**

There was a mystery: two mesons were observed having the same mass and properties except parity: θ^+ decayed to two pions, $\theta^+ \rightarrow 2\pi$, whereas the other one to three: $\tau^+ \rightarrow 3\pi$. The pion is a pseudo-scalar state, $J^P = 0^-$, so τ^+ and θ^+ had to have opposite parities unless the weak interaction violates the conservation of parity.

Tsung-Dao Lee and Chen-Ning Yang at the University of Columbia studied the question and concluded in 1956 that all proofs of parity conservation were made in electromagnetism. They assumed that τ^+ and θ^+ are the same particle (indeed, today it is called the K$^+$ meson) and the weak interaction does not conserve parity. They also proposed several experiments to check it. Their theory was experimentally confirmed, and they were awarded the
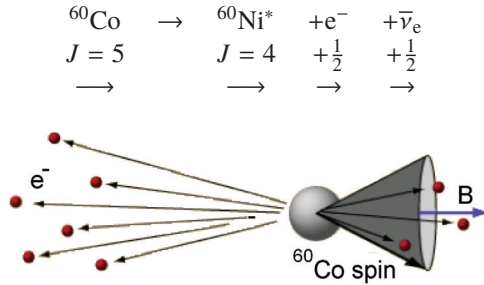
$$
\begin{array}{cccc}
{}^{60}\text{Co} & \rightarrow & {}^{60}\text{Ni}^* & +e^- \quad +\bar{\nu}_e \\
J = 5 & & J = 4 & +\frac{1}{2} \quad +\frac{1}{2} \\
\longrightarrow & & \longrightarrow & \rightarrow \quad \rightarrow
\end{array}
$$

Figure 11.1: The Wu experiment: decay of magnetically oriented cobalt nuclei

Nobel Prize in physics in 1957.

11.1.2 Wu's experiment

Chien-Shiung Wu also at Columbia together with a group at Washington made a thorough test of this idea. They oriented the spins of ^{60}Co nuclei in a magnetic field at very low temperatures ($T < 0.1$ K) to minimize precession and detected the electrons from beta decay. ^{60}Co has a nuclear spin $J = 5$, so when it decays to ^{60}Ni* whose spin is $J = 4$ the emitted electron and anti-neutrino must have spins oriented to that of ^{60}Co, i.e. along the magnetic field (Fig. 11.1).

The angular distribution of emitted electrons was found to be completely antisymmetric:

$$ I(\theta) = 1 + \alpha \frac{v}{c} \cos \theta $$

with the direction coefficient $\alpha = -1$. Later, when similar β^+ reactions were studied, $\alpha = +1$ was found for the e^+ emission.

Thus the weak interaction maximally violates parity conservation as it prefers left-polarized particles and right-polarized antiparticles. When *Wolfgang Pauli*, the father of neutrinos, the exclusion principle and spin matrices learned about the Wu experiment, he exclaimed: *"I cannot believe God is a weak left-hander!"*

11.1.3 Parity violation in pion decay

In the weak decay of pions to muons: $\pi^+ \rightarrow \mu^+ \nu_\mu$ there are only two possible emission directions, A and B in Fig. 11.2, but only B is realized in Nature: this means a maximal possible parity violation. As muons also decay in weak

Figure 11.2: Parity violation in pion decay to muon and neutrino: only process B is realized in Nature
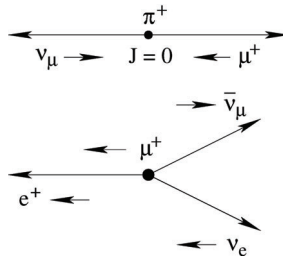

Figure 11.3: Positive pion decay produces right-polarized positive muons and those emit positrons in the direction of polarization

interaction parity violation is manifested in that as well, in the $\mu^+ \rightarrow e^+ \nu_e \bar{\nu}_\mu$ reaction. The zero-spin pions decay to polarized muons, and those will emit the electrons in the direction of their polarization.

R.L. Garwin, L.M. Lederman and *M. Weinrich* (also at Columbia University) used the reaction of pion decay to test parity conservation in weak decays: they stopped positive pions in a carbon target placed in a magnetic field and measured the number of positrons from muon decay in a given direction as a function of the field strength (in the given experiment as a function of the magnet current). The number of detected positrons has shown the precession of the muons in the magnetic field, the violation of mirror symmetry i.e. parity violation. This experiment was much simpler than Madame Wu's, but the results were published simultaneously: Lederman's group had waited for the Wu group to finish their work before submitting their result for publication and acknowledged the precedence of Wu's result.

11.1.4 Muon spin rotation (μSR)

When positive pions are stopped in matter they decay to muons, $\pi^+ \rightarrow \mu^+ \nu_\mu$ with a lifetime of $\tau_\pi = 26$ ns. As the pion has zero spin and the neutrino is
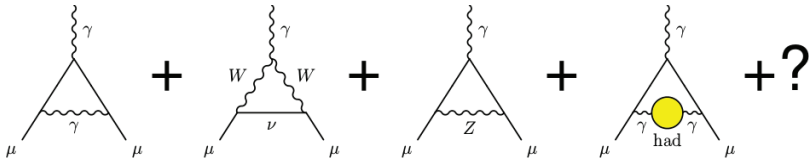
Figure 11.4: Corrections to the magnetic moment of the muon: electromagnetic, weak, hadronic terms and possibly new physical phenomena beyond the standard model.

forced to be left polarized, the emitted positive muons are also left polarized, and they can be used to study local magnetic fields in solid, liquid or gaseous matter just by detecting the direction of the positrons emitted at muon decay. The muons first slow down via Coulomb scattering (not losing their polarization) and then get trapped somewhere in the sample. In a magnetic field the slow muons decay with a lifetime of $\tau_\mu = 2.2\mu s$ while precessing with a frequency ω proportional to the magnetic field strength B (Fig. 11.3):

$$\omega = g_\mu \frac{qB}{mc} S \approx \frac{qB}{mc}$$

where $q = \pm e$ is the charge and m is the mass of the muon. For several decades μSR was used to study the behaviour and measure the field strength of local magnetic fields in solid state physics and chemistry, even meson factories were built to facilitate this method. Today it is much less cultivated.

11.2 Anomalous magnetic moment of the muon

The magnetic moment of the muon,

$$\vec{\mu}_\mu = g \frac{q}{2m} \vec{S} \tag{11.1}$$

is a very important physical quantity as it can detect the effects of heavier particles, i.e. possible new physical phenomena. In Eq. (11.1) g, e and m are the giro-magnetic factor, charge and mass of the muon and $\vec{S}$ is its spin vector. The Dirac equation assumes a g factor of exactly 2, but other heavy particles via Feynman loops may add sizeable contributions to it. As shown in Fig. 11.4, the charged muon can emit and absorb virtual photons before and after the interaction with the external field, the virtual photons, in their turn, can be converted into fermion-anti-fermion pairs (all that as long as the uncertainty principle allows it).

The anomalous part of the magnetic moment, $a = \frac{g-2}{2}$ is due to all kinds of corrections. The standard model predicts it to be

$$a_\mu(\text{SM}) = a_\mu(\text{QED}) + a_\mu(\text{weak}) + a_\mu(\text{hadr}).$$

However, if there is physics beyond the standard model with new particles, they could also contribute to the corrections, that is why the anomalous magnetic moment of the muon is one of those important quantities which could make it possible to discover new physics even at low energies. Thus it is continuously probed at higher and higher precision. If we find a deviation from the standard model prediction, it can be due to new physics or incomplete calculation, and thus useful in any case. Let us add that precise measurements are *always* useful in physics, many discoveries were made just by trying to make a measurement more precise. Two bright examples are cosmic background radiation and *CP* violation: both discoveries changed our view of Nature and earned Nobel Prizes for the researchers.

11.2.1 $(g-2)_\mu$: non-relativistic measurement

Recall that the magnetic moment of the muon is[1] $\vec{\mu} = g\frac{q\hbar}{2mc}\vec{S}$ where the Dirac equation predicts $g = 2$. In a non-relativistic case the Larmor precession of the muon in a magnetic field of strength B will have the frequency

$$\omega_S = \frac{g}{\hbar}\left(\frac{q\hbar}{2mc}\right)B = \frac{qB}{mc}\cdot\frac{g}{2} = \frac{qB}{mc}\left(1 + \frac{g-2}{2}\right) = \frac{qB}{mc}(1 + a).$$

A particle with spin $S = \frac{1}{2}$ will precess around its momentum in field $\vec{B}$ at a frequency which is the difference between its spin and cyclotron frequencies:

$$\omega_a = \omega_S - \omega_c = \omega_S - \frac{qB}{mc} = a\frac{qB}{mc}$$

if it is polarized along its momentum (which is natural for the muon emitted in pion decay). The stored muons decay to positrons, $\mu^+ \rightarrow e^+ \nu_e \bar{\nu}_\mu$ with velocity into the direction of the muon spin, at a rate of the time dependence $N(t) = N_0 e^{-\frac{t}{\tau}}[1 - A\cos(\omega_a t + \phi)]$ where $\tau = 2.2\mu s$ is the muon lifetime and ϕ is the angle of measurement.

Such an experiment was made first at CERN in a muon storage ring in 1965 (with the leadership of *Georges Charpak*, who was awarded the Nobel Prize in physics 30 years later for constructing the multiwire proportional

---

[1]We use SI units in this section.

chamber). The experiment was made with muons of $p_\mu = 90$ MeV/c momentum, in a field of $B=1.6$ T and it gave the result $a_\mu = 1162(5) \times 10^{-6}$, i.e. a large anomaly.

11.2.2 $(g - 2)_\mu$ with relativistic muons

One of the obvious ways to make the $(g - 2)_\mu$ measurement more precise is to extend the lifetime of the muons by making them relativistic. The spin precession frequency of relativistic muons will have a contribution from Thomas precession:

$$\omega_s = g\frac{eB}{2mc} + (1 - \gamma)\frac{eB}{mc\gamma},$$

their cyclotron frequency is $\omega_c = \frac{eB}{mc\gamma}$ where $\gamma = \frac{1}{\sqrt{1-v^2/c^2}}$ is the usual Lorentz factor. Thus the measurable difference will be the same as in the non-relativistic case:

$$\omega_a = \omega_s - \omega_c = a\frac{eB}{mc} \tag{11.2}$$

This experiment was performed also at CERN in 1972 by J. Bailey et al. They used muons at $p_\mu = 1.9$ GeV/c which meant a relativistic factor of $\gamma = 12$ and the muon lifetime extended by an order of magnitude to $\gamma\tau_\mu = 26\mu s$. The $B = 1.7$ T inhomogeneous magnetic field helped to focus the muons and keep them on orbit, but it also smeared the result. Nevertheless it was still more precise than before: $a_\mu = 116616(31) \times 10^{-8}$.

11.2.3 $(g - 2)_\mu$ with magic momentum

The inhomogeneous magnetic field focuses the stored muons, but it also causes a serious systematic smearing by broadening of the muon momentum distribution, thereby reducing the experimental precision. The solution is to separate focusing from the magnetic field of storage: electrostatic focusing. In an electric field $\vec{E}$ for a muon of velocity $\vec{v}$ the frequency connected to the anomalous magnetic moment will be

$$\vec{\omega}_a = \frac{e}{mc}\left[a\vec{B} - \left(a - \frac{1}{\gamma^2 - 1}\right)\frac{\vec{v} \times \vec{E}}{|\vec{v}|}\right] \tag{11.3}$$

One can see from Eq. (11.3) that for muons having a *magic momentum* (hence speed) for which $a - \frac{1}{\gamma^2-1} = 0$ the electric field effect is completely

Figure 11.5: The storage ring of the muon g-2 experiment at Brookhaven National Laboratory, 1999-2006

eliminated from the measured frequency. This experiment was first made at CERN in 1979 by *J. Bailey et al.* in a homogeneous magnetic field of strength $B = 1.5$ T with the following parameters: $p_\mu = 3.094$ GeV/c magic momentum; $\gamma_\mu = 29.37$; $\gamma\tau_\mu = 64.4\mu$s. Using the method of magic momentum increased the precision of the measurement by another factor of 3 to $a_\mu = 1165924(85) \times 10^{-9}$.

The last such experiment was made at the AGS accelerator of Brookhaven National Laboratory using the same magic momentum method. The storage ring (Fig. 11.5) with 24 detectors collecting the electrons from μ^- and the positrons from μ^+ decay was operated in 1999–2002, and measured separately the anomalous magnetic moments for μ^+ and μ^-. The results agreed with each other and their average [Patrignani et al., 2016] was $(116592089 \pm 54\text{stat} \pm 33\text{syst}) \times 10^{-11}$, two orders of magnitude better than the CERN result. There is a 3.5σ (σ is the experimental uncertainty) difference between theory and experiment. This could mean some new physics, but may also be due to the incomplete calculation of hadronic contributions, so the muon $(g-2)$ value is worth further improvement. The experiment will continue at Fermilab and for that the storage ring was transported from New York to Chicago. As it was much too large for trains, airplanes or trucks, it was shipped via the Atlantic Ocean, the Mexican Bay and the Mississippi river, see the home page at http://muon-g-2.fnal.gov/bigmove/. The ring is

in operation already, we can expect the first results in the near future.

Exercise 11.1
Why is the polarization of the muon definite when the muon is emitted in pion decay?

Exercise 11.2
Derive Eq. (11.2).

Exercise 11.3
Show how the muon storage ring facilitates direct measurement of the anomalous magnetic moment of the muon.

Exercise 11.4
How could new physics phenomena beyond the standard model be discovered via measuring $(g - 2)$ *of the muon?*

Exercise 11.5
How do we measure the polarization of the muon?

Exercise 11.6
Why does the muon have deeper penetration in matter than both the much lighter electron or the much heavier proton and neutron?

Chapter 12

Kaons and CP violation

MOTTO:

Alice laughed. "There's no use trying," she said: "one can't believe impossible things."
"I daresay you haven't had much practice," said the Queen. "When I was your age, I always did it for half-an-hour a day. Why, sometimes I've believed as many as six impossible things before breakfast."

(Lewis Carroll: Through the Looking Glass)

12.1 Kaons

As discussed in Chapter 1, *CPT* invariance is one of the most fundamental symmetries in physics. As for elementary particle interactions the time reversal invariance is also quite basic and generally established by experimental evidence, it was generally assumed that *CP* invariance also has to be valid for all microscopic processes, even when parity symmetry has proved to be completely violated by the weak interaction. Fig. 12.1 shows the four possible *CP*-variations for pion decay: only two of them will be allowed, both *C* and *P* have to be reflected in order to get from the case where the neutrino is left-polarized to the right-polarized anti-neutrino.

125
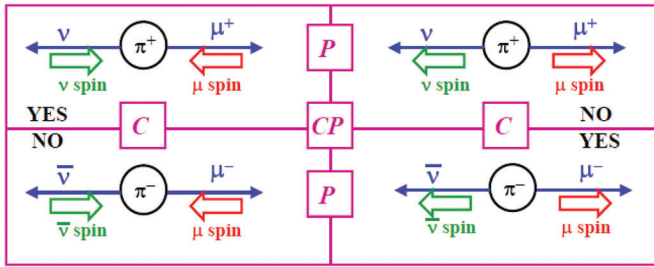
Figure 12.1: Pion decay: out of the four possible *CP*-variations only two will be allowed, both *C* and *P* have to be reflected.

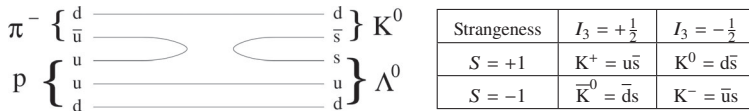| Strangeness	$I_3 = +\frac{1}{2}$	$I_3 = -\frac{1}{2}$
$S = +1$	$K^+ = u\bar{s}$	$K^0 = d\bar{s}$
$S = -1$	$\overline{K}^0 = \bar{d}s$	$K^- = \bar{u}s$

Figure 12.2: The lightest K-mesons. Left: kaon formation in pion-nucleon collisions. Right: the strong eigenstates of kaons.

Kaons are the second lightest mesons after the pions (Fig. 12.2). They contain s quarks which carry the *strangeness S* flavour quantum number. Pseudo-scalar mesons, their spin-parity quantum number is $J^P = 0^-$. We met them already in Chapter 11: Lee and Yang discovered parity violation when noted that K^+, the positive kaon appeared as two different particles in the experiment. Among the kaons, in addition to $K^\pm$ we have another particle-antiparticle pair: K^0 and $\overline{K}^0$.

12.2 Neutral kaons

Neutral kaons are among the so-called V-particles: their decay appeared in bubble chamber experiments as two tracks out of nothing (as neutral particles do not leave tracks in chambers) curving into opposite directions in the magnetic field. They were copiously produced and slowly decayed, so they are created in strong and decay in weak processes. There is a slight difference in masses between charged and neutral kaons: $m_{K^\pm} = 493.7 \, \text{MeV}/c^2$ and $m_{K^0} = m_{\overline{K}^0} = 497.6 \, \text{MeV}/c^2$.

Kaons are formed when pions collide with nucleons at high enough energies (Fig. 12.2): a light quark-antiquark pair annihilates into a gluon and

makes an $s\bar{s}$ pair which then separate in two particles carrying strangeness. In pion scattering on protons at certain pion energies (around a few GeV) well regulated beams can be produced of given kinds of kaons. One can produce neutral kaons at accelerators at $1 < T(\pi^-) < 6$ GeV where T denotes kinetic energy: $\pi^- p \to \Lambda K^0$ with the subsequent decay of the Λ hyperon (with the lifetime of $\tau_\Lambda = 0.26$ ns) via:

$$\Lambda \to \begin{cases} p\pi^- & (64\%) \\ n\pi^0 & (36\%) \end{cases}$$

that helps to tag the production of the kaon.

Neutral anti-kaons can be made with positive pion scattering,

$$\pi^+ p \to K^+ \overline{K^0} p \quad (T(\pi^+) > 1.5\,\text{GeV}),$$

or in

$$\pi^- p \to \overline{\Lambda}\,\overline{K^0}\,n\,n \quad (T(\pi^-) > 6\,\text{GeV}).$$

The kaons are created via colour interaction in flavour eigenstates and decay via weak interaction in weak eigenstates. Assuming that the weak interaction conserves CP parity, one can look for weak decays in the forms of CP eigenstates. K^0 and $\overline{K}^0$, however, are not those: $CP\,|K^0> = |\overline{K^0}>$ and $CP\,|\overline{K^0}> = |K^0>$. We can construct CP eigenstates:

$$\left.\begin{matrix} K_1^0 \\ K_2^0 \end{matrix}\right\} = \frac{1}{\sqrt{2}}(K^0 \pm \overline{K^0}) = \frac{1}{\sqrt{2}}(d\bar{s} \pm \bar{d}s)$$

As the pion is pseudo-scalar meson, its CP eigenvalue is $\kappa(CP) = -1$. CP conservation demands that K_1^0 with $\kappa(CP) = +1$ decays to two pions, but the K_2^0 with $\kappa(CP) = -1$ to three pions only, which increases its lifetime by 3 orders of magnitude as zero orbital momentum dominates between the emitted particles: $K_1^0 \to \pi\pi$ ($\tau_1 \sim 89$ ps) whereas $K_2^0 \to \pi\pi\pi$ ($\tau_2 \sim 52$ ns). Because of the slightly different virtual loop corrections, even their masses are different, although the difference is extremely small.

12.3   Kaon oscillation

Thus a free K^0 meson will decay via weak interaction in two different modes with two different lifetimes. After a long enough flight only the longer-lived component will survive. The amplitude of the free meson when it forms

at $t = 0$ is $K^0 = \frac{1}{\sqrt{2}}(K_1 + K_2)$, a mixture of two states with different time-dependencies: $a_1(t) = \frac{1}{\sqrt{2}} \exp\{-\frac{\Gamma_1 t}{2} + im_1 t\}$ and $a_2(t) = \frac{1}{\sqrt{2}} \exp\{-\frac{\Gamma_2 t}{2} + im_2 t\}$. The time dependence of the total squared wave function is

$$I_{K^0}(t) = \frac{1}{2}(a_1 + a_2) \cdot (a_1^* + a_2^*) = \frac{1}{4}(e^{-\Gamma_1 t} + e^{-\Gamma_2 t} + \text{Re}(a_1 a_2^*))$$

where

$$\text{Re}(a_1 a_2^*) = \exp\left(-\frac{\Gamma_1 t}{2} - im_1 t - \frac{\Gamma_2 t}{2} + im_2 t\right) + \exp\left(-\frac{\Gamma_1 t}{2} + im_1 t - \frac{\Gamma_2 t}{2} - im_2 t\right)$$

$$= \exp\left(-\frac{\Gamma_1 + \Gamma_2}{2} t\right)[e^{i(m_2 - m_1)t} + e^{-i(m_2 - m_1)t}].$$

Using $e^{ix} = \cos(x) + i\sin(x)$, the expression in the brackets can be written as $\cos(\Delta mt)$,

$$I_{K^0}(t) = \frac{1}{4}\left[e^{-\Gamma_1 t} + e^{-\Gamma_2 t} + 2\exp\left(-\frac{\Gamma_1 + \Gamma_2}{2} t\right) \cos \Delta mt\right],$$

where $\Delta m = |m_1 - m_2|$. This means a periodic changing mixture of the two states with the frequency $\omega = \Delta m$. If a particle is produced in the state K^0, the probability to detect it in the same state at time t is proportional to $I_{K^0}(t)$.

Thus we see a *kaon oscillation* between the two flavour states with a frequency depending on the mass difference, $\Delta m = 3.5 \cdot 10^{-6}$ eV, implying a relative difference $\Delta m/m = 0.7 \cdot 10^{-14}$. Assuming also the exchange of quarks, the measured mass difference allowed to make predictions for the mass of a fourth quark, the c quark. The study of kaon oscillation with the small mass difference between the weak eigenstates facilitated to achieve the most precise experimental test of *CPT* invariance:

$$\frac{|m(K^0) - m(\overline{K}^0)|}{m(\text{mean})} < 10^{-18}$$

Another interesting feature of kaon physics is the *regeneration* process (Fig. 12.4). After a long flight the neutral kaon beam consists mostly of long-lived $K_2^0 = \frac{1}{\sqrt{2}}(d\bar{s} - \bar{d}s)$. As shown by *Pais and Piccioni* in 1955, if it is injected into matter, the d quark is just scattered on nucleons, whereas its antiparticle component can annihilate and so K^0 is partially reconfigured.
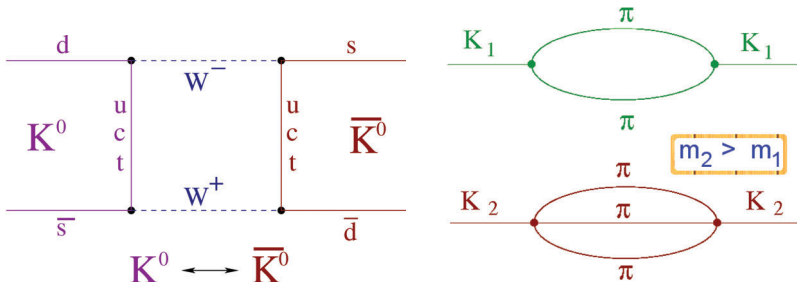
Figure 12.3: Kaon oscillation between two *CP* eigenstates. Left: exchange of weak bosons, right: origin of the mass difference.
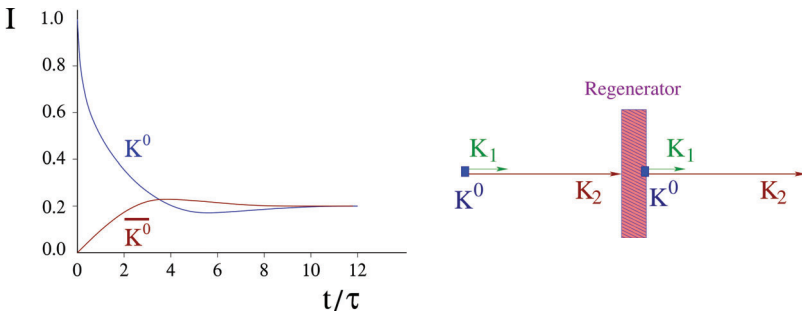

Figure 12.4: Kaon oscillation. Left: A kaon starting as K^0 becomes in time a mixture of K^0 and $\overline{K^0}$. Right: K^0 regeneration: anti-quarks annihilate and K^0 is reconfigured from the long-lived mixture

12.4 *CP* violation

Around 1960 everybody believed in the conserved *CP* symmetry, but after the discovery of parity violation, *CP* invariance called for experimental testing as well. *J.H. Christenson, James W. Cronin, Val L. Fitch and R. Turlay* published the observation of the *CP*-violating decay $K_2^0 \to \pi\pi$ in 1964, (Cronin and Fitch were awarded the Nobel Prize in 1980). Their method was based on the different kinematics of 2- and 3-pion decay modes of the neutral kaon: a 3-pion decay produces pions more-or-less uncorrelated in angle, but for the 2-pion decay the kinematic conditions are determined. The experiment fixed the angle and energy of the detected pions and gave 45 ± 9 $\pi^+\pi^-$ pairs above background (note the 5σ excess!). This means
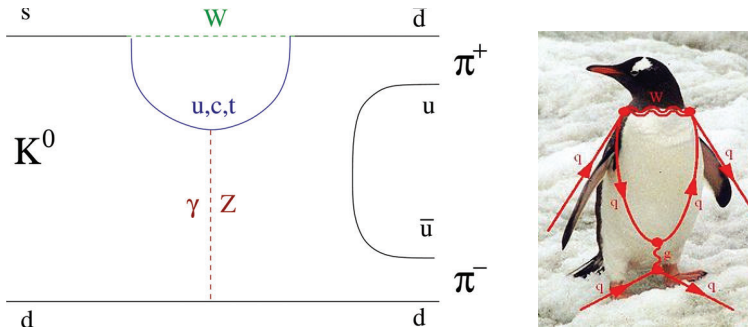
Figure 12.5: Penguin diagram describing direct CP-violation. Its name is the result of a bet: the loser, John R. Ellis, had to introduce the word *penguin* in his next paper.

that the long-lived neutral kaon is not a clean CP-odd eigenstate, it has a CP-even component as well. This mixing can be written as $K_S = K_1 + \epsilon K_2$ and $K_L = K_2 + \epsilon K_1$ where K_S is the short-lived and K_L is the long-lived neutral kaon. Here $|\epsilon| = (2.28 \pm 0.02) \cdot 10^{-3}$ so — as opposed to parity violation — CP invariance is just a little bit violated.

CP invariance would mean $|e^+ \nu_e \pi^-> = |e^- \overline{\nu}_e \pi^+>$, but CP violation should violate that as well. We expect that in the decay of the long-lived neutral kaon,

$$K_L \to \left\{ \begin{array}{c} e^+ \nu_e \pi^- \\ e^- \overline{\nu}_e \pi^+ \end{array} \right\}$$

a charge asymmetry can be present. This *direct CP-violation* (Fig. 12.5) was observed at CERN by the NA48 experiment. With a very sophisticated setup they simultaneously observed kaon decay in four channels with very similar geometric conditions and detection efficiencies. They deduced the following ratio:

$$R = \frac{N(K_L \to \pi^0 \pi^0)}{N(K_S \to \pi^0 \pi^0)} \frac{N(K_S \to \pi^+ \pi^-)}{N(K_L \to \pi^+ \pi^-)}.$$

This helped to eliminate quite a few systematic effects: calibration and geometry.

Experiment NA48 at the SPS of CERN did not go without problems: once the chambers around the beam line imploded and the whole setup had

to be rebuilt. Finally, the result was the following:

$$\frac{N(K_L \to \pi^0\pi^0)}{N(K_S \to \pi^0\pi^0)} \frac{N(K_S \to \pi^+\pi^-)}{N(K_L \to \pi^+\pi^-)} = 0.99098 \pm 0.00101 \pm 0.00126$$

with the first uncertainty being statistical, the second one systematic. Clearly, the experiment has demonstrated the direct CP-violation.

Exercise 12.1
In what sense can we speak of anti-kaons? How are antiparticles introduced in particle physics?

Exercise 12.2
Show that K_1^0 and K_2^0 are CP eigenstates and that is why they can only decay to 2 and 3 pions.

Exercise 12.3
How can energy and momentum conservation simultaneously fulfilled when the kaon changes its mass in flight?

Exercise 12.4
What is the mechanism of kaon regeneration? How does the short-lived kaon become long-lived again?

Exercise 12.5
What is the most precise test of CPT invariance and why?

Chapter 13

Neutrinos

13.1 Weak currents

The weak interaction has two kinds of currents, a charged current when the interaction is mediated by $W^{\pm}$ bosons and a neutral one with the Z boson. When an unstable particle decays to leptons it produces particle-antiparticle pairs or a lepton with a neutrino. Typical weak decays are shown in Fig. 13.1. We have determined the number of fermion families via studying the decay of the Z boson to neutrino pairs by measuring its *invisible width* (see Section 10.1.1) and obtained 3. Thus there are 3 kinds of light neutrinos with charged leptons associated.

As neutrinos are produced overwhelmingly in the nuclear reactions in stars (most of the energy of a supernova is carried away by neutrinos) space is full of them, 60 billion neutrinos fly through our fingertips every second, most of them from the Sun. Let us list the main neutrino sources, noting the kind of neutrinos and their distance between production and eventual detection on the surface of Earth.
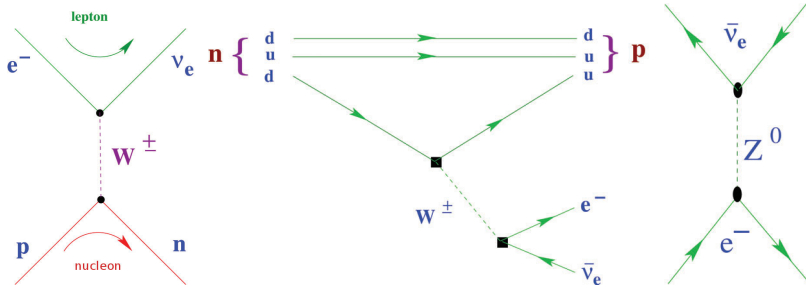
Figure 13.1: Weak interaction processes. From left to right: neutron beta-decay at nucleon level, depicted in a crossing symmetric diagram, and at quark level (charged currents); antineutrino scattering on an electron (neutral current). The arrows follow the *CPT* convention

- *Cosmic neutrinos*: all kinds from cosmic distances.

- *Sun neutrinos*: nuclear fusion, $4\,H \rightarrow He + 2\,e^+ + 2\,\nu_e$. They are electron neutrinos coming from a distance of $L \simeq 10^8$ km.

- *Atmospheric neutrinos*: secondary particles of cosmic rays.
  $\pi^\pm \rightarrow \mu^\pm \nu_\mu$; $\mu^\pm \rightarrow e^\pm \nu_\mu \nu_e$; $L \simeq 30$ km, ν_e, $2\,\nu_\mu$, ν representing both neutrinos and antineutrinos.

- *Neutrino beam from an accelerator*: Analogous to the atmospheric case, $L \simeq 1$–700 km.

- *Geo-neutrinos*: Geological antineutrinos from natural radioactivity: β-decay of uranium and thorium: $n \rightarrow p + e + \bar{\nu}_e$.

- *Reactor neutrinos*: In nuclear reactors the energy is produced by nuclear fission resulting in neutron-rich daughter nuclei that subsequently undergo β^- decay releasing low-energy electron-antineutrinos.

Neutrinos were first observed by *Clyde L. Cowan* and *Frederick Reines* in 1952-56 with antineutrinos from a nuclear reactor. They used the reaction of neutrino scattering on the proton, $\bar{\nu}_e p \rightarrow e^+ n$ with double identification: the two prompt photons from positron annihilation and the delayed photons from the capture of the neutron in cadmium. F. Reines received the Nobel Prize almost 40 years later, in 1995. Since then neutrinos have been in the front line of particle research: at the moment there are dozens of working neutrino experiments (some of them are noted in Fig. 17.26). Most of them

are large, built under water, in deep mines, or tunnels under earth, and one is sunk in the ice of the Antarctica.

It was quite a breakthrough when in 1987 the neutrinos from supernova SN1987A were detected by the existing large neutrino experiments, the Irvine–Michigan–Brookhaven (IMB) detector in the USA, Kamiokande in Japan and Baksan in Russia, although the whole neutrino burst lasted 13 seconds only.

13.2   Neutrino mass

In the original formulation of the standard model neutrinos were postulated to have zero mass. Many experiments were done in the last almost hundred years to measure their mass. Most of them rely on tritium decay $t \rightarrow {}^3He + e^- + \bar{\nu}_e$ and study the high-energy end of the electron spectrum for deviations, as the end point should be sensitive to neutrino mass. One of the largest and newest such experiment is KATRIN, the KArlsruhe TRItium Neutrino experiment (Fig. 17.27). It is so large that when built in Germany it could not be transported on the highway. Similarly to the Brookhaven muon storage ring, it was shipped down the Danube, along the Black Sea, the Mediterranean, the Atlantic Ocean, and up the Rhine River, altogether a travel of 8600 km instead of the 400 km as the crow flies. KATRIN hopes to measure the mass of the electron neutrino with the precision of $\sim 1\,eV$ (Fig. 13.2). Cosmological observations suggest that the sum of the masses of the three neutrino types is below 1 eV.

13.3   Early neutrino mysteries

The first mystery was connected to neutrinos from the Sun. The nuclear fusion of the Sun makes helium from hydrogen in several steps resulting in

$$4\,{}^1H \rightarrow {}^4He + 2e^+ + 2\nu_e,$$
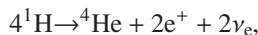
i.e. producing 2 ν_e with energies up to 18 MeV. Those neutrinos were first observed by the Homestake Experiment of Raymond Davis and his group in 1964-69 (he was awarded the Nobel Prize in 2002). The enormous difficulty of detecting neutrinos is well demonstrated by *Solar Neutrino Unit* of detection:

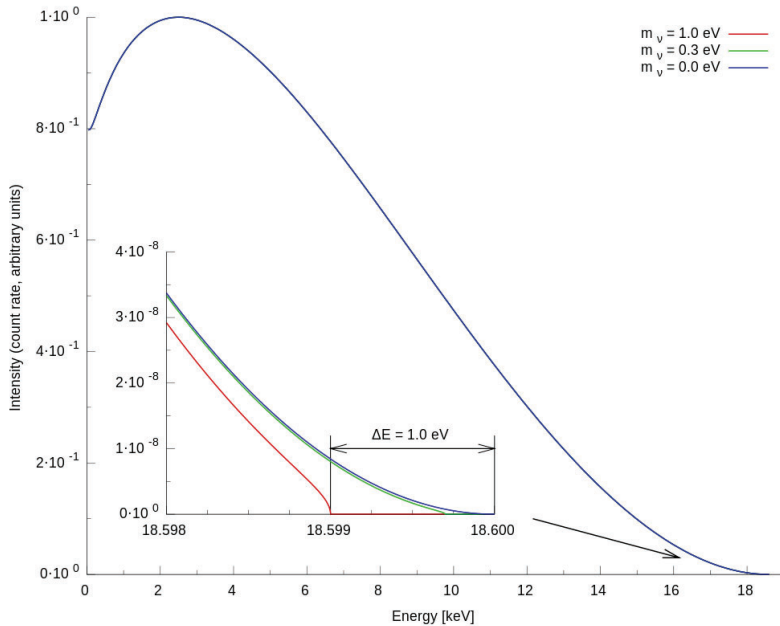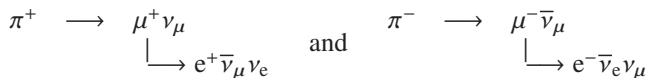$$1\,SNU = \frac{10^{-36} \; \nu\text{-interactions}}{atom \cdot sec},$$

Figure 13.2: The expected sensitivity of the KATRIN spectrometer for determining the mass of the electron neutrino.

which practically means one detected neutrino interaction a day per 10^{30} atoms, i.e. per 10–100 tons of material. The Homestake experiment of Davis collected and analysed radioactive ^{37}Ar atoms from the reaction

$$\nu_e +^{37} Cl \rightarrow ^{37}Ar + e^-.$$
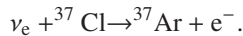
The expected rate from the standard solar model was 8.2 ± 1.8 SNU, but they found only 2.56 ± 0.23 SNU. As all subsequent measurements confirmed both this result and the validity of the model, this huge discrepancy remained mysterious for a long time.

A second mystery is connected to the disappearance of the atmospheric muon neutrinos. As cosmic particles (mostly protons and helium nuclei) hit the atmosphere they produce pions which decay to muons and the muons to electrons :

$$\pi^+ \longrightarrow \mu^+ \nu_\mu \qquad \text{and} \qquad \pi^- \longrightarrow \mu^- \bar{\nu}_\mu$$
$$ \hookrightarrow e^+ \bar{\nu}_\mu \nu_e \qquad\qquad\qquad \hookrightarrow e^- \bar{\nu}_e \nu_\mu$$
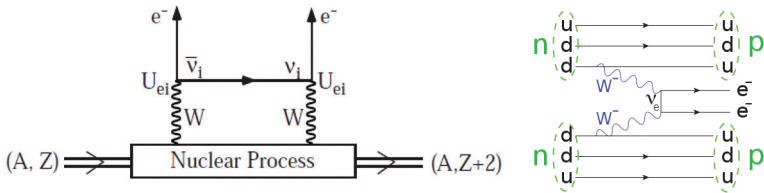
Figure 13.3: Neutrino-less double beta decay with a Majorana neutrino in nuclear decays and on parton level.

These processes should yield twice as many muon neutrinos than electron ones, but the measurements gave much less than the expected factor of two.

As the neutrinos are neutral point-like fermions, they could be *Majorana particles* which are their own antiparticles with the opposite polarization: $\nu_L = \bar{\nu}_R$. In that case, however, the neutrino-less double beta-decay should be possible as shown in Fig. 13.3. Many experiments were and are looking for such a process, and so far upper limits were estimated only for its half-life, typically about 10^{21} years (on a 90 % confidence level).

13.4 Neutrino oscillation

13.4.1 Phenomenology

Bruno Pontecorvo (Joint Institute for Nuclear Research, Dubna, Russia) developed in 1963 the theory of neutrino oscillations to explain the lack of detected atmospheric and Sun neutrinos, but he passed away before they were experimentally observed. Let us assume two kinds of neutrinos, with flavour eigenstates ν_e and ν_μ. Weak interaction will mix them into mass eigenstates ν_1 and ν_2 and they can oscillate between the two states: $\nu_e \Leftrightarrow \nu_\mu$ (similarly to the $K^0 \Leftrightarrow \bar{K}^0$ case, see Chapter 12). Obviously, energy and momentum cannot be conserved at the same time.

If the momentum is conserved, then the energy difference is ($c = 1$)

$$E_2 - E_1 = \sqrt{p^2 + m_2^2} - \sqrt{p^2 + m_1^2} \approx p\left[1 + \frac{m_2^2}{2p^2} - \left(1 + \frac{m_1^2}{2p^2}\right)\right]$$

$$= \frac{m_2^2 - m_1^2}{2p} \equiv \frac{\Delta m^2}{2p}.$$

In the case of energy conservation the momentum difference is

$$p_2 - p_1 = \sqrt{E^2 - m_2^2} - \sqrt{E^2 - m_1^2} = \frac{m_2^2 - m_1^2}{2E} \equiv \frac{\Delta m^2}{2E}.$$

As the neutrino mass is very small, it is quite relativistic and $E_\nu \approx p_\nu$, so the two approaches yield similar results.

A free neutrino can be treated as a propagating field of plane wave: $e^{-ip\cdot x}$ where a difference in mass leads to a change in phase. This phase change for a neutrino of energy E in time t and on a distance of $L \approx ct$ is

$$\Delta(p \cdot x) = \Delta(Et - px) \approx \frac{\Delta m^2 t}{2E} \approx \frac{\Delta m^2 L}{2E}.$$

Of course, for this to be valid one needs small enough violation of the conservation laws to fit in the uncertainty relation of Heisenberg, or an interaction with some outside field or medium. The Sun neutrinos do have a thick dense medium to interact with, but in the case of the atmosphere we need the uncertainty relation. There the momentum change is $\delta p_\nu \approx 10^{-12}$ eV, much lower than the pion or muon natural widths: $\Gamma_\pi \approx 10^{-8}$ eV, $\Gamma_\mu \approx 10^{-10}$ eV.

13.4.2 Super-Kamiokande experiment

Super-Kamiokande (SKK) is a huge detector in the Kamioka mine in Japan under 1 km of earth. It was originally built to detect proton decays (Kamiokande stands for KAMIOKA Nucleon Decay Experiment). Its heart is a Cherenkov detector with 50000 tons of extra clean water watched by 11146 photo-multiplier tubes of 50 cm diameter (Fig. 17.28). It has 100% efficiency of detecting muons (and thus converted muon neutrinos) with $p_\mu > 100$ MeV/c. It committed "suicide" after the discovery of the oscillation of the atmospheric neutrinos: in 2001 one of its phototubes imploded during water refilling and the shock wave destroyed more than half of its phototubes. By 2006 it was completely reconstructed.

SKK was looking for muon and electron events originating inside the detector as the incoming neutrinos leave no other trace. It could identify from the Cherenkov cones the type of particles (muon or electron) and their energies. Even the direction of the detected neutrinos could be reconstructed by measuring the shape and timing of the Cherenkov ellipse (Figs. 17.28 and 17.29).

SKK confirmed the lack of Sun neutrinos with a very high precision:

$$\frac{\text{SKK data}}{\text{SSM MC}} = 0.406 \pm 0.004 \begin{cases} +0.014 \\ -0.013 \end{cases}$$

where the first uncertainty is statistical, the second one systematic. Thus it was confirmed that only 40% of the electron neutrinos of the Sun predicted by the standard solar model arrive to Earth. The Sun neutrinos were identified by type and energy only and their origin reconstructed by the Cherenkov cones nicely showed the shape of the Sun (Fig. 17.29).

Part of the atmospheric muon neutrinos also disappeared, SKK measured the following yield:

$$\frac{(N_\mu/N_e)_{\text{data}}}{(N_\mu/N_e)_{\text{MC}}} = 0.688 \pm 0.016 \pm 0.050$$

where, as usual, the first uncertainty is statistical, the second one systematic. However, SKK could also separate muons and electrons, and sort them by energy and direction, which allowed to make an amazing discovery: the electron neutrinos of cosmic origin (i.e. of higher energies than those from the Sun) are in order, whereas the higher energy muon neutrinos from the atmosphere at the opposite side of Earth partially disappear (Fig. 17.30). The ratio (flux up)/(flux down)

$$\frac{N(-1.0 < \cos\theta < -0.2)}{N(0.2 < \cos\theta < 1.0)} = 0.54 \pm 0.04$$

The conclusion from the SKK results was that (1) low-energy electron neutrinos oscillate into other types on the Sun-Earth distance and (2) high-energy muon neutrinos at the distance of Earth's diameter oscillate into τ neutrinos as they do not appear in the electron neutrino spectra. The measured flux ratio was consistent with $1.3 \times 10^{-3}\,\text{eV}^2 \leq \Delta M^2_{\text{atm}} \leq 3.0 \times 10^{-3}\,\text{eV}^2$. Note that these measurements cannot determine the neutrino masses, just the differences in their mass squares.

13.4.3 SNO experiment (1999-2003)

The Sudbury Neutrino Observatory (SNOlab) is located in the Creighton nickel mine of Sudbury, Canada at 2 km underground. The SNO detector worked in 1999-2003, it contained 1000 t of 99.92% pure D_2O inside an acrylic ball (Fig. 17.31) floating in 7500 t of H_2O. For the experiment SNOlab borrowed the heavy water from the Canadian Atomic Energy Agency. SNO used three different reactions to detect neutrinos:

- $\nu_e + d \rightarrow p + p + e^-$: charged current, sensitive to electron neutrinos only;

- $\nu_x + d \rightarrow p + n + \nu_x$: neutral current , sensitive to all neutrinos;

- $\nu_x + e^- \rightarrow \nu_x + e^-$: electron scattering, sensitive to all neutrinos.

Thus SNO could measure the fluxes of electron neutrinos separately and of all neutrinos simultaneously. Between 2001 and 2003 the heavy water had 2 tons of Na^{35}Cl dissolved to catch the neutrons released from deuterons in the interaction with neutrinos. As neutron capture in ^{35}Cl produces several gamma photons, adding Na^{35}Cl helped to distinguish between the neutral current and electron scattering reactions.

The result of SNO has consolidated the proof of the oscillation of the Sun neutrinos. It has shown that although some of the electron neutrinos disappear, the total flux of Sun neutrinos agrees very well with the expectations of the standard solar model, so the missing electron neutrinos transit into the other two kinds on the Sun-Earth distance.

For the observation of cosmic neutrinos with the Super-Kamiokande experiment *Masatoshi Koshiba* received the Nobel Prize in 2002. For the discovery of neutrino oscillations the 2015 Nobel Prize in physics was awarded to *Takaaki Kajita* (SKK) and *Arthur B. McDonald* (SNOlab).

13.4.4 Neutrino mixing and masses

Thus at least two of the three neutrinos have masses (most likely all three) and the mass eigenstates are different from the weak eigenstates, so they mix. The mixing can be described by the *Pontecorvo-Maki-Nakagawa-Sakata* mixing matrix U_{fi}, see Section 22.8.

We have found two mass differences among the three neutrinos: the atmospheric neutrinos oscillate with a mass-square-difference of

$$(\Delta M^2)_{\text{atm}} \approx 2.4 \times 10^{-3} \text{eV}^2$$

and the Sun neutrinos with

$$(\Delta M^2)_{\text{Sun}} \approx 7.6 \times 10^{-5} \text{eV}^2.$$

This does not allow to determine the *neutrino mass hierarchy*, the ordering of neutrinos by mass eigenvalues. For simplicity let us assume $m_1 < m_2$ for the two masses closer to each other (from the oscillation of the Sun neutrinos), then m_3 will be more different from the first two and either $m_1 < m_2 < m_3$ or $m_3 < m_1 < m_2$.

Recent data by many experiments confirmed [Patrignani et al., 2016] that the mixing angle Θ_{12} is associated mainly with the solar ν_e, and Θ_{23} with the atmospheric ν_μ oscillations. That is why in the literature the 12 index is often substituted by $\odot$ and 23 by atm or A, like $\Theta_{12} \rightarrow \Theta_\odot$ and $\Theta_{23} \rightarrow \Theta_{\text{atm}}$. It is also agreed upon that $\sin \Theta_{13}$ must be quite small.

13.4.5 Neutrino experiments at nuclear reactors

As mentioned above, the first detection of neutrinos was made near a nuclear power plant. The experimental proof of flavour oscillations of neutrinos along distances from the Sun and through the diameter of Earth raised the interest to study neutrino oscillations on various distances. We shall briefly describe three examples of such experiments: the *Daya Bay* experiment made at a few kilometres from a nuclear power plant, two long-distance neutrino beam accelerator experiments and two short-distance ones at accelerators.

Reactor anti-neutrinos are commonly detected by the reaction

$$\overline{\nu}_e + p \rightarrow e^+ + n$$
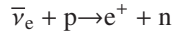
with energies between 1.8 and 8 MeV. Energy conservation prohibits the reactions involving muons or tau-leptons, and the oscillation is detected by the disappearance of the electron anti-neutrinos.

For three families the survival probability of $\overline{\nu}_e$ is [An et al., 2017]

$$P_{sur} \approx 1 - \cos^4 \Theta_{13} \sin^2(2\Theta_{12}) \sin^2 \Delta_{21} - \sin^2(2\Theta_{13}) \sin^2 \Delta_{ee},$$

where Θ_{ij} is the mixing angle between two mass states, and

$$\Delta_{ij} \approx 1.267 \, \Delta m_{ij}^2 [\text{eV}^2] \, \frac{L[m]}{E_\nu[\text{MeV}]}$$

with the mass-squared difference measured in eV, the flight distance in meters and the neutrino energy in MeV. The effective neutrino *disappearance phase* Δ_{ee} (not to be mixed with Δ_{ij}) is an empirical quantity independent of the neutrino mass hierarchy. The reactor experiments help to determine the two quantities Θ_{13} and Δ_{ee}. From the latter an empirical mass-squared difference Δm_{ee}^2 can be deduced, characterizing the disappearance of reactor anti-neutrinos.

The Daya Bay experiment (Fig. 17.32) is built near Hong Kong in China. It consists of eight $\overline{\nu}$ detectors in three groups in the vicinity of six nuclear reactors. Each detector contains 20 tons of liquid scintillator. It is aimed at determining the mixing of neutrinos of the first and third families. The results published in 2017 [An et al., 2017] were the following:

- For the $\nu_1 \leftrightarrow \nu_3$ mixing they measured a mixing angle of

$$\sin^2(2\Theta_{13}) = (8.41 \pm 0.27 \text{ stat} \pm 0.19 \text{ syst}) \times 10^{-2},$$

a very well established experimental result.

- For the empirical $\overline{\nu}$ neutrino mass-squared difference they got

$$|\Delta m^2_{\text{ee}}| = 2.50 \pm 0.06 \text{ stat} \pm 0.06 \text{ syst}) \times 10^{-3} \ \text{eV}^2.$$

- They have excluded the existence of an additional ν_4 *sterile neutrino* (that does not belong to a charged lepton) in the mass range of $10^{-3} < \Delta m^2_{14} < 0.1 \text{ eV}^2$.

13.4.6   Long distance neutrino experiments

As neutrino oscillations were confirmed both at the Sun–Earth distance and at the distance of Earth's diameter, several experiments were set up to check shorter distances. We shall consider later LSND at 30 m and MiniBooNE at 500 m. The CNGS (CERN Neutrinos to Gran Sasso) experiment creates a neutrino beam with the 450 GeV proton beam of CERN's Super Proton Synchrotron and shoots neutrinos toward the Gran Sasso National Laboratory, built in a tunnel 1 km underground south from Rome at a distance of 732 km from CERN. The relativistic pions decay in vacuum, they produce muons and muon neutrinos. The charged muons will slow down and decay or get absorbed by nuclei, but the muon neutrinos follow the forward direction of the pions and form a beam: at Gran Sasso the beam diameter is about 2.8 km. A similar setup operates at Fermilab: there is a 736 km distance between the injector synchrotron of the Tevatron and the Soudan mine where the MINOS neutrino detector is located.

Gran Sasso has several neutrino experiments. The OPERA experiment, e.g. managed to observe the oscillation of ν_μ into ν_τ on the CNGS beam. They measured the neutrino flight time between CERN and Gran Sasso as well. When — as a result of a faulty cable connection — they announced that they saw neutrinos travelling faster than the speed of light in vacuum, another experiment in their neighbourhood, ICARUS, immediately checked it and found ordinary subluminal neutrinos only.

13.4.7   Sterile neutrinos?

One of the numerous mysteries of neutrino physics is connected to the Liquid Scintillator Neutrino Detector (LSND) experiment. LSND collected data from 1993 to 1998 at Los Alamos: the 800 MeV proton beam from LAMPF, the Los Alamos Meson Physics Facility was injected in a thick water target where hadrons, mostly positive and negative pions were produced. The pions were stopped in a copper target that absorbed the negative pions and
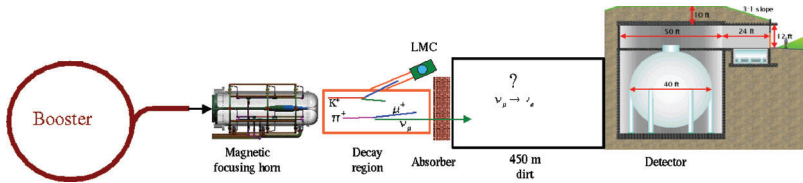
Figure 13.4: The beam line of the MiniBooNE experiment at Fermilab. The booster protons are injected into the target, produce pions of which the negative ones get absorbed in nuclei and the positive pions decay into muons and neutrinos. The result is 3 kinds of neutrinos, ν_μ, $\overline{\nu}_\mu$ and ν_e. The appearance of $\overline{\nu}_e$ is interpreted as $\overline{\nu}_\mu \to \overline{\nu}_e$ oscillation.

muons (they get captured in atomic orbits and then absorbed by the nuclei), whereas the positive particles decay: $\pi^+ \to \mu^+ + \nu_\mu$, $\mu^+ \to e^+ + \overline{\nu}_\mu + \nu_e$. These reactions produce three kinds of neutrinos, but not electron antineutrinos; if they appear, it is a sign of $\overline{\nu}_\mu \to \overline{\nu}_e$ oscillation.

LSND saw a 4σ excess of $\overline{\nu}_e$ above expected background using the $\overline{\nu}_e p \to e^+ n$ reaction. Considering that we do not see this oscillation with the atmospheric neutrinos, the difference has to be connected to the different energy of neutrinos (in Los Alamos it was up to 52.8 MeV) and their different flight distances (30 m between target and detector). The conclusion of the collaboration was that $M_\nu > 0.4$ eV.

The LSND result contradicts the other experiments. If it is valid then a fourth, sterile neutrino must exist. As usual, no new observation is accepted in particle physics before another experiment confirms it (although the LSND result did not reach the required 5σ level). A new collaboration was formed and it built the MiniBooNE (Booster Neutrino Experiment) detector at Fermilab (Fig. 13.4) in 2005 to confirm or refute the LSND result.

Fig. 13.4 presents the beam line of the MiniBooNE experiment at Fermilab. It reproduces the conditions of LSND at an order of magnitude higher energy and distance. LSND was located at $L_1 = 30$ m from the target and received $E_1 = 30$ MeV neutrinos on average. The MiniBooNE detector is located at $L_2 = 500$ m from the production target which provides $E_2 = 500$ MeV neutrinos. Thus the ratios determining the oscillation frequency were the same, $E_1/L_1 = E_2/L_2$.

In 2007 the MiniBooNE Collaboration stated that they did not see the antineutrinos of LSND. In 2009 they announced that they started seeing something and in 2012 they published a 3.8σ excess, almost exactly the

same as LSND. Again, this excess is not considered to be significant enough to accept as the signal of new physics.

13.5   Present neutrino mysteries

One would think that the neutrino mysteries are solved, we found the missing neutrinos: the atmospheric ν_μ transforms into ν_τ on the way through Earth, and the Sun's ν_e metamorphoses into ν_μ and ν_τ while travelling from the Sun to Earth. The oscillations are well described by three neutrino flavours and the PMNS mixing matrix.

Unfortunately (or fortunately!) the observation of neutrino oscillations added more to the mysteries that were already known for the neutrinos. Although we may add neutrino masses to the Lagrangian of the standard model like we do with the charged leptons, we would not be able to explain any phenomenology with such an addition. The standard model has to be extended in order to accommodate non-zero neutrino masses.

- If the neutrinos have masses, there could exist right-polarized neutrinos, ν_R, and left-polarized antineutrinos, $\overline{\nu}_L$, with zero hypercharge $Y = 0$, i.e. with no charged lepton attached (*sterile neutrinos*), with no interaction within the standard model. While this would be a natural extension of the standard model, such particles were not observed in experiment, except by the LSND experiment which was not confirmed.

- Maybe the neutrinos are Majorana particles, $\nu = \overline{\nu}$: the neutrinoless double-beta-decay experiments so far did not observe such phenomena.

- Maybe there is an extended Higgs-sector with more symmetry-breaking potentials to create those masses? The LHC experiments found just one Higgs-boson and its properties are close to those predicted by the standard model.

- Why do neutrinos oscillate? They feel only the weak interaction, no reason for them to have different eigenstates. Maybe there is another, so far unobserved interaction mixing those states?

- Why the neutrino masses are so unreasonably small? The *see-saw* mechanism is proposed to solve this problem. It assumes that the neutrinos exist in pairs: light Dirac and heavy sterile neutrinos, but such heavy ones were not observed yet.

• What is really the mass of the neutrinos? The oscillation gives the difference of mass-squares only.

We can conclude that neutrinos present a real enigma: they are bright signal posts showing the holes and deficiencies in our standard model in spite of all its success in describing the experimental data, and also a way to extend our knowledge.

Exercise 13.1
Why does the existence of neutrino oscillations point toward the existence of new physics beyond the standard model whereas that of kaon oscillation does not?

Exercise 13.2
How can energy and momentum conservation simultaneously fulfilled while the neutrino changes its mass during flight?

Exercise 13.3
What is the difference between mass and flavour eigenstates for neutrinos?

Exercise 13.4
How was the number of light neutrinos measured?

Exercise 13.5
How does the existence of neutrino oscillations prove the non-zero mass of neutrinos?

Exercise 13.6
What is the difference between left and right polarised neutrinos and antineutrinos?

Chapter 14

Higgs boson

The standard model seems to describe all experimental data so well that any observed deviation from it is looked upon with deep suspicion. For almost 40 years, more and more precise new data have been acquired at the particle accelerators and all seem to agree very well with the predictions of the standard model. Hundreds of experiments are summarized in Fig. 17.33 according to the LEP Electroweak Working Group [Schael et al., 2013]. It shows the 2012 situation of the analysis of electroweak data: all experimental data and theoretical estimates agree within the experimental uncertainties. The only parameter which deviates at more than 2σ uncertainty is the forward-backward asymmetry of the decay of the Z boson to two b quarks.

Since the observation of the top quark in 1995 the Higgs boson was the only *missing* elementary particle of the standard model. Its observation in 2012 put the dot on i, proving the mechanism of mass creation via spontaneous symmetry breaking.

14.1 Search for the Higgs boson

The search for the Higgs boson is the best example to show how systematic data handling and analysis are organized in high-energy physics. For 40 years larger and larger experiments tried to find it or exclude its existence, until finally, in 2012 the ATLAS and CMS experiments at the Large Hadron Collider managed to observe it.

14.1.1 Methodology

When searching for a new particle, what we usually try to observe is a resonance. As described in Chapter 2, for a particle with lifetime $\tau = \Gamma^{-1}$ and decay rate Γ the event rate against the energy corresponding to the invariant mass of the decay products is

$$|\chi(E)|^2 = \frac{1}{(E-M)^2 + \Gamma^2/4},$$

i.e. a Lorentz curve. It shows a peak at the invariant mass M of the decaying system with a full width Γ at half maximum. We claim the discovery of a new particle if we see a resonance with a confidence level at least 5σ at the same invariant mass of the particle in all expected decay channels, by all related experiments.

The search involves several consecutive steps as outlined already in Chapter 9.

- Compose a complete *standard model background* using Monte Carlo simulation taking into account all types of possible events normalized to their cross sections.

- Compose *Higgs-boson signals*, simulations of all possible production and decay processes at all possible Higgs-boson masses.

- Put all these through the *detector simulation* to get events analogous to the expected measured ones.

- *Optimize the event selection* via reducing the B background and enhancing the S signal via maximizing some figure of merit.

- *Check the background*, i.e. the description of data by the simulation for the given luminosity: the simulation should reproduce the observed background distributions in all details. For instance, you can check the background of the decay of a neutral particle to charged leptons by selecting lepton pairs of identical charges.

- *Check the signal:* does it agree with the expectation by the theoretical model?

Once we are happy with the simulations and the event selection, we must choose a test statistic. That could be any kind of probability variable characteristic of the given phenomenon: probabilities for having background only, signal or combinations. One of the favourite is the Q likelihood ratio of signal + background over background: $Q = \mathcal{L}_{s+b}/\mathcal{L}_b$. What most frequently plotted is

$$-2\ln Q(m_H) = 2\sum_{k=1}^{N_{\mathrm{ch}}}\left[s_k(m_H) - \sum_{j=1}^{n_k}\ln\left(1 + \frac{s_k(m_H)S_k(x_{jk};m_H)}{b_k B_k(x_{jk})}\right)\right]$$

where the variables are the following:

- n_k: events observed in channel k, $\quad k = 1\dots N_{\mathrm{ch}}$.

- $s_k(m_H)$ and b_k: signal and background events in channel k for Higgs-boson mass m_H.

- $S_k(x_{jk};m_H)$ and $B_k(x_{jk})$: signal and background probability distributions for events for Higgs-boson mass m_H at test point x_{jk}.

- x_{jk}: position of event j of channel k on the plane of its reconstructed Higgs-boson mass and cumulative testing variable, the latter constructed of various special features of the event like b-tagging, signal likelihood, neural network output etc.

Several other testing variables can be constructed on the same basis, rather frequently used ones are probabilities of *not* having the expected signal on the basis of the expected background and the collected data:

- CL_b, the signal confidence level assuming background only, i.e. the complete absence of the signal, or

- The so-called *p-value*: the probability of obtaining a test statistic at least as extreme as the one that was actually observed, assuming that the null hypothesis is true. Translated to our language that means the probability that a random fluctuation of the measured background could give the observed excess.

14.2   Exclusion at LEP

Although the four large experiments at the Large Electron Positron (LEP) collider saw no new physics, no deviation from the standard model, LEP provided an incredible amount of very precise measurements, some of which are presented in Fig. 17.33. In its last two years of working, LEP was mostly devoted to the search for the Higgs boson, collecting more luminosity at higher energies than in the previous 10 years together.

At LEP the dominant formation process is *Higgs-strahlung* e⁻e⁺→ZH (the name comes from the funny *English* word Bremsstrahlung[1]), the associated production of Higgs and Z bosons. The dominant Higgs boson decay at these low masses is to a b$\bar{\text{b}}$-quark pair (Fig. 17.34). The various channels are different only due to the various decay processes of the accompanying Z boson.

Statistics, the master of bad jokes at particle physics experiments (see the Foreword of [Patrignani et al., 2016]), have shown up at LEP as well: one of the experiments, ALEPH, saw in one of the possible Higgs decay channels a quite strong signal corresponding to a Higgs boson of a mass of 115 GeV, while the rest of LEP have not seen anything [Barate et al., 2003] (Fig. 17.36). ALEPH saw the excess in 4-jet events only, in those events where the Higgs boson decays to a pair of b quarks and the accompanying Z boson also decays to a quark pair (Fig. 17.35). The b quark is identified by its long lifetime leading to a secondary decay vertex in the event. Another strange thing was that the Higgs signal seen by ALEPH by far exceeded the expectations of the standard model. Also, the observed Higgs mass was critical as it coincided with the average kinematic limit of LEP: in 2000 the average collision energy of LEP was about 206 GeV and the observed resonance was found at 115 GeV, the difference was very close to the mass of the Z boson, 91 GeV.

A quite interesting feature of data analysis was the plotting of *spaghetti diagrams*. Those are signal weight distributions of each selected event as a function of the assumed Higgs mass. Fig. 17.37 shows the weight distributions of 17 selected Higgs-like candidate events observed by the four LEP experiments [Barate et al., 2003]. The ALEPH events crowd around 115 GeV whereas for the other three experiments there are less of them with a rather random mass distribution. This caused quite an excitement at LEP: many physicists signed the petition to the Director General of CERN to extend the life of LEP by another year, but that was refused: the simulated

---

[1]Other languages use the simple mirror translation of the German word: *braking radiation*

projections were not very promising for a discovery of the SM Higgs boson (the effect seen by ALEPH only was far too large, much higher than the prediction of the standard model), and the contractors for building the LHC were already prepared to start.

14.3   Search and observation at LHC

Figure 17.38 shows the cross sections of various production processes of the SM Higgs boson in p-p collisions at the LHC. The dominant reaction is gluon fusion, but vector boson fusion is also significant.

Just like LEP had, the Large Hadron Collider has also four interaction points (Fig. 17.7) with a major experiment (and sometimes a smaller one as well) in each. The two largest ones, ATLAS and CMS were designed with the main aim of discovering the Higgs boson, ALICE is specialized on heavy ion collisions and LHCb on studying rare processes involving b quarks. The authors belong to CMS, so most of the results we mention are from CMS, but all will be compared to those of ATLAS pointing out the similarities and the (very few and not significant) differences.

The ATLAS and CMS collaborations are really huge. According to the official statistics at the time of the Higgs discovery CMS had 3275 physicists (including 1535 students) and 790 engineers and technicians from 179 institutions of 41 countries (ATLAS was even somewhat larger). The largest participant of CMS is the USA, then Italy, Germany and Russia. It is quite remarkable how similar and different are ATLAS and CMS. ATLAS uses a lot of new detector techniques while CMS consists of mostly traditional parts. CMS is based on the largest superconducting solenoid on Earth whereas ATLAS has a smaller solenoid encircled by 8 huge magnets making a toroidal field. CMS is full of steel, it weighs 14000 tons, twice the weight of ATLAS in an order of magnitude smaller volume. The event triggering was also different, CMS developed a quite innovative, two-level trigger scheme, while the ATLAS trigger had three levels. And in spite of all these differences, the two collaborations got (and still get) very similar results, and that makes all their observations most reliable.

The design of the LHC and its experiments started well before the actual start of LEP, which means that the construction of the LHC detectors took two decades of hard work before the actual data acquisition started. The LHC devoted its first two years of operation to development rather than data taking, which really started in 2011 only.

Even before the LHC started, the parameter fitting of the standard model

had pointed toward a light Higgs boson with a mass around 100 GeV. As LEP excluded the Higgs boson below 114 GeV the LHC experiments had to be prepared for detecting the Higgs boson in the most complicated mass region, around 120 GeV, with several competing decay channels (Fig. 17.34). It is well seen that below 110 GeV the b$\bar{\text{b}}$ decay, above 160 GeV the WW dominates, that is why those mass regions could be excluded earlier. Theoretical calculations have shown that the best channels to observe a light Higgs boson at the LHC should be the two-photon, H→$\gamma\gamma$ and four-lepton, H→ZZ*→$\ell^+\ell^-\ell^+\ell^-$ channels. The hadronic decay channels are hampered by the very high hadron background. However, these signal channels have very low branching ratios, for H→$\gamma\gamma$ it is BR = 2.27×10^{-3} and the signal/background ratio is small, $S/B \ll 1$, and for H $\to$ ZZ$^* \to \ell^+\ell^-\ell^+\ell^-$ (as usual, ℓ = e, μ, i.e. in the experiment only the electron and the muon are considered leptons, because the taus can decay to hadrons as well) it is even lower, BR = 1.24×10^{-4}, but with a much cleaner signal, S/B > 1. In 2012 the LHC luminosity was already so high that every bunch crossing (event in every 50 ns) contained 10–20 p-p collisions leading to copious hadron production. Both large experiments, CMS and ATLAS designed their tracking systems and electromagnetic calorimeters with these two processes in mind. The electromagnetic calorimeter of CMS consists of 75,848 PbWO$_4$ single crystal scintillators, whereas that of ATLAS is a sampling calorimeter based on liquid argon shower detectors.

By the beginning of 2012, when all 2011 data were analysed, the possible mass of the SM Higgs boson was already confined to the region of 114 < M_H < 127 GeV by CMS with very similar results from ATLAS. In that region 2– 3 σ excesses were found at $\simeq$125 GeV in the two main decay channels, H →$\gamma\gamma$ and H → ZZ. It seemed more and more probable that the Higgs boson would be observed at the LHC in 2012. It was even decided by the CERN administration to extend the data taking scheduled for 2012 before the long shutdown for accelerator development (for increasing its p-p collision energy from 8 to 13 TeV and the event rate from 20 to 40 MHz) if necessary for the discovery.

On July 4th, at the beginning of the large annual high-energy physics congress in Melbourne, the spokespersons of ATLAS and CMS gave talks from CERN (in internet connection to the whole word, including, of course, the main auditorium of the Australian conference) on Higgs search. They announced that at the LHC collision energies 7 and 8 TeV, in the two most significant decay channels H → $\gamma\gamma$ and H → ZZ → $\ell^+\ell^-\ell^+\ell^-$, at an invariant mass of $m \simeq$ 125 GeV a new boson is seen by both experiments at a convincing statistical significance of 5σ confidence level, with properties

corresponding to those of the standard model Higgs boson. The fact that the new particle could decay to two photons or Z bosons confined its spin to an even integer, i.e. a boson of $S = 0$ or $S = 2$. Of course, as the data analysis was optimized to find the SM Higgs, it was very unlikely to find something very different. Nevertheless, the two experiments emphasized that it has to be studied, whether or not its spin is really zero with a + parity (the pseudo-scalar mesons have spin 0 with negative parity), and that its decay probabilities to various final states follow the predictions of the standard model. After reanalysing their data the Tevatron experiments, CDF and D0 also found an excess at this mass (after the LHC started the Tevatron accelerator of Fermilab was stopped).

14.3.1 Reactions of the media

The saying that *three people can keep something secret only if two of them are dead* is attributed to Benjamin Franklin. As any result of a collaboration has to be approved by all members before it is made public, the more than 6000 participants of ATLAS and CMS knew well in advance the developing result. Thus two days before the 4th July announcement *Nature Online* already reported the discovery. Of course, the fact that the CERN management invited to the seminar all leading scientists of the field, including the theoreticians who developed spontaneous symmetry breaking for the standard model, also helped people to guess that something dramatic would be announced.

CERN produced some figures concerning the media echo of the day: 55 media organizations were represented at the talks of 4 July. The talks were broadcasted via close to half a million internet connections (many of them being conference rooms in partner institutions, 1034 TV stations devoted 5016 news broadcasts to the event for more than a billion (10^9) people. Many-many news articles and even more blogs and talks discussed the conditions and importance of the discovery.

14.3.2 Observations

On 31 July the two experiments submitted papers of the discovery to Physics Letters B, they were published 14 August. Both papers, [Aad et al., 2012] and [Chatrchyan et al., 2012b], were 15 pages long followed by 16 pages long lists of close to 3000 authors, and both were dedicated to the memory of those participants who could not live to see the result of the more than two decades of construction work. Their measured mass distributions, after analysing about a quarter of the data to be collected in 2012, are shown in

Figs. 17.41 and 17.42. The mass distributions of the di-photon and 4-lepton decay channels were quite similar for the two experiments. They showed a significant peak at the same invariant mass of about 125 GeV. In all cases the signal strengths agreed within uncertainties to the predictions of the standard model.

What was really convincing of the observation was the distribution of the p-values of the events selected in the various decay channels of the hypothetical Higgs boson. It was a joke of statistics that in July 2012 adding together two decay channels, H $\rightarrow \gamma\gamma$ and H $\rightarrow 4\ell$ gave the same 5σ significance for both ATLAS and CMS, whereas adding to it the results for other channels increased the significance to 6σ for ATLAS and left it at 5σ for CMS (Fig. 17.42).

14.3.3   Is it really the Higgs boson?

Analysing most of the data collected in 2012 confirmed the existence of the new boson and led to the conclusion that all observed properties of the newly discovered particle were close to those predicted for the Higgs boson of the standard model within statistics. All these results were further confirmed by the LHC data collected in 2016-17 at higher energy (13 TeV p-p collisions) and much higher luminosity. The corresponding 4-lepton and 2-photon spectra are presented in Figs. 17.43 and 17.44.

The fact that the new boson decays to two photons points to its having spin 0 or 2. The charged lepton spectra bore the features of its having $S = 0^+$ as ascertained by both experiments. The measured signal strengths of the new particle were fully compatible with that expected for the standard model Higgs boson: for CMS it was ~ 20% less while for ATLAS ~ 40% more than the SM prediction, but both deviations were within the experimental uncertainties. As a theoretician remarked, whenever ATLAS had an excess CMS came up for everybody's annoyance with a deficit, bringing the average close to the SM prediction.

The final analysis of the 2012 data resulted in a joint mass value by ATLAS and CMS as [Aad et al., 2015]

$$m_H = 125.09 \pm 0.21(\text{stat}) \pm 0.11(\text{syst}) \text{ GeV} .$$

The LHC experiments studied the cross sections of the processes connected to the new particle. Fig. 17.45 shows the signal strengths of production and decay in various possible channels of the Higgs-like boson measured by CMS [Chatrchyan et al., 2013] as compared to those predicted by the standard model for the Higgs boson with a mass of 125 GeV. The amplitudes of

all observed signals are in agreement with the expectations of the standard model. ATLAS got similar results, of course.

Thus what we found is most likely the standard model Higgs boson. On one hand this is a great success of particle physics. On the other hand this is somewhat of a disappointment as the SM has theoretical shortcomings which need new physics to resolve. Just to list a few of them: it cannot unite the interactions at large energies, cannot include gravitation, cannot account for the dark matter of the Universe or for the dominance of matter against antimatter, and cannot explain neutrino masses and oscillations. There are many extensions of the theory, that can resolve some of those problems, most popular among them is *supersymmetry*, which among other things predicts 5 kinds of Higgs bosons, but none of its predicted phenomena could be found yet experimentally. The observables of the Higgs boson should be sensitive to some of the features of new physics and these studies will be the main job of the LHC experiments in the future.

Right after the confirmation of the discovery, in 2013 *François Englert* and *Peter Higgs* were awarded the Nobel Prize in physics.

It is very interesting that the 125 GeV mass of the Higgs boson seems to be exciting for theoreticians. There was even a special workshop in Madrid organized to discuss this mass in 2013. The reason is that $m_H = 125$ GeV is at the border line of the stability of electroweak vacuum on the plane of top mass against Higgs mass.

14.4   Vacuum stability

Let us recall that in the standard model the potential of the symmetry-breaking BEH field is $V(\phi) = \mu^2|\phi|^2 + \lambda|\phi|^4$ where the second term with $|\phi|^4$ is the self-interaction of the field with a strength depending on λ.

The observation of the Higgs boson at mass 125 GeV proved that the vacuum of our world has a non-zero minimum potential value. The strengths of all interactions depend on the energy of interaction, at LHC energies and at $m_H \simeq 125$ GeV $\lambda \simeq 0.13$. Well before the introduction of the BEH potential it was stated that the coupling of a self-interacting scalar field (λ in this case) can change sign at high energies, which is called *vacuum instability*. The question is, of course, at what energy we can expect this sign change. This energy dependence is affected by the interaction of the field with all particles. As the t quark has the largest mass, hence highest interaction potential with the BEH field, it has the largest effect on λ.

In certain conditions several BEH minima could exist [Lee and Wick, 1974].

If the BEH vacuum has one minimum only, our vacuum is stable, if it has more, then it can be metastable. If our vacuum is metastable and we are not in the deepest minimum, then the universe exist in a *false vacuum*, and the world can shift into the deeper one by a quantum mechanical tunnelling effect. In some sense it could be the end of our world as we know it. At the new BEH minimum all the particles would have different masses and also the strength of the weak interaction would change. Of course, this assumes that the standard model is valid up to extreme high energies. As Turner and Wilczek stated in 1982 [Turner and Wilczek, 1982], even if our vacuum is metastable, its expected lifetime could be much longer than the age of the Universe, hence appear stable to us.

These estimations were refined in time and as the mass of the Higgs boson became definite, it became clear that our world is located somewhere at the edge of stability. Fig. 17.46 shows such an estimation, presently most precise in the standard model. The location point of the measured masses of the Higgs boson and of the t quark fall in a narrow metastable region.

14.5   BEH field and inflation

According to the generally accepted model of cosmology our world was born in a *Big Bang*. The theory has many shortcomings and for their solution *Alan Guth* proposed the model of *inflation*, according to which the space of the Universe in the first 10^{-32} second expanded by 10^{20}–10^{40} times. This needed a force field called *inflaton* which had to disappear after the inflation. There are many speculations about its nature, here we quote one connected to the Higgs boson. *Bezrukov* and *Shaposhnikov* [Bezrukov and Shaposhnikov, 2008] have shown that the BEH field is a suitable candidate for that assuming that its ξ coupling to gravity is strong enough. Then the Lagrangian of the standard model should be completed by $-\frac{1}{2}M^2R - \xi H^\dagger H R$, where R is the gravitational space curvature and H is the strength of the BEH field. M is a mass-like parameter, less than the Planck mass related to the gravitational constant, $0 < M < M_\mathrm{P} = 1/\sqrt{8\pi/G} \simeq 2.4 \cdot 10^{18}\,\mathrm{GeV}$. $M = M_\mathrm{P}$ should result in too high initial density fluctuations, and $M = 0$ in too large Higgs boson masses. Subsequent estimation showed that the Higgs boson should be light, $m_\mathrm{H} < 135\,\mathrm{GeV}/c^2$ for the model to function. From the demand that the instability of the BEH field coupled to gravity, started at the Planck scale only, *Shaposhnikov and Wetterich* [Shaposhnikov and Wetterich, 2010] *predicted* $m_\mathrm{H} = 126\,\mathrm{GeV}/c^2$. Of course, this assumes that the standard model is valid

up to the Planck scale. If below that energy some new physics starts, the picture is invalid.

Thus we do not have to be afraid that our Universe shifts into another vacuum. At the same time we see another excellent feature of the BEH mechanism: it could explain the cosmic inflation without assuming another force field. Apparently we get more and more proof for Lederman's joke that the Higgs boson and the BEH mechanism remind him of the *deus-ex-machina* in the Greek-Roman dramas, that puts everything in order.

Exercise 14.1
Why do we need symmetry breaking in order to create masses? Why does the existence of the Higgs boson prove the validity of the symmetry breaking mechanism?

Exercise 14.2
Why do we need such overly sophisticated statistical methods like $-2\ln Q$ or the p-value in order to exclude or discover new physics?

Exercise 14.3
Why do hadron colliders have higher chance to discover new physics in spite of the more difficult data analysis requirements than the electron-positron colliders with their much cleaner events?

Exercise 14.4
What reactions helped to discover the Higgs boson at the LHC? Why those decay channels were used which have the lowest yields?

Exercise 14.5
How can we tell that the Higgs-like signal observed at the LHC belongs to the Higgs boson predicted by the standard model?

Chapter 15

Heavy ion physics

MOTTO:

"It seems very pretty, ... but it's RATHER hard to understand! ... Somehow it seems to fill my head with ideas — only I don't exactly know what they are!"

(Lewis Carroll: Through the Looking Glass)

15.1   Quark gluon plasma

The basic idea of heavy ion physics is to reproduce and study the properties of matter right after the Big Bang. That extremely hot matter is assumed to have been a soup of de-confined quarks and gluons, the *quark gluon plasma*.

Figure 17.47 shows a simulated collision of heavy ions. As they are accelerated to high energies, they are relativistic. In the direction of the beam the ions are Lorentz-contracted, which also increases the density and temperature of the plasma. The fire ball will expand and cool down, and the quarks hadronize, form colourless hadrons that can be detected experimentally. Most of the components and also the hadrons formed in the collision will fly forward. If a new particle forms and decays in the soup, it will decay in more-or-less its own centre-of-mass system and emit its decay products in all directions. Thus what is really interesting should fly to some extent

perpendicularly to the colliding beams. Let us recall the definitions of *transverse momentum*, $p_T = \sqrt{p_x^2 + p_y^2}$ and *pseudorapidity*, $\eta = -\ln \operatorname{tg}\frac{\theta}{2}$. The latter is used instead of polar angle at hadron colliders. These variables have important use in heavy ion physics.

Note that in heavy ion physics the reaction yields are determined by the energy of the individual nucleon-nucleon collisions and not by the total energy of the projectiles, so it expresses the collision energies in units of GeV/nucleon pair (GeV/NN) or at LHC energies TeV/NN. Thus, when protons are accelerated to 3.5 TeV on each side, the total energy of p-p collisions will be 7 TeV, whereas in the case of Pb-Pb collisions its characteristic energy will be 2.76 TeV/NN.

Generally speaking, heavy ion physics is very much related to quantum chromodynamics as it treats quasi-free, interacting quarks and gluons. Citing the recent review [Busza et al., 2018]: "Heavy ion collisions are a laboratory that is rich with unique ways to probe fundamental aspects of QCD empirically, with some control over varying conditions." According to the theory of heavy ion collisions, the appearance of the quark-gluon plasma, as a phase transition, should be characterized by the following experimental signatures:

- *High pressure* in the medium, increasing p_T of the released particles.

- *Jet quenching*: As the medium becomes coloured, the stopping power for coloured particles increases, quarks and gluons have difficulties getting out of the system, so the number of detected jets should be reduced.

- *Low-viscosity liquid*: The quarks and gluons move quasi-free reflecting to some extent the original nucleon-like *lumpiness* of the system, which at higher viscosity should even out.

- *Direct photons*: With the appearance of quasi-free quarks the medium contains fast decelerating charged particles that should radiate high-energy direct photons, similarly to ordinary *bremsstrahlung*.

- *Effective hadron masses*: In the high-temperature plasma the chiral symmetry is partially restored, heavier quarks become lighter, so the identified heavy mesons should have lighter masses .

- *Debye screening*: When the colour content of the medium becomes generally large because of release of quarks and gluons, that will decrease the binding energy of individual hadrons. This will lead
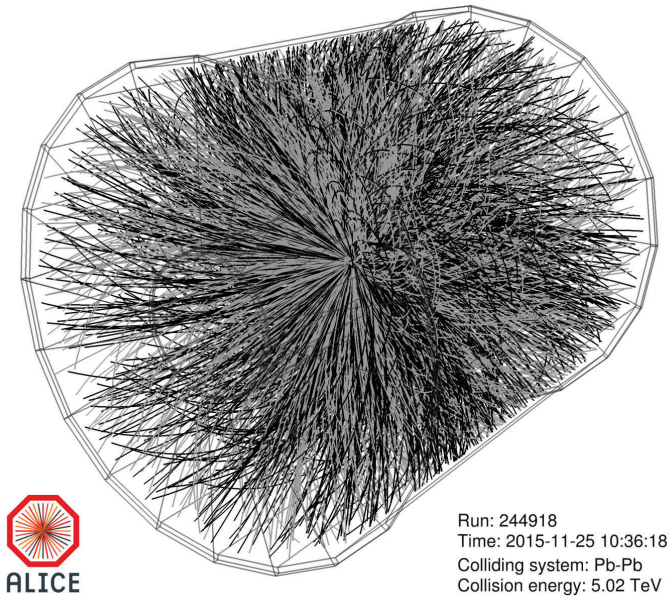
Figure 15.1: Lead-lead collision event at LHC energy of 5.02 TeV per nucleon pair recorded by the time projection chamber of the ALICE detector in November 2015. In this collision 1582 positively-charged (darker tracks) and 1579 negatively-charged (lighter tracks) particles are produced; about 80 % of them are pions

to such effects as the break-up of heavy hadrons, like the reduced detection of J/ψ = (c$\bar{\text{c}}$) mesons.

15.2 Hydrodynamics

As mentioned above, due to the low internal viscosity of the quark gluon plasma its partons move almost free. If their interaction were stronger, the system could not possibly remember its structure before the collisions, but it does: hydrodynamics converts spatial anisotropies into momentum anisotropy. Another characteristic feature is the elliptic flow. The centrality (related to the overlap) of the nuclei in nucleus–nucleus collisions (see Fig. 15.2) is rarely perfect. If the newly formed quark matter were gas-like
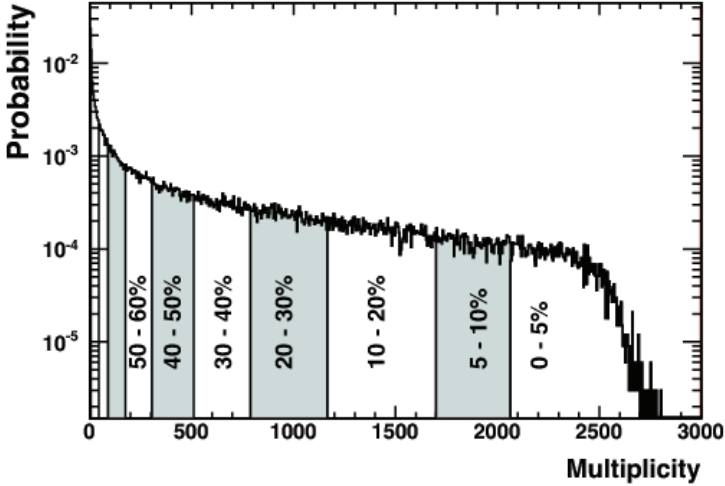
Figure 15.2: Centrality regions and charged particle multiplicities in Pb-Pb collisions at 2.76 TeV/nucleon-pair energy measured by ALICE [Aamodt et al., 2010]. Note that 0 % corresponds to the highest centrality. Regions 60–70 % and 70–80 % are not labelled

then it should expand in all directions with the same momentum. However, it seems to behave as an almost perfect liquid and expands elliptically (Fig. 17.47). This azimuthal anisotropy in particle production can be quantitatively characterized by the *elliptic flow*, the coefficient v_2 of the second term in the Fourier transform of the angular distribution of measured (charged) particles:

$$\frac{d\overline{N}}{d\phi} = \frac{\overline{N}}{2\pi} \left(1 + 2 \sum_{n=1}^{\infty} \overline{v}_n \cos\left(n(\phi - \overline{\psi}_n)\right) \right). \qquad (15.1)$$

The observables are the following: ϕ is the angle in the transverse plane, $\overline{\psi}_n$ are the event plane angles (where the nth harmonic component has its maximal track multiplicity) and $\overline{N}$ is the average number of particles per event. They can be measured for different particle species as functions of rapidity, centrality and transverse momentum. v_2 is the elliptic flow reflecting two-parton correlations in the quark gluon plasma. Higher correlation coefficients can also be measured and calculated. Useful quantities are also the event-by-event values of these data, not only the averages.

Elliptic flow is one of the most important measured quantities in heavy

ion physics as it can be predicted theoretically using various hydrodynamic models.

15.3 Experiments

For heavy ion experiments the main problem is to follow and identify the thousands of emitted particles (Fig. 15.1). The detectors of heavy ion physics look very similar to those in high-energy particle physics: a large magnet, a vertex detector closest to the beam pipe, an inner tracker, usually a chamber encircled by electromagnetic and hadronic calorimeters, and muon detectors outside. The experiment specialized on heavy ion physics at LHC, ALICE (A Large Ion Collider Experiment) sacrificed data acquisition speed for precision: it has the largest existing time projection chamber (TPC, see Chapter 7) around its beam pipe, which helps to follow and identify thousands of particles, but cannot handle the amount of luminosity ATLAS and CMS accept with their semiconductor tracker systems. ALICE was placed in and around the huge magnet of the former LEP experiment L3. Fig. 15.2 shows the correlation between centrality and particle multiplicity measured by ALICE at 2.76 TeV/NN [Aamodt et al., 2010].

The measuring apparatus of the fixed-target NA49 experiment, now continued as NA61 (NA stands for North Area of SPS and the number is a sequence number of accepted experimental proposals) also based on TPC's. It mapped the transition from ordinary nuclear matter to quark-gluon plasma by comparing the following reactions from the point of view of particle yields:

- Pb+Pb collisions at 158, 80, 40, 30, 20 GeV/NN;

- C+C, Si+Si collisions at 158 and 40 GeV/NN;

- p+Pb, p+C, p+p and n+p at 158 GeV/NN;

- π+p and π+Pb also at 158 GeV/NN.

They had a beam of 10^5 Pb-ion/sec in about 1 mm diameter at 158 GeV/NN and typical event multiplicities of more than 1500 charged hadrons in every collision.

Another place of heavy ion experiments is RHIC, the Relativistic Heavy Ion Collider at Brookhaven National Laboratory, USA. RHIC accelerates two beams of copper and gold ions and collides them at several interaction points. Its two largest experiments are PHENIX and STAR. The RHIC

experiments were the first to demonstrate the transition from nuclear matter to quark matter by detecting jet quenching in central Au+Au collisions as compared to proton-proton, proton-Au, deuteron-Au events and peripheral Au+Au collisions. In the case of peripheral collisions most of the nucleons will avoid collisions and just shoot along the beam pipe. In the case of central collisions there is a large activity in the transverse directions, which is easily measured by the cylindrically built detector systems. Every heavy ion experiment has a *zero degree calorimeter*, a detector close to the beam pipe, in order to check the centrality of the collisions by detecting the forward-scattered particles and also for measuring the total number of collisions, the luminosity.

15.4   Jet quenching

The observation of jet quenching was a real break-through in heavy ion physics as it proved that at high enough energies the quarks are released from the nucleons and the matter becomes all coloured in a volume much larger than the size of the nucleon.

In Fig. 17.48 RHIC results are shown. The π^0 yield observed by the PHENIX experiment (Fig. 17.48, upper) from central Au+Au collisions is suppressed as compared to the d+Au collisions of minimum bias, i.e. at minimal selection criteria [Adler et al., 2003]. In other spectra PHENIX has shown how the suppression depends on the energy and collision centrality. The suppression of neutral pions proves that this is not a Coulomb effect, but the result of the coloured medium.

The STAR experiment made a very similar discovery (Fig. 17.48, lower). They measured the azimuthal angles of tracks in the events taking $\phi = 0$ at the track with the largest p_T for 2-jet events in d+Au and Au+Au collisions [Adams et al., 2003] for *minimum-bias* events. In central Au+Au collisions the track with the highest p_T will more probably come from $2 \rightarrow 2$ collisions near the surface of the fireball. Then the other particle produced in the collision flies in the opposite direction. As it has to traverse thicker coloured medium, it is more likely stopped inside the fireball. There is no such effect in d+Au collisions. This was observed at the very beginning of RHIC and published in 2003. All RHIC experiments saw similar effects both with neutral and with charged hadrons, and have shown the formation of coloured matter in high-energy heavy-ion collisions.

15.5 Heavy ions at LHC

At the end of every p+p run (usually lasting 6–8 months) the LHC collides heavy ions for a few weeks. There were Pb+Pb runs at the maximal LHC-energies, but there were also p+Pb collisions and p-p runs at lower energies (corresponding to the per-nucleon-pair energies of heavy ions) to establish reference measurements for the interpretation of the Pb+Pb data. There was also a Xe–Xe run at the end of 2017.

At the low-luminosity start-up of LHC, ALICE could handle the p+p collisions very well and produced the first paper with LHC results, a test of QCD at high energy. It made many measurements with heavy ions later.

We saw that the RHIC experiments had observed the one-sided suppression of the tracks of two-jet events from central collisions of heavy ions as compared to those from collisions with protons or deuterons. This was interpreted as quenching of partons going through the bulk of the coloured quark matter. At the LHC ATLAS reproduced this result (Fig. 17.49) with the observation of direct event-by-event jet quenching [Aad et al., 2010].

The natural reference for determining the effect of the coloured medium on the observables is the nuclear modification factor,

$$R_{AA}(p_T) = \frac{dN_{AA}/dp_T}{< N_{coll} > dN_{pp}/dp_T}$$

where $< N_{coll} >$ is the average number of colliding nucleons, N_{AA} and N_{pp} are the numbers of events selected for AA and pp collisions and p_T is the transverse momentum. The effect of the nuclear medium is demonstrated in comparison of peripheral and central p-p and Pb-Pb collisions by the CMS experiment [Chatrchyan et al., 2012a] (Fig. 17.50). CMS also observed an interesting new effect on particle correlations: apparently the degree of two-particle correlations increases with the event multiplicity, the number of tracks in the event.

15.6 Big questions

In spite of the great wealth of data collected at SPS, RHIC and LHC there are several open questions [Busza et al., 2018] in heavy ion physics. How does a strongly coupled liquid emerge from an asymptotically free gauge theory? How can the quark-gluon-plasma behave as a freely flowing liquid with strong coupling among its constituents? How could such a liquid form within 1 fm/c? What are the limits of the applicability of hydrodynamics in heavy ion collisions?

Exercise 15.1
Why pions dominate the hadron jets?

Exercise 15.2
What is the importance of the transverse momentum of jets and collision centrality in heavy ion collisions?

Exercise 15.3
What are the characteristic features of the transition of nuclear matter into quark-gluon plasma?

Exercise 15.4
What are the advantages and disadvantages of using time projection chambers for studying heavy ion collisions?

Exercise 15.5
Deduce how one gets $2.76\,GeV/NN$ collision energy at colliding $3.5\,TeV$ Pb beams. At what beam energies one gets $2.76\,GeV/NN$ for Pb-Pb collisions in the case of a fixed Pb target?

Chapter 16

Practical applications

MOTTO:

Prediction is very difficult, especially about
the future.

(Niels Bohr)

Particle physics is, of course, basic research, driven by the curiosity of
the researchers. However, as shown in this chapter, its spin-off has proven to
be extremely useful for the general society. In general one can state that any
kind of basic research can bring applications in the long run, even if we do
not know exactly how and when.

16.1   Informatics

The experiments at high-energy accelerators generate large amount of data.
At the LHC more than 10 PB data are recorded every year. Special techniques
were and are developed to handle them. Some of these techniques have found
already their ways into society.

16.1.1 World Wide Web

The first and probably most important example is the *World Wide Web*. It was invented and first developed by Tim Berners-Lee and his group at CERN in 1989-90. As presented in the CERN museum, his boss in 1989 wrote on the original proposal *Vague but exciting*. Tim Berners-Lee wrote in 1991: *"The WWW project was started to allow high energy physicists to share data, news, and documentation. We are very interested in spreading the web to other areas, and having gateway servers for other data."* First, of course, it was used at HEP laboratories like Stanford, Fermilab and at the associated universities, but in 1992 CERN announced that anybody can use the Web free of royalty and the platform-independent Mosaic browser was opened for the public: that began such an information explosion in the world that seems to surpass even Gutenberg's printing. Since Mosaic many browsers have been developed and a lot of features added. Of course, with time the Web became commercial as more and more companies use it for trading, but it retains its completely free access established by CERN. Thus the free use of the internet browsers is due to particle physics research. We mean free in the monetary sense. Internet providers recognized quickly that information is a new source of wealth and they collect information from their users

16.1.2 Grid computing

At the start of designing the LHC it was clear that it would become impossible quickly to store and analyse all its data at CERN, so CERN established its *Worldwide LHC Computing Grid, WLCG*. The experimental data at LHC are analysed in several steps, in a distributed manner. The WLCG consists of tiers. The centre, called Tier-0, is located at CERN and in the Wigner data centre in Budapest. It receives the primary data from the LHC. After a preliminary event reconstruction the data are distributed to the Tier-1 data storage centres, for instance these stations of CMS are located in Lyon, Barcelona, Oxford, Bologna, Karlsruhe, Fermilab (near Chicago) and Taipei. The actual data analysis is done at about a hundred Tier-2 computer centres which get their data from the Tier-1 storage stations. This system was developed by CERN for the LHC, but it helps other applications as well. For a few years CERN helped to establish MammoGrid, a virtual organization for diagnosing breast cancer.

16.1.3 Computer simulation

For the detection and interpretation of new physics at high-energy particle collisions need elaborate Monte Carlo techniques. The experience in programming in general and in simulation methods in particular, that young scientists learn by the time they obtain their degrees can be used in other fields as well. Several researchers with PhD-s in high-energy physics went to work in the insurance or banking sectors to make financial and industrial forecasts using simulations. CERN has developed the GEANT general simulation program package [Agostinelli et al., 2003] which is now widely used, far outside high energy physics.

16.2 Radiation

Some of the discoveries in particle physics were immediately used in practice, mostly in medicine. Wilhelm Röntgen discovered the X-rays in 1895 and used it right away to photograph the bones in his wife's hand. He refused to patent the X-rays as he realized its enormous significance for the society. In 1901 Röntgen was awarded the very first Nobel Prize in Physics, which he donated to his university.

Henri Becquerel discovered natural radioactivity in 1896, which was followed the separation of radium by Pierre and Marie Curie in 1898, the three of them were awarded the 1903 Nobel Prize in Physics. As early as in 1902 radioactive irradiation was already used in Stockholm for local tumour therapy.

16.3 Accelerators

There are nearly 40 000 particle accelerators in operation worldwide, about half of them employed for biomedical uses and the other half in industry (for surface treatment and to produce microchips). These days less than 200 accelerators are used for particle and nuclear research.

The first cyclotron was created in Berkeley by Ernest Lawrence in 1930, it was as small as his palm. This was followed by larger and larger machines (Fig. 17.51) and Lawrence was awarded a Nobel Prize in physics in 1939. His brother, John Lawrence, a physician, also worked at Berkeley and in 1936 together they produced phosphorus-32 and used it as the first artificial radioactive isotope for treating leukaemia. This is an excellent example of how an interdisciplinary environment helps both science and applications.

The neutron was discovered by James Chadwick in 1932 (Nobel Prize, 1935) and since then it is used to form artificial radioactive isotopes. In 1934 an Italian group led by Enrico Fermi (Nobel Prize, 1938) created 50 new radioactive isotopes (including those of iodine, very popular in medicine) using slow neutrons.

The linear accelerator was invented by Wideroe in 1927, and the first modern linac was built by Alvarez in 1946. Electron linacs are used in hospitals worldwide, see Fig. 17.51.

16.4   Medical diagnostics

The particle detectors are more than eyes for particle physicists, they became irreplaceable in medical diagnosis as well. The multiwire proportional chamber invented by Georges Charpak in 1968 (Nobel Prize, 1992) not only made a revolution in experimental physics, it also started very serious applications in everyday life. Its faster image registration means also lower radiation doses for the studied tissues. When they are combined with tomography (Fig. 17.52, right) they can produce a 3-dimensional picture of the inner organs.

Here we just list some of these methods in medicine.

- *Magnetic resonance imaging (MRI)* is based on the nuclear magnetic resonance method and gives morphological information by measuring the density of water (actually, of hydrogen in various molecules) in the tissues. More than simple morphology it can give information even on the operation of organs.

- *Technetium-99m* ("m" stands for metastable, its lifetime is $\tau = 6$ h) can be produced by irradiating molybdenum by slow neutrons:

$$^{98}\text{Mo} + \text{n} = ^{99}\text{Mo} + \gamma$$

$$^{99}\text{Mo}(\tau = 66\text{h}) = ^{99\text{m}}\text{Tc}(\tau = 6\text{h}) + \text{e}^- + \overline{\nu}_\text{e}$$
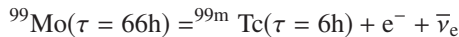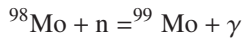
and the ^{99}Tc isotope emits a 0.14 MeV photon. 85% of the nuclear medical diagnoses use this isotope.

- *Positron emission tomography* (PET) uses proton-bombarded glucose to produce Fluoro-Deoxy-D-Glucose (FDG): proton absorption makes ^{18}F of ^{18}O. ^{18}F emits positrons and their annihilation tells us the location of the glucose. The glucose metabolism of the tumours is much faster than that of healthy tissue, so the tumours will appear as hot spots of the tomography picture (Fig. 17.52).

16.5   Medical therapy with radiation

There are three kinds of radiotherapy used to cure various kinds of cancer:

- *Teletherapy* or external beam radiotherapy is the most common form of radiotherapy. The patient sits or lies on a couch and an external source of radiation is pointed at a particular part of the body. Most frequently, X-rays of keV energies are used for treating skin cancer and superficial structures and MeV X-rays are used to treat deep-seated tumours. Electron beams are also used, but nowadays hadron therapy (with protons or carbon ions) is spreading more.

- *Brachytherapy* is internal radiotherapy or sealed source radiotherapy. It is the type of radiotherapy when radioactive sources are put straight into the tumour to be destroyed. Fig. 17.53 shows the treatment of prostate cancer with Brachytherapy. About 100 radioactive seeds, pins with radioactive isotopes are placed into the tumour. The positions of the seeds are continuously checked with an ultrasound probe.

- In *radio-immunotherapy* the radioactive isotope is carried by a molecule aimed at the organ to be cured. In cancer therapy, an antibody specific for a tumour-associated antigen is used to deliver a lethal dose of radiation to the tumour cells. For instance, α particles from Bismuth-213 are used for leukaemia, while electrons from the *beta* decay of Yttrium-90 for glioblastoma (a kind of brain tumour).

16.5.1   Teletherapy

The main problem of teletherapy is that the irradiation is not selective, it destroys tissue not only in the tumour, but also that around it. In the case of X-rays several beams are used from different directions with collators (Intensity Modulation Radiation Therapy, IMRT): using computer simulations the crossing beams are shaped to minimize the dose in the healthy organs at risk. Fig. 17.54 shows a simulation of a 3-dimensional conformal radiation therapy, in which the profile of each radiation beam is shaped to fit the profile of the target using a multi-leaf collimator and a variable number of beam shots. Note that the radiation dose is most commonly measured in absorbed radiation energy per unit mass: 1 Gy = 1 J/kg.

Another modern way of applying conformal radiation therapy is *tomotherapy*: the accelerator rotates around the patient with changing collimators. The *gamma knife* uses hundreds of ^{60}Co sources for local operation

of brain tumours or arteries. The *cyber knife* is similar, but uses X-rays from an electron linac (Fig. 17.54).

There is a way to prevent *loosing* cancerous tissue during operations, which can cause metastasis, achieved by electron irradiation of the tumour area during operation. Usually electrons of 3–9 MeV energy are applied for a couple of minutes delivering a dose of about 10 Gy.

16.5.2   Hadron therapy

All these teletherapies hurt the tissue around the tumour, especially at entering the body. This can be minimized using *hadron therapy*. Charged particles lose most of their energy at the end of their flight path (see the *Bragg curve*, see Fig. 17.55). This makes it advantageous to use protons and carbon ions to irradiate tumours. With careful planning one hardly hurts the healthy tissue and destroys the tumour.

As shown in Fig. 17.55 the apparatus for proton therapy is rather sophisticated and expensive. More than that, it needs a proton or heavy ion synchrotron to provide the ion beam. Nevertheless, many developed countries have such facilities in hospitals. There are dozens in the USA, Europe and Asia. Hadron therapy can be made much more cost-efficient with compact proton synchrotrons, one for each gantry without sophisticated beam lines. There exist designs for such *tabletop* accelerators.

16.5.3   Neutron therapy

Slow neutrons can easily be captured by nuclei and cause very high local dose deposits. The depth can be modulated by irradiation with neutrons of varying energy. As early as in 1936 (just four years after the discovery of the neutron) G. L. Locher suggested to use neutrons for cancer treatment by putting such nuclei in the cancer cells which undergo nuclear fission after neutron absorption and release a lot of local energy. For that the ^{10}B boron isotope seems to be ideal as it absorbs neutrons, its fragments are not tissue unfriendly and its chemistry is well know. The problem is that it is hard to bring it selectively into the tumour.

16.6   Conclusion

We see that particle physics offers useful methods to many other fields of science, especially to informatics and medicine. For the latter physicists, engineers and medical doctors should closely work together. Thus particle

physics brings not only new knowledge about Nature, but also useful new techniques and technologies.

Exercise 16.1

Why was the World Wide Web developed for particle physics?

Exercise 16.2

What is the advantage of hadrons to photons (X- or γ-rays) for cancer therapy?

Exercise 16.3

Why should we prefer to use protons and carbon ions for hadron therapy to other nuclei?

Chapter 17

Coloured figures

MOTTO:

Colour in certain places has the great value of making the outlines and structural planes seem more energetic.

(Antoni Gaudí)
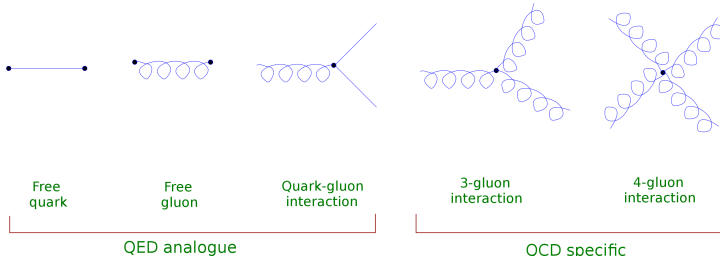
Figure 17.1:
Graphic picture of the Lagrangian of quantum chromodynamics (QCD)
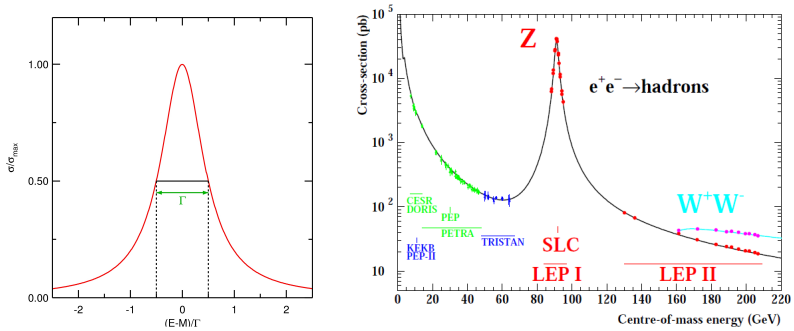
Figure 17.2: Resonance curves. Left: Breit-Wigner resonance curve: normalized cross section against centre-of-mass energy. Right: The Z-resonance: hadronic decay cross section against centre-of-mass energy as measured in high-energy electron-positron collisions
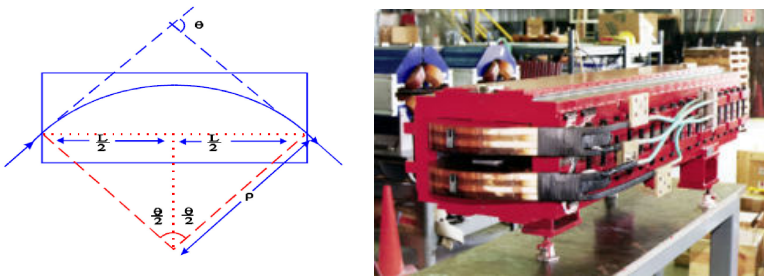
Figure 17.3: Left: Bending of charged particles in a dipolar magnetic field. Right: a dipole magnet, with two (blue) quadrupoles in the back
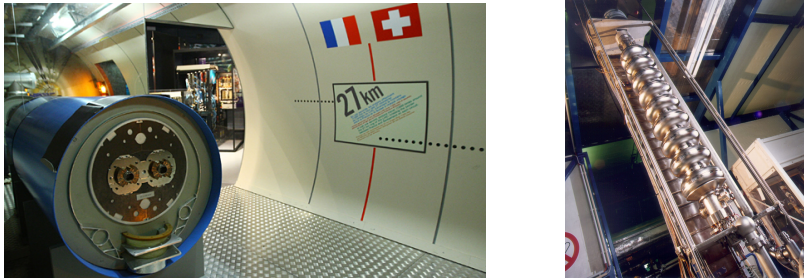
Figure 17.4: Left: Cross section of a dipole magnet of the Large Hadron Collider. Right: Microwave resonator to accelerate electrons for the TESLA project at DESY, Hamburg
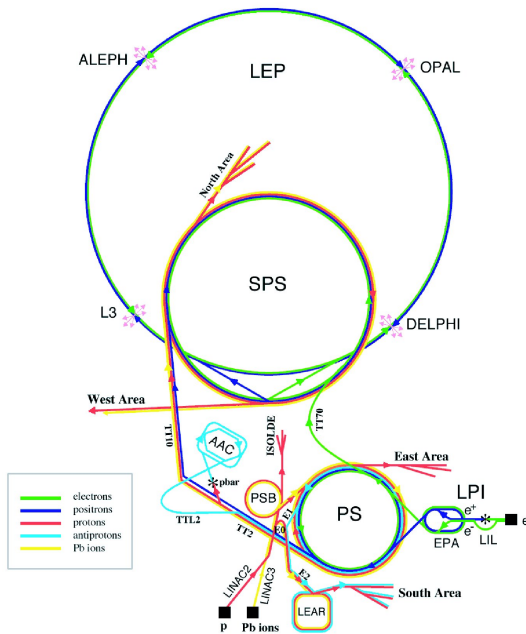
Figure 17.5: The accelerator complex of CERN in the LEP era. LEAR: Low Energy Antiproton Ring, EPA: Electron-Positron Accumulator, PS: Proton Synchrotron, PSB: Proton Synchrotron Booster, AAC: Antiproton Accumulator Collector, SPS: Super Proton Synchrotron, LEP: Large Electron-Positron collider
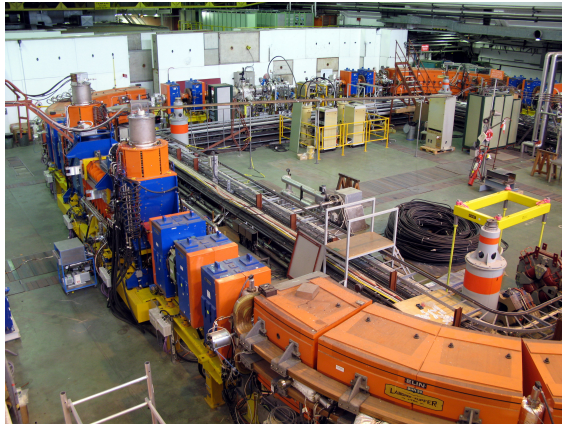
Figure 17.6: The Low Energy Ion Ring (LEIR) at CERN. The Pb ions are collected and stored in the ring while continuously cooled. The pipes of the stochastic cooling are above the ring. The electron cooling is set up on left: the two guns are for introducing and removing the electron cloud. The bending magnets are painted orange, the quadrupole doublets and triplets blue. LEIR uses the elements of the former Low Energy Antiproton Ring (LEAR) functioning in 1982–1996
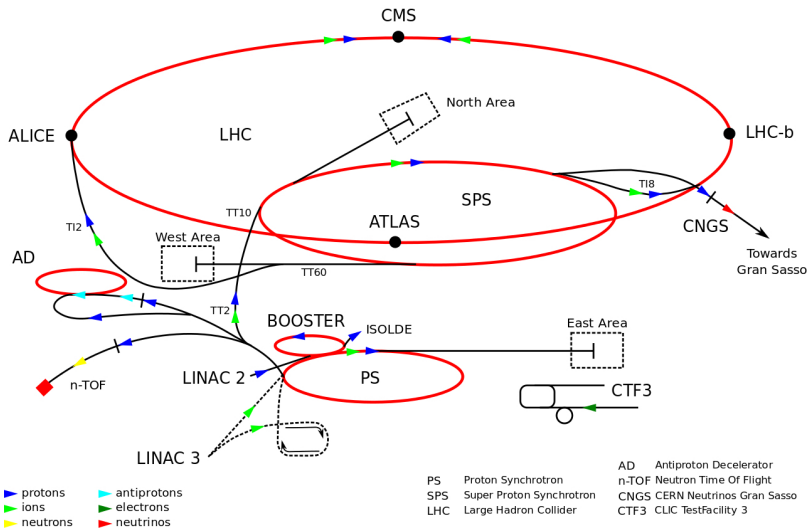
Figure 17.7: The accelerator complex of CERN in the LHC era, after 2008

Figure 17.8: Left: LHC dipoles waiting for installation. They are 15 m long, weigh 35 tons, maintain up to $B = 8$ T magnetic field at $T = 1.9$ K. Right: The radio-frequency cavities accelerating the particles in the LHC ring
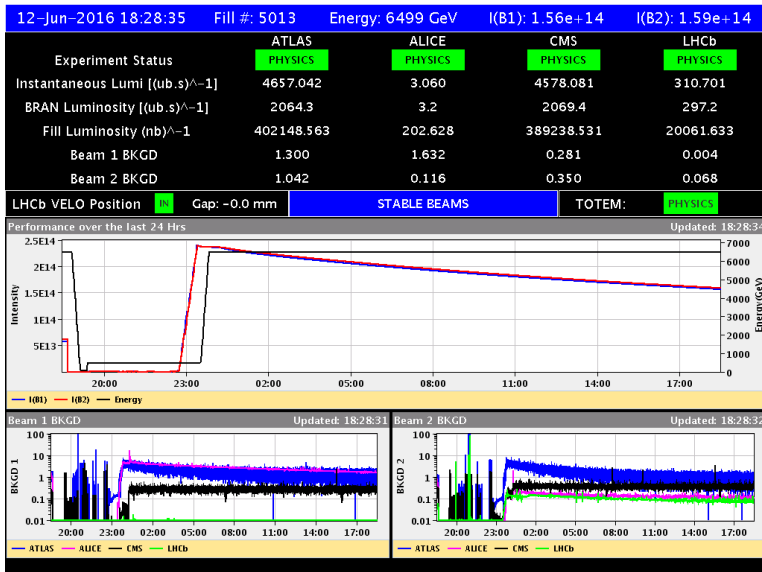
Figure 17.9: Normal LHC operation at 13 TeV p-p collision energy . The upper plot shows the energy (black line corresponding to the right scale) and the intensities of the two beams (red and blue lines). On the bottom the background radiations of the two lines around the four experiments. ATLAS and CMS needed the maximal possible luminosities, whereas ALICE and LHCb much less

Figure 17.10: The Antiproton Decelerator of CERN: its building and main experimental area
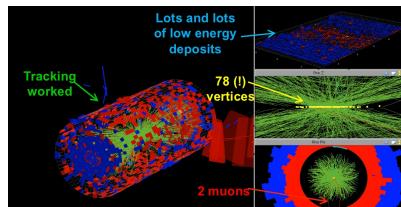
Figure 17.11: 78 identified proton-proton collisions in the same CMS event. Note that the vertices (collision points) are practically lined up. This event was recorded, because it contains two energetic muons
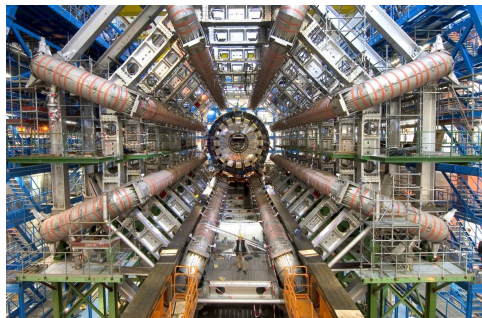
Figure 17.12: The toroidal magnet of the ATLAS detector before the detection elements and the solenoid magnet were installed in it
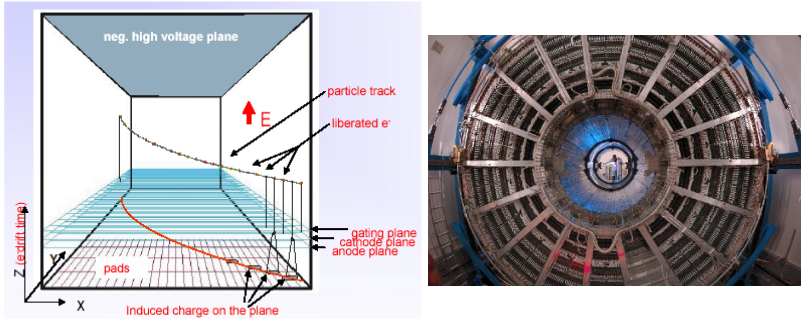
Figure 17.13: Left: Working principle of a time projection chamber. Right: The time projection chamber of the ALICE detector at the LHC

Figure 17.14: Structure and main parts of the CMS detector at the LHC

Figure 17.15: Preparation of the PbWO$_4$ single crystal scintillators for CMS. The electromagnetic calorimeter of CMS consists of 75,848 such crystals read by avalanche photo-diodes
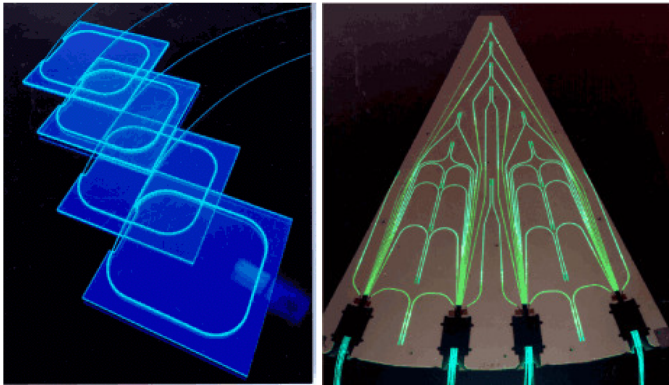
Figure 17.16: Scintillation tiles of CMS: the wavelength-shifting fibres collect and carry the light to hybrid photo-diodes to be converted to electronic signals
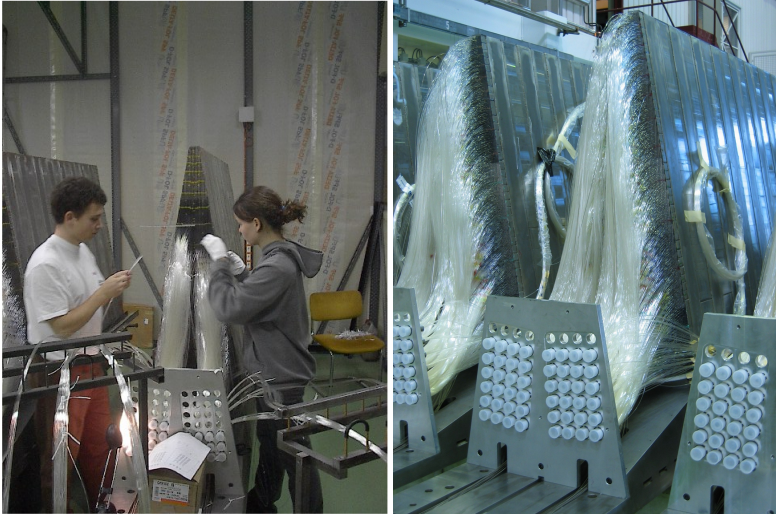
Figure 17.17: The forward part of the hadron calorimeter of CMS: quartz fibres in steel to collect Cherenkov light from secondary electrons
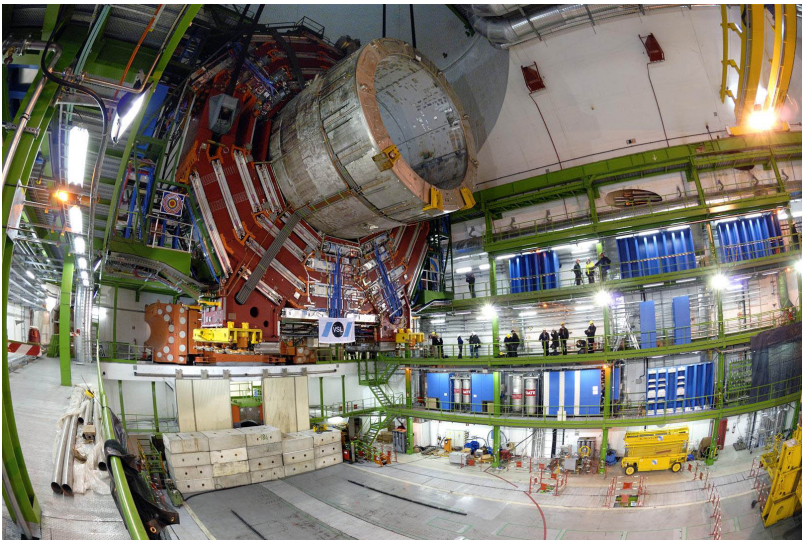
Figure 17.18: Inserting the central ring with the superconducting solenoid into the CMS detector in the experimental cave of LHC underground
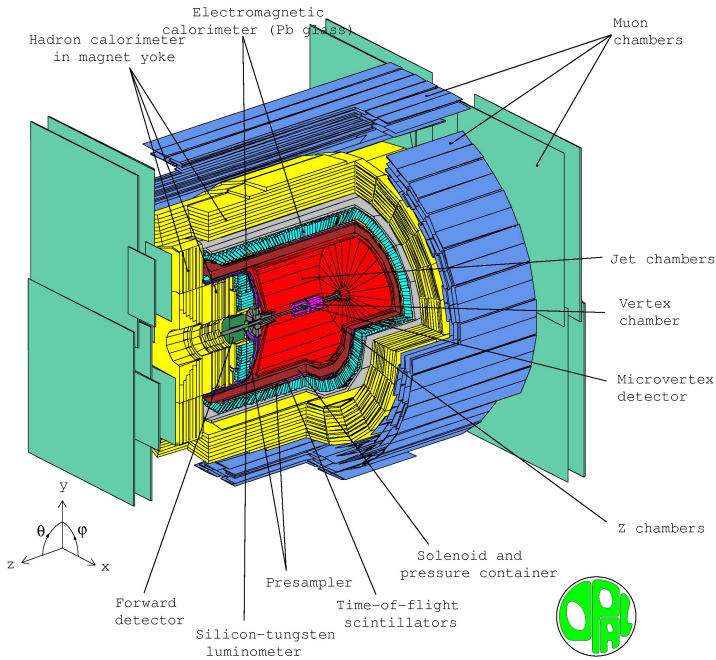
Figure 17.19: The detection system of the OPAL experiment at LEP
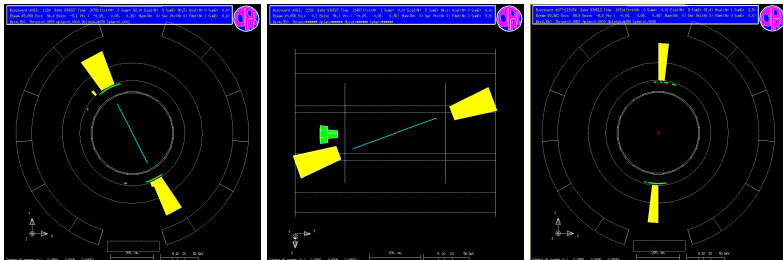
Figure 17.20: Electron-photon events recorded by the OPAL experiment. The yellow blocks show the energy deposits in the electromagnetic calorimeter. Left: Bhabha scattering $e^+e^-{\to}e^+e^-$; middle: Bhabha scattering with photon emission $e^+e^-{\to}e^+e^-\gamma$; right: electron-positron annihilation $e^+e^-{\to}\gamma\gamma$
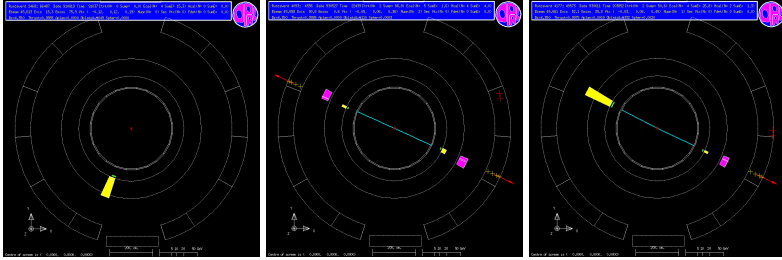
Figure 17.21: Leptonic decays of Z bosons recorded by the OPAL experiment. The yellow blocks show the energy deposits in the electromagnetic calorimeter, the purple ones those in the hadron calorimeter. Left: Z decay to neutrinos with photon emission from the initial state (i.e. by the electron or the positron), $e^+e^-{\rightarrow}Z\gamma{\rightarrow}\nu\nu\gamma$; middle: Z decay to muons, $e^+e^-{\rightarrow}Z{\rightarrow}\mu\mu$; right: Z decay to a tau pair with their subsequent decay to electron, muon and neutrinos: $e^+e^-{\rightarrow}Z{\rightarrow}\tau^+\tau^-{\rightarrow}\mu e + 4\nu$
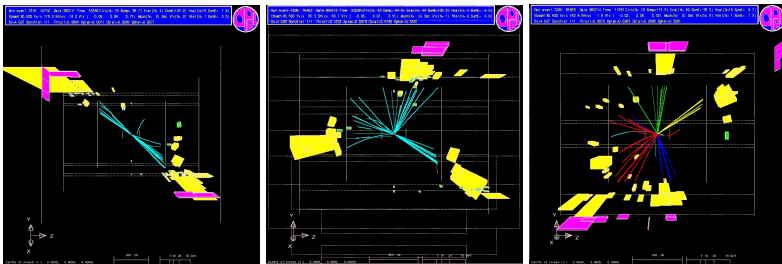
Figure 17.22: Hadron jets recorded by the OPAL experiment. The yellow blocks show the energy deposits in the electromagnetic calorimeter, the purple ones those in the hadron calorimeter. Left: two-jet event, Z decay to a quark pair, $e^+e^-{\rightarrow}Z{\rightarrow}q\bar{q}$; middle: three-jet event, Z decay to a quark pair when one of them emits a gluon: $e^+e^-{\rightarrow}Z{\rightarrow}q\bar{q}g$; right: WW production and decay to quark pairs, $e^+e^-{\rightarrow}W^+W^-{\rightarrow}q\bar{q}q\bar{q}$ where the quarks have different flavours to conserve charge
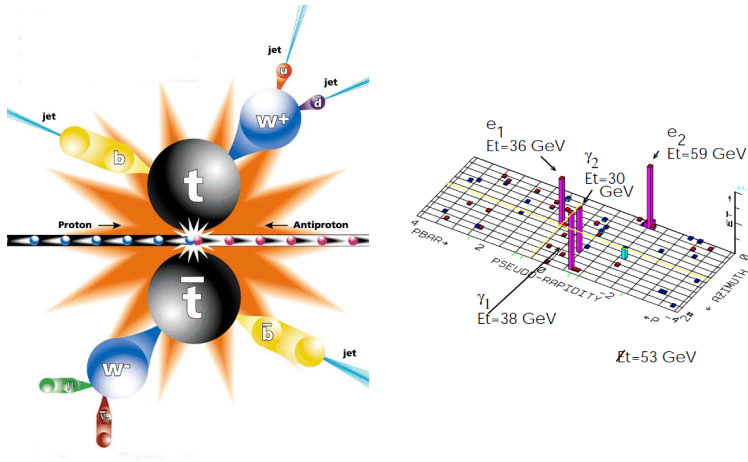
Figure 17.23: Events recorded in $\bar{p}p$ collisions at the Tevatron. Left: Observation of the t quark in the reaction $\bar{p}p \to t\bar{t} \to bW^+\bar{b}W^- \to \ell\nu jjjj$. Right: Energy deposit on the plane of pseudorapidity vs. azimuthal angle of the mysterious CDF event $\bar{p}p \to e^+e^-\gamma\gamma + E_{\mathrm{miss}}$
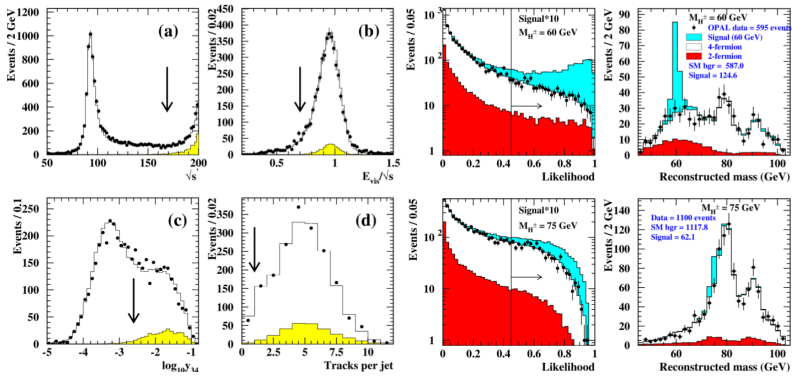
Figure 17.24: Search for charged Higgs-bosons at LEP. Left: Preselection cuts of the OPAL search in the 4-jet channel [Horvath, 2003]. Right: Likelihood analysis in the 4-jet channel for two assumed $H^\pm$ masses [Abbiendi et al., 2012]. Note how well the data (black dots) are described by the background simulation. The signal curves are filled yellow (left) and blue (right). The cut values are denoted by arrows
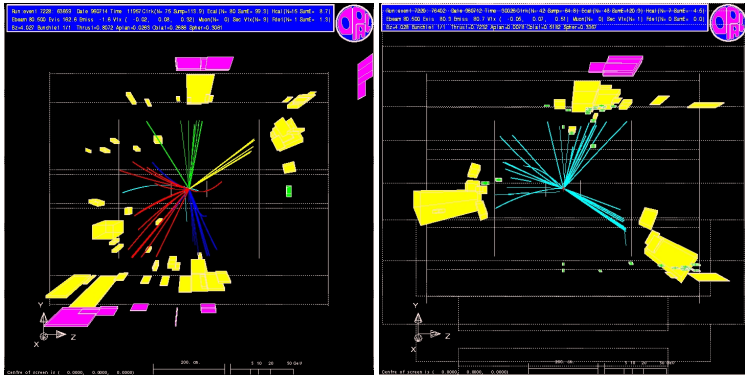
Figure 17.25: Multi-hadronic events detected by the OPAL experiment at LEP. Left: $e^+e^- \to W^+W^- \to qqqq \to 75$ charged particles in 4 hadron jets. Right: a 3-jet event characteristic for gluon production.

Figure 17.26: Some of the major neutrino experiments. At the end of 2017 there were 37 such detector systems under earth, water, ice, and near nuclear power plants
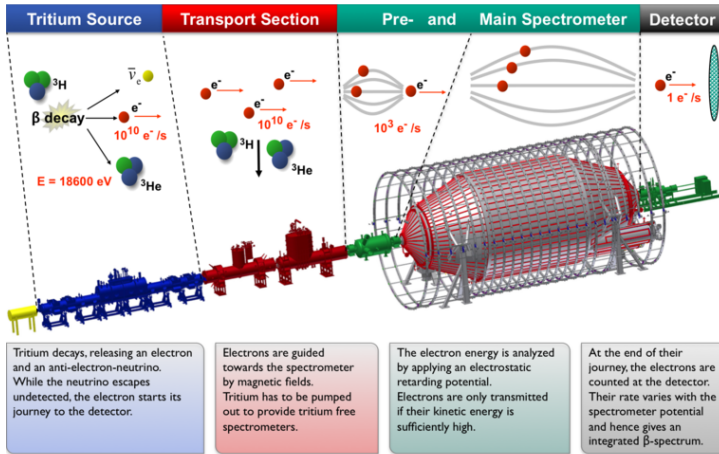
Figure 17.27: KATRIN, the KArlsruhe TRItium Neutrino experiment. The spectrometer lets one electron of the 10^{10} tritium decays per second through into the detector
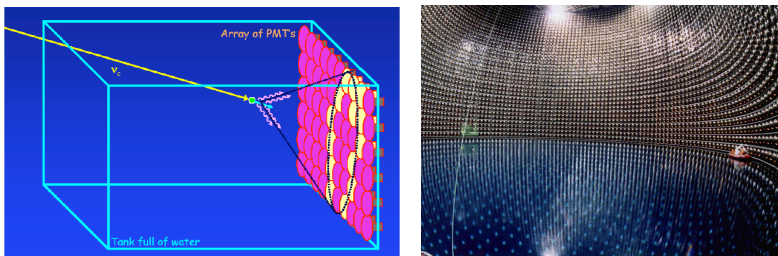
Figure 17.28: Detecting neutrinos in water. Left: Cherenkov light detection in water from neutrino reactions. Right: Filling the Super-Kamiokande detector with water, three technicians in a boat check the phototubes
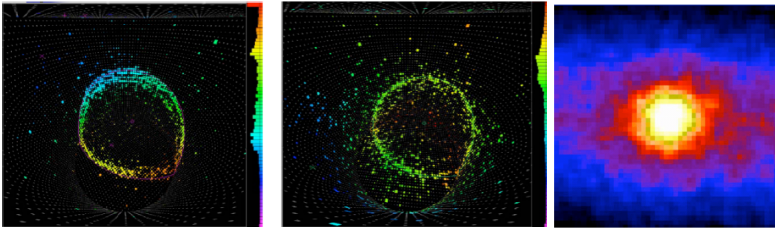
Figure 17.29: Left and middle: Neutrino events detected by Super-Kamiokande. Right: The shape of the Sun depicted by the identified electron neutrinos of the Sun
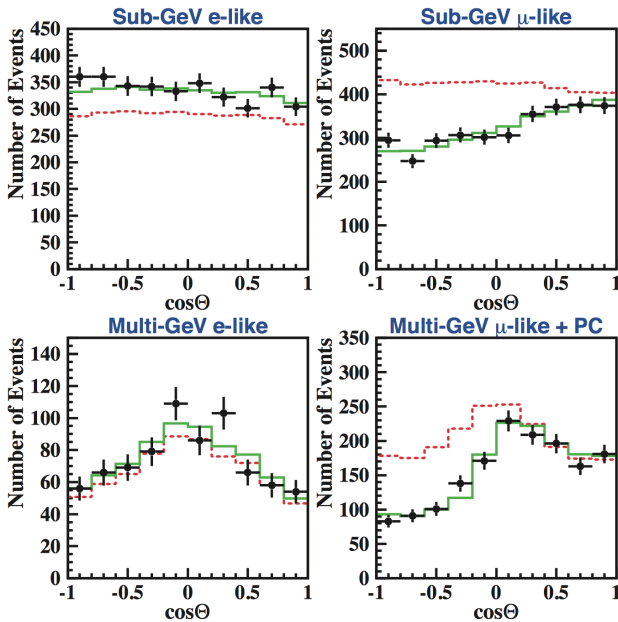
Figure 17.30: The discovery of neutrino oscillations by Super-Kamiokande: neutrino yields vs. zenith angle for electron-like and muon-like events of sub-GeV and multi-GeV energies. The dashed red line is simulation without, the thick green line is with oscillation, the measurement is in black
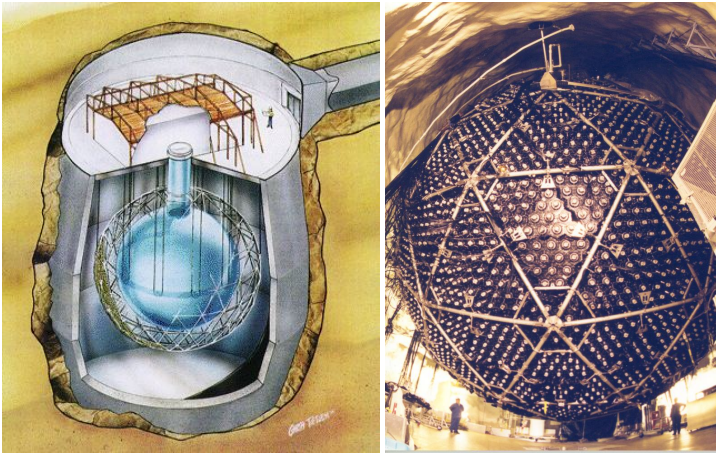
Figure 17.31: The SNO detector in the Sudbury Neutrino Observatory (1999-2003).
Left: a 3-dimensional drawing of the apparatus, right: the acrylic ball

p
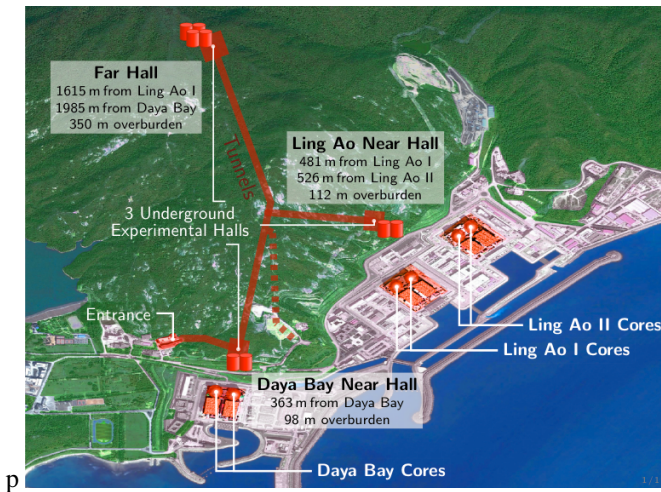
Figure 17.32: The Daya Bay experiment near Hong Kong: eight $\overline{\nu}$ detectors in
three halls in the vicinity of six nuclear reactors

	Measurement	Fit	$|O^{meas} - O^{fit}|/\sigma^{meas}$
$\Delta\alpha_{had}^{(5)}(m_Z)$	0.02750 ± 0.00033	0.02759	
m_Z [GeV]	91.1875 ± 0.0021	91.1874	
Γ_Z [GeV]	2.4952 ± 0.0023	2.4959	
σ_{had}^0 [nb]	41.540 ± 0.037	41.478	
R_l	20.767 ± 0.025	20.742	
$A_{fb}^{0,l}$	0.01714 ± 0.00095	0.01645	
$A_l(P_\tau)$	0.1465 ± 0.0032	0.1481	
R_b	0.21629 ± 0.00066	0.21579	
R_c	0.1721 ± 0.0030	0.1723	
$A_{fb}^{0,b}$	0.0992 ± 0.0016	0.1038	
$A_{fb}^{0,c}$	0.0707 ± 0.0035	0.0742	
A_b	0.923 ± 0.020	0.935	
A_c	0.670 ± 0.027	0.668	
$A_l(SLD)$	0.1513 ± 0.0021	0.1481	
$\sin^2\theta_{eff}^{lept}(Q_{fb})$	0.2324 ± 0.0012	0.2314	
m_W [GeV]	80.385 ± 0.015	80.377	
Γ_W [GeV]	2.085 ± 0.042	2.092	
m_t [GeV]	173.20 ± 0.90	173.26	

March 2012

Figure 17.33: Parameters of the standard model [Schael et al., 2013] as determined by the experiment (2nd column) with uncertainties (3rd column), its prediction or fit by the standard model (4th column) and a bar plot showing the difference between theory and experiment divided by the experimental uncertainty. The agreement is purely statistical as the difference is in only one case more than 2 uncertainties
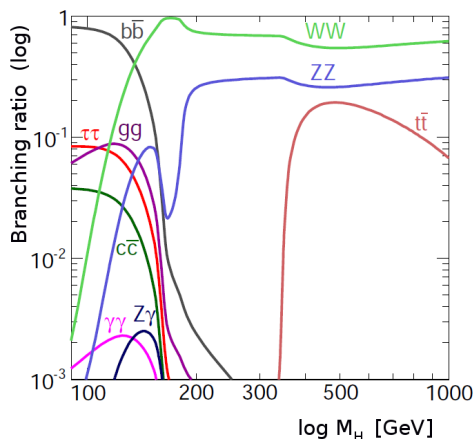
Figure 17.34: The various decay channels of the Higgs boson according to the standard model. At lower masses b̄b, at higher ones W⁺W dominates. Note how small is the contribution of the important $\gamma\gamma$ channel
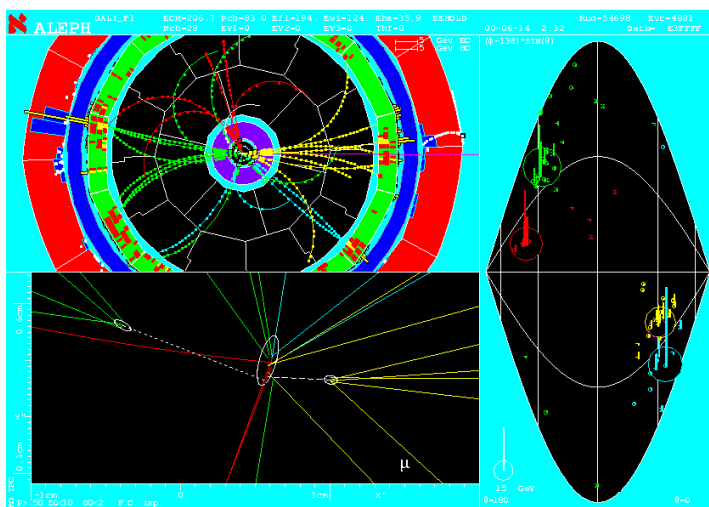

Figure 17.35: Higgs-like event detected by the ALEPH experiment at LEP: an e^+e^- collision produced four hadron jets containing b quarks recognized by their secondary vertices due to longer lifetimes
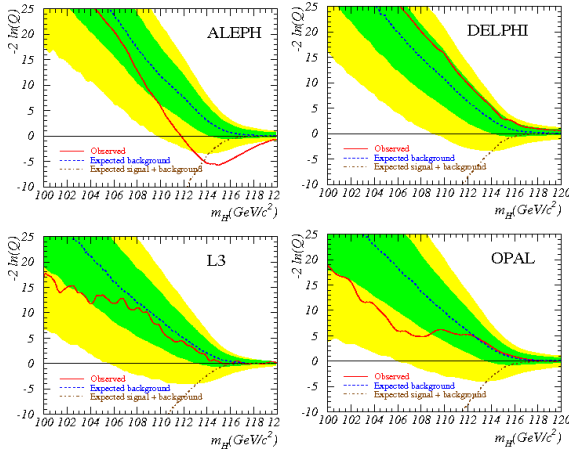
Figure 17.36: Exclusion of the Higgs boson at LEP [Barate et al., 2003]. The test statistic, $-2\ln Q$ shows a significant signal (well above the standard model expectation) for ALEPH and nothing for the other three LEP experiments at equivalent statistical and experimental conditions
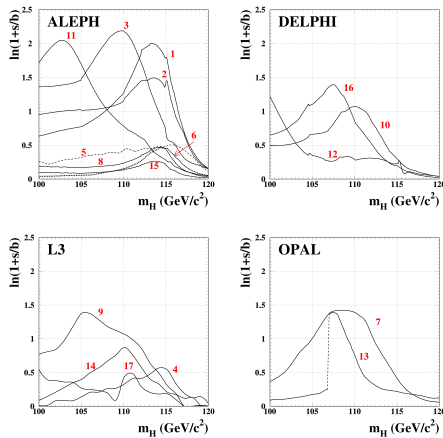
Figure 17.37: Exclusion of the Higgs boson at LEP [Barate et al., 2003]. *Spaghetti diagrams* of 17 Higgs-like events detected by the four LEP experiments: signal weights against the simulated Higgs mass. The ALEPH events crowd around 115 GeV, whereas for the other three experiments there are less of them with a rather random mass distribution
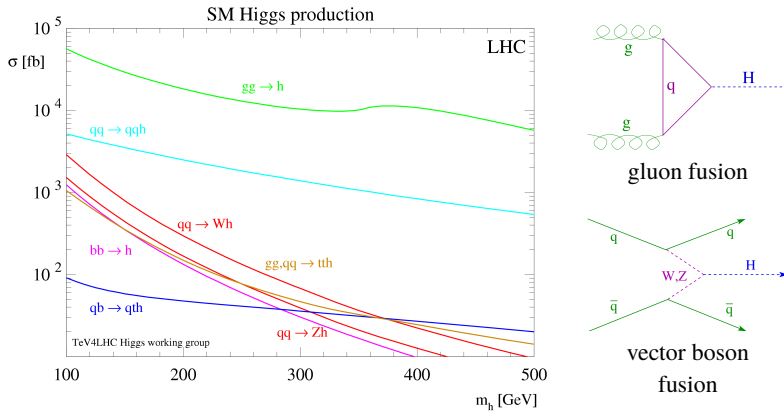
Figure 17.38: Production of the SM Higgs boson in p-p collisions at LHC. Gluon fusion (upper right) has the highest cross section, vector boson fusion (lower right) comes next
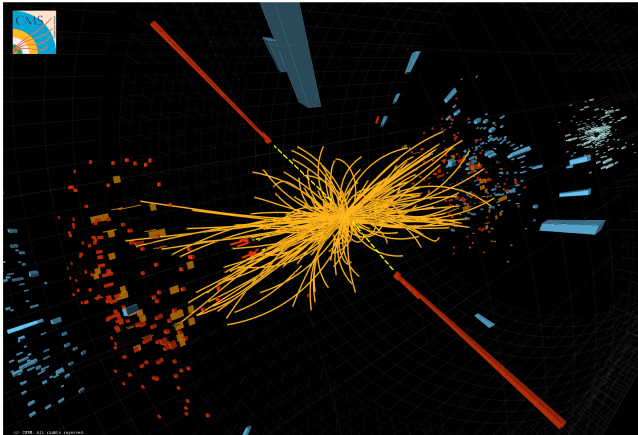
Figure 17.39: Higgs-boson-like event detected by the CMS experiment at LHC: a boson is formed in a p-p collision and decays to two energetic gamma photons. The block sizes at the end of the invisible photon trajectories correspond to the photon energies deposited in the electromagnetic calorimeter
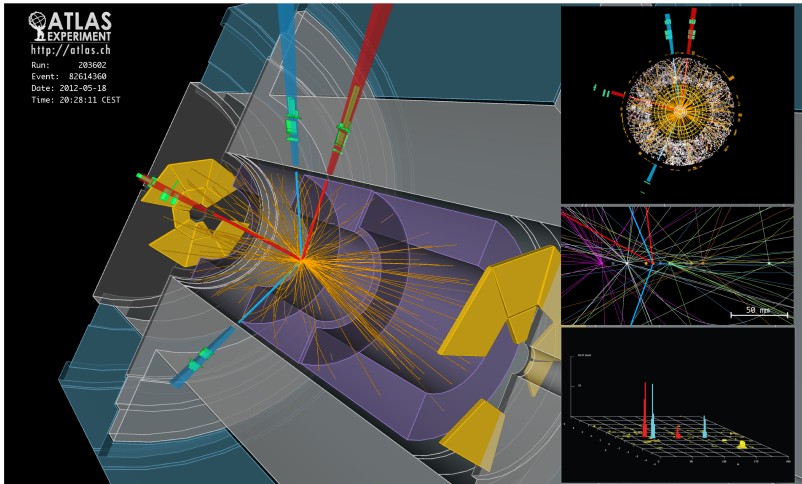
Figure 17.40: Higgs-boson-like event detected by the ATLAS experiment at LHC: a p-p collision produces 4 electrons, one pair is from Z-decay as identified by the invariant mass. The 4-electron mass corresponds to a decaying mass of 125 GeV. Upper right: $x - y$ view, lower right: lego plot of energy deposits in the calorimeters. Middle right shows that there were 9 other identified vertices of p-p collisions in the neighbourhood of the candidate Higgs decay belonging to the same LHC bunch crossing.
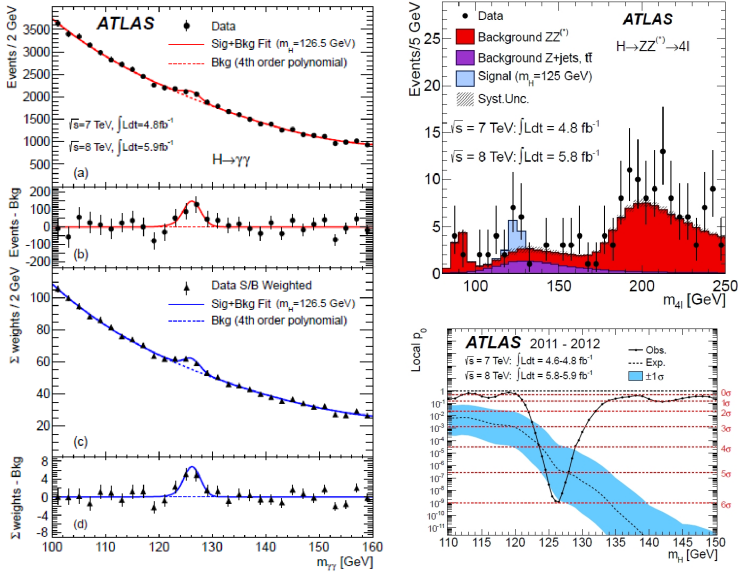
Figure 17.41: First observation of the Higgs-like boson in invariant mass distributions at around 125 GeV by ATLAS [Aad et al., 2012]. Left: H→γγ, the raw events and also the sum of event weights according to their signal-likelihood. Top right: H→ℓ⁺ℓ⁻ℓ⁺ℓ⁻. Bottom right: the local p-values averaged for all channels. The total p values have shown more excess events than the prediction of the standard model (dotted line in the lower right plot)
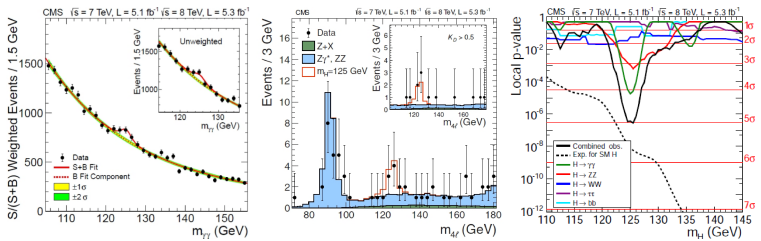

Figure 17.42: First observation of the Higgs-like boson in invariant mass distributions at around 125 GeV by CMS [Chatrchyan et al., 2012b]. Left: H→γγ, the raw events and also the sum of event weights according to their signal-likelihood. Middle: H→ℓ⁺ℓ⁻ℓ⁺ℓ⁻. Right: the local p-values for the individual channels and their averages. CMS saw somewhat less events than the prediction of the standard model (dotted line in the right plot)
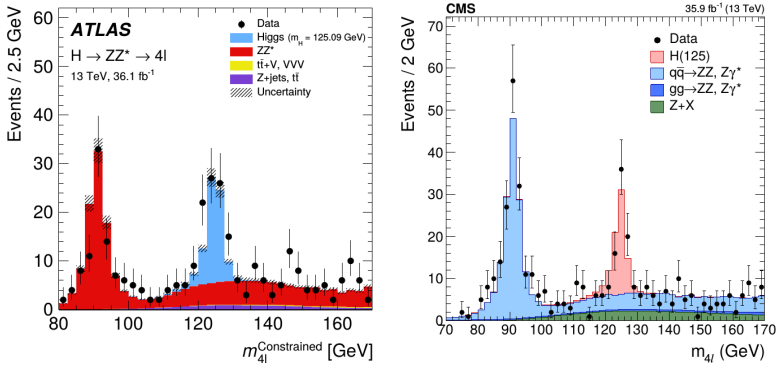
Figure 17.43: Invariant mass spectra obtained by ATLAS [Aaboud et al., 2017] and CMS [Sirunyan et al., 2017] with 13 TeV p-p collisions for the H→$\ell^+\ell^-\ell^+\ell^-$ reaction
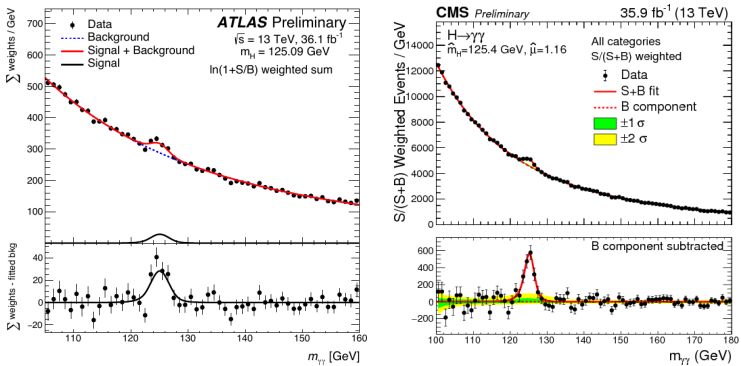

Figure 17.44: Invariant mass spectra obtained by ATLAS [ATLAS, 2017] and CMS [Sirunyan et al., 2017] with 13 TeV p-p collisions for the H → $\gamma\gamma$ reaction
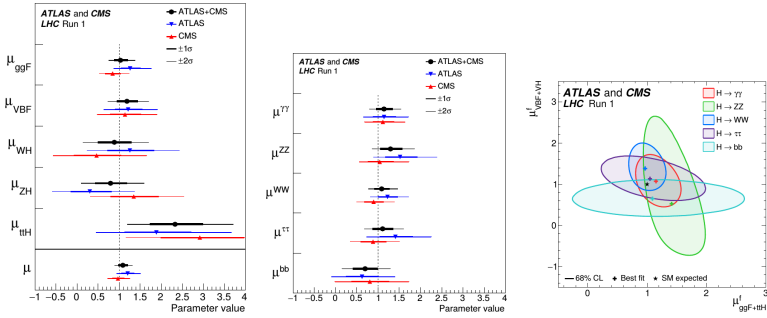
Figure 17.45: Relative signal strengths in the most significant decay channels normalized to the predictions of the standard model as measured by ATLAS and CMS [Aad et al., 2016] for M_H = 125 GeV. Left: for various production channels against the invariant mass of the new boson. Middle: for the various decay channels. Right: 68% contours for various decay channels when produced in weak vs. strong processes. All results agree within statistics with each other and with the expectations of the standard model
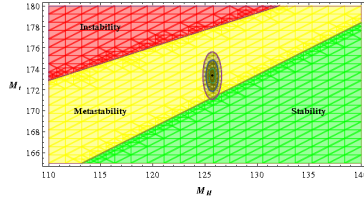

Figure 17.46: Stable, unstable and metastable regions of the BEH vacuum on the plane of the masses of the Higgs boson and the t quark according to the standard model [Branchina et al., 2014]. The experimental point of the two masses at m_H ≃ 125 and m_t ≃ 173 GeV are encircled by 1σ, 2σ and 3σ contours
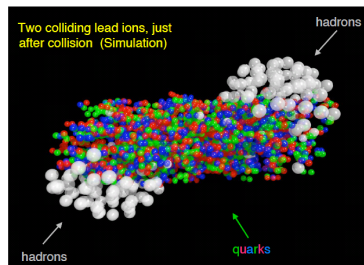

Figure 17.47: Simulated collision of heavy ions. In the central part the temperature is high enough to de-confine coloured quarks and gluons
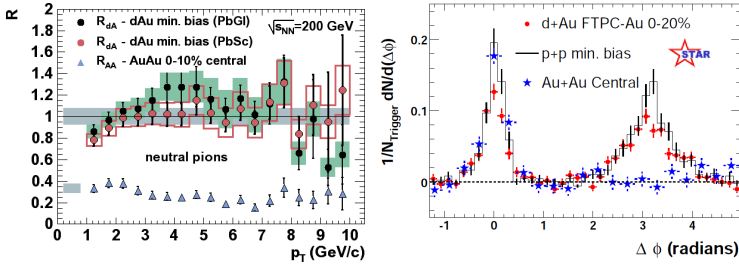
Figure 17.48: Jet quenching observed at RHIC. Left: The π^0 yield observed by PHENIX from central Au+Au collisions is suppressed as compared to the d+Au collisions of minimum bias. Right: The 2-jet events in STAR are suppressed on the side opposite to the highest energy track for central Au+Au collisions, whereas they are free to come out in d+Au collisions

Figure 17.49: Jet quenching in lead-lead collisions at the LHC observed by the ATLAS experiment [Aad et al., 2010] at $\sqrt{s_{NN}} = 2.76$ TeV per nucleon pair

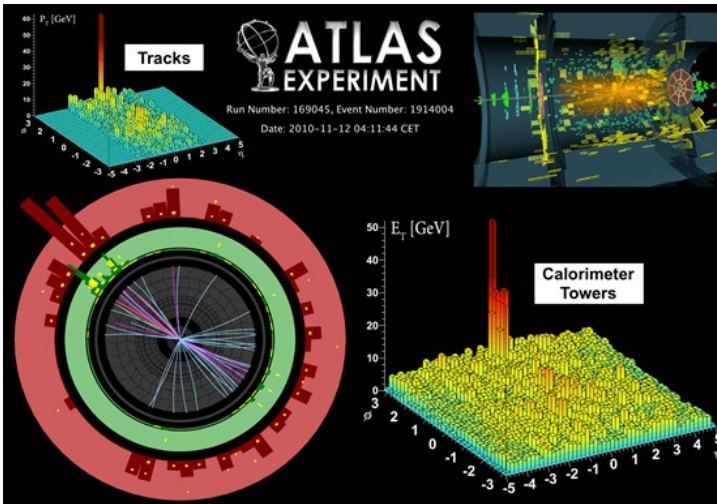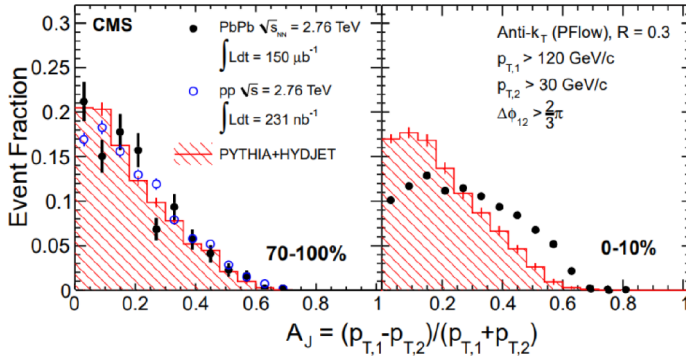Figure 17.50: Jet–jet asymmetry in peripheral (left) and central (right) p-p and Pb-Pb collisions at the LHC observed by the CMS experiment [Chatrchyan et al., 2012a] at $\sqrt{s_{NN}} = 2.76$ TeV per nucleon pair. The simulation shows the expected asymmetry with no nuclear medium

Figure 17.51: Left: Cyclotron used in medicine to produce radioactive isotopes. Right: Linear accelerator used in a hospital
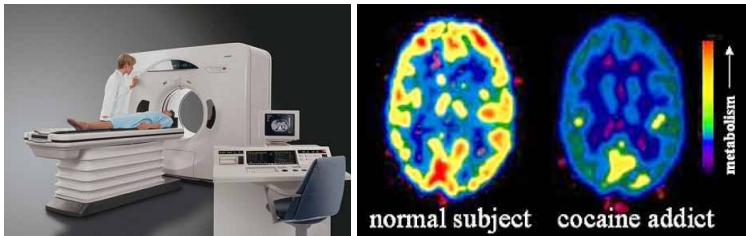
Figure 17.52: Left: computer tomography at work. Right: PET pictures of healthy and cocaine-addict brains
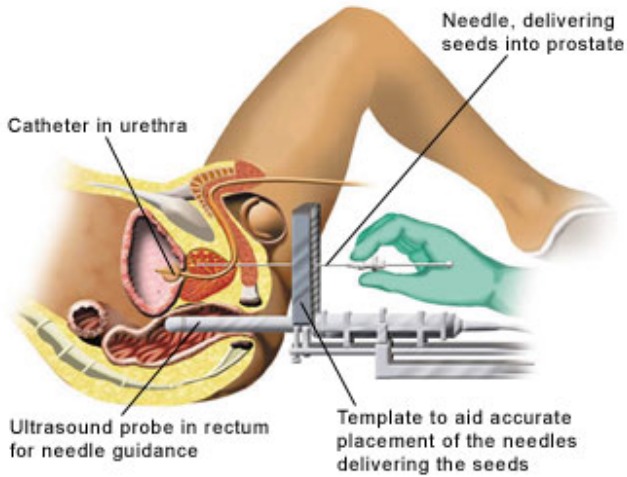
Figure 17.53: Brachytherapy on prostate cancer: about 100 radioactive pins are placed in the tumour, while checking the placement with an ultrasound probe
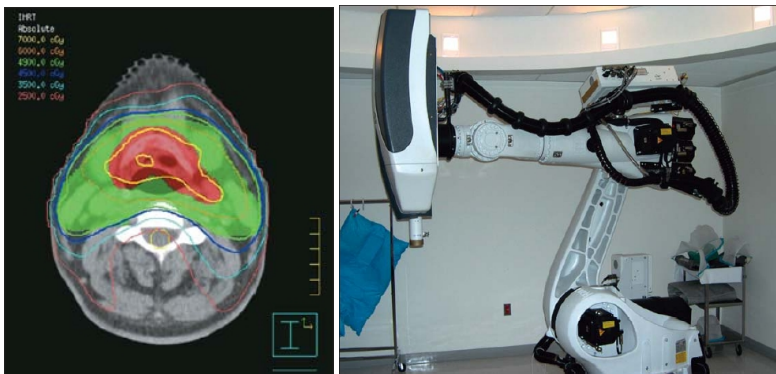
Figure 17.54: Left: conform dose distribution with IMRT: the tumour gets 70 Gy, the metaphase region 50 Gy and the spinal cord less than 25 Gy dose. Right: Cyber knife, electron linac on a robot arm with very precise, multiple orientations and depth penetration
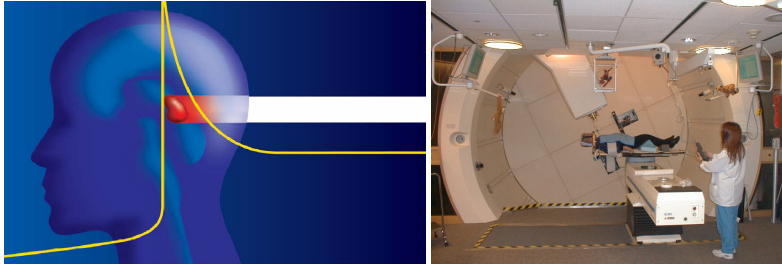
Figure 17.55: Left: a charged particle when penetrating matter loses most of its energy at the end of its flight path (Bragg curve). Right: Gantry for proton therapy at a hospital
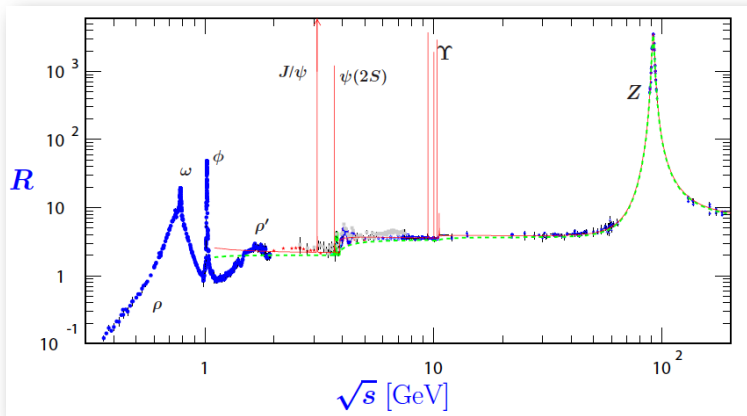
Figure 17.56: Experimental measurements of the R-ratio as a function of the total centre-of mass energy (taken from Ref. [Beringer et al., 2012]).
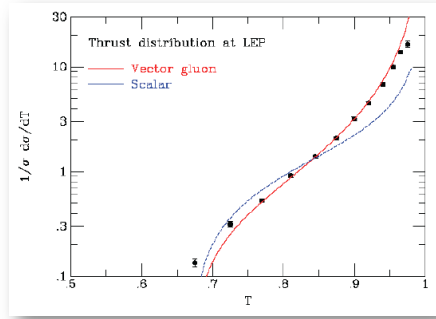
Figure 17.57: Distribution of thrust as measured at LEP compared to perturbative QCD predictions obtained assuming vector and scalar gluon
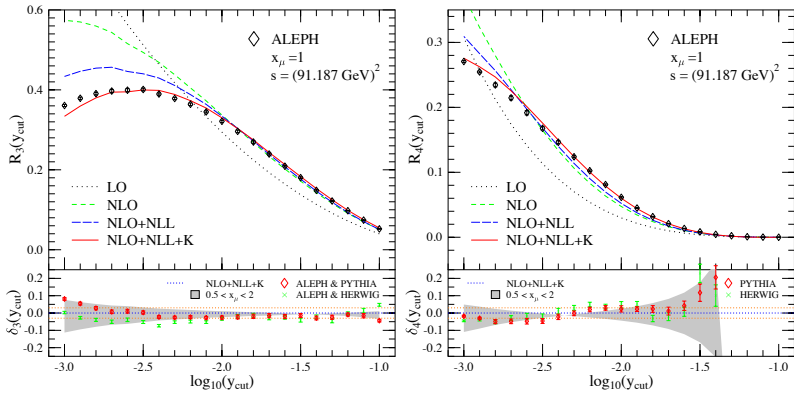
Figure 17.58: Comparison of perturbative QCD predictions to data for three- and four-jet rates R_3 and R_4 at LEP [Nagy and Trocsanyi, 1999]. The data points include corrections from hadrons to partons based on Monte Carlo simulations. The lower panels show the differences between theoretical predictions and experimental data, normalized by the latter. $x_\mu = \mu/\sqrt{s}$, while K refers to some well-defined terms (called cusp anomalous dimension) of the NNLL corrections
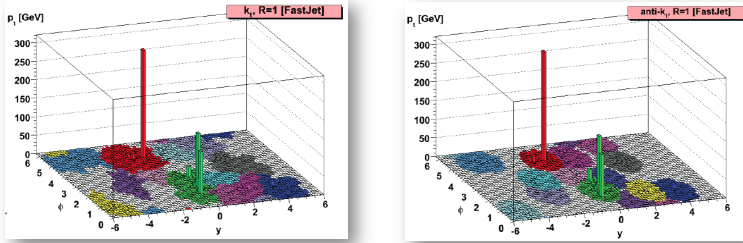
Figure 17.59: Jets in a proton-proton scattering event obtained with the k_T (left), anti-k_T (right) clustering algorithms
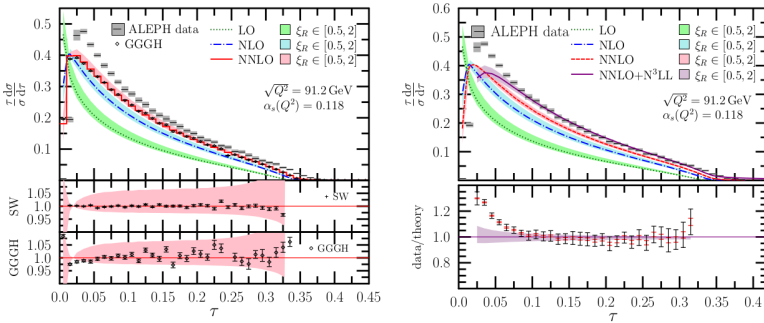
Figure 17.60: QCD predictions for the thrust distribution ($\tau = 1 - T$) in electron-positron annihilation. Left: Predictions obtained by using the CoLoRFulNNLO method compared to data measured by the ALEPH collaboration. The lower panels show the comparison to the predictions of Ref. [Weinzierl, 2009] (denoted by SW) and to those of Ref. [Gehrmann-De Ridder et al., 2007] (denoted by GGGH). Right: Same as the left one supplemented with the prediction obtained by matching the NNLO prediction to resummed NNNLL one
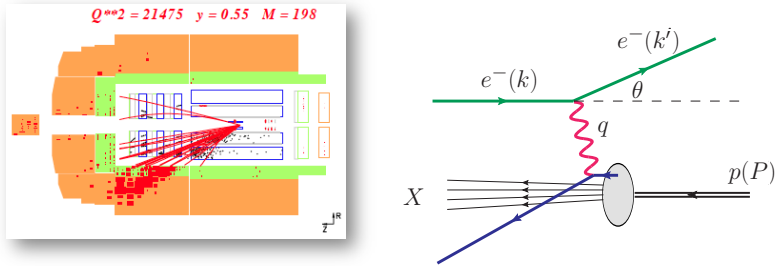
Figure 17.61: Deeply inelastic electron-proton scattering in the H1 detector (left) and parton model interpretation of such an event (right). X denotes the unobserved final state (hadrons)
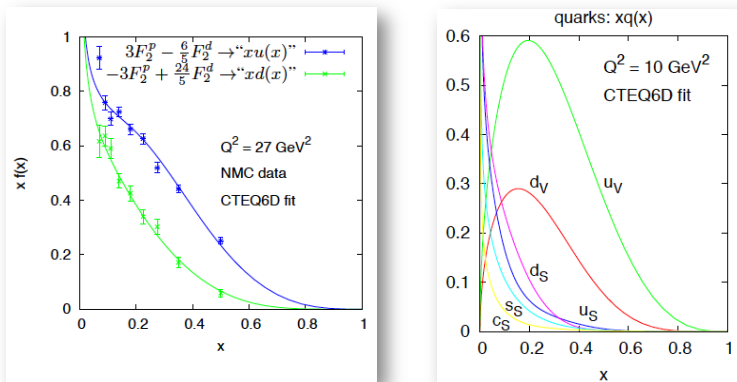
Figure 17.62: Left: Combination of F_2 structure functions on proton and deuteron targets measured by the NMC collaboration and fitted with CTEQ6D parton distribution functions. Right: CTEQ6D valence and sea quark distributions
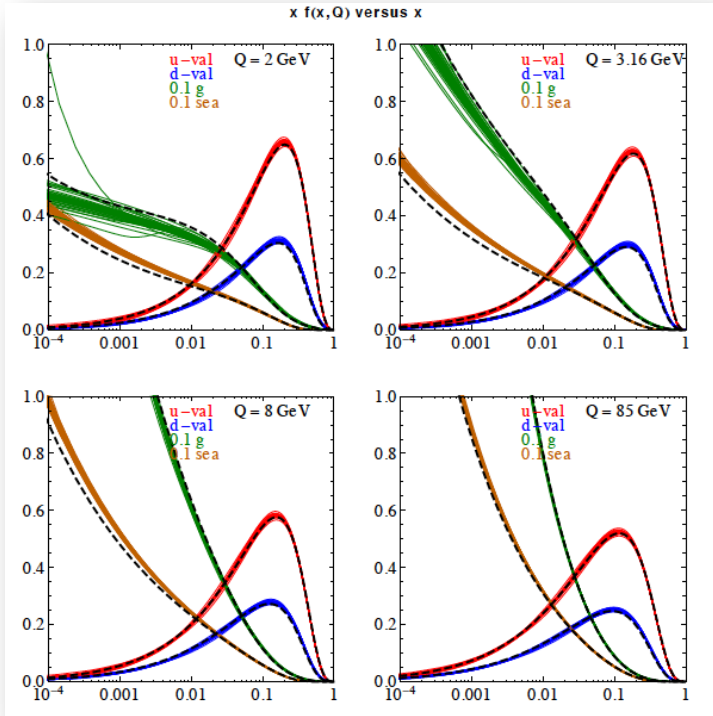
Figure 17.63: Evolution of valence quark, sea quark and gluon distributions
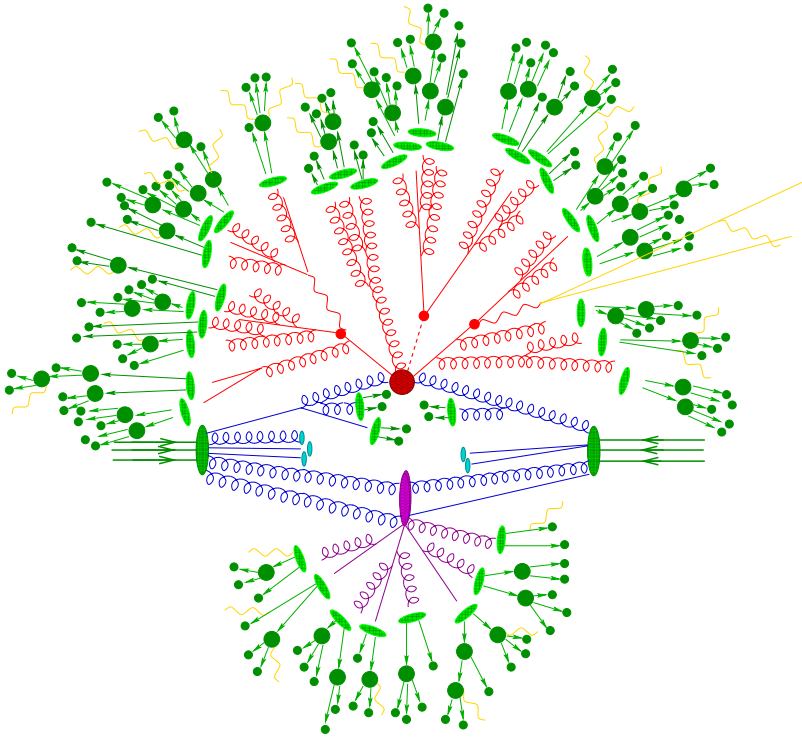
Figure 17.64: Artistic view of a proton-proton scattering event at high energy (courtesy of F. Krauss)

Intermezzo

MOTTO:

What is it that breathes fire into the equations and makes a universe for them to describe? . . . Why does the universe go to all the bother of existing?

(Stephen Hawking)

The first three parts of this book discussed the most important results of experimental particle physics during the past fifty (or in some cases more) years. As a consequence we know with certainty that the physical manifestations of the three fundamental particle interactions–the weak, the electromagnetic, and the strong forces–below the TeV energy scale can be described by a model based on local quantum field theory that we call the standard model of particle interactions. There are three almost identical copies of particle families, containing two quarks and two leptons each (see Table 3.5), the only difference being the mass of the particles. In the standard model the neutral leptons are massless, but we already have experimental evidence (the observation of neutrino oscillations) that they have masses even

if we have not been able to measure them directly. While the experimental evidence for the existence of only three families is strong, it remains a mystery why there are exactly three families and how neutrinos get masses.

The mathematical model that describes the interaction is a gauge field theory based on the $SU(3)_c \otimes SU(2)_L \otimes U(1)_Y$ symmetry where "c" refers to colour degrees of freedom, Y stands for hypercharge and "L" abbreviates *left-handed*. The gauge fields that emerge due to the gauge symmetries mediate the forces. These are the massless mediators of the electromagnetic and strong forces, the photon and the gluon, furthermore the massive mediators of the weak force, the W and Z bosons. In addition there is also a scalar boson, the elementary excitation of the BEH field, called Higgs particle that emerge in the spontaneous symmetry breaking of the BEH field together with the longitudinal components of the W and Z bosons. There is continuously increasing evidence that the scalar particle observed at the LHC has the exact properties as predicted in the standard model. The interaction of the BEH field with the fermions explains the masses of the fermions, although the reason for the large hierarchy of the fermion masses is unknown. According to the standard model the interactions between the Higgs particle and the fermions are proportional to the masses of the fermions, but complete experimental verification will require new accelerators. The same is true for the precise experimental exploration of the Higgs potential. We also lack the reason for the particular choice for the gauge interactions by Nature and we do not know if there is only one scalar particle.

We mentioned that apart of the continuous symmetries of gauge interactions and space-time, there are the discrete symmetries of charge conjugation, parity and time reversal, too. We discussed at length the experimental proof for the chiral characteristics of the electroweak interactions, which means that weak force violate the parity symmetry maximally. We also argued that the combined symmetry of CPT is expected to be a fundamental symmetry of Nature and mentioned the strong constraints on the experimental searches for CPT violation. As a result, the naive expectation that particle interactions respect time reversal symmetry would imply combined CP symmetry, which is however weakly violated. While this violation can be explained in the standard model, there is also another symmetry violation — called baryon-anti-baryon asymmetry — that the standard model cannot explain.

There are two more big mysteries at the fundamental level in Nature. The energy density in the Universe comes from several main sources. Some of these are well known, like electromagnetic radiation (which turns out to provide a small fraction, not reaching 1 % of the total energy density) and baryonic matter that has also a quite small contribution of about 5 %. The

rest of the energy density is in unknown forms, called dark matter and dark energy. While these results emerge in cosmological observations, it might be that the explanations will come from particle physics, but clearly beyond the standard model, therefore these subjects are omitted from this book.

We devote the last part of our book to the introduction to the quantum field theoretical basis of the standard model of elementary particle interactions, needed to understand high energy collision events. We explore what we can learn from studying the theory of the standard model, to what extent the experimental observations mentioned above can be understood theoretically, and what calls for a new theory beyond the standard model. In order to facilitate the comprehension of the mathematical details, most of the computations are performed step by step, or in some cases left to the exercises. As prerequisite familiarity with quantum electrodynamics is assumed, although its basics are summarized.

Our primary goal is to describe collisions at the LHC, i.e. proton-proton scatterings at high momentum transfer. As the initial state contains particles composed of coloured constituents of the proton–quarks and gluons–, quantum chromodynamics (QCD) is the key to the mathematical description. QCD is a predictive theory due to its two main features: (i) asymptotic freedom that allows for a perturbative description and (ii) the factorization theorem that separates the short and long-distance physics in a universal (process independent) way. Thus we put significant emphasis to develop these two concepts in detail and exhibit the *theoretical uncertainties that are inherent in this theoretical framework, which is crucial to estimate the theoretical systematics of experimental results correctly*. In closing the book we discuss the basics of the theory of electroweak interactions.

Part IV

Standard model of elementary particles

Chapter 18

Gauge theories in the standard model

MOTTO:

We need something new. We can't predict
what that will be or when we will find it be-
cause if we knew that, we would have found it
already!

(Stephen Hawking)

18.1   Underlying gauge group

The standard model (SM) of elementary particle interactions in based upon
the principle of local gauge invariance, which means that the Lagrangian
remains invariant if the fields are transformed by an arbitrary element of a
continuous group. The underlying gauge group is

$$G = SU(3)_{\text{c}} \otimes SU(2)_{\text{L}} \otimes U(1)_Y \,,$$

where c stands for "colour", L for "left-handed" and Y for "hypercharge".
The meaning of these terms will be explained later. $U(1)$ is an abelian
group, which means that its elements, $e^{\mathrm{i}\varphi} \in U(1)$ commute ($\varphi \in \mathbb{R}$ is a real

number). Quantum electrodynamics (QED) is the prototype gauge theory with a local $U(1)$ symmetry. $SU(N)$ are non abelian groups: their elements $e^{iH} \in SU(N)$ do not commute. H is not a number any more, but an Hermitian matrix $H^\dagger = H$ with $\operatorname{Tr} H = 0$. There are $N^2 - 1$ generators T^a of $SU(N)$ that satisfy the $SU(N)$ algebra:

$$\left[T^a, T^b\right] = i f^{abc} T^c, \quad \text{with normalization} \quad \sum_{i,j}(T^a)_{ij}(T^b)_{ji} = T_R \delta^{ab}$$

(18.1.1)

where $T_R \in \mathbb{R}$ is the normalization factor. A general matrix H can be written as a linear combination of the generators,

$$H = \sum_{a=1}^{N^2-1} \epsilon^a T^a, \qquad \epsilon^a \in \mathbb{R}.$$

The constants f^{abc} are the structure constants of the Lie algebra. The structure constants are completely antisymmetric. For $SU(2)$ the generators satisfy the well-known angular momentum algebra

$$\left[J^a, J^b\right] = i\epsilon^{abc} J^c.$$

In this case the structure constants $f^{abc} = \epsilon^{abc}$ are the Levi-Civita symbols (if any two of its indices are equal, the symbol is zero, otherwise $\epsilon^{abc} = (-1)^p \epsilon^{123}$, with $\epsilon^{123} = 1$ where p is the number of interchanges of indices necessary to unscramble a, b and c into the order 1, 2, 3). In the SM the $SU(3)_c$ symmetry is unbroken, this means that $SU(3)$ is a symmetry of the Lagrangian and also of the vacuum, whereas the $SU(2)_L \otimes U(1)_Y$ symmetry is spontaneously broken to $U(1)$. First we shall discuss the unbroken part and turn to the broken part in the last chapter.

The gauge theory based on local $SU(3)_c$ invariance is called quantum chromodynamics (QCD). There are many similarities and some important differences between QED and QCD. In order to see these clearly, we recall the basics of QED.

18.2   Basics of quantum electrodynamics

First of all a remark about the notation and the units: we use the notation $i = \sqrt{-1}$, e for the unit charge, natural units $\hbar = c = 1$ and the convention

$$g^{\mu\nu} = \operatorname{diag}(1, -1, -1, -1)$$

for the metric tensor (see (Eq. (4.1)).

The classical Dirac Lagrangian (see chapter 4) for n types of non-interacting fermion fields is

$$\mathcal{L}_f = \sum_{j=1}^{n} \bar{f}_j \left(i\slashed{\partial} - m_j \right) f_j$$

(in QED $n = 1$, the electron) where

- f_j is the spinor valued wave function describing a plane wave of momentum p_j,

- $\bar{f}_j = f_j^\dagger \gamma^0$ is the Dirac adjoint of f_j,

- $\slashed{a} = \gamma^\mu a_\mu$ where the γ^μ matrices (see chapter 4) satisfy the Clifford algebra,

$$\{\gamma^\mu, \gamma^\nu\} = 2g^{\mu\nu}, \qquad \{\gamma^\mu, \gamma^5\} = 0. \qquad (18.2.2)$$

Let us perform a global (i.e., independent of the space-time coordinate) phase transformation of the field, $f_j \rightarrow f_j' = \exp\left[i\, e_j\, \theta\right] f_j$ where $\theta \in \mathbb{R}$ and e_j expresses the charge of the fermion j in units of e (e.g. for the electron $e_j = -1$). The Lagrangian is invariant under such a global phase shift, $\mathcal{L}(f_j) = \mathcal{L}(f_j')$, which implies the existence of a conserved charge, the electric charge, according to Noether's theorem.

One may wonder whether we can modify $\mathcal{L}_f$ such that it is also invariant under local changes of gauge,

$$f_j(x) \rightarrow f_j'(x) = \exp[i\, e_j\, \theta(x)]\, f_j(x) \equiv U_j(x) f_j(x).$$

The physical meaning of this question is the following: can we choose the phase of the fermion field at any x^μ at will, without changing observable quantities? The answer is yes! To make the Lagrangian invariant under local phase transformations, called *gauge transformations*, we have to take the following steps:

1. Introduce a vector-valued field $A_\mu(x)$ with transformation property

$$A_\mu(x) \rightarrow A_\mu'(x) = A_\mu(x) + \frac{i}{e}[\partial_\mu U(x)]U^{-1}(x),$$
$$U(x) = \exp\left[i\,\theta(x)\right].$$

2. Replace the partial derivative ∂_μ with $D_\mu[A] \equiv \partial_\mu + ie\hat{Q}A_\mu$,

$$\mathcal{L}_f = \sum_{j=1}^{n} \bar{f}_j \left(i\slashed{D}(A) - m_j \right) f_j$$

where $\hat{Q}f_j = e_j f_j$ is the electric charge operator. If

$$f_j(x) \rightarrow f'_j(x) = U_j(x)f_j(x),$$

then

$$D_\mu[A]f_j(x) \rightarrow D_\mu[A']f'_j(x) = U_j(x)D_\mu[A]f_j(x),$$

so $D_\mu[A]f_j(x)$ transforms the same way as the fermion field $f_j(x)$, hence $D_\mu[A]$ is called covariant derivative.

3. The new field requires a gauge-invariant kinetic term:

$$\mathcal{L}_A = -\frac{1}{4}F_{\mu\nu}[A] F^{\mu\nu}[A] \qquad F_{\mu\nu}[A] = \partial_\mu A_\nu - \partial_\nu A_\mu .$$

$\mathcal{L}_A$ is a Lorentz scalar and therefore Lorentz-invariant. Since $F^{\mu\nu}[A]$ is gauge invariant (the proof is left as exercise), $\mathcal{L}_A$ is also gauge invariant: $\mathcal{L}_A = \mathcal{L}_{A'}$.

The Feynman rules can be read off the action

$$S = i \int d^4x (\mathcal{L}_f + \mathcal{L}_A) \equiv S_0 + S_I ,$$

where

$$S_0 = i \int d^4x \mathcal{L}_0 \qquad S_I = i \int d^4x \mathcal{L}_I .$$

$\mathcal{L}_0$ contains all terms that are bilinear in the fields, $\mathcal{L}_I$ contains the rest (called interactions). The photon propagator $\Delta_{\gamma_{\mu\nu}}$ is the inverse of the bilinear term in A_μ [Ryder, 1996]. In momentum space we have the condition

$$\Delta_{\gamma_{\mu\nu}}(p) \cdot i \left[p^2 g^{\nu\rho} - p^\nu p^\rho \right] = \delta_\mu^\rho ,$$

i.e. equal to the unit matrix in Lorentz space. However,

$$\left[p^2 g^{\nu\rho} - p^\nu p^\rho \right] p_\rho = 0 ,$$

which means that the inverse does not exist, the matrix $\left[p^2 g^{\nu\rho} - p^\nu p^\rho \right]$ is not invertible. We can exploit gauge invariance to rewrite $\mathcal{L}$ in a physically

equivalent form (action remains the same) such that $\Delta_{\gamma\mu\nu}$ exists, which is called gauge fixing. For example, the *covariant gauges* are defined by requiring $\partial_\mu A^\mu(x) = 0$ for any space-time point x^μ. Adding

$$\mathcal{L}_{GF} = -\frac{1}{2\lambda}\left(\partial_\mu A^\mu\right)^2, \qquad \lambda \in \mathbb{R},$$

to $\mathcal{L}$, the action S remains the same. The term $\mathcal{L}_{GF}$ can be seen as a constraint, taken into account in the Lagrangian by a term with Lagrange multiplier (like in classical mechanics). The bilinear term becomes in this case

$$i\left(p^2 g^{\nu\rho} - \left(1 - \frac{1}{\lambda}\right)p^\nu p^\rho\right),$$

with inverse

$$\Delta_{\gamma\mu\nu}(p) = -\frac{i}{p^2}\left[g_{\mu\nu} - (1 - \lambda)\frac{p_\mu p_\nu}{p^2}\right].$$

Of course, physical results must be independent of λ. It is customary to choose $\lambda = 1$ (called Feynman gauge). In covariant gauges unphysical degrees of freedom (longitudinal and time-like polarizations) also propagate, which can be avoided by choosing *axial (physical) gauges*, defined with an arbitrary, but fixed vector n^μ (different from p^μ):

$$\mathcal{L}_{GF} = -\frac{1}{2\lambda}\left(n^\mu A_\mu\right)^2,$$

which leads to

$$\Delta_{\gamma\mu\nu}(p,n) = -\frac{i}{p^2}\left(g_{\mu\nu} - \frac{p_\mu n_\nu + n_\mu p_\nu}{p \cdot n} + \frac{(n^2 + \lambda p^2)\,p_\mu p_\nu}{(p \cdot n)^2}\right).$$

Since $p^2 = m^2 = 0$, we have:

$$\Delta_{\gamma\mu\nu}(p,n)\,p^\mu = 0, \qquad \Delta_{\gamma\mu\nu}(p,n)\,n^\mu = 0.$$

Thus, only 2 degrees of freedom propagate (transverse ones in the $n^\mu + p^\mu$ rest frame). A usual choice is $n^2 = 0$, $\lambda = 0$ (light cone gauge). The price we pay by choosing this gauge instead of a covariant one is that the propagator looks more complicated and the integral over p^μ diverges when p^μ becomes parallel to n^μ. In this gauge

$$\Delta_{\gamma\mu\nu}(p,n) = \frac{i}{p^2}\,d_{\mu\nu}(p,n)$$
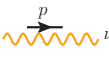
with
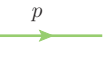
$$d_{\mu\nu}(p, n) = -g_{\mu\nu} + \frac{p_\mu n_\nu + n_\mu p_\nu}{p \cdot n} = \sum_{\lambda=1,2} \epsilon_\mu^{(\lambda)}(p)\epsilon_\nu^{(\lambda)}(p)^*, \qquad (18.2.3)$$
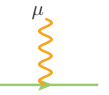
where $\epsilon_\mu^{(\lambda)}(p)$ is the polarization vector of the photon.

Feynman rules

In the Feynman gauge we have the following Feynman rules:

photon propagator: $\mu \overset{p}{\wwww} \nu = \Delta_{\gamma_{\mu\nu}}(p) = -i\frac{g_{\mu\nu}}{p^2}$

electron propagator: $\overset{p}{\longrightarrow} = \Delta_j(p) = i\frac{\slashed{p}+m_j}{p^2-m_j^2}$

vertex: $= \Gamma^\mu_{\gamma f_j \bar{f}_j} = -ie_j\, e\gamma^\mu$

- outgoing fermion: $\bar{u}(p)$
- incoming fermion: $u(p)$
- outgoing photon: $\epsilon_\mu^{(\lambda)}(p)^*$
- outgoing antifermion: $v(p)$
- incoming antifermion: $\bar{v}(p)$
- incoming photon: $\epsilon_\mu^{(\lambda)}(p)$.

Exercise 18.1
Show that in QED the covariant derivative transforms the same way as the field itself, namely if $f(x) \to U(x)f(x)$, then $D_\mu f(x) \to U(x)D_\mu f(x)$ where $D_\mu = \partial_\mu + i\, e\, A_\mu$.

Exercise 18.2
Show that in QED

$$\left[D_\mu, D_\nu\right] = i\, e\, F_{\mu\nu}$$

where $D_\mu = \partial_\mu + i\, e\, A_\mu$.

Exercise 18.3
Show that the generators of a special unitary group are traceless and hermitian.

Exercise 18.4

The generators of the SU(2) group in the fundamental representation are the Pauli matrices divided by two:

$$t_f^a = \frac{\sigma^a}{2}, \quad \sigma_1 = \begin{pmatrix} 0 & 1 \\ 1 & 0 \end{pmatrix}, \quad \sigma_2 = \begin{pmatrix} 0 & -i \\ i & 0 \end{pmatrix}, \quad \sigma_3 = \begin{pmatrix} 1 & 0 \\ 0 & -1 \end{pmatrix}$$

The adjoint representation of a group is defined as

$$(t_A^b)_{ac} = i f^{abc}$$

- *Compute the generators in the adjoint representation of SU(2)*

We define the constant T_R for a representation R by the condition

$$\mathrm{Tr}[t_R^a t_R^b] = \delta^{ab} T_R$$

- *compute this constant from the explicit form of the fundamental (T_F) and the adjoint (T_A) representation.*

The quadratic Casimir factor $C_2(R)$ of a representation R is defined by

$$C_2(R)\mathbb{1} = \sum_a t_R^a t_R^a$$

- *compute the quadratic Casimir factor in the fundamental (C_F) and the adjoint (C_A) representation of SU(2) using the explicit form of the representation matrices*

18.3   Cross sections

The cross section of a given elementary scattering process is given by

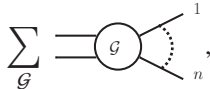$$\sigma = \frac{1}{2E_{CM}^2} \int d\phi_n\,(p_1, \ldots, p_n; Q) \frac{1}{S} \sum_{\mathrm{spin}} |\mathcal{M}_n|^2, \tag{18.3.4}$$

where E_{CM} is the total incoming energy, Q^μ is the total incoming four-momentum (in the centre-of-mass system $E_{CM} = \sqrt{Q^2}$), and

$$d\phi_n = (2\pi)^d \delta^d \left(Q^\mu - \sum_{j=1}^n p_j^\mu \right) \prod_{j=1}^n \frac{d^d p_j}{(2\pi)^{d-1}} \delta_+ \left(p_j^2 - m_j^2 \right) \tag{18.3.5}$$
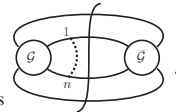
is the phase space for n final state particles in $d = 4 - 2\epsilon$ dimensions (in reality $\epsilon \to 0$ such that $d = 4$, but we allow $\epsilon \neq 0$ for later purposes). The index $+$ of the δ-function means that we consider only positive-energy solutions $E = +\sqrt{m^2 + \vec{p}^2}$, in other words

$$\delta_+ \left(p_j^2 - m_j^2 \right) = \delta \left(p_j^2 - m_j^2 \right) \Theta(E),$$

where $\Theta(E)$ is the Heaviside step-function (equals one if E is positive and zero otherwise). The amplitude $\mathcal{M}_n$ is obtained from all possible Feynman diagrams $\mathcal{G}$. The factor S^{-1} stands for the symmetry factor of identical particles in the final state and factors needed for averaging over incoming quantum (e.g. spin) states. One can obtain the integral of $\sum |\mathcal{M}_n|^2$ over the phase space directly from the so called "cut" diagrams following the Cutkosky rules. Computing the amplitude for n final state partons from Feynman diagrams,

$$i\mathcal{M}_n = \sum_{\mathcal{G}} \quad \text{} \quad ,$$

the cross section for the scattering of two incoming particles p_a and p_b into n final-state particles obtained as the sum over all possible squared diagrams and over all possible cuts of these diagrams:

$$\sigma(p_a p_b \to p_1, \ldots, p_n) = \frac{1}{2s} \frac{1}{S} \sum_{\mathcal{G},\text{cuts}} \quad \text{} \quad .$$

The Feynman rules for the cut diagrams are the usual ones with the following additional rules:

1. The sign of explicit factors of $i = \sqrt{-1}$ and directions of fermion arrows and those of all momenta are reversed in $\tilde{\mathcal{G}}$ as compared to $\mathcal{G}$.

2. We do not integrate over the loop momentum of initial-state momenta,

3. A cut line j in the initial state means a factor of

   - $\not{p}_j + m_j$ if j is a fermion,
   - $\not{p}_j - m_j$ if j is a anti-fermion,
   - $d_{\mu\nu}(p_j)$ if j is a (massless) gauge boson.

   In the final state the corresponding factors are

- $\left(\not{p} \pm m_j\right) 2\pi\delta_+\left(p_j^2 - m_j^2\right)$ if j is a fermion/anti-fermion,

- $d_{\mu\nu}(p_j)\, 2\pi\,\delta_+\left(p_j^2\right)$ if j is a (massless) gauge boson.

The δ_+ distributions express the on mass-shell conditions. These convert an integral over a loop momentum into the element of a one-particle phase-space measure.

Example: $e^+e^- \to \mu^+\mu^-$

We consider the reaction $e^+e^- \to \mu^+\mu^-$ as a very simple application of the Cutkosky rules. At leading-order (LO) accuracy there is only one Feynman diagram, shown in Fig. 18.1, that contributes to the amplitude at lowest order to this reaction.

In order to describe the kinematics of the reaction we use the *Mandelstam variables* (see Section 5.3)

$$s = (p_{e^-} + p_{e^+})^2 = (p_{\mu^-} + p_{\mu^+})^2,$$
$$t = (p_{e^-} - p_{\mu^-})^2 = (p_{e^+} - p_{\mu^+})^2,$$
$$u = (p_{e^-} - p_{\mu^+})^2 = (p_{e^+} - p_{\mu^-})^2.$$
$$(18.3.6)$$
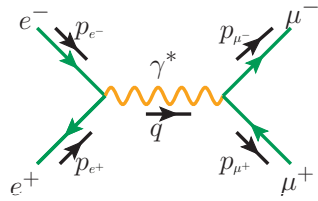
Figure 18.1: Feynman diagram for $e^+e^- \to \mu^+\mu^-$ at LO

Furthermore we express the coupling as $e^2 = 4\pi\,\alpha$. The cross section is then given by

$$\sigma(e^+e^- \to \mu^+\mu^-) = \frac{1}{2s}\frac{1}{S}\ \ \raisebox{-1em}{}\ \ .$$

Using the Feynman rules we obtain the squared matrix element from this diagram as

$$\sum_{\text{spin}} |\mathcal{M}_2|^2 = \frac{(4\pi\alpha)^2}{s^2}\, \mathrm{Tr}\left[\left(\not{p}_{e^+} - m_e\right)\gamma^\alpha\left(\not{p}_{e^-} + m_e\right)\gamma^\beta\right]$$
$$\times \mathrm{Tr}\left[\left(\not{p}_{\mu^-} + m_\mu\right)\gamma_\alpha\left(\not{p}_{\mu^+} - m_\mu\right)\gamma_\beta\right]$$

Evaluating the traces[1] we obtain for the squared matrix element, summed over spins

$$\sum_{\text{spin}} |\mathcal{M}_2|^2 = 8 \left(4\pi\alpha\right)^2 \left[\frac{(u - m_{\text{e}}^2 - m_{\mu}^2)^2 + (t - m_{\text{e}}^2 - m_{\mu}^2)^2}{s^2} + 2\frac{m_{\mu}^2 + m_{\text{e}}^2}{s} \right].$$

(18.3.7)

We leave the integration over the phase space as an exercise. As $m_\mu \simeq 200 m_{\text{e}}$, we usually neglect the mass of the electron.

Exercise 18.5
Derive the result in Eqn. (18.3.7) and integrate it over the two-particle phase space $\mathrm{d}\phi_2$.

Exercise 18.6
Use Mathematica and the Package Tracer.m (or FORM) to compute the following traces:

$$\text{Tr}\left(\slashed{p}_2 \gamma^\nu (\slashed{p}_1 - \slashed{k}_1) \gamma^\mu \slashed{p}_1 \gamma_\mu (\slashed{p}_1 - \slashed{k}_1) \gamma_\nu \right)$$

$$\text{Tr}\Big(\gamma^{\mu_1} \gamma^{\mu_2} \gamma^{\mu_3} \gamma^{\mu_4} \gamma^{\mu_5} \gamma^{\mu_6} \gamma^{\mu_7} \gamma^{\mu_8} \gamma^{\mu_9} \gamma^{\mu_{10}}$$
$$\times \gamma_{\mu_1} \gamma_{\mu_2} \gamma_{\mu_3} \gamma_{\mu_4} \gamma_{\mu_5} \gamma_{\mu_6} \gamma_{\mu_7} \gamma_{\mu_8} \gamma_{\mu_9} \gamma_{\mu_{10}} \Big)$$

18.4 Quantum chromodynamics

In quantum chromodynamics the matter fields are again fermions with an additional (inner) degree of freedom: the colour, which can take N_{c} values. (We shall see in the next chapter that in QCD $N_{\text{c}} = 3$, but it is useful to keep it arbitrary and specify only when making comparison with experiment.) These fields are called quark fields: q_f^k (with $f = 1, \ldots, n_f$, where n_f is the number of different flavours, and $k = 1, \ldots, N_{\text{c}}$). The precise matter content is shown in Table 18.1. Thus, the Lagrangian becomes

$$\mathcal{L}_q = \sum_{f=1}^{n_f} \sum_{k,l=1}^{N_{\text{c}}} \bar{q}_f^k \left(\mathrm{i}\slashed{\partial} - m_f \right) \delta_{kl} \, q_f^l.$$

---

[1] The *Mathematica* package `Tracer.m` is useful for computing the traces. (see http://library.wolfram.com/infocenter/MathSource/2987/)

f	1	2	3	4	5	6
q_f	u	d	s	c	b	t
m_f	2.12 MeV	4.69 MeV	92.5 MeV	1.27 GeV	4.2 GeV	172.6 GeV

Table 18.1: The six quark flavours. Their baryon number is $B = 1/3$. For light flavours the masses correspond to running $\overline{\text{MS}}$ quark masses (see definition in section 19.4) at 2 GeV, for heavy flavours c and b the mass values of Ref. [Bazavov et al., 2018] and for t quark it is the pole mass.

If we apply a transformation $q^k \to q^{k'} = U_{kl} q^l$, with

$$U_{kl} = \exp\left\{ i \sum_{a=1}^{N_c^2-1} t^a \, \theta^a \right\}_{kl} \equiv \exp\left\{ i\boldsymbol{t} \cdot \boldsymbol{\theta} \right\}_{kl}$$

where $\theta^a \in \mathbb{R}$, then the Lagrangian again remains invariant under the global $SU(N_c)$ transformation: $\mathcal{L}_q(q) = \mathcal{L}_q(q')$, therefore the colour charges are conserved. The $(t^a)_{kl}$ are $N_c \times N_c$ matrices, which constitute the fundamental representation of the generators T^a (called colour-charge operators). Both satisfy Eq. (18.1.1). For $SU(3)$ the matrices t^a are the Gell-Mann matrices.

Can we make $\mathcal{L}_q(q)$ invariant under local $SU(N_c)$ transformations? The answer is again yes, we can and the steps are similar as in the case of QED:

1. Introduce an A_μ^a coloured vector field with the following transformation property under $SU(N_c)$ transformations:

$$\boldsymbol{t} \cdot A_\mu \to \boldsymbol{t} \cdot A_\mu' = U(x)\boldsymbol{t} \cdot A_\mu U^{-1}(x) + \frac{i}{g_s}(\partial_\mu U(x))U^{-1}(x),$$

where $U(x) = \exp\{i\boldsymbol{t} \cdot \boldsymbol{\theta}(x)\}$.

2. Replace $\partial_\mu \delta_{kl}$ with $D_\mu[A]_{kl} = \partial_\mu \delta_{kl} + ig_s(\boldsymbol{t} \cdot A_\mu)_{kl}$, where g_s is the strong coupling. $D_\mu[A]_{kl} q_l(x)$ transforms covariantly, i.e. the same way as the quark field $q_k(x)$.

3. Introduce a kinetic term

$$\mathcal{L}_A = -\frac{1}{4} F_{\mu\nu}^a[A] F^{a\mu\nu}[A],$$

with the non-abelian field strength $F_{\mu\nu}^a$ given by

$$F_{\mu\nu}^a[A] = \partial_\mu A_\nu^a - \partial_\nu A_\mu^a - g_s \underbrace{f^{abc} A_\mu^b A_\nu^c}_{\equiv \left(\boldsymbol{A}_\mu \times \boldsymbol{A}_\nu\right)^a},$$

so the Lagrangian contains cubic and quartic self-interactions.

Thus we find that the gauge boson field is now self-interacting. In fact, these self-interactions are the sources of the main difference between QED and QCD. We shall see that as a result QCD is a 'perfect theory' in the sense that it is asymptotically free.[2] Furthermore, *among quantum field theories in d = 4 dimensions only non-abelian gauge theories are asymptotically free*. It is also plausible that the self-interactions are the sources of colour confinement, i.e. the colour neutrality of hadrons, but we do not have a proof based on first principles of QCD dynamics.

Similarly to QED, the quantization requires a gauge fixing. For example, the covariant gauge fixing is achieved by adding the term

$$\mathcal{L}_{\text{GF}} = -\frac{1}{2\lambda} \left(\partial^\mu A_\mu\right)^2$$

to the Lagrangian (the boldface means vector in colour space and λ is a Lagrange multiplicator). As opposed to QED, in this case the covariant gauge requires the introduction of ghost fields (coloured complex scalars with Fermi statistics!–hence the name) η, with the following kinetic term:

$$\mathcal{L}_G = \sum_{a,b} \partial^\mu \eta^{a\,\dagger} D_\mu[A]_{ab}\, \eta^b.$$

The necessity and form of the ghost-field Lagrangian can most easily be derived from the path integral formalism. For a physical motivation we refer to [Ellis, 1988].

In summary, the complete Lagrangian of QCD is

$$\mathcal{L}_{\text{QCD}} = \mathcal{L}_{\text{cl}} + \mathcal{L}_{\text{GF}} + \mathcal{L}_G,$$

where 'cl' stand for the gauge invariant classical Lagrangian

$$\mathcal{L}_{\text{cl}} = \sum_{f=1}^{6} \mathcal{L}_q(q_f, m_f) + \mathcal{L}_g(A). \tag{18.4.8}$$

---

[2]To be defined precisely later.

In Eq. (18.4.8)

$$\mathcal{L}_q(q_f, m_f) = \sum_{k,l=1}^{N_c} \bar{q}_f^k \left(i\gamma_\mu D^\mu[A] - m_f\right)_{kl} q_f^l,$$

with

$$(D_\mu)[A]_{ab} = \left(\partial_\mu + ig_s \sum_{c=1}^{N_c^2-1} A_\mu^c T^c\right)_{ab}$$

and the kinetic term for the gluon field, the gauge field of QCD:

$$\mathcal{L}_g(A) = -\frac{1}{4} \sum_{a=1}^{N_c^2-1} F_{\mu\nu}^a[A] F^{a\,\mu\nu}[A].$$

The ghost fields are absent if we use physical gauges, which will be our choice (defined precisely later).

It is clear that there is an unprecedented large number of degrees of freedom we have to sum over:

1. spin and space-time as in any field theory, not exhibited above,

2. flavour and colour, specific to QCD.

As a result, computations in QCD are rather cumbersome. During the last 25 years a lot of effort was invested to find simpler ways of computing QCD cross sections and to automate the computations.
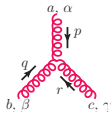
Feynman rules of QCD
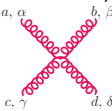
Propagators (Feynman's '+iϵ'-prescription is assumed, but not shown):

gluon propagator: a, μ b, ν $= \Delta_{g,\mu\nu}^{ab}(p) = \delta^{ab} \Delta_{\gamma,\mu\nu}(p)$

quark propagator: i j $= \Delta_q^{ij}(p) = \delta^{ij} \Delta_q(p)$

ghost propagator: a b $= \Delta^{ab}(p) = \delta^{ab} \frac{i}{p^2}$ (not needed in physical gauges)

Vertices:

quark-gluon: $= \Gamma_{gq\bar{q}}^{\mu,a} = -ig_s (t^a)_{ij} \gamma^\mu$

three-gluon:

$$\equiv \Gamma^{a,\,b,\,c}_{\alpha,\,\beta,\,\gamma}(p,q,r) =$$

$$= -\mathrm{i}g_s\,(F^a)_{bc}\,V_{\alpha,\beta,\gamma}(p,q,r)\,,\quad p+q+r=0$$

with $V_{\alpha,\beta,\gamma}(p,q,r) = (p-q)_\gamma\,g_{\alpha\beta} + (q-r)_\alpha\,g_{\beta\gamma} + (r-p)_\beta\,g_{\alpha\gamma}$

four-gluon:

$$\equiv \Gamma^{a,b,c,d}_{\alpha,\beta,\gamma,\delta}$$

ghost-gluon: $\equiv \Gamma^{\mu,\,a}_{g\eta\bar\eta} = -\mathrm{i}g_s\,(F^a)_{ab}\,p^\mu$ (not needed in physical gauges)

The matrices F^a constitute the representation of the generators of the colour algebra in the adjoint representation and are defined below.
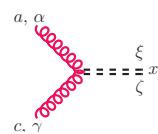
The four-gluon vertex, given by

$$
\begin{aligned}
\Gamma^{abcd}_{\alpha\beta\gamma\delta} = -\mathrm{i}g_s^2\,\big[&+ f^{xac}\,f^{xbd}\,(g_{\alpha\beta}g_{\gamma\delta} - g_{\alpha\delta}g_{\beta\gamma}) \\
&+ f^{xad}\,f^{xbc}\,(g_{\alpha\beta}g_{\gamma\delta} - g_{\alpha\gamma}g_{\beta\delta}) \\
&+ f^{xab}\,f^{xcd}\,(g_{\alpha\gamma}g_{\beta\delta} - g_{\alpha\delta}g_{\beta\gamma})\big]\,,
\end{aligned}
$$

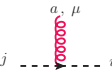differs from the rest of the Feynman rules in the sense that it is not in a factorized form of a colour factor and a tensor factor. This is an inconvenient feature because it prevents the separate summation over colour and Lorentz indices and complicates automation. We can circumvent this problem by introducing a *fake* field with propagator

 $= \tfrac{\mathrm{i}}{2}\delta^{ab}(g^{\alpha\beta}g^{\gamma\delta} - g^{\alpha\delta}g^{\beta\gamma})$

that couples only to the gluon with vertex

 $= \mathrm{i}\sqrt{2}g_s\,f^{xac}\,g^{\alpha\xi}\,g^{\gamma\zeta}.$

We can check that a single four-gluon vertex can be written as a sum of three diagrams (see exercise). This way the summation over colour and Lorentz indices factorize completely, which helps automation and makes possible for us to concentrate on the colour algebra independently of the rest of the Feynman rules.

Exercise 18.7
Show that in SU(N) gauge theories

$$\left[D_\mu, D_\nu\right] = \mathrm{i}g F^a_{\mu\nu} T^a \quad \text{where} \quad F^a_{\mu\nu} = \partial_\mu A^a_\nu - \partial_\nu A^a_\mu - g f^{abc} A^b_\mu A^c_\nu .$$

Exercise 18.8
Show that $F^a_{\mu\nu}$ transforms according to the adjoint representation of SU(N):

$$F^a_{\mu\nu} \to F^a_{\mu\nu} - f^{abc} \theta^b F^c_{\mu\nu} .$$

Exercise 18.9
Show that the four-gluon vertex can be written as a sum of three graphs with the help of the fake field such that in each graph the colour and Lorentz indices are factorized.

18.5   Basics of colour algebra
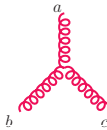
Examining the Feynman rules, we find that there are two essential changes as compared to QED. One is that there is an additional degree of freedom: colour. Another is that there are new kind of couplings: the self couplings of the gauge field. We now explore the effect of the first, and leave the second to the next chapter.

In order to see how to treat the colour degrees of freedom, we set to unity all but the colour part of the Feynman rules and try first to develop an efficient technique to compute the coefficients involving the colour structure. This is possible because the colour degrees of freedom factorize from the other degrees of freedom completely. We use the following graphical representation for the colour charges in the fundamental representation:

 $= (t^a)_{ij}$. The normalization of these matrices is given by

$\mathrm{Tr}\left(t^a t^b\right) \equiv {}_a\!\!\!$ $_b = {}_{T_R\,a}$ $_b = T_R\,\delta^{ab}$. The usual choice is $T_R = \frac{1}{2}$, but $T_R = 1$ is also often used. We shall use both.

In the adjoint representation the colour charge T^a is represented by the matrix $(F^a)_{bc}$ that is related to the structure constants by

$$(F^a)_{bc} = \left(F^b\right)_{ca} = (F^c)_{ab} = -\mathrm{i}\, f_{abc} =$$

where F^a with $a = 1, \ldots, (N_c^2 - 1)$ are $(N_c^2 - 1) \times (N_c^2 - 1)$ matrices that again satisfy the commutation relation (18.1.1). The graphical notation in the adjoint representation is not unique. For the matrix $(F^a)_{bc}$ we assume an arrow pointing from index c to b, opposite to which we read the indices of (F^a). On the structure constants the indices are not distinguished, therefore arrows do not appear. However, these are completely antisymmetric in their indices, so the ordering matters. By convention, in the graphical representation the ordering of the indices is counterclockwise. The representation matrices are invariant under $SU(N)$ transformations.

The sums $\sum_a t_{ij}^a t_{jk}^a$ and $\mathrm{Tr}\big(F^a F^b\big)$ have two free indices in the fundamental and adjoint representations. These are invariant under $SU(N)$ transformations, so must be proportional to the unit matrix,
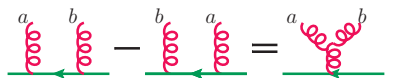
$$\sum_{j,a} t_{ij}^a t_{jk}^a = C_{\mathrm{F}}\, \delta_{ik}, \qquad \mathrm{Tr}\left(F^a F^b\right) = C_{\mathrm{A}}\, \delta^{ab}. \qquad (18.5.9)$$

Eq. (18.5.9) is depicted graphically as

Here C_{F} and C_{A} are the eigenvalues of the quadratic Casimir operator in the fundamental and adjoint representations. In the familiar case of angular momentum operator algebra ($SU(2)$), the quadratic Casimir operator is the square of the angular momentum with eigenvalues $j(j+1)$. The fundamental representation is two dimensional, realized by the ($\frac{1}{2}$ times the) Pauli matrices acting on two-component spinors, when $j = 1/2$ and $C_{\mathrm{F}} = 1/2(1/2 + 1) = 3/4$. In the adjoint representation $j = 1$ and $C_{\mathrm{A}} = 2$. Below we derive the corresponding values for general $SU(N)$.

The commutation relation (18.1.1) can be represented graphically by

Let us first multiply this commutator with another colour charge operator. Next, sum over the fermion index and then multiply with δ_{ik}. As a result, we obtain the resolution of the three-gluon vertex as products of colour charges:

 $\Rightarrow \mathrm{Tr}(t^a t^b t^c) - \mathrm{Tr}(t^c t^b t^a) = \mathrm{i}\, T_R f^{abc}$.

The expression $\sum_a t_{ij}^a t_{kl}^a$ is invariant under $SU(N)$ transformations, thus has to be expressible as a linear combination of $\delta_{il}\delta_{kj}$ and $\delta_{ij}\delta_{kl}$ (the third combination of Kronecker δ's is not possible, the direction of arrows do not match). The two coefficients can be obtained by making contractions with $\delta_{il}\delta_{jk}$ and $\delta_{ij}\delta_{kl}$. Thus we obtain the Fierz identity,

$$\sum_a t_{ij}^a t_{kl}^a = T_R \left(\delta_{il}\delta_{kj} - \frac{1}{N_c}\delta_{ij}\delta_{kl} \right),$$

or graphically

We now show some examples of how one can compute the colour algebra structure of a QCD amplitude, in particular we will also find explicit values for C_F and C_A in the exercises. Taking the trace of the identity in the fundamental and in the adjoint representation we obtain

 $= N_c$, $= N_c^2 - 1$.

Then, using the expressions for the fermion and gluon propagator corrections, we immediately find

 $= C_F N_c$, $= C_A \left(N_c^2 - 1 \right)$.

The generators are traceless,

$$= \text{Tr}\,(t^a) = 0\;,\qquad\qquad = \text{Tr}\,(F^a) = 0\,.$$

These graphical rules make the evaluation of colour algebra easy. Nevertheless, nowadays computer algebra codes make computation of colour sums an automated procedure. For instance, you can type $\texttt{In[1]:= Import["http://www.feyncalc.org/install.m"]}$ in a *Mathematica* session to explore some code for that purpose.

Exercise 18.10
Consider the process $q\bar{q} \to ggg$. Compute the colour structures that appear in the squared matrix element.

Exercise 18.11
Insert a quark loop on a single gluon loop and try to find the value of C_F. Compute C_A in a similar way. Hint: use the resolution of the three-gluon vertex.

Exercise 18.12
Determine the colour factors A,B,C in

18.6   Are we done?

We now have the Feynman rules with colour and the rest (momentum and couplings) factorized and we gained some insight how to perform the colour algebra. Thus it seems that we are in the position to compute the cross section of any process up to the desired accuracy in perturbation theory, just

as we can do in QED. So it may appear that conceptually we are done. Well, we are going to see big surprises!

The first conceptual challenge is due to a phenomenological observation. In QED perturbation theory is applicable because the elementary excitations of the quantum fields, the electrons and photons can be observed as stable, free particles. Thus asymptotic states are parts of the physical reality. On the contrary, free quarks and gluons (usually called simply partons) have never been observed in nature. This experimental fact can be reformulated saying that the probability of observing a final state with any *fixed number of on-shell partons* is zero. This negative result has been turned into the principle of 'quark confinement'. Thus it is questionable whether a quantum field theory (QFT) of quark and gluon fields can describe the observed world of particles where in addition to leptons only hadrons have been found. In fact, a main research project at the Large Electron Positron collider (LEP) was to find an answer to this question in a well controlled and quantitative manner. It turned out that the answer is positive if we make an assumption that we cannot prove from first principles:

> The result of a low-order perturbative computation in QCD is an approximation to sufficiently inclusive hadronic cross section if (i) the total centre-of-mass energy Q of partons is much larger than the mass of quarks, $Q \gg m_q$, and (ii) Q is far from hadronic resonances and thresholds.

We shall define precisely what 'sufficiently inclusive' means later. Predictions made on the basis of this assumption agree with measurements (e.g. made at LEP) within the expected accuracy of the prediction, which we are to define also later.

Based on this assumption, it makes sense to make predictions with quark and gluon asymptotic states. However, in QCD the complexity of the Feynman rules will make higher order computations prohibitive. Indeed, the largest effort in QCD computations during the past 25 years went into devising ever more efficient methods to decrease the algebraic complexity of the computations. This research is driven by the observation that the QCD Lagrangian is highly symmetric, which has to be reflected in the final results. Thus the complications somehow appear mainly because with our rules we artificially introduce complications at intermediate steps of the computations, which cancels to large extent in the final formulae. In the next subsection we shall see an example of simplifications. But learning about the symmetries of QCD is interesting and useful not only for technical purposes, so let us make an inventory of those.
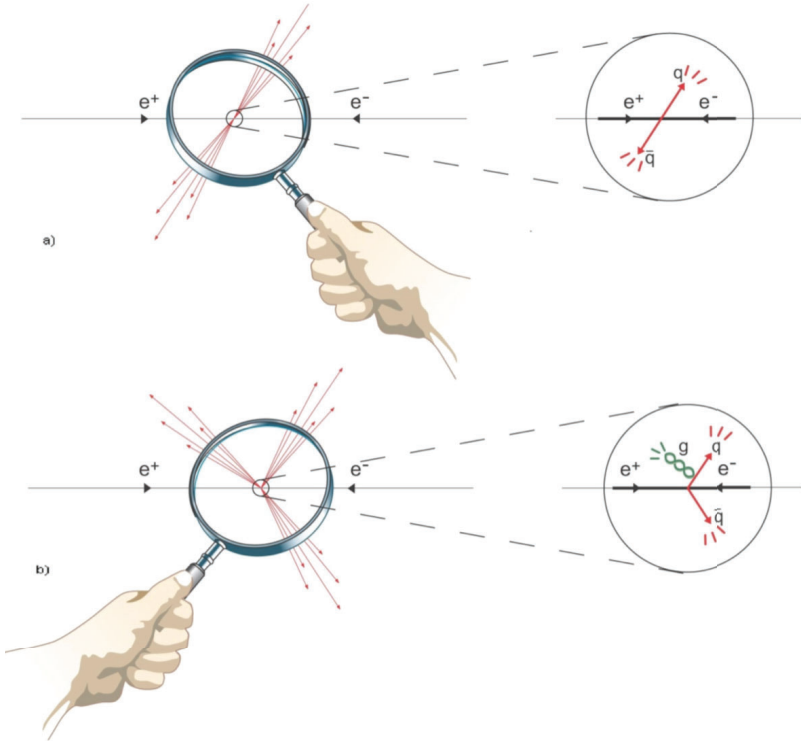
Figure 18.2: Illustration of the approximation of hadronic final states by partonic events in electron-positron annihilation.

18.7   Symmetries of the classical Lagrangian

The symmetries can be grouped into two large categories: exact symmetries and approximate ones. Space-time symmetries are exact. These consist of invariance against continuous transformations: translations and Lorentz-transformations (rotations and boosts). In addition QCD is invariant under scale transformation:

$$x^\mu \to \lambda x^\mu \quad A_\mu(x) \to \lambda^{-1} A_\mu(\lambda x) \quad q(x) \to \lambda^{-3/2} q(\lambda x) \qquad (18.7.10)$$

and conformal transformations. The Lagrangian is also invariant under parity (P) transformation, as well as simultaneous charge conjugation (C), space and time reversal (PT)–recall Chapter 1–, in agreement with observed

properties of strong interactions (C, P and T violating strong decays are not observed).

We have already discussed exact symmetry in colour space: gauge invariance. In addition to the classical Lagrangian of Eq. (18.4.8), there exists an additional gauge invariant dimension-four operator, the Θ-term:

$$\mathcal{L}_\Theta = \frac{\Theta g_s}{32\pi^2} \sum_a F^a_{\mu\nu} \tilde{F}^{a,\mu\nu}, \quad \text{with} \quad \tilde{F}^{a,\mu\nu} = \frac{1}{2} \epsilon^{\mu\nu\alpha\beta} F^a_{\alpha\beta},$$

that violates P and T. As experimentally $\Theta < 10^{-9}$, we set $\Theta = 0$ in perturbative QCD.

Another interesting feature of $\mathcal{L}_{cl}$ is that it is almost supersymmetric.[3] For one massless flavour

$$\mathcal{L}_{cl} = -\frac{1}{4} \sum_a F^a_{\mu\nu} F^{a,\mu\nu} + \bar{q} i \slashed{D} q,$$

which is very similar to the Lagrangian of $N = 1$ supersymmetric gauge theory,

$$\mathcal{L}_{cl}^{SUSY} = -\frac{1}{4} \sum_a F^a_{\mu\nu} F^{a,\mu\nu} + \bar{\lambda} i \slashed{D} \lambda.$$

The only difference is that the quark q transforms under the fundamental, while the gluino λ under the adjoint representation of the gauge group.

An important approximate symmetry of the classical Lagrangian is related to the quark mass-matrix. Let us introduce the quark flavour triplet

$$\psi = \begin{pmatrix} u \\ d \\ s \end{pmatrix} = \begin{pmatrix} q_1 \\ q_2 \\ q_3 \end{pmatrix},$$

with each component being a four-component Dirac spinor , and the combinations

$$P_\pm = \frac{1}{2}(\mathbb{1} \pm \gamma_5), \qquad \gamma_5 = i\gamma_0\gamma_1\gamma_2\gamma_3. \tag{18.7.11}$$

The latter are projections:

$$P_+ P_- = P_- P_+ = 0, \quad P_\pm^2 = P_\pm, \quad P_+ + P_- = \mathbb{1}.$$

---

[3]We note this interesting feature without detailed explanation of supersymmetry, which can be found in [Martin, 1997].

It follows from Clifford algebra that $\gamma_\mu P_\pm = P_\mp \gamma_\mu$. We define $\psi_\pm = P_\pm \psi$. Using $\gamma_5^2 = \mathbb{1}$, we find that $\psi_\pm$ are eigenvectors of γ_5 with ± 1 eigenvalues:

$$\gamma_5 \psi_\pm = \pm \psi_\pm \,.$$

From the definition of the Dirac adjoint, $\overline{\psi} = \psi^\dagger \gamma_0$, we obtain $\overline{\psi_\pm} = \overline{\psi} P_\mp$. Thus the quark sector of the Lagrangian can be rewritten in terms of the chiral fields $\psi_\pm$:

$$\begin{aligned}
\mathcal{L}_{\text{cl}} = \overline{\psi}\, i\, \gamma_\mu D^\mu\, \psi &= \overline{\psi}(P_+ + P_-) i\, \gamma_\mu D^\mu\, (P_+ + P_-)\psi = \\
&= \overline{\psi} P_+ i\, \gamma_\mu D^\mu\, P_- \psi + \overline{\psi} P_- i\, \gamma_\mu D^\mu\, P_+ \psi = \\
&= \overline{\psi}_- i\, \gamma_\mu D^\mu\, \psi_- + \overline{\psi}_+ i\, \gamma_\mu D^\mu\, \psi_+ = \\
&= \mathcal{L}_- + \mathcal{L}_+ \equiv \mathcal{L}_{\text{L}} + \mathcal{L}_{\text{R}} \,.
\end{aligned}$$

This decomposition would not work if the gluon field in the covariant derivative were not a Lorentz-vector. In this chiral form the left- and right-handed fields decouple, so the Lagrangian is invariant under separate $U(N_{\text{f}})$ transformations for the left- and right-handed fields, i.e. under $U_{\text{L}}(N_{\text{f}}) \times U_{\text{R}}(N_{\text{f}})$, hence it is called chiral symmetry. Indeed, if $(g_{\text{L}}, g_{\text{R}}) \in U_{\text{L}}(N_{\text{f}}) \times U_{\text{R}}(N_{\text{f}})$, then under the transformation

$$\psi_{\text{L}} \to g_{\text{L}} \psi_{\text{L}}, \qquad \overline{\psi}_{\text{L}} \to \overline{\psi}_{\text{L}} g_{\text{L}}^\dagger, \qquad g_{\text{R}} = 1$$

$\mathcal{L}_{\text{L}}$ remains invariant. This symmetry is exact if the quarks are massless. The group elements can be parametrized using $2N_{\text{f}}^2$ real numbers $\{\alpha, \alpha_a, \beta, \beta_b\}$ $(a, b = 1, \ldots N_{\text{f}}^2 - 1)$,

$$\begin{aligned}
(g_{\text{L}}, g_{\text{R}}) = \Bigg(&\exp(i\alpha) \exp(i\beta) \exp\Bigg(i \sum_a \alpha_a T^a\Bigg) \exp\Bigg(i \sum_b \beta_b T^b\Bigg), \\
&\exp(i\alpha) \exp(-i\beta) \exp\Bigg(i \sum_a \alpha_a T^a\Bigg) \exp\Bigg(-i \sum_b \beta_b T^b\Bigg)\Bigg) \\
&\in U_{\text{V}}(1) \otimes SU_{\text{L}}(N_{\text{f}}) \otimes U_{\text{A}}(1) \otimes SU_{\text{R}}(N_{\text{f}})
\end{aligned}$$

where the matrices T^a represent the generators of the group ($N_{\text{f}} \times N_{\text{f}}$ matrices). The transformations $(\exp(i \sum_a \alpha_a T^a), \exp(i \sum_a \alpha_a T^a))$, acting as $\psi \to \exp(i \sum_a \alpha_a T^a \mathbb{1})\psi$, form a vector subgroup $SU_{\text{V}}(N_{\text{f}})$. However, the transformations $(\exp(i \sum_b \beta_b T^b), \exp(-i \sum_b \beta_b T^b))$, acting as $\psi \to \exp(i \sum_b \beta_b T^b \gamma_5)\psi$, do not form an axial-vector subgroup because the algebra is not closed,

$$[T^a \gamma_5, T^b \gamma_5] = i \sum_c f^{abc} T^c \mathbb{1} \qquad (\gamma_5^2 = \mathbb{1} \neq \gamma_5).$$

This chiral symmetry is not observed in the hadron spectrum. Therefore, we assume that vacuum has a non-zero vacuum expectation value (VEV) of the light-quark operator,

$$\langle 0|\bar{q}q|0\rangle = \langle 0|\bar{u}u + \bar{d}d|0\rangle \simeq (250\,\text{MeV})^3 \, ,$$

a chiral condensate that connects left- and right-handed fields,

$$\langle 0|\bar{q}q|0\rangle = \langle 0|\bar{q}_\text{L}q_\text{R} + \bar{q}_\text{R}q_\text{L}|0\rangle \, .$$

The condensate breaks chiral symmetry spontaneously to $SU_\text{V}(N_\text{f}) \otimes U_\text{V}(1)$. This remaining symmetry explains the existence of good quantum numbers of isospin and baryon number, as well as the appearance of $N_\text{f}^2 - 1 = 8$ massless mesons, the Goldstone bosons. As non-zero quark masses violate the chiral symmetry, which is broken spontaneously, the Goldstone bosons are not exactly massless. Thus we have natural candidates for the Goldstone bosons: we can identify those with the pseudo scalar meson octet. In practice, we assume exact chiral symmetry and treat the quark masses as perturbation. This procedure leads us to chiral perturbation theory (χPT), which is capable to predict the (ratios of) masses of light quarks, scattering properties of pions and many more. Although, χPT is a non-renormalizable QFT[4], it can be made predictive order by order in perturbation theory if the measured values of sufficiently many observables are used to fix the couplings of interaction terms at the given order.

The QCD Lagrangian was written 45 years ago. Since then many attempts were tried to solve it and mature fields emerged that aim at solving the theory in a limited range of physical phenomena. For instance, χPT is a perturbation theory that uses low-energy information (in the MeV range) to explain the world of hadrons and the masses of light quarks. In the same energy range non-perturbative approaches, notably lattice QCD and sum rules, have been developed for the same purpose. By now it is possible to explain the spectrum of the light hadrons from first principles using lattice QCD [Durr et al., 2008]. The main goal at colliders, our focus in this book, is different. We shall prove that perturbation theory can give reliable predictions for scattering processes at high energies, that is the topic of jet physics.

We have seen that the classical QCD Lagrangian shows many interesting symmetry properties that can be utilized for (i) easing computations, (ii) checking results, (iii) hinting on solving QCD. We shall see that some of these symmetries are violated by quantum corrections, which leads to important physical consequences. In QCD an important example is scaling violations.

---

[4]We discuss renormalization in section 19.2.

Another example is the axial anomaly that provides strong constraints on
possible QFT's.

_____

Exercise 18.13
*Show that the classical action of QCD in Eq. (18.4.8) is invariant under scale
transformations (18.7.10). Is the classical Lagrangian also scale invariant?*

Exercise 18.14
*Show that the classical Lagrangian of QCD in Eq. (18.4.8) is invariant under
the charge conjugation defined by $C(\psi) = -i\gamma_2\psi^*$.*

18.8 $SU(N)$-amplitudes at tree level

Let us see an explicit example how we can exploit symmetry properties to
make QCD computations more efficient. The number of algebraic terms that
contribute to QCD amplitudes as obtained from the Feynman rules increase
dramatically with increasing number of multiplicity (number of partons in the
final state). For instance, the number of diagrams for the reaction $gg \rightarrow ng$
at tree level is (n_d denotes the number of diagrams):

n	2	3	4	5	6	7	8	9
n_d	4	25	220	2485	34300	559405	10525900	224449225

Furthermore, these diagrams contain complicated non-abelian vertices. The
number of terms belonging to a given amplitude increases factorially. We can
organize the calculation of $|M_n|^2$ better if we divide the full amplitude into
sums of gauge invariant contributions. These can be found by expanding the
amplitude in colour space using an orthogonal basis. Then each coefficient
of a basis vector has to be gauge invariant.

A purely gluonic tree[5] amplitude can be written as

$$M_{n\epsilon_1...\epsilon_n}^{a_1...a_n}(p_1,\ldots,p_n) = \sum_{\{1,2,...,n\}'} \text{Tr}\,(t^{a_1}\ldots t^{a_n})\,m\,(p_1,\epsilon_1;\ldots;p_n,\epsilon_n)$$

where the sum runs over $(n-1)!$ non-cyclic permutations of the indices,
denoted by the prime on $\{\ldots\}$. The usual normalization used in this repre-
sentation is $T_R = 1$. The different traces are orthogonal only at leading order

_____

[5]Similar, but more complex decomposition can be given also for loop amplitudes.

in N_c:

$$\sum_{a_i=1}^{N_c^2-1} \text{Tr}\left(t^{a_1} \ldots t^{a_n}\right) \text{Tr}\left(t^{b_1} \ldots t^{b_n}\right)^* = N_c^{n-2}\left(N_c^2 - 1\right)\left[\delta_{\{a\}\{b\}} + O\left(\frac{1}{N_c^2}\right)\right]$$

where $\{b\}$ is a permutation of $\{a\} \equiv (a_1, \ldots, a_n)$. However, gauge invariance must hold order-by-order in the $1/N_c$-expansion. So we find that the *colour sub-amplitudes* $m(1, 2, \ldots, n) \equiv m(p_1, \epsilon_1; \ldots; p_n \epsilon_n)$ have the following properties:

1. they are gauge invariant,

2. they are invariant under cyclic permutations of indices,

3. they obey the relation $m(n, n-1, \ldots, 1) = (-1)^n \; m(1, 2, \ldots, n)$,

4. they obey the relation

$$m(1, 2, 3, \ldots, n) + m(2, 1, 3, \ldots, n) + m(2, 3, 1, \ldots, n) + \ldots$$
$$+ m(2, 3, \ldots, 1, n) = 0,$$

5. they factorize on multi-gluon poles (this feature will be discussed later),

6. they sum independently in the squared matrix element to leading order in N_c:

$$\sum_{\text{colour}} |\mathcal{M}_n|^2 = N_c^{n-2}\left(N_c^2 - 1\right)\left[\sum |m(1, \ldots, n)|^2 + O\left(N_c^{-2}\right)\right]$$

18.9 Spinor helicity formalism

We compute amplitudes of fixed helicities of the external legs, which has the following advantages:

- Helicity is conserved along massless fermion lines (vector interaction conserves helicity).

- We can exploit gauge invariance and select an explicit representation for the polarization vectors.

- Different helicity configurations do not interfere. Thus, in computing $\sum_{\text{helicity}} |\mathcal{M}_n|^2$, we sum the helicity amplitudes incoherently.

We introduce the following formalism from Ref. [Mangano and Parke, 1991]:

- $\psi(p)$ is a massless Dirac spinor that satisfies the Dirac equation, $\not{p}\psi(p) = 0$, and the on-shell condition, $p^2 = 0$.

- We define two chiral projections

$$\psi_\pm(p) \equiv P_\pm \psi(p) = \frac{1}{2}(\mathbb{1} \pm \gamma_5)\psi(p) = \psi_\mp(p)^c,$$

$$P_+ + P_- = \mathbb{1}, \qquad P_\pm^2 = P_\pm,$$

where $\psi(p)^c = C\psi(p)^*$ and $C\gamma_\mu^* C^{-1} = \gamma_\mu$ is the charge conjugation.

- Furthermore, we use the following notation:

$$|p\pm\rangle \equiv \psi_\pm(p), \qquad\qquad \langle p\pm| \equiv \overline{\psi_\pm}(p)$$

where $\langle p\pm|$ is an outgoing fermion, while $|p\pm\rangle$ is an outgoing antifermion of momentum p and helicity $\pm$ and

$$\langle pq\rangle \equiv \langle p-|q+\rangle = \overline{\psi_-}(p)\,\psi_+(q)$$
$$[pq] \equiv \langle p+|q-\rangle = \overline{\psi_+}(p)\,\psi_-(q)$$

with normalization $\langle p\pm|\gamma_\mu|p\pm\rangle = 2p_\mu$. In this formalism, the following properties hold:

$$\langle pq\rangle = -\langle qp\rangle, \qquad [pq] = -[qp] \qquad \text{(hence} \quad \langle pp\rangle = [pp] = 0)$$

$$\langle pq\rangle^* = \operatorname{sign}(p\cdot q)\,[qp], \qquad |\langle pq\rangle|^2 = |2p\cdot q| \equiv \left|s_{pq}\right|$$

which imply $s_{pq} = \langle pq\rangle[qp]$. Furthermore,

$$2\,|p\pm\rangle\,\langle q\pm| = \frac{1}{2}(\mathbb{1}\pm\gamma_5)\gamma^\mu\,\langle q\pm|\gamma_\mu|p\pm\rangle$$

$$\Rightarrow \; |p\pm\rangle\,\langle p\pm| = \frac{1}{2}(\mathbb{1}\pm\gamma_5)\not{p} \text{ and } \not{p} = |p+\rangle\,\langle p+| + |p-\rangle\,\langle p-|.$$

Furthermore,

$$\langle p\pm|\gamma_{\mu_1}\ldots\gamma_{\mu_{2n+1}}|q\pm\rangle = \langle q\mp|\gamma_{\mu_{2n+1}}\ldots\gamma_{\mu_1}|p\mp\rangle,$$
$$\langle p\pm|\gamma_{\mu_1}\ldots\gamma_{\mu_{2n}}|q\mp\rangle = -\langle q\pm|\gamma_{\mu_{2n}}\ldots\gamma_{\mu_1}|p\mp\rangle,$$

$$\langle AB\rangle\langle CD\rangle = \langle AD\rangle\langle CB\rangle + \langle AC\rangle\langle BD\rangle \text{ (the same holds with } [\ldots]),$$

$$\langle A+| \, \gamma_\mu \, |B+\rangle \, \langle C-| \, \gamma^\mu \, |D-\rangle = 2 \, [AD] \, \langle CB \rangle \ .$$

For the polarization vectors we make the choice

$$\epsilon_\mu^\pm (p, k) = \pm \frac{\langle p\pm| \, \gamma_\mu \, |k\pm\rangle}{\sqrt{2} \, \langle k \mp |p\pm\rangle} \tag{18.9.12}$$

where k^μ is the reference momentum needed to define the transverse directions in addition to p^μ. Thus

$$\epsilon_\mu^\pm (p, k) \, \gamma^\mu = \pm \frac{\sqrt{2}}{\langle k \mp |p\pm\rangle} \, (|p\mp\rangle \, \langle k\mp| \, + \, |k\pm\rangle \, \langle p\pm|) \ .$$

Moreover,

$$\epsilon_\mu^\pm (p, k) = \left(\epsilon_\mu^\mp (p, k) \right)^* , \tag{18.9.13}$$

$$\epsilon_\mu^\pm (p, k) \, p^\mu = \epsilon_\mu^\pm (p, k) \, k^\mu = 0, \tag{18.9.14}$$

$$\epsilon_\mu^+ (p, k) \, \epsilon_\nu^- (p, k) + \epsilon_\mu^- (p, k) \, \epsilon_\nu^+ (p, k) = d_{\mu\nu} (p, k) \, , \tag{18.9.15}$$

$$\epsilon^h (p_i, k) \cdot \epsilon^h (p_j, k) = 0, \ \text{with} \ h = +, -, \tag{18.9.16}$$

$$\epsilon^h (p_i, k) \cdot \epsilon^{-h} (p_j, p_i) = 0, \ \text{with} \ h = +, -, \tag{18.9.17}$$

$$\not{\epsilon}^h (p_i, p_j) \left| p_j^h \right\rangle = 0, \ \text{with} \ h = +, -, \tag{18.9.18}$$

$$\left\langle p_j^h \right| \not{\epsilon}^{-h} (p_i, p_j) = 0, \ \text{with} \ h = +, - \ . \tag{18.9.19}$$

18.9.1 Helicity Feynman rules for colour sub-amplitudes (with massless fermions)

We introduce the following notation:

- external outgoing fermion of momentum p, helicity $\pm$: $\langle p\pm|$,

- external outgoing antifermion of momentum p, helicity $\pm$: $|p\mp\rangle$,

- external outgoing vector of momentum p, reference k, helicity $\pm$:
  $\epsilon_\mu^\pm (p, k) = \pm \frac{\langle p\pm|\gamma_\mu|k\pm\rangle}{\sqrt{2}\langle k\mp|p\pm\rangle}.$

The fermion propagator of momentum p^μ in the direction of the fermion arrow is $i\frac{\not p}{p^2}$. The vector propagator of momentum p^μ is: $-\frac{i}{p^2}g_{\mu\nu}$.

$$\Gamma^\mu_{gq\bar q} = i\frac{g_s}{\sqrt2}\gamma^\mu \quad \text{the factor of } \sqrt2 \text{ is due to } T_R = 1,$$

$$\Gamma_{\alpha\beta\gamma}(p,q,r) = i\frac{g_s}{\sqrt2}V_{\alpha\beta\gamma}(p,q,r) \quad \text{all momenta incoming,} \tag{18.9.20}$$

$$\Gamma_{\alpha\beta\gamma\delta} = i\frac{g_s^2}{2}\left(2g_{\alpha\gamma}g_{\beta\delta} - g_{\alpha\delta}g_{\beta\gamma} - g_{\alpha\beta}g_{\gamma\delta}\right).$$

18.9.2 A simple application of the helicity formalism

We now compute the leading order contribution to the process $e^+e^- \to \mu^+\mu^-$ using the helicity formalism. Although it is not a physical choice, we consider the following crossing invariant kinematic configuration, which is useful for obtaining the squared matrix element in either the annihilation or in the scattering channels in a single computation:

$$0^\mu \to p_1^\mu + p_2^\mu + p_4^\mu + p_5^\mu.$$

As for the labelling convention, we anticipate further use of the result, with an additional particle that will be labelled by '3', which is omitted here. There is only one Feynman diagram:
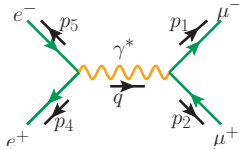
A general amplitude is given by

$$\mathcal{A}_4\left(1^{h_1}, 2^{h_2}, 4^{h_4}, 5^{h_5}\right) = e^2\, a_4\left(1^{h_1}, 2^{h_2}, 4^{h_4}, 5^{h_5}\right)$$

where the numbers are just a short-hand notation for the momenta, $j \equiv p_j$, which is a standard in the helicity formalism. Choosing a specific helicity configuration and applying the Feynman rules, we find

$$
\begin{aligned}
a_4\left(1^+, 2^-, 4^+, 5^-\right) &\equiv a_4(+,-,+,-) = \langle 1+|\,i\gamma_\mu\,|2+\rangle\,\frac{(-ig^{\mu\nu})}{s_{12}}\,\langle 5-|\,i\gamma_\nu\,|4-\rangle \\
&= i\,\frac{2\,[14]\,\langle 52\rangle}{\langle 12\rangle\,[21]}\,\frac{\langle 45\rangle}{\langle 45\rangle} = -i\,\frac{2\,[12]\,\langle 25\rangle\,\langle 52\rangle}{[21]\,\langle 12\rangle\,\langle 45\rangle} \\
&= -i\,\frac{2\,\langle 25\rangle^2}{\langle 12\rangle\,\langle 45\rangle}, \tag{18.9.21}
\end{aligned}
$$

where $s_{ij} = (p_i + p_j)^2$ and in the third line we used momentum conservation ($\not{4} = -\not{1} - \not{2} - \not{5}$) to rewrite $[14]\langle 45\rangle$ as

$$[14]\langle 45\rangle = \langle 1 + |\not{4}|5+\rangle = \langle 1 + |-\not{1} - \not{2} - \not{5}|5+\rangle = \langle 1 + |-\not{2}|5+\rangle$$
$$= -[12]\langle 25\rangle. \tag{18.9.22}$$

The other helicity amplitudes can be found from Eq. (18.9.21), using discrete symmetry transformations of parity and charge conjugation. Parity transformation reverses all helicities of the helicity amplitude. It is implemented by the complex conjugation operation which substitutes $\langle ij\rangle \leftrightarrow [ji]$. Charge conjugation changes anti-fermions into fermions and vice versa, which in the present case amounts to interchanging indices 4 with 5 and/or 1 with 2. Thus,

$$a_4(+,-,-,+) = a_4(+,-,+,-)|_{4\leftrightarrow 5} \quad \text{(from charge conjugation)}$$
$$= -i\,\frac{2\langle 24\rangle^2}{\langle 12\rangle\langle 54\rangle} \tag{18.9.23}$$
$$a_4(-,+,-,+) = a_4(+,-,+,-)|_{\langle ij\rangle \leftrightarrow [ji]} \quad \text{(from parity transformation)}$$
$$= -i\,\frac{2[25]^2}{[12][45]} \tag{18.9.24}$$
$$a_4(-,+,+,-) = -i\,\frac{2[24]^2}{[12][54]}. \tag{18.9.25}$$

Computing the square of the amplitude, summed over helicities, we obtain

$$\sum_{\text{helicity}} |\mathcal{A}|^2 = e^4\, 2\,\frac{4\left(s_{25}^2 + s_{24}^2\right)}{s_{12}s_{45}} = 8\,(4\pi\alpha)^2\,\frac{t^2 + u^2}{s^2},$$

where we adopted the usual notation of the *Mandelstam variables*, s, t and u:

$$s_{12} = s_{45} = s, \qquad s_{24} = t, \qquad s_{25} = u.$$

The advantage of considering a kinematic configuration $0 \to p_1^\mu + p_2^\mu + p_4^\mu + p_5^\mu$ is that it is easy to compute the matrix element for analogous reactions that can be obtained by crossing symmetry. Depending on the crossed momenta we speak of s- or t-channel. Integrating the squared matrix element over the phase space of the two final state particles, averaging over the initial spin states and dividing with the flux factor, the cross section is

$$\sigma = \frac{1}{4}\frac{1}{2s}\int_{-s}^{0}\frac{dt}{8\pi s}\,8\,(4\pi\alpha)^2\,\frac{t^2 + u^2}{s^2} = \frac{4\pi\alpha^2}{3s}. \tag{18.9.26}$$

Exercise 18.15
Consider highly relativistic fermions in QED. Show that the electromagnetic interaction conserves helicity. Is helicity conserved also for axial currents?

Exercise 18.16
Show that for colour ordered amplitudes $m(1, \ldots, n) \equiv m(p_1, \epsilon_1; \ldots; p_n, \epsilon_n)$ the following statements hold:

- *they are invariant under cyclic permutations and that*

- $m(n, n - 1, \ldots, 1) = (-1)^n \, m(1, 2, \ldots, n).$

Exercise 18.17
Show the following properties of spinor products:

- $\langle\, i\, j\,\rangle [\, j\, i\,] = 2k_i \cdot k_j$

- $\langle\, i|\, \gamma^\mu \,|\, j] = [\, j|\, \gamma^\mu \,|\, i\rangle$

- *Fierz identity:* $[\, i|\, \gamma^\mu \,|\, j\rangle\, \langle\, k|\, \gamma_\mu \,|\, l] = 2\,[\, i\, l\,]\,\langle\, k\, j\,\rangle$

- *Schouten identity:* $\langle\, i\, j\,\rangle\langle\, k\, l\,\rangle = \langle\, i\, k\,\rangle\langle\, j\, l\,\rangle + \langle\, i\, l\,\rangle\langle\, k\, j\,\rangle$

The notation introduced here is

$$| i\rangle \equiv | i^+\rangle \qquad \langle i| \equiv \langle i^-|$$
$$| i] \equiv | i^-\rangle \qquad [i| \equiv \langle i^+|$$

Exercise 18.18
Consider the matrix element $\epsilon_\mu^*(k_1)\epsilon_\nu^*(k_2)\mathcal{M}^{\mu\nu}\,(e^+e^- \rightarrow \gamma(k_1)\gamma(k_2))$ for the QED process $e^+e^- \rightarrow \gamma(k_1)\gamma(k_2)$ in leading order of perturbation theory. Verify the Ward identity

$$k_1^\mu \mathcal{M}_{\mu\nu} = 0\,.$$

Exercise 18.19
What changes in QCD? We consider the matrix element $\mathcal{M}\,(q\bar{q} \rightarrow g(k_1)g(k_2))$.

- *Which diagrams contribute?*

- *Verify that*

$$\epsilon^\mu(k_1)k_2^\nu \mathcal{M}_{\mu\nu}(q\bar{q} \to g(k_1)g(k_2)) = 0,$$

  in case of a transversely polarized gluon $g(k_2)$, namely if $k_2^\mu \epsilon_\mu(k_2) = 0$. The requirement that the external vector bosons must be transversely polarized was not needed in QED (see the previous exercise).

Exercise 18.20
Nevertheless, in QCD the Ward-identity holds thanks to additional (unphysical) fields called ghosts. Square the above amplitude both in covariant and in physical gauge. Do the results match? Why?

Exercise 18.21
Compute the cross section for $e^+e^- \to q\bar{q}$ in leading order in perturbation theory.

Exercise 18.22
Consider the matrix element $\mathcal{M}(q\bar{q} \to g(k_1)g(k_2))$ for the QCD process $q_1\bar{q}_2 \to g(k_1)g(k_2)$ in leading order in perturbation theory.

- *Determine graphically the colour structures and the corresponding colour subamplitudes $m(q_1, q_2, g_1, g_2)$.*

- *Decompose the latter into contributions of fixed helicities.*

Now determine which helicity amplitudes have to be calculated explicitly:

- *Make use of helicity conservation (see also exercise 18.15).*

- *Use invariance under charge conjugation.*

- *Carefully choose two reference momenta q_1 and q_2 of the polarization vector of the gluons. Note for example $\epsilon^+(k_i, k_j) \cdot \epsilon^-(k_j, q) = 0$, $\epsilon^+(k_i, q) \cdot \epsilon^-(k_j, q) = 0$ etc. (see also Eqs. (18.9.14)–(18.9.19)).*

Exercise 18.23
Compute the remaining colour-ordered subamplitudes from the previous exercise. Use the spinor helicity formalism.

Chapter 19

Electron-positron annihilation into hadrons

19.1 Electron-positron annihilation into hadrons

MOTTO:

"Well, in OUR country," said Alice, still panting a little, "you'd generally get to somewhere else — if you ran very fast for a long time, as we've been doing."
"A slow sort of country!" said the Queen. "Now, HERE, you see, it takes all the running YOU can do, to keep in the same place. If you want to get somewhere else, you must run at least twice as fast as that!"

(Lewis Carroll: Through the Looking Glass)

We now use the assumption that a low-order perturbative computation in QCD is an approximation to sufficiently inclusive hadronic cross section, and make predictions for the cross section of electron-positron annihilation into hadrons.

The leading-order (LO) perturbative contribution to the cross section

$\sigma (e^+e^- \to$ hadrons) is $e^+e^- \to q\bar{q}$. The calculation is like in the case of $e^+e^- \to \mu^+\mu^-$, supplemented with colour and fractional electric charge of q_j where the subscript is index of flavour. The colour graph is a loop in the fundamental representation that corresponds to a factor N_c as we have seen in the previous chapter. While the annihilation into $\mu^+\mu^-$ contains only one flavour in the final state, quarks can have three, four or five flavours depending on the centre-of-mass (CM) energy.[1] We have to sum over all possible flavours that can appear. The ratio of the two cross sections is thus given by

$$R \equiv \frac{\sigma (e^+e^- \to q\bar{q})}{\sigma (e^+e^- \to \mu^+\mu^-)} = \left(\sum_q e_q^2 \right) N_c, \qquad (19.1.1)$$

where $e_u = e_c = \frac{2}{3}$ and $e_d = e_s = e_b = -\frac{1}{3}$. If we consider only the u, d, s and c quarks (the CM energy is above the threshold of producing a c-quark pair, but below the threshold of a b-quark pair) $\sum_q e_q^2 = 2\frac{4}{9} + 2\frac{1}{9} = \frac{10}{9}$. Considering also the contribution of the b quark above the b-quark pair threshold, $\sum_q e_q^2 = \frac{11}{9}$. This step-wise increasing behaviour of the R-ratio was observed (see figure 17.56), providing an experimental confirmation of the existence of three families of quarks with fractional charges and of the $SU(N_c)$ gauge symmetry of QCD with $N_c = 3$.

19.2   Ultraviolet renormalization of QCD

The strong coupling is rather large as compared to the other couplings in the SM and as a result, the QCD radiative corrections are also large. Therefore, it is always important to compute at least the next-to-leading order (NLO), but if possible, even higher order corrections.[2]

   The computation of QCD radiative corrections is technically quite involved and a good organization of the calculations is very important. Thus, first we introduce some notation. The tensor product of the ket vectors $|c_1, \ldots, c_m\rangle \otimes |s_1, \ldots, s_m\rangle$ denotes a basis vector in colour and helicity space, $|\mathcal{A}_m (p_1, \ldots, p_m)\rangle$ is a state vector of $n = m - 2$ final-state particles in colour and helicity space. (The remaining two indices stand for the incoming leptons.) The amplitude for producing n final-state particles of

---

[1] The sixth flavour, the t quark is so heavy that it cannot contribute at CM energies attained in e^+e^- experiments so far.

[2] There is even a more serious reason that we shall point out at the end of this chapter.

colour $(c_1, \ldots, c_n)$, spin $(s_1, \ldots, s_n)$, momentum $(p_1, \ldots, p_n)$ is

$$\mathcal{A}_m^{c_1 \ldots c_m, s_1 \ldots s_m} (p_1 \ldots p_m) = \langle c_1 \ldots c_m | \otimes \langle s_1 \ldots s_m | \mathcal{A}_m (p_1, \ldots, p_m) \rangle$$

($m = n + 2$ and appears in subscript as opposed to m denoting mass of the particles, that never appears in subscript) so

$$\sum_{\text{colour}} \sum_{\text{helicity}} \left| \mathcal{A}_m^{\{c_i\}, \{s_i\}} (p_1, \ldots, p_m) \right|^2 = \langle \mathcal{A}_m (p_1, \ldots, p_m) | \mathcal{A}_m (p_1, \ldots, p_m) \rangle .$$

The loop expansion in terms of the bare coupling $g_s^{(0)} \equiv \sqrt{4\pi \alpha_s^{(0)}}$, which is the coupling that appears in the classical Lagrangian, is as follows:

$$|\mathcal{A}_m\rangle = \left(\frac{\alpha_s^{(0)}}{4\pi} \right)^{\frac{q}{2}} \left[\left| \mathcal{A}_m^{(0)} \right\rangle + \left(\frac{\alpha_s^{(0)}}{4\pi} \right) \left| \mathcal{A}_m^{(1)} \right\rangle + O\left((\alpha_s^{(0)})^2 \right) \right], \qquad (19.2.2)$$

where q is a non-negative integer. When we compute loop corrections, we shall find divergent integrals in $d = 4$ dimensions that can be regularized using dimensional regularization. In order to keep α_s dimensionless in $d = 4 - 2\epsilon$ dimensions we have to introduce a mass scale μ, called the dimensional regularization scale. Each factor of α_s acquires a factor of $\mu^{2\epsilon}$ that we include in the $\left| \mathcal{A}_m^{(i)} \right\rangle$ amplitudes, not shown explicitly in Eq. (19.2.2). The exponent $\frac{q}{2}$ in the prefactor takes account of the power of α_s at leading-order (LO) accuracy. For instance, $q = 0$ for $e^+e^- \to q\bar{q}$, while $q = 1$ for $e^+e^- \to q\bar{q}g$. The one-loop correction to $\mathcal{A}_4^{(0)} (1, 2, 4, 5)$ is computed from three diagrams:

We first look at the fermion propagator correction Σ_μ in covariant Feynman gauge,

 $\equiv i\Sigma (p, m) =$

$$= C_F \int \frac{d^d \ell}{(2\pi)^d} \frac{4\pi \alpha_s \mu^{2\epsilon}}{[(p-\ell)^2 - m^2] \, \ell^2} \left[\gamma_\mu \left(\not{p} - \not{\ell} + m \mathbb{1} \right) \gamma_\nu \left(-g^{\mu\nu} \right) \right]$$

$$= C_F \delta_{kl} \, 4\pi \alpha_s \, \mu^{2\epsilon} \int \frac{d^d \ell}{(2\pi)^d} \frac{(d-2) (\not{p} - \not{\ell}) - d \, m \mathbb{1}}{[(p-\ell)^2 - m^2] \, l^2} ,$$

where $\mathbb{1}$ is the 4×4 unit matrix, and we used $-\gamma_\mu \slashed{a} \gamma^\mu = (d-2) \slashed{a}$, valid for any four-momentum a^μ in arbitrary dimensions d. The momentum of the external fermion of mass m is denoted by p^μ. $\slashed{\Sigma}$ is diagonal in the colour indices of the external quarks, therefore we have suppressed these indices. The necessary integrals are

$$
\begin{aligned}
I_2 &= \int \frac{d^d \ell}{(2\pi)^d} \frac{1}{\left[(\ell - p)^2 - m^2 \right] \ell^2} \\
&= \frac{i}{(4\pi)^{2-\epsilon}} \Gamma(\epsilon) \left(p^2 \right)^{-\epsilon} \int_0^1 dx \left(x \frac{m^2}{p^2} - x(1-x) - i\varepsilon \right)^{-\epsilon} \quad (19.2.3) \\
I_2^\mu &= \int \frac{d^d \ell}{(2\pi)^d} \frac{\ell^\mu}{\left[(\ell - p)^2 - m^2 \right] \ell^2} \\
&= \frac{i}{(4\pi)^{2-\epsilon}} \Gamma(\epsilon) \left(p^2 \right)^{-\epsilon} p^\mu \int_0^1 dx \left(x \frac{m^2}{p^2} - x(1-x) - i\varepsilon \right)^{-\epsilon} x \quad (19.2.4)
\end{aligned}
$$

where the gamma (or factorial) function $\Gamma(\epsilon)$ has the property

$$
\Gamma(\epsilon) = \frac{\epsilon \Gamma(\epsilon)}{\epsilon} = \frac{1}{\epsilon} \Gamma(1 + \epsilon).
$$

It is important to distinguish the deviation from four dimensions, represented by ϵ, from the Feynman prescription in the propagator, represented by ε. Finally we obtain

$$
i \slashed{\Sigma}(p, m) \equiv i \left[m \Sigma_1 \left(p^2, m \right) + (\slashed{p} - m) \Sigma_2 \left(p^2, m \right) \right]
$$

where

$$
\begin{aligned}
\Sigma_1 \left(p^2, m \right) &= \frac{\alpha_s}{4\pi} \frac{1}{\epsilon} \Gamma(1 + \epsilon) \left(\frac{4\pi \mu^2}{p^2} \right)^\epsilon (-3 C_F) + O\left(\epsilon^0 \right), \\
\Sigma_2 \left(p^2, m \right) &= \frac{\alpha_s}{4\pi} \frac{1}{\epsilon} \Gamma(1 + \epsilon) \left(\frac{4\pi \mu^2}{p^2} \right)^\epsilon (+C_F) + O\left(\epsilon^0 \right).
\end{aligned}
$$

This result becomes meaningless if $\epsilon = 0$ (that is $d = 4$), which is cured by ultraviolet renormalization. The philosophy behind ultraviolet renormalization is the following. The (bare) parameters in the (classical) Lagrangian are not physically observable. Ultraviolet renormalization is a reformulation of the Lagrangian using physical quantities, which means that instead of the bare quantities, one should write the Lagrangian using renormalized ones

that are related to the bare ones by simple multiplication, hence the name renormalization (R):

$$q^{(0)} = \sqrt{Z_q}\, q^{(R)}, \qquad A^{(0)} = \sqrt{Z_A}\, A^{(R)}, \qquad \eta^{(0)} = \sqrt{Z_\eta}\, \eta^{(R)},$$
$$m^{(0)} = Z_m m^{(R)}, \qquad \mu^\epsilon g_s^{(0)} = \mu_R^\epsilon Z_g g_s^{(R)}, \qquad \lambda^{(0)} = Z_\lambda \lambda^{(R)} .$$

Any physical observable can be calculated as a function of the renormalized parameters (in perturbation theory) and their values can be extracted from measured values of the physical observables. In perturbation theory each Z has a perturbative expansion of the form

$$Z = \sum_{n=0}^{\infty} \left(\frac{\alpha_s}{4\pi}\right)^n \sum_{j=0}^{n} \frac{Z^{(n,j)}}{\epsilon^j} = 1 + \left(\frac{\alpha_s}{4\pi}\right)\left[Z^{(1,0)} + \frac{Z^{(1,1)}}{\epsilon}\right] + O\left(\alpha_s^2\right), \quad (19.2.5)$$

where we simplified slightly the notation, denoting $\alpha_s^{(R)}$ with α_s. The $Z^{(n,j)}$ coefficients ($j > 0$) can be determined order by order in perturbation theory from the requirement that the renormalized Lagrangian,

$$\mathcal{L}^{(R)}\left(q^{(R)}, A^{(R)}, \eta^{(R)}, m^{(R)}, g^{(R)}, \lambda^{(R)}\right) =$$
$$= \mathcal{L}\left(q^{(0)}, A^{(0)}, \eta^{(0)}, m^{(0)}, g^{(0)}, \lambda^{(0)}\right)$$
$$- \mathcal{L}_{CT}\left(q^{(R)}, A^{(R)}, \eta^{(R)}, m^{(R)}, g^{(R)}, \lambda^{(R)}\right)$$

generates finite Green functions. Thus $\mathcal{L} = \mathcal{L}^{(R)} + \mathcal{L}_{CT}$ where CT stands for counter terms. $\mathcal{L}_{CT}$ must have the same functional dependence as $\mathcal{L}$ on its arguments. Renormalizability means that such Z constants exist (in any order of perturbation theory). The counter-term Lagrangian can be written as

$$\mathcal{L}_{CT} = (Z_q - 1)\,\bar{q} i \slashed{\partial} q - (Z_q Z_m - 1)\, m \bar{q} q - \frac{1}{4}(Z_A - 1)\left(\partial_{[\mu} A_{\nu]}\right)^2$$
$$+ (Z_\eta - 1)\left(\partial_\mu \eta\right)^\dagger (\partial^\mu \eta) - \left(Z_g Z_q \sqrt{Z_A} - 1\right)\mu_R^\epsilon \sqrt{4\pi\alpha_s}\, \bar{q}\,(T \cdot \slashed{A})\, q$$
$$+ \frac{1}{2}\left(Z_g Z_A^{\frac{3}{2}} - 1\right)\mu_R^\epsilon \sqrt{4\pi\alpha_s}\, \partial_{[\mu} A_{\nu]} A^\mu \times A^\nu$$
$$+ \left(Z_g^2 Z_A^2 - 1\right)\mu_R^{2\epsilon}\, 4\pi\alpha_s\, (A_\mu \times A_\nu)(A^\mu \times A^\nu)$$
$$+ \left(Z_g Z_\eta \sqrt{Z_A} - 1\right)\mu_R^\epsilon \sqrt{4\pi\alpha_s}\, \partial^\mu \eta^\dagger\,(iT \cdot A_\mu)\, \eta$$

$$(19.2.6)$$

(the counter-term for gauge fixing is not included). In principle, the renormalization factors of the various terms in the Lagrangian have to be computed independently for each term. However, one can derive relations among those, called Slavnov-Taylor identities, which reflect the symmetry of the original Lagrangian. These relations have been already taken into account, when we expressed the vertex renormalization factors as combinations of field renormalization factors and Z_g. We have also omitted the superscript (R) for the sake of brevity. The constants $Z^{(n,0)}$ are not determined by the requirement of ultraviolet renormalizability. The simplest choice is $Z^{(n,0)} = 0$, which defines the minimal subtraction (MS) scheme. In QCD the *modified minimal subtraction* ($\overline{\text{MS}}$) scheme is used, which is defined by

$$Z^{(n,0)} = Z^{(n,1)} \left(\ln 4\pi - \gamma_E \right) \qquad (19.2.7)$$

at one loop, with γ_E being the Euler constant, emerging in the expansion

$$\Gamma \left(1 + \epsilon \right) = 1 + \epsilon \, \gamma_E - O \left(\epsilon^2 \right).$$

Eq. (19.2.7) holds at one-loop accuracy. To go beyond, one has to be a little more careful. However for the purpose of this book the given definition is enough. In this scheme

$$Z_m = 1 + \Sigma_1 \left(p^2, m \right) \mid_{p^2 = m^2} = 1 - c_\epsilon \, 3C_F + O \left(\alpha_s^2 \right)$$

$$Z_q^{-1} = 1 + 2m^2 \frac{\partial}{\partial p^2} \Sigma_1 \left(p^2, m \right) \mid_{p^2 = m^2} + \Sigma_2 \left(p^2, m \right) \mid_{p^2 = m^2}$$

$$= 1 + c_\epsilon \, C_F + O \left(\alpha_s^2 \right),$$

where

$$c_\epsilon = \frac{\alpha_s}{4\pi} \frac{1}{\epsilon} \Gamma \left(1 + \epsilon \right) (4\pi)^\epsilon$$

thus

$$Z_q^{(1,1)} = -C_F \lambda_R, \qquad Z_m^{(1,1)} = -3C_F,$$

$$Z_A^{(1,1)} = \left[C_A \left(\frac{13}{6} - \frac{\lambda_R}{2} \right) - \frac{4}{3} T_R n_f \right], \qquad Z_\eta^{(1,1)} = C_A \frac{3 - \lambda_R}{4},$$

$$Z_g^{(1,1)} = -\frac{\beta_0}{2}, \qquad Z_g^{(2,1)} = -\frac{\beta_1}{4}, \qquad\qquad (19.2.8)$$

where

$$\beta_0 = \frac{11}{3} C_A - \frac{4}{3} T_R n_f > 0, \qquad \beta_1 = \frac{34}{3} C_A^2 - \frac{20}{3} C_A T_R n_f - 4 C_F T_R n_f.$$

The results in Eq. (19.2.8) are valid for any value of the gauge parameter λ_R.

When computing scattering amplitudes in massless QCD at one-loop accuracy, the renormalization amounts to the simple substitution

$$\alpha_s^{(0)} \mu^{2\epsilon} S_\epsilon^{\overline{MS}} \rightarrow \alpha_s \left(\mu_R^2\right) \mu_R^{2\epsilon} \left[1 - \frac{\alpha_s\left(\mu_R^2\right)}{4\pi} \frac{\beta_0}{\epsilon} + O\left(\alpha_s^2\right)\right] \qquad (19.2.9)$$

where $S_\epsilon^{\overline{MS}} = (4\pi)^\epsilon \exp(-\epsilon\gamma_E)$. The renormalized coupling α_s depends on μ_R. In applying the substitution (19.2.9) μ disappears and μ_R appears in the amplitude. The meanings of scales μ and μ_R are different:

- μ is the dimensional regularization scale to keep $\alpha_s^{(0)}$ dimensionless,

- μ_R is the renormalization scale: when we extract α_s from measurements, we have to define μ_R. We will come back to this and clarify it later.

Why does (19.2.9) work correctly? Each Feynman diagram consists of vertices with propagators connecting those and external lines. Moreover,

- each vertex receives a factor Z_g (or Z_g^2 for quartic vertex) and factors of $\sqrt{Z_i}$, $i = q, A$ for each field connected to the vertex,

- each propagator of field i receives a factor of Z_i^{-1},

- each external leg of field i receives a factor of $Z_i^{-\frac{1}{2}}$.

Thus the renormalization field factors cancel from each diagram and only the charge renormalization (Z_g) is needed in practice! This can be seen as a consequence of the fact that in massless QCD the only free parameter besides the gauge-fixing parameter λ is α_s. The scattering amplitudes are physical, and any physical quantity has to be independent of λ, so the only remaining parameter, which the amplitudes may depend on, is the coupling. The renormalization factor Z_g is most easily computed in background-field gauge [Abbott, 1981], defined by

$$\mathcal{L}_{GF} = -\frac{1}{2\lambda} \sum_a \left(\partial^\mu A_\mu^a - g f^{abc} \mathcal{A}_\mu^b A^{\mu c}\right)^2,$$

where $\mathcal{A}_\mu^b$ is a background field and A_μ^c describes the quantum fluctuations on this background. It can be shown that in this gauge
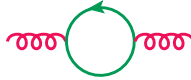
$$Z_{\mathcal{A}}^{-\frac{1}{2}} = Z_g,$$

and $Z_{\mathcal{A}}$ can be computed from loop insertions into the propagator.

Exercise 19.1

Compute the contribution to the beta function from the fermion loop:

1. *Write down carefully the amplitude and compute the trace assuming n_f number of massless quarks..*

2. *The following types of integrals occur*:

$$I_2^\mu = \int \frac{d^d\ell}{(2\pi)^d} \frac{\ell^\mu}{\ell^2 (\ell - p)^2} , \qquad I_2^{\mu\nu} = \int \frac{d^d\ell}{(2\pi)^d} \frac{\ell^\mu \ell^\nu}{\ell^2 (\ell - p)^2}$$

(19.2.10)

   Express these as linear combination of

$$I_2(p) = \int \frac{d^d\ell}{(2\pi)^d} \frac{1}{\ell^2 (\ell - p)^2} . \qquad (19.2.11)$$

3. *Obtain I_2 from*

$$I_2(p, m) = \int \frac{d^d l}{(2\pi)^d} \frac{1}{\left[(l - p)^2 - m^2\right] l^2}$$

$$= \frac{i}{(4\pi)^{2-\epsilon}} \Gamma(\epsilon) \left(p^2\right)^{-\epsilon} \int_0^1 dx \left(x \frac{m^2}{p^2} - x(1 - x) - i\varepsilon\right)^{-\epsilon}$$

(19.2.12)

   and find the divergent pieces.

The contribution to β_0 is the coefficient of the $1/\epsilon$ pole without the coupling factor.

19.3 Running coupling

We consider a dimensionless quantity that depends on a single dimensionful parameter, $R = R(Q^2)$. This could, for example, be the ratio of cross sections of the production of hadrons and a $\mu^+\mu^-$ pair in e^+e^- collisions, that we already discussed before:

$$R = \frac{\sigma(e^+e^- \to \text{hadrons})}{\sigma(e^+e^- \to \mu^+\mu^-)},$$

and $Q = \sqrt{s} = E_{e^+} + E_{e^-}$ (the second equality is valid in the centre-of-mass frame). If R depends on other dimensionful parameters such as masses, we assume that Q is much bigger than all those, which can be set to zero. Classically, dim $R = 0$ and, since Q is dimensionful, it follows that $\frac{dR}{dQ} = 0$. So $\lim_{Q^2 \to \infty} R =$ constant. In renormalized QFT, R depends also on μ_R, thus it need not be a constant,

$$R = R\left(\frac{Q^2}{\mu_R^2}, \alpha_s\left(\mu_R^2\right)\right) \neq \text{constant}.$$

This is called *scaling violation*. Note that the first term in parenthesis is only a dimensionless combination of Q and μ_R. However, μ_R is arbitrary. If R depended on μ_R, then its value could not be predicted. From now on we drop the subscript "R" from μ_R and write μ, meaning μ_R. As R cannot depend on μ, we can write:

$$0 = \mu^2 \frac{d}{d\mu^2} R\left(\frac{Q^2}{\mu^2}, \alpha_s\left(\mu^2\right)\right) = \left(\mu^2 \frac{\partial}{\partial\mu^2} + \mu^2 \frac{\partial\alpha_s}{\partial\mu^2} \frac{\partial}{\partial\alpha_s}\right) R. \quad (19.3.13)$$

Eq. (19.3.13) is called the *renormalization group equation* (RGE). Keeping $\alpha_s^{(0)}$ fixed, setting $t = \ln\frac{Q^2}{\mu^2}$ and defining

$$\beta(\alpha_s) = \mu^2 \left.\frac{\partial\alpha_s}{\partial\mu^2}\right|_{\alpha_s^{(0)} \text{ fixed}} = -\frac{\partial\alpha_s(\mu^2)}{\partial t},$$

we obtain the partial differential equation

$$\left(-\frac{\partial}{\partial t} + \beta(\alpha_s)\frac{\partial}{\partial\alpha_s}\right) R\left(e^t, \alpha_s\right) = 0. \quad (19.3.14)$$

We can solve this equation by defining $\alpha_s(Q^2)$, the running coupling as

$$t = \int_{\alpha_s(\mu^2)}^{\alpha_s(Q^2)} \frac{dx}{\beta(x)}. \quad (19.3.15)$$

This gives $\alpha_s\left(Q^2\right)$ implicitly for a known, arbitrarily fixed number $\alpha_s \equiv \alpha_s\left(\mu^2\right)$. The derivative with respect to the variable t of (19.3.15) gives

$$1 = \frac{1}{\beta\left(\alpha_s\left(Q^2\right)\right)} \frac{\partial \alpha_s\left(Q^2\right)}{\partial t},$$

which implies

$$\beta\left(\alpha_s\left(Q^2\right)\right) = \frac{\partial \alpha_s\left(Q^2\right)}{\partial t}.$$

The derivative of (19.3.15) with respect to α_s gives

$$0 = \frac{1}{\beta\left(\alpha_s\left(Q^2\right)\right)} \frac{\partial \alpha_s\left(Q^2\right)}{\partial \alpha_s} - \frac{1}{\beta(\alpha_s)} \frac{\partial \alpha_s}{\partial \alpha_s},$$

from which it follows that

$$\frac{\partial \alpha_s\left(Q^2\right)}{\partial \alpha_s} = \frac{\beta\left(\alpha_s\left(Q^2\right)\right)}{\beta(\alpha_s)}.$$

It is now easy to prove that $R\left(1, \alpha_s\left(Q^2\right)\right)$ solves (Eq. (19.3.14)):

$$-\frac{\partial}{\partial t} R\left(1, \alpha_s\left(Q^2\right)\right) = -\frac{\partial R}{\partial \alpha_s\left(Q^2\right)} \frac{\partial \alpha_s\left(Q^2\right)}{\partial t} = -\beta\left(\alpha_s\left(Q^2\right)\right) \frac{\partial R}{\partial \alpha_s\left(Q^2\right)}$$

and

$$\beta(\alpha_s) \frac{\partial}{\partial \alpha_s} R\left(1, \alpha_s\left(Q^2\right)\right) = \beta(\alpha_s) \frac{\partial \alpha_s\left(Q^2\right)}{\partial \alpha_s} \frac{\partial R}{\partial \alpha_s\left(Q^2\right)}$$

$$= \beta\left(\alpha_s\left(Q^2\right)\right) \frac{\partial R}{\partial \alpha_s\left(Q^2\right)}.$$

Thus if we know $\alpha_s\left(Q^2\right)$, we automatically know the Q^2-dependence of R. To get $\alpha_s\left(Q^2\right)$, we need the $\beta\left(\alpha_s\left(Q^2\right)\right)$ function:

$$Q^2 \left.\frac{\partial \alpha_s}{\partial Q^2}\right|_{\alpha_s^{(0)} \text{ fixed}} = \beta(\alpha_s). \qquad (19.3.16)$$

Our discussion so far is valid generally, with the single condition that R depends on Q^2 only and our computations were non-perturbative.

We can obtain the β function in perturbation theory. In the MS scheme $\mu^{2\epsilon} \alpha_s^{(0)} = \mu_R^{2\epsilon} Z_g^2 \alpha_s$. Taking the derivative $\mu_R^2 \frac{d}{d\mu_R^2}$ on both sides we obtain

$$0 = \left[\epsilon \alpha_s + \alpha_s \mu_R^2 \frac{d}{d\mu_R^2} + \beta\left(\alpha_s, \epsilon\right)\right] Z_g^2$$

and thus

$$\beta\left(\alpha_s, \epsilon\right) = -\epsilon\alpha_s - \alpha_s \frac{\mu_R^2}{Z_g^2} \frac{d\,Z_g^2}{d\mu_R^2}.$$

Let us define $f(\alpha_s) = \frac{\mu_R^2}{Z_g^2} \frac{d\,Z_g^2}{d\mu_R^2}$. By definition, in the MS scheme Z_g depends on μ_R only through $\alpha_s\left(\mu_R^2\right)$, so

$$Z_g^2\, f(\alpha_s) = \beta\left(\alpha_s, \epsilon\right) \frac{\partial\, Z_g^2}{\partial\alpha_s} = -\epsilon\alpha_s \frac{\partial\, Z_g^2}{\partial\alpha_s} - \alpha_s\, f(\alpha_s) \frac{\partial\, Z_g^2}{\partial\alpha_s}.$$

Since ϵ is arbitrary, the equality must hold at each power of ϵ. The terms independent of ϵ are

$$1 \cdot f(\alpha_s) = -\epsilon\,\alpha_s \sum_{n=1}^{\infty} n \left(\frac{\alpha_s}{4\pi}\right)^{n-1} \frac{2\,Z_g^{(n,1)}}{4\pi\epsilon}$$

('1' refers to the first term in the expansion of Z_g^2). Thus,

$$\beta(\alpha_s) = \beta\left(\alpha_s, \epsilon = 0\right) = -\alpha_s\, f(\alpha_s) = \alpha_s^2 \sum_{n=1}^{\infty} n \left(\frac{\alpha_s}{4\pi}\right)^{n-1} \frac{2\,Z_g^{(n,1)}}{4\pi}$$

$$= -\alpha_s \sum_{n=0}^{\infty} \beta_n \left(\frac{\alpha_s}{4\pi}\right)^{n+1}, \tag{19.3.17}$$

where we used the convention of setting $Z_g^{(n,1)} = -\frac{\beta_{n-1}}{2n}$. Another often used convention is

$$\beta(\alpha_s) = -b_0\alpha_s^2 \left[1 + \sum_{n=1}^{\infty} b_n\, \alpha_s^n \right], \tag{19.3.18}$$

where $b_0 = \frac{\beta_0}{4\pi}$ and $b_0 b_1 = \frac{\beta_1}{(4\pi)^2}$, thus $b_1 = \frac{\beta_1}{4\pi\beta_0}$. The first two coefficients in the expansion of the β function are independent of the renormalization scheme.

If $\alpha_s\left(Q^2\right)$ is small we can truncate the series. The solution at leading order (LO) is

$$Q^2 \frac{\partial\alpha_s}{\partial\, Q^2} = \frac{\partial\alpha_s}{\partial\, t} = -b_0\alpha_s^2,$$

$$\Rightarrow \quad -\left[\frac{1}{\alpha_s\left(Q^2\right)} - \frac{1}{\alpha_s\left(\mu^2\right)}\right] = -b_0 t,$$

$$\Rightarrow \quad \alpha_s\left(Q^2\right) = \frac{\alpha_s\left(\mu^2\right)}{1 + b_0 t\, \alpha_s\left(\mu^2\right)}, \tag{19.3.19}$$

which gives $\alpha_s \left(Q^2\right)$ as a function of $\alpha_s \left(\mu^2\right)$ if both are small. The coupling $\alpha_s \left(\mu^2\right)$ is a number to be extracted from data. We observe that the running coupling tends to zero at asymptotically large energies,

$$\alpha_s \left(Q^2\right) \xrightarrow{Q^2 \to \infty} \frac{1}{b_0 t} \to 0 \,. \tag{19.3.20}$$

This behaviour is called *asymptotic freedom*. The sign of b_0 plays a crucial role in establishing whether or not a theory is asymptotically free. If it is positive, so the β function is negative, then the use of perturbation theory is justified: the higher Q^2, the smaller the coupling. The coefficient b_0 is easiest to compute in background-field gauge where only two diagrams contribute:

The contribution of the quark loop is negative $-\frac{4}{3} T_R n_f$, while that of the gluon loop is positive $\frac{11}{3} C_A$. The net result is that the β function is negative up to $n_f < 16$ in QCD. In 2004 David J. Gross, Hugh D. Politzer and Frank Wilczek received the Nobel prize for their discovery of asymptotic freedom in QCD.

Clearly, it is the gluon self-interaction that makes QCD perfect in perturbation theory. In QED $b_0 < 0$, hence the coupling increases with energy, but remains perturbative up to the Planck scale where we expect that any known physics breaks down.

The analysis is also simple at next-to-leading order (NLO):

$$\left[\alpha_s^2 (1 + b_1 \alpha_s)\right]^{-1} \frac{\partial \alpha_s}{\partial t} = -b_0 \,.$$

$\alpha_s \left(Q^2\right)$ is then given implicitly by the equation

$$\frac{1}{\alpha_s \left(Q^2\right)} - \frac{1}{\alpha_s \left(\mu^2\right)} + b_1 \ln \frac{\alpha_s \left(Q^2\right)}{\alpha_s \left(\mu^2\right)} - b_1 \ln \frac{1 + b_1 \alpha_s \left(Q^2\right)}{1 + b_1 \alpha_s \left(\mu^2\right)} = bt \,,$$

which can be solved numerically.

Measuring $\alpha_s(\mu^2)$

We know $\alpha_s \left(Q^2\right)$ if $\alpha_s \left(\mu^2\right)$ is known. Therefore, we have to measure α_s at some scale μ. The perturbative solution of the renormalization group

equation (RGE, Eq. (19.3.13)) is never unique. The difference between two solutions at $O\left(\alpha_s^n\right)$ is suppressed by α_s, i.e. at $O\left(\alpha_s^{n+1}\right)$. Nevertheless, this difference can lead to a significant numerical difference in $\alpha_s\left(Q^2\right)$ if μ^2 and Q^2 are far from each other, which is important in present day precision measurements. Therefore, the scale μ is chosen to be $\mu = M_Z$ because $M_Z \simeq 91.2\,\text{GeV}$ is not far from the scales where $\alpha_s(Q^2)$ is used in current experimental analyses.

Another approach to solving the RGE is to introduce a reference scale Λ by

$$\ln\frac{Q^2}{\Lambda^2} = \int_{\alpha_s\left(Q^2\right)}^{\infty} \frac{\mathrm{d}x}{\beta(x)}\ .$$

The scale Λ indicates where the coupling becomes strong. The following exercise is to explore the characteristics of this choice.

Exercise 19.2

The running of the strong coupling is given by Eq. (19.3.16). The perturbative expansion of the QCD beta function is given by Eq. (19.3.18) with $b_0, b_1 \geq 0$. Determine (i) the expression for the coupling in leading order ($b_0 \neq 0$, $b_1 = 0$) and the corresponding scale Λ_0 (see below) (ii) the expression for the coupling in next-to-leading order ($b_0 \neq 0$, $b_1 \neq 0$) and the corresponding scale Λ_1 (see below).
  Suggested steps:

1. *Solve the differential equation for $\alpha_s(\mu)$; you'll get an integration constant.*

2. *Express your result in the form*

$$\alpha_s(\mu) = \frac{1}{K \ln(\frac{\mu^2}{\Lambda_0^2})}$$

   where K is a constant.

3. *Solve the differential equation using $b_1 \neq 0$*

$$\int \mathrm{d}\alpha_s \frac{1}{-b_0\alpha_s^2 - b_1\alpha_s^3} = \frac{b_0 + b_1\alpha_s \log(\alpha_s) - b_1\alpha_s \log(b_0 + b_1\alpha_s)}{b_0^2\alpha_s} + K$$

4. *This time the solution cannot be solved for α_s analytically. One can nevertheless find an approximate solution by expanding α_s in $\log \frac{\mu^2}{\Lambda_1^2}$. The constant K is not equal to the one in the first part of this exercise.*

5. *Cast your equation for α_s into the form*

$$\alpha_s = \frac{1}{K \ln \frac{\mu^2}{\Lambda_1^2}} \frac{1}{1 + c_1 \frac{\ln(c_2 + b_0 \alpha_s)}{\ln \frac{\mu^2}{\Lambda_1^2}}}$$

with a suitable choice of Λ_1.

6. *Expand the right hand side of your equation in $t = \frac{1}{\ln \frac{\mu^2}{\Lambda_1^2}}$ and keep only the first order term. Use the expansion*

$$\frac{1}{1 + C_1 t \ln(C_3 \frac{1}{t} + C_2)} = 1 - t C_1 \ln\left(\frac{1}{t}\right) + O(t).$$

19.4   Quark masses and massless QCD

Quark masses m_q are parameters of $\mathcal{L}_{QCD}$ like the gauge coupling, which need to be renormalized. In QED the electron mass is measured in the laboratories at $\mu_R^2 = 0$ (classical limit). We cannot similarly isolate a quark at $\mu_R^2 = 0$ (at low scale quarks are confined). Instead, we can perform a similar RGE analysis as with α_s. For simplicity we assume one quark flavour with mass m, which is yet another dimensionful parameter, so the RGE becomes:

$$\left[\mu^2 \frac{\partial}{\partial \mu^2} + \beta(\alpha_s) \frac{\partial}{\partial \alpha_s} - \gamma_m(\alpha_s) m \frac{\partial}{\partial m} \right] R\left(\frac{Q^2}{\mu^2}, \alpha_s, \frac{m}{Q} \right) = 0, \quad (19.4.21)$$

where γ_m is called the mass anomalous dimension and the minus sign before γ_m is a convention. In perturbation theory we can write the mass anomalous dimension as

$$\gamma_m(\alpha_s) = c_0 \alpha_s \left(1 + c_1 \alpha_s + O\left(\alpha_s^2\right) \right), \quad (19.4.22)$$

with known coefficients up to c_3. At NLO accuracy we need only $c_0 = \frac{1}{\pi}$ and $c_1 = \frac{303 - 10 n_f}{72\pi}$. As R is dimensionless, the dependence on the dimensionful parameters has to cancel

$$\left(Q^2 \frac{\partial}{\partial Q^2} + \mu^2 \frac{\partial}{\partial \mu^2} + m^2 \frac{\partial}{\partial m^2} \right) R\left(\frac{Q^2}{\mu^2}, \alpha_s, \frac{m}{Q} \right) = 0. \qquad (19.4.23)$$

The difference of Eqs. (19.4.21) and (19.4.23) gives the dependence of R on Q:

$$\left[Q^2 \frac{\partial}{\partial Q^2} - \beta(\alpha_s) \frac{\partial}{\partial \alpha_s} + \left(\frac{1}{2} + \gamma(\alpha_s) \right) m \frac{\partial}{\partial m} \right] R\left(\frac{Q^2}{\mu^2}, \alpha_s, \frac{m}{Q} \right) = 0. \qquad (19.4.24)$$

This equation is solved by introducing the running mass (in addition to the running coupling) $m(Q^2)$ obeying

$$Q^2 \frac{\partial m}{\partial Q^2} = -\gamma_m(\alpha_s) m\left(Q^2 \right), \qquad (19.4.25)$$

from which

$$\ln \frac{m(Q^2)}{m(\mu^2)} = -\int_{\mu^2}^{Q^2} \frac{dq^2}{q^2} \gamma_m\left(\alpha_s\left(q^2 \right) \right).$$

Exponentiating and using the definition of the β function, we obtain

$$m\left(Q^2 \right) = m\left(\mu^2 \right) \exp\left[-\int_{\alpha_s(\mu^2)}^{\alpha_s(Q^2)} d\alpha_s \frac{\gamma_m(\alpha_s)}{\beta(\alpha_s)} \right] \overset{Q^2 \to \infty}{\longrightarrow} 0, \qquad (19.4.26)$$

which means that asymptotically free QCD is a massless theory at asymptotically high energies. Thus we can use the massless approximation of QCD for scattering processes at large energies. At LO in perturbation theory the solution of (19.4.26) is given by

$$-\frac{\gamma_m(\alpha_s)}{\beta(\alpha_s)} = \frac{c_0}{b_0 \alpha_s} \quad \Rightarrow \quad m\left(Q^2 \right) = \overline{m} \left[\alpha_s\left(Q^2 \right) \right]^{\frac{c_0}{b_0}},$$

where we introduced the abbreviation $\overline{m} = m(\mu^2) \left[\alpha_s(\mu^2) \right]^{-\frac{c_0}{b_0}}$. At NLO the solution becomes

$$m\left(Q^2 \right) = \overline{m} \left[\alpha_s\left(Q^2 \right) \right]^{\frac{c_0}{b_0}} \left(1 + \frac{c_0}{b_0} (c_1 - b_1) \left(\alpha_s\left(Q^2 \right) - \alpha_s\left(\mu^2 \right) \right) + O\left(\alpha_s^2 \right) \right).$$

In terms of the running coupling and mass $R\left(1, \alpha_{\mathrm{s}}(Q^2), \frac{m(Q^2)}{Q}\right)$ is a solution of Eq. (19.4.24), proven similarly as $R\left(1, \alpha_{\mathrm{s}}(Q^2)\right)$ being the solution of Eq. (19.3.13). Expanding around $m(Q^2) = 0$, we obtain

$$R\left(1, \alpha_{\mathrm{s}}(Q^2), \frac{m(Q^2)}{Q}\right) = R\left(\frac{Q^2}{\mu^2}, \alpha_{\mathrm{s}}, 0\right) + \sum_{n=1}^{\infty} \frac{1}{n!} \left(\frac{m(Q^2)}{Q}\right)^n R^{(n)}\left(\frac{Q^2}{\mu^2}, \alpha_{\mathrm{s}}, 0\right).$$

$$(19.4.27)$$

We see from Eq. (19.4.27) that derivative terms are suppressed by factors of $1/Q^n$ at large Q^2. From the dependence of R on $\frac{m(Q^2)}{Q}$ we can conclude that the effect of mass is suppressed at high Q^2 by its physical dimension and also by its anomalous dimension, which justifies the assumption about negligible quark masses for $Q^2 \gg m^2$, i.e. for the first three, four or five flavours depending on the characteristic energy scale of the collision. The condition $Q^2 \gg m_t^2$ is not generally fulfilled for the t quark in colliders at present.

Exercise 19.3
Find the definition of $\gamma_m(\alpha_S)$ in (19.4.21). How does one determine γ_m using $Z_m(\mu)$? Compute the value of c_0 in the perturbative expansion of the mass anomalous dimension (in Eq. (19.4.22)).

19.5   Consequences of renormalization and renormalization group equation

We now summarize several important consequences we could read off the analysis carried out in the previous sections.

1. QCD is an asymptotically free theory, the gauge coupling and quark masses decrease with increasing Q^2.

2. If we want to avoid large logarithms of $\frac{m(Q^2)}{Q}$, we should consider physical observables (that is physically measurable quantities) that

have a finite zero-mass limit (called infrared-safe observable quantity):

$$
R\left(\frac{Q^2}{\mu^2}, \alpha_s\left(Q^2\right), \frac{m\left(Q^2\right)}{Q}\right) = \underbrace{R\left(\frac{Q^2}{\mu^2}, \alpha_s\left(Q^2\right), 0\right)}_{\text{infrared-safe observable}} + O\left(\left(\frac{m}{Q}\right)^p\right),
$$

($p > 0$). As a result, light quarks (u, s, d, always, c usually, and often b too) are considered massless. For massless quarks helicity is conserved in the interaction with a vector boson, which can be exploited to simplify computations significantly (see the spinor helicity method).

3. For scattering amplitudes, renormalization is achieved by the substitution

$$
\alpha_s^{(0)} \mu^{2\epsilon} S_\epsilon^{\overline{\text{MS}}} \to \alpha_s\left(\mu_R^2\right) \mu_R^{2\epsilon}\left[1 - \frac{\alpha_s\left(\mu_R^2\right)}{4\pi} \frac{\beta_0}{\epsilon} + \dots\right], \quad (19.5.28)
$$

with

$$
S_\epsilon^{\overline{\text{MS}}} = (4\pi)^\epsilon \exp(-\gamma_E \epsilon),
$$

which amounts to a simple shift in the amplitude:

$$
\left|\mathcal{M}_m^{(0)}\right\rangle = C(\mu_R, \mu, q; \epsilon)\left|\mathcal{A}_m^{(0)}\right\rangle \qquad q \in \mathbb{N} \qquad (19.5.29)
$$

$$
\left|\mathcal{M}_m^{(1)}\right\rangle = C(\mu_R, \mu, q; \epsilon)
$$
$$
\times \frac{\alpha_s\left(\mu_R^2\right)}{4\pi}\left[\left(\frac{\mu_R^2}{\mu^2}\right)^\epsilon \left(S_\epsilon^{\overline{\text{MS}}}\right)^{-1}\left|\mathcal{A}_m^{(1)}\right\rangle - \frac{q}{2}\frac{\beta_0}{\epsilon}\left|\mathcal{A}_m^{(0)}\right\rangle\right]
$$
$$
(19.5.30)
$$

where $C(\mu_R, \mu, q; \epsilon) = \left(4\pi\alpha_s\left(\mu_R^2\right)\right)^{\frac{q}{2}}\left(\frac{\mu_R^2}{\mu^2}\right)^{\frac{q}{2}\epsilon}\left(S_\epsilon^{\overline{\text{MS}}}\right)^{-\frac{q}{2}}$. The amplitudes $\mathcal{A}_m^{(i)}$ are the terms in the expansion of the unrenormalized amplitude, whereas the formal perturbative expansion of the renormalized amplitude is $|\mathcal{M}_m\rangle = \left|\mathcal{M}_m^{(0)}\right\rangle + \left|\mathcal{M}_m^{(1)}\right\rangle + \dots$. The factors μ_R^2/μ^2 remove the dependence on the dimensional regularization scale μ and introduce the dependence on the renormalization scale μ_R.

4. The renormalized theory is ultraviolet finite. We shall see that $\left|\mathcal{M}_m^{(1)}\right\rangle$ is divergent also in the infrared. We can use dimensional regularization

to regulate the amplitudes in the infrared by continuing into $d > 4$ ($\epsilon < 0$). The integrals that are scaleless in $d = 4$ have $(q^2)^{-\epsilon}$ mass dimension in $d = 4 - 2\epsilon$. Therefore, in the massless limit all integrals can depend only on momentum invariants raised to a positive fractional power ($\epsilon < 0!$). We conclude that when all external invariants vanish, the continued integral must also vanish ("scaleless integrals vanish in dimensional regularization").

5. For infrared-safe observables the radiative corrections are finite in $d = 4$, we can thus take the limit $\epsilon \to 0$, or for the sake of simpler book-keeping, we can set $C(\mu_R, \mu, q; \epsilon) \to (4\pi\alpha_s)^{\frac{q}{2}}$ from the beginning of the computations.

19.6 $R_{e^+e^-}$ at NLO

We have seen that the loop insertion on a fermion propagator

 $\propto \left(p^2\right)^{-\epsilon}$ where p^μ is the four-momentum leaving the loop and for the UV-renormalized theory $\epsilon < 0$ to regulate the IR divergences. On a massless external leg, which is on-shell, $p^2 = 0$, so

 $= 0$. Therefore, only the vertex correction gives a contribution, given by the graph

 $\equiv \mathcal{A}_4^{(1)}\left(1^{h_1}, 2^{h_2}, 4^{h_4}, 5^{h_5}\right).$

Applying the helicity Feynman rules, we find

$$\frac{\alpha_s}{4\pi}\mathcal{A}_4^{(1)}\left(1^{h_1}, 2^{h_2}, 4^{h_4}, 5^{h_5}\right) = C_F\, e^2\, e_q\, \frac{4\pi\alpha_s\mu^{2\epsilon}}{2}$$

$$\int \frac{d^d\ell}{(2\pi)^d}\, \langle 1^{h_1}|\gamma^\mu \ell \gamma^\alpha \left(\ell - p_1 - p_2\right)\gamma^\nu |2^{-h_2}\rangle$$

$$\times \frac{(-g_{\mu\nu})(-g_{\alpha\beta})}{\ell^2\,(\ell - p_1)^2\,(\ell - p_1 - p_2)^2\, s_{12}}\, \langle 5^{h_5}|\gamma^\beta |4^{-h_4}\rangle \quad (19.6.31)$$

$$= C_F\, e^2\, e_q\, \frac{4\pi\alpha_s\mu^{2\epsilon}}{2s_{12}}\, I_{\rho\sigma}\,(p_1, p_2)$$

$$\times \langle 1^{h_1}|\gamma^\mu \gamma^\rho \gamma^\alpha \gamma^\sigma \gamma_\mu |2^{-h_2}\rangle \langle 5^{h_5}|\gamma_\alpha |4^{-h_4}\rangle,$$

where

$$I^{\rho\sigma}(p_1, p_2) = I_3^{\rho\sigma}(p_1, p_2) - (p_1 + p_2)^\sigma I_3^\rho(p_1, p_2)$$

$$I_3^{\rho\sigma}(p_1, p_2) = \int \frac{\mathrm{d}^d\ell}{(2\pi)^d} \frac{\ell^\rho \ell^\sigma}{\ell^2 (\ell - p_1)^2 (\ell - p_1 - p_2)^2} =$$

$$a_0 g^{\rho\sigma} s_{12} + a_{11} p_1^\rho p_1^\sigma + a_{22} p_2^\rho p_2^\sigma + a_{12} \left(p_1^\rho p_2^\sigma + p_1^\sigma p_2^\rho\right)$$

$$I_3^\rho(p_1, p_2) = \int \frac{\mathrm{d}^d\ell}{(2\pi)^d} \frac{\ell^\rho}{\ell^2 (\ell - p_1)^2 (\ell - p_1 - p_2)^2} = a_1 p_1^\rho + a_2 p_2^\rho .$$

(19.6.32)

We now use algebraic relations to express these tensor integrals as a linear combination of two scalar integrals (procedure called *reduction to master integrals*),

$$\begin{aligned} I_2(p) &= \int \frac{\mathrm{d}^d\ell}{(2\pi)^d} \frac{1}{\ell^2 (\ell - p)^2} \\ &= \frac{i}{(4\pi)^{2-\epsilon}} \left(-p^2\right)^{-\epsilon} \Gamma(\epsilon) B(1 - \epsilon, 1 - \epsilon) \\ &= \frac{i}{(4\pi)^{2-\epsilon}} \frac{1}{\epsilon} \frac{\Gamma^2(1 - \epsilon) \Gamma(1 + \epsilon)}{\Gamma(2 - 2\epsilon)} \left(-p^2\right)^{-\epsilon} , \end{aligned}$$

(19.6.33)

$$\begin{aligned} I_3(p_1, p_2) &= \int \frac{\mathrm{d}^d\ell}{(2\pi)^d} \frac{1}{\ell^2 (\ell - p_1)^2 (\ell - p_1 - p_2)^2} \\ &= -\frac{i}{(4\pi)^{2-\epsilon}} \frac{1}{\epsilon^2} \frac{\Gamma^2(1 - \epsilon) \Gamma(1 + \epsilon)}{\Gamma(1 - 2\epsilon)} (-s_{12})^{-1-\epsilon} \\ &= \frac{1}{s_{12}} \frac{1 - 2\epsilon}{\epsilon} I_2(p_1 + p_2) , \end{aligned}$$

(19.6.34)

which we can obtain using Feynman parametrization. The algebraic relations can be derived by contracting the integrals with the external momenta and

the metric tensor.

$$2\, p_1^\mu\, I_\mu^{(3)}(p_1, p_2)\ = a_2 s_{12}, \tag{19.6.35}$$

$$2\, p_2^\mu\, I_\mu^{(3)}(p_1, p_2)\ = a_1 s_{12}, \tag{19.6.36}$$

$$g^{\mu\nu}\, I_{\mu\nu}^{(3)}(p_1, p_2)\ = (d\, a_0 + a_{12})\, s_{12}, \tag{19.6.37}$$

$$4\, p_1^\mu\, p_2^\nu\, I_{\mu\nu}^{(3)}(p_1, p_2)\ = s_{12}^2\, (2a_0 + a_{12}), \tag{19.6.38}$$

$$4\, p_1^\mu\, p_1^\nu\, I_{\mu\nu}^{(3)}(p_1, p_2)\ = s_{12}^2 a_{22}, \tag{19.6.39}$$

$$4\, p_2^\mu\, p_2^\nu\, I_{\mu\nu}^{(3)}(p_1, p_2)\ = s_{12}^2 a_{11}. \tag{19.6.40}$$

We can substitute the numerators in the integrands on the left hand sides of Eqs. (19.6.35)–(19.6.40) with denominator factors using the algebraic relations

$$2\ell \cdot p_1 = \ell^2 - (\ell - p_1)^2 \qquad\qquad \left(p_1^2 = 0\right),$$

$$2\ell \cdot p_2 = (\ell - p_1)^2 - (\ell - p_1 - p_2)^2 + s_{12} \qquad \left(p_1^2 = p_2^2 = 0\right).$$

We do not need all coefficients in our calculation. We now perform the spinor algebra.

$$\gamma^\mu \gamma^\rho \gamma^\alpha \gamma^\sigma \gamma_\mu = (4 - d)\, \gamma^\rho \gamma^\alpha \gamma^\sigma - 2\gamma^\sigma \gamma^\alpha \gamma^\rho.$$

The gamma matrices γ^ρ and γ^σ will be contracted with either

(a) $g_{\rho\sigma}$, giving $\gamma^\mu \gamma^\rho \gamma^\alpha \gamma_\rho \gamma_\mu = (d - 2)^2\, \gamma^\alpha$, or

(b) p_1 and p_2.

- Case (a):

$$\left\langle 1^{h_1}\middle| \gamma^\mu \gamma^\rho \gamma^\alpha \gamma_\rho \gamma_\mu \middle| 2^{-h_2}\right\rangle \left\langle 5^{h_5}\middle| \gamma_\alpha \middle| 4^{-h_4}\right\rangle =$$
$$= (d - 2)^2 \underbrace{\left\langle 1^{h_1}\middle| \gamma^\alpha \middle| 2^{-h_2}\right\rangle \left\langle 5^{h_5}\middle| \gamma_\alpha \middle| 4^{-h_4}\right\rangle}_{-i\, s_{12}\, a_4(h_1, h_2, h_4, h_5)}$$

  where $a_4\,(h_1, h_2, h_4, h_5)$ was computed in Eqs. (18.9.21)–(18.9.25).

- Case (b): the only non-zero contributions are

$$\left\langle 1^{h_1}\middle| \gamma^\rho \gamma^\alpha \gamma^\sigma \middle| 2^{-h_2}\right\rangle\, p_{1\sigma}\, p_{2\rho} = \left\langle 1^{h_1}\middle| \slashed{2}\gamma^\alpha \slashed{1} \middle| 2^{-h_2}\right\rangle$$
$$= \left\langle 1^{h_1}\middle| 2^{-h_1}\right\rangle \left\langle 2^{-h_1}\middle| \gamma^\alpha \middle| 1^{h_2}\right\rangle \left\langle 1^{h_2}\middle| 2^{-h_2}\right\rangle$$
$$\tag{19.6.41}$$

$$\langle 1^{h_1}| \gamma^\sigma \gamma^\alpha \gamma^\rho |2^{-h_2}\rangle \, p_{1\rho} \, p_{2\sigma} = \langle 1^{h_1}| 2^{-h_1}\rangle \langle 2^{-h_1}| \gamma^\alpha |1^{h_2}\rangle \langle 1^{h_2}| 2^{-h_2}\rangle$$
$$= -s_{12} \langle 1^{h_1}| \gamma^\alpha |2^{-h_2}\rangle$$

$$(19.6.42)$$

where we used $h_1 = -h_2$. Therefore, we need to compute a_0, a_1, a_2 and a_{12} only. From Eqs. (19.6.35) and (19.6.36) we find

$$
\begin{aligned}
a_1 &= \frac{1}{s_{12}} \int \frac{d^d \ell}{(2\pi)^d} \frac{(\ell - p_1)^2 - (\ell - p_1 - p_2)^2 + s_{12}}{\ell^2 (\ell - p_1)^2 (\ell - p_1 - p_2)^2} \\
&= \frac{1}{s_{12}} \left[I_2(p_1 + p_2) - \underbrace{I_2(p_1)}_{=0} + s_{12} I_3(p_1, p_2) \right] \\
&= \frac{1}{s_{12}} \left(\frac{1}{\epsilon} - 1 \right) I_2(p_1 + p_2), \qquad (19.6.43) \\
a_2 &= \frac{1}{s_{12}} \int \frac{d^d \ell}{(2\pi)^d} \frac{\ell^2 - (\ell - p_1)^2}{\ell^2 (\ell - p_1)^2 (\ell - p_1 - p_2)^2} \\
&= \frac{1}{s_{12}} \left[\underbrace{I_2(p_2)}_{=0} - I_2(p_1 + p_2) \right] \\
&= -\frac{1}{s_{12}} I_2(p_1 + p_2). \qquad (19.6.44)
\end{aligned}
$$

From Eqs. (19.6.37) and (19.6.38) we find

$$(d\, a_0 + a_{12}) s_{12} = I_2(p_2) = 0$$

$$
\begin{aligned}
(2a_0 + a_{12}) s_{12}^2 &= \int \frac{d^d \ell}{(2\pi)^d} \\
&\quad \times \left(\frac{\ell^2 (\ell - p_1)^2 - \ell^2 (\ell - p_1 - p_2)^2 + \ell^2 s_{12} - \left[(\ell - p_1)^2 \right]^2}{\ell^2 (\ell - p_1)^2 (\ell - p_1 - p_2)^2} \right. \\
&\quad \left. + \frac{(\ell - p_1)^2 (\ell - p_1 - p_2)^2 - (\ell - p_1)^2 s_{12}}{\ell^2 (\ell - p_1)^2 (\ell - p_1 - p_2)^2} \right) \\
&= s_{12} I_2(p_2) + 2 p_{1\mu} I_2^\mu (p_1 + p_2) - s_{12} I_2(p_1 + p_2) \\
&= -\frac{s_{12}}{2} I_2(p_1 + p_2).
\end{aligned}
$$

In the last step we used

$$I_2^\mu (p) = \int \frac{\mathrm{d}^d \ell}{(2\pi)^d} \frac{\ell^\mu}{\ell^2 (\ell - p)^2} = a(p) p^\mu,$$

where contraction with p_μ yields an equation for the unknown coefficient $a(p)$,

$$a(p) p^2 = \frac{1}{2} \int \frac{\mathrm{d}^d l}{(2\pi)^d} \frac{l^2 - (l-p)^2 + p^2}{l^2 (l-p)^2} = \frac{p^2}{2} I^{(2)}(p).$$

Therefore,

$$a_0 = \frac{1}{2(d-2)} s_{12}^{-1} I_2 (p_1 + p_2)$$

and

$$a_{12} = -\frac{d}{2(d-2)} s_{12}^{-1} I_2 (p_1 + p_2) .$$

From Eqs. (19.6.39) and (19.6.40) we can also compute the coefficients that are not needed in our calculation:

$$a_{11} = -\frac{d}{2(d-4)} s_{12}^{-1} I_2 (p_1 + p_2) , \qquad (19.6.45)$$

$$a_{22} = -\frac{1}{2} s_{12}^{-1} I_2 (p_1 + p_2) . \qquad (19.6.46)$$

We can now simply collect all contributions to the vertex correction. We obtain

$$\frac{\alpha_s}{4\pi} \mathcal{A}_4^{(1)} \left(1^{h_1}, 2^{h_2}, 4^{h_4}, 5^{h_5} \right) = C_F\, e^2 e_q \frac{4\pi \alpha_s \mu^{2\epsilon}}{2 s_{12}} \left[-i s_{12}\, a_4 \left(1^{h_1}, 2^{h_2}, 4^{h_4}, 5^{h_5} \right) \right]$$

$$\times \left\{ a_0\, s_{12}\, (d-2)^2 + a_{12} \left[(4-d)(-s_{12}) - 2(-s_{12}) \right] \right.$$

$$\left. - \left[(4-d) a_2 (-s_{12}) - 2 a_1 (-s_{12}) \right] \right\}$$

$$= C_F\, e^2 e_q \frac{\alpha_s}{4\pi} \left(-\frac{4\pi \mu^2}{s_{12}} \right)^\epsilon \frac{1}{\epsilon} \frac{\Gamma^2 (1-\epsilon) \Gamma (1+\epsilon)}{\Gamma (1-2\epsilon)}$$

$$\times a_4 \left(1^{h_1}, 2^{h_2}, 4^{h_4}, 5^{h_5} \right) \left[-\frac{1}{\epsilon} - \frac{3}{2} - 4\epsilon + O \left(\epsilon^2 \right) \right] .$$

Remember that in the helicity formalism $T_R = 1$ and $C_F = \frac{N_c^2 - 1}{N_c}$. To get the result for $T_R = \frac{1}{2}$ one can multiply the expression in [...] with 2 and use $C_F = \frac{N_c^2 - 1}{2 N_c}$, which of course, does not change the amplitude itself.

The above method of computing the vertex correction is general, but it becomes rather involved for more legs. At one loop the problem is considered being solved although the algebraic complexity grows so fast that the general method to compute the one-loop amplitudes is numerical, which becomes computationally expensive and may become unstable for many external legs.

For the second term $\left|\mathcal{M}_n^{(1)}\right\rangle$ in the loop-expansion of the renormalized amplitude a general form is known (with $T_R = \frac{1}{2}$ normalization):

$$\left|\mathcal{M}_n^{(1)}\right\rangle = \boldsymbol{I}_n\left(\epsilon, \mu^2, \{p_i\}\right) \frac{\alpha_s^{(R)}}{4\pi}\left|\mathcal{M}_n^{(0)}\left(\{p_i\}\right)\right\rangle + \left|\mathcal{M}_n^{(1)\,\mathrm{fin}}\left(\mu^2, \{p_i\}\right)\right\rangle + O\left(\epsilon\right)$$

where

$$\left|\mathcal{M}_n^{(1)}\right\rangle = \boldsymbol{I}_n\left(\epsilon, \mu^2, \{p_i\}\right)\left|\mathcal{M}_n^{(0)}\left(\{p_i\}\right)\right\rangle + \left|\mathcal{M}_n^{(1)\,\mathrm{fin}}\left(\mu^2, \{p_i\}\right)\right\rangle + O\left(\epsilon\right)$$

and the upper index "fin" indicates a term in the amplitude that remains finite as $\epsilon \to 0$. The factor $\boldsymbol{I}_n\left(\epsilon, \mu^2; \{p_i\}\right)$ in massless QCD is given by[3]

$$\boldsymbol{I}_n\left(\epsilon, \mu^2; \{p_i\}\right) = \frac{(4\pi)^\epsilon}{\Gamma\left(1-\epsilon\right)}\left\{\sum_i^n \sum_{k \neq i}^n \boldsymbol{T}_i \cdot \boldsymbol{T}_k \left(\frac{\mu^2}{-s_{ik}}\right)^\epsilon \frac{1}{\epsilon^2} - \frac{1}{\epsilon}\sum_i^n \gamma_i\right\},$$

where the sums run over all coloured external legs. Note that

$$\left(\frac{\mu^2}{-s_{ik}}\right)^\epsilon \frac{1}{\epsilon^2} = \left(\frac{\mu^2}{|s_{ik}|}\right)^\epsilon \frac{1}{\epsilon^2} + \left(\frac{1}{\epsilon}i\pi - \frac{\pi^2}{2}\right)\Theta\left(s_{ik}\right) + O(\epsilon)$$

where the second term on the right hand side is related to the $+i\epsilon$ prescription in the Feynman propagator. The flavour constant γ_i are $\gamma_q = \frac{3}{2}C_F$ and $\gamma_g = \frac{1}{2}\beta_0$. $\boldsymbol{T}_i$ denotes the colour charge associated with the emission of a gluon from parton i,

$$\boldsymbol{T}_i = T_i^c \left|c\right\rangle \implies$$
$$\left\langle c_1, \ldots, c_i, \ldots c_n, c \left|\boldsymbol{T}_i\right| b_1, \ldots, b_i, \ldots, b_n\right\rangle = \delta_{c_1 b_1} \ldots T_{c_i b_i}^c \ldots \delta_{c_n b_n}$$

where $T_{cb}^a = F_{cb}^a$ and $T_{kl}^a = t_{kl}^a$ are the representation matrices in the adjoint and fundamental representations. The colour algebra is as follows:

$$\boldsymbol{T}_i \cdot \boldsymbol{T}_k = \boldsymbol{T}_k \cdot \boldsymbol{T}_i \quad \text{if} \quad i \neq k \quad \text{and} \quad \boldsymbol{T}_i^2 = C_i \quad (C_A \text{ or } C_F).$$

---

[3]The $\boldsymbol{I}_n$ operator is known also with finite quark masses and also for the two-loop amplitude.

The amplitude $|\mathcal{M}_m\rangle$ is gauge invariant, i.e., it is a singlet in colour space,

$$\langle c_1, \ldots, c_m | \mathcal{M}_m \rangle = \left\langle c_1, \ldots, c_m \left| \prod_j \left(e^{i\varepsilon_a T_j^a} \right) \right| \mathcal{M}_m \right\rangle$$

$$= \langle c_1, \ldots, c_m | \mathcal{M}_m \rangle + i\varepsilon_a \left\langle c_1, \ldots, c_m \left| \sum_j T_j^a \right| \mathcal{M}_m \right\rangle + O(\varepsilon_a^2).$$

The infinitesimal parameters ε_a are arbitrary, so we find

$$\left\langle c_1, \ldots, c_m \left| \sum_j T_j^a \right| \mathcal{M}_m \right\rangle = 0$$

for any a and consequently $\sum_{i=1}^n \boldsymbol{T}_i |\mathcal{M}_n\rangle = 0$. We denote the general colour connected squared matrix element as

$$\langle \mathcal{M}_n | \boldsymbol{T}_i \cdot \boldsymbol{T}_k | \mathcal{M}_n \rangle \equiv \left| \mathcal{M}_{n(i,k)} \right|^2 .$$

In our example $q = 0$, $n = 2$, $s_{12} = s > 0$, $\frac{\Gamma^2(1-\epsilon)\Gamma(1+\epsilon)}{\Gamma(1-2\epsilon)} = \frac{1}{\Gamma(1-\epsilon)} + O(\epsilon^3)$ so

$$\boldsymbol{I}\left(\epsilon, \mu^2; p_1, p_2\right) = \frac{(4\pi)^\epsilon}{\Gamma(1-\epsilon)} \left[-2C_F \left(\frac{\mu^2}{-s_{12}} \right)^\epsilon \frac{1}{\epsilon^2} - \frac{3}{\epsilon} C_F \right]. \qquad (19.6.47)$$

The comparison to our explicit computations gives

$$\left| \mathcal{M}_4^{(1)\,\text{fin}}\left(\mu^2; p_1, p_2\right) \right\rangle = C_F e^2 e_q \, (-8) \left| \mathcal{M}_4^{(0)} \right\rangle \qquad \left(\text{remember: } C_F = \frac{N_c^2 - 1}{2N_c} \right).$$
$$(19.6.48)$$

The cross section σ is computed from

$$\langle \mathcal{M}_m | \mathcal{M}_m \rangle = \left\langle \mathcal{M}_m^{(0)} \middle| \mathcal{M}_m^{(0)} \right\rangle + 2\text{Re} \left\langle \mathcal{M}_m^{(0)} \middle| \mathcal{M}_m^{(1)} \right\rangle + \ldots. \qquad (19.6.49)$$

In our case the virtual corrections are

$$\text{Re}\langle \mathcal{M}_4^{(0)} | \mathcal{M}_4^{(1)} \rangle = \text{Re}\left\langle \; \rule[-2ex]{0pt}{4ex} \; \middle| \; \rule[-2ex]{0pt}{4ex} \; \right\rangle$$

$$= \left\langle \mathcal{M}_4^{(0)} \middle| I_2(\epsilon) \middle| \mathcal{M}_4^{(0)} \right\rangle - 8C_F \left\langle \mathcal{M}_4^{(0)} \middle| \mathcal{M}_4^{(0)} \right\rangle.$$

19.6.1   Real corrections in $d = 4$ dimensions

Another contribution to the cross section at the same order is given by the *real corrections*

$$|\mathcal{M}_{m+1}|^2 = \left(\frac{\alpha_s^{(0)} \mu^{2\epsilon}}{4\pi}\right)^q 4\pi \alpha_s^{(0)} \mu^{2\epsilon} \left[\left\langle \mathcal{A}_{m+1}^{(0)} \middle| \mathcal{A}_{m+1}^{(0)} \right\rangle + O\left(\alpha_s^{(0)}\right)\right].$$

Two diagrams contribute to $\left|\mathcal{M}_5^{(0)}\right|$: $\left\langle \mathcal{M}_5^{(0)} \middle| \mathcal{M}_5^{(0)} \right\rangle = \left| \begin{array}{c} \text{\small (diagram)} + \text{\small (diagram)} \end{array} \right|^2$.

We compute them first using the helicity formalism and considering the crossing symmetric channel $0 \to p_1^\mu + p_2^\mu + p_3^\mu + p_4^\mu + p_5^\mu$ (the new label '3' refers to the gluon). Both diagrams contribute to the only colour structure $t_{i_1 i_2}^{c_3}$ and thus a single helicity amplitude has the form

$$\mathcal{A}_5\left(1^{h_1}, 2^{h_2}, 3^{h_3}, 4^{h_4}, 5^{h_5}\right) = e^2 \, e_q \, t_{i_1 i_2}^{c_3} \, a_5\left(h_1, h_2, h_3, h_4, h_5\right),$$

where the colour amplitude's are given by

$$
\begin{aligned}
a_5\left(\{h_i\}\right) = & -\frac{i}{\sqrt{2}} \frac{1}{s_{45}} \left[\frac{1}{s_{13}} \left\langle 1^{h_1}\middle| \gamma^\mu \left(\slashed{p}_1 + \slashed{p}_3\right) \gamma^\nu \middle| 2^{-h_2}\right\rangle \right. \\
& \left. + \frac{1}{s_{23}} \left\langle 1^{h_1}\middle| \gamma^\nu \left(-\slashed{p}_2 - \slashed{p}_3\right) \gamma^\mu \middle| 2^{-h_2}\right\rangle \right] \\
& \times \left\langle 5^{h_5}\middle| \gamma_\nu \middle| 4^{-h_4}\right\rangle \epsilon_\mu^{h_3}(p_3, k_3) \\
= & -i \frac{h_3}{2} \frac{\left\langle 3^{h_3} \middle| \gamma_\mu \middle| k_3^{h_3}\right\rangle}{s_{45} \left\langle k_3^{-h_3} \middle| 3^{h_3}\right\rangle} \left\langle 5^{h_5}\middle| \gamma_\nu \middle| 4^{-h_4}\right\rangle \\
& \times \left[\frac{1}{s_{13}} \left(\left\langle 1^{h_1}\middle| \gamma^\mu \middle| 1^{h_1}\right\rangle \left\langle 1^{h_1}\middle| \gamma^\nu \middle| 2^{-h_2}\right\rangle \right. \right. \\
& \left. + \left\langle 1^{h_1}\middle| \gamma^\mu \middle| 3^{h_1}\right\rangle \left\langle 3^{h_1}\middle| \gamma^\nu \middle| 2^{-h_2}\right\rangle \right) \\
& - \frac{1}{s_{23}} \left(\left\langle 1^{h_1}\middle| \gamma^\nu \middle| 2^{h_1}\right\rangle \left\langle 2^{h_1}\middle| \gamma^\mu \middle| 2^{-h_2}\right\rangle \right. \\
& \left. \left. + \left\langle 1^{h_1}\middle| \gamma^\nu \middle| 3^{h_1}\right\rangle \left\langle 3^{h_1}\middle| \gamma^\mu \middle| 2^{-h_2}\right\rangle \right)\right].
\end{aligned}
$$

For helicity configuration $h_3 = h_1 = -h_2$ we choose reference momentum for the gluon polarization (see Eq. (18.9.12)) $k_3 = p_2$, whereas for $h_3 = h_2 = $

$-h_1$ we choose $k_3 = p_1$. The only terms which do not vanish are

$$
\begin{aligned}
&\langle 3^{h_3}|\gamma_\mu|2^{h_3}\rangle\,\langle 1^{h_1}|\gamma^\mu|1^{h_1}\rangle = 2\,\langle 3^{h_3}\,|1^{-h_3}\rangle\langle 1^{-h_3}\,|2^{h_3}\rangle\,,\\
&\langle 3^{h_3}|\gamma_\mu|2^{h_3}\rangle\,\langle 1^{h_1}|\gamma^\mu|3^{h_1}\rangle = \delta_{h_1 h_3}2\,\langle 3^{h_3}\,|1^{-h_3}\rangle\langle 3^{-h_3}\,|2^{h_3}\rangle\,,\\
&\langle 3^{h_3}|\gamma_\mu|1^{h_3}\rangle\,\langle 2^{h_1}|\gamma^\mu|2^{-h_2}\rangle = 2\,\langle 3^{h_3}\,|2^{-h_3}\rangle\langle 2^{-h_3}\,|1^{h_3}\rangle\,,\\
&\langle 3^{h_3}|\gamma_\mu|1^{h_3}\rangle\,\langle 3^{h_1}|\gamma^\mu|2^{-h_2}\rangle = \delta_{h_2 h_3}2\,\langle 3^{h_3}\,|2^{-h_3}\rangle\langle 3^{-h_3}\,|1^{h_3}\rangle\,.
\end{aligned}
\tag{19.6.50}
$$

In the case $h_3 = h_1 = -h_2$ the amplitudes are

$$
\begin{aligned}
a_5\,(+,-,+,-,+) &= -\frac{i}{s_{45}\,\langle 23\rangle}\,\frac{2}{s_{13}}\Big([31]\,\langle 12\rangle\,[15]\,\langle 42\rangle + [31]\,\langle 32\rangle\,[35]\,\langle 42\rangle\Big)\\
&= i\frac{\langle 24\rangle}{\langle 23\rangle\,\langle 31\rangle\,\langle 45\rangle}\,\frac{2}{[45]}\underbrace{\Big(\langle 12\rangle\,[15] + \langle 32\rangle\,[35]\Big)}_{\langle 24\rangle[45]}\\
&= 2i\,\frac{\langle 24\rangle^2}{\langle 23\rangle\,\langle 31\rangle\,\langle 45\rangle}
\end{aligned}
\tag{19.6.51}
$$

and from charge conjugation on the lepton line

$$
a_5\,(+,-,+,+,-) = -2i\,\frac{\langle 25\rangle^2}{\langle 23\rangle\,\langle 31\rangle\,\langle 45\rangle}\,.
$$

In the case $h_3 = h_2 = -h_1$ the amplitudes are

$$
\begin{aligned}
a_5\,(+,-,-,+,-) &= -\frac{i}{s_{45}\,[13]}\left(-\frac{2}{s_{23}}\right)\\
&\quad \times\Big(\langle 32\rangle\,[21]\,[14]\,\langle 52\rangle + \langle 32\rangle\,[31]\,[14]\,\langle 53\rangle\Big)\\
&= i\frac{[14]}{[23]\,[31]\,[45]}\,\frac{2}{\langle 54\rangle}\underbrace{\Big([21]\,\langle 52\rangle + [31]\,\langle 53\rangle\Big)}_{[14]\langle 54\rangle}\quad (19.6.52)\\
&= -2i\,\frac{[14]^2}{[23]\,[31]\,[45]}
\end{aligned}
$$

and

$$
a_5\,(+,-,-,-,+) = 2i\,\frac{[15]^2}{[23]\,[31]\,[45]}\,.
\tag{19.6.53}
$$

The amplitudes in the other four cases (for $h_1 = -$ and $h_2 = +$) are obtained from parity inversion

$$a_5 (h_1, h_2, h_3, h_4, h_5) = a_5 (-h_1, -h_2, -h_3, -h_4, -h_5) |_{\langle ij \rangle \leftrightarrow [ji]}$$

and give a factor of 2 in the squared matrix element, which is then given by

$$\sum_{\text{hel.\& col.}} \left| \mathcal{A}_5^{(0)} \right|^2 = e^4 \, e_q^2 \, N_c \, C_F \, 8 \, \frac{s_{14}^2 + s_{24}^2 + s_{15}^2 + s_{25}^2}{s_{23} s_{13} s_{45}}.$$

There is a mismatch between these calculations of real and virtual corrections:

- in the loop calculation the gluon was treated in $d = 4 - 2\epsilon$ dimensions (had $d - 2$ polarization states),

- in the real correction the gluon had 2 polarization states.

In order to be consistent, we have to perform the calculation of real corrections in $d = 4 - 2\epsilon$, for which the helicity formalism is inconvenient. (At the end of this chapter we shall discuss, how we can yet use the $d = 4$ result, obtained using the helicity formalism.)

19.6.2   Real corrections in arbitrary d dimensions

If we are not interested in the angular correlations between initial and final states, we can simplify the calculation (the full calculation in $d = 4 - 2\epsilon$ is rather lengthy). We can parametrize the total cross section as

$$\sigma_{\text{tot}} \left(e^+ e^- \longrightarrow \text{hadrons} \right) = L^{\mu\nu} (k_1, k_2) \, \frac{1}{s^2} \, H_{\mu\nu} (Q),$$

where $s = Q^2$ and $Q^\mu = (k_1 + k_2)^\mu$ (formerly $(p_4 + p_5)$). $H_{\mu\nu} (Q)$ describes the hadronic (or partonic) final state that depends only on the photon momentum (after summing over all final states and integrating over the phase space). It also includes the flux factor $1/(2s)$ of the cross section. The only possible Lorentz structure it can be decomposed into is

$$H^{\mu\nu} = -H_1 (s) \, g^{\mu\nu} + H_2 (s) \, \frac{Q^\mu Q^\nu}{s}.$$

$L^{\mu\nu}$ describes the leptonic part and is equal to (we take into account the negative sign due to the fermion loop on the left hand side)

$$-L^{\mu\nu} = \frac{1}{4}\ \mu\ \text{〜〜} \bigcirc \text{〜〜}\ \nu = \frac{e^2}{4}\text{Tr}\,(\gamma^\mu \not{k}_1 \gamma^\nu \not{k}_2)$$

$$= e^2\,\left(k_1^\mu k_2^\nu + k_1^\nu k_2^\mu - k_1\cdot k_2\, g^{\mu\nu}\right)\ .$$

The lepton tensor is gauge invariant

$$q_\mu L^{\mu\nu} = e^2\,\left[k_1\cdot k_2 k_2^\nu + k_1\cdot k_2 k_1^\nu - k_1\cdot k_2\,(k_1 + k_2)^\nu\right] = 0\,.$$

As a result, contracting $H_{\mu\nu}$ with $L^{\mu\nu}$, only $H_1(s)$ contributes to σ_{tot}. From

$$g_{\mu\nu}\,L^{\mu\nu} = e^2\,(d-2)\,k_1\cdot k_2 = e^2\,(1-\epsilon)\,s = 4\pi\alpha\,s\,(1-\epsilon)\,,$$

it follows by dimensional analysis that

$$\dim \sigma_{\text{tot}} = \dim \frac{1}{s} = \dim \frac{1}{s^2}L^{\mu\nu}\,,$$

so that $\dim H_1(s) = 0$ and thus $H_1(s)$ must be a constant. $H_{\mu\nu}$ is also $U(1)$ (of QED) gauge invariant and so

$$H_1(s) = H_2(s) \equiv H(s) = -\frac{g^{\mu\nu}H_{\mu\nu}}{d-1}\,.$$

There is one cut diagram that contributes to the hadron tensor $H_{\mu\nu}(s)$ at LO in perturbative QCD. It is formally the same as for the lepton tensor, only the fermion lines refer to quarks of momenta p_1 and p_2. Thus,

$$-H^{\mu\nu} = \frac{1}{2s}\sum_q \int d\phi_2\,(p_1, p_2; Q)\ e^2\,e_q\,N_c\,4\,\left(p_1^\mu p_2^\nu + p_1^\nu p_2^\mu - p_1\cdot p_2 g^{\mu\nu}\right)\,,$$

$$\tag{19.6.54}$$

where $d\phi_2$ is the two-particle phase-space measure (see Eq. (18.3.5) for $n = 2$) and summation extends over quark flavours whose masses are much smaller than $\sqrt{s}$. From Eq. (19.6.54) we find

$$-H^{(0)}(s) = -\frac{e^2\,\left(\sum_q e_q^2\right)N_c}{2(d-1)\,s}\,2s\,(2-d)\int d\phi_2$$

$$= N_c\,e^2\left(\sum_q e_q^2\right)\frac{d-2}{d-1}\int d\phi_2 \tag{19.6.55}$$

$$= \frac{\alpha}{3}N_c\left(\sum_q e_q^2\right)(1 + O(\epsilon))\,.$$

Then

$$\sigma_{\text{tot}} = \lim_{\epsilon \to 0} \left[L^{\mu\nu} \frac{1}{s^2} \left(-g_{\mu\nu} H^{(0)}(s) \right) \right] = \frac{4\pi\alpha^2}{3s} N_c \sum_q e_q^2 \,,$$

which we knew already, cf. with Eq. (19.1.1).

At NLO accuracy we apply all possible cuts on the three possible diagrams:

The virtual correction emerges from cuts that lead to the loop×tree diagrams:

We already know that only the vertex correction is non-zero, which gives (cf. Eqs. (19.6.47) and (19.6.48))

$$H_V(s) = \frac{C_F \alpha_s}{2\pi} \frac{1}{\Gamma(1-\epsilon)} \left(\frac{4\pi\mu^2}{s} \right)^\epsilon \left(-\frac{2}{\epsilon^2} - \frac{3}{\epsilon} - 8 + \pi^2 + O(\epsilon) \right) H^{(0)}(s) \,.$$

The real correction comes from cuts that lead to the tree×tree diagrams:

We write the real correction symbolically as:

$$-H_R(s) = \frac{1}{d-1} g^{\mu\nu} \int d\phi_3 \left[d_1(1,2,3) + d_2(1,2,3) \right.$$
$$\left. + d_1(2,1,3) + d_2(2,1,3) \right]_{\mu\nu},$$

where

$$g^{\mu\nu} \int d\phi_3 \, d_1(1,2,3)_{\mu\nu} = \int d\phi_3 \, \mu \quad \text{⟿} \quad \mu$$

$$= -4\pi\alpha_s \mu^{2\epsilon} e^2 \left(\sum_q e_q^2 \right) \frac{1}{2s} N_c C_F \int d\phi_3(p_1, p_2, p_3; q)$$

$$\times \frac{1}{s_{13}^2} \text{Tr} \left[\gamma_\mu \left(-\slashed{p}_2 \right) \gamma^\mu \left(\slashed{p}_1 + \slashed{p}_3 \right) \gamma_\alpha \slashed{p}_1 \gamma^\alpha \left(\slashed{p}_1 + \slashed{p}_3 \right) \right]$$

(the negative sign is due to the fermion loop). We can evaluate the trace using

$$\gamma_\mu \left(-\not{p}_2\right) \gamma^\mu = (d-2)\,\not{p}_2, \qquad\qquad \gamma_\alpha \not{p}_1 \gamma^\alpha = -(d-2)\,\not{p}_1,$$

which leads to

$$\begin{aligned}
\mathrm{Tr}\,[\ldots] &= -(d-2)^2\,(p_1+p_3)^\alpha\,(p_1+p_3)^\beta\,\mathrm{Tr}\left[\not{p}_2 \gamma_\alpha \not{p}_1 \gamma_\beta\right]\\
&= -(d-2)^2\,(p_1+p_3)^\alpha\,(p_1+p_3)^\beta\,4\left(p_{1\alpha}\,p_{2\beta} + p_{1\beta}\,p_{2\alpha} - p_1\cdot p_2\,g_{\alpha\beta}\right)\\
&= -(d-2)^2\,[2s_{13}\,(s_{12}+s_{23}) - 2s_{13}\,s_{12}] = -8\,(1-\epsilon)^2\,s_{13}\,s_{23}
\end{aligned}$$

and thus

$$\int d\phi_3\,g^{\mu\nu}d_1\,(1,2,3)_{\mu\nu} = \underbrace{4\pi\alpha_s\mu^{2\epsilon}\,e^2\left(\sum_q e_q^2\right)\frac{1}{2s}\,N_c\,C_F}_{\text{the other diagrams have the same prefactor}}$$

$$\times \int d\phi_3\,(p_1,p_2,p_3;q)\,8\,(1-\epsilon)^2\,\frac{s_{23}}{s_{13}}\,.$$

Similarly

$$g^{\mu\nu}\int d\phi_3 d_2\,(1,2,3)_{\mu\nu} = \int d\phi_3\,\mu\ \ \text{\small\mmmm}\bigcirc\text{\small\mmmm}\ \mu$$

$$\propto \int d\phi_3\,(p_1,p_2,p_3;q)\,\frac{-1}{s_{13}s_{23}}$$

$$\times \mathrm{Tr}\left[\underbrace{\gamma_\mu\left(-\not{p}_2\right)\gamma_\nu\left(-\not{p}_2-\not{p}_3\right)\gamma^\mu\ \not{p}_1 \gamma^\nu\left(\not{p}_1+\not{p}_3\right)}_{(4-d)[\not{p}_2\gamma_\nu(\not{p}_2+\not{p}_3)]-2(\not{p}_2+\not{p}_3)\gamma_\nu\not{p}_2}\right].$$

Using the equality $\gamma_\nu\gamma_\alpha\gamma_\beta\gamma^\nu = 4\,g_{\alpha\beta} - (4-d)\,\gamma_\alpha\gamma_\beta$, we find for the trace

$$\begin{aligned}
\mathrm{Tr}\,[\ldots] = (4-d)&\left\{2\,(s_{12}+s_{13})\,\mathrm{Tr}\left[\not{p}_2\left(\not{p}_1+\not{p}_3\right)\right]\right.\\
&\left. - (4-d)\,\mathrm{Tr}\left[\not{p}_2\left(\not{p}_2+\not{p}_3\right)\not{p}_1\left(\not{p}_1+\not{p}_3\right)\right]\right\}\\
&- 2\left\{2s_{12}\,\mathrm{Tr}\left[\left(\not{p}_2+\not{p}_3\right)\left(\not{p}_1+\not{p}_3\right)\right]\right.\\
&\left. - (4-d)\,\mathrm{Tr}\left[\left(\not{p}_2+\not{p}_3\right)\not{p}_2\not{p}_1\left(\not{p}_1+\not{p}_3\right)\right]\right\}
\end{aligned}$$

$$= 2(4-d)\Big[(s_{12} + s_{13})\, 2\, (s_{12} + s_{23}) + s_{23}\, s_{13}$$

$$- (s_{12} + s_{13})\,(s_{12} + s_{23}) + (s_{12} + s_{13} + s_{23})\, s_{12}\Big]$$

$$- (4-d)^2 \Big[s_{23}\, s_{13} - s_{12}\,(s_{12} + s_{13} + s_{23}) + (s_{12} + s_{23})\,(s_{12} + s_{13})\Big]$$

$$- 4 s_{12} 2\,(s_{12} + s_{13} + s_{23})$$

$$= -8 s_{12} s + 4\epsilon\,[2 s_{12} s + 2 s_{13}\, s_{23}] - 4\epsilon^2 2 s_{13}\, s_{23}$$

$$= -8\,(1-\epsilon)\,[s\, s_{12} - \epsilon\, s_{13} s_{23}],$$

where $s_{12} + s_{13} + s_{23} = s$. Collecting the contributions from the four cut diagrams, we finally have

$$-H_R(s) = \frac{1}{d-1} \int g^{\mu\nu}\Big[d_1\,(1,2,3) + d_1\,(2,1,3)$$

$$+ d_2\,(1,2,3) + d_2\,(2,1,3)\Big]_{\mu\nu}$$

$$= 4\pi\alpha_s \mu^{2\epsilon} e^2 \sum_q e_q^2 N_c C_F \frac{1}{2s} \int d\phi_3\,(p_1, p_2, p_3; q)$$

$$\times 4\frac{d-2}{d-1}\left[(1-\epsilon)\left(\frac{s_{23}}{s_{13}} + \frac{s_{13}}{s_{23}}\right) + 2\frac{s\, s_{12}}{s_{13} s_{23}} - 2\epsilon\right]$$

where the three-body phase space can be rewritten as

$$d\phi_3\,(p_1, p_2, p_3; q) = (2\pi)^{3-2d}\, 2^{-1-d}\left(q^2\right)^{d-3} d^{d-2}\Omega\, d^{d-3}\Omega$$

$$\times (y_{12}\, y_{13}\, y_{23})^{\frac{d-4}{2}}\, dy_{12}\, dy_{13}\, dy_{23}$$

$$\times \delta\,(1 - y_{12} - y_{13} - y_{23})\,[dy_{123}\,\delta\,(1 - y_{123})],$$

with scaled invariants $y_{ij} = \frac{s_{ij}}{s}$ and $y_{123} = y_{12} + y_{13} + y_{23} = 1$. $d^{d-1}\Omega$ is the measure of the hyper-surface element in d dimensions

$$\int d^{d-1}\Omega = \Omega_d = \frac{2\pi^{\frac{d}{2}}}{\Gamma\left(\frac{d}{2}\right)}.$$

Ω_d is the surface of the hyper-sphere of unit radius in d dimensions, for instance $\Omega_2 = 2\pi$ and $\Omega_3 = 4\pi$ ($\Gamma(3/2) = \sqrt{\pi}/2$). Since the integrand depends only on y_{ij}, we can use the two-body phase space

$$d\phi_2\,(p_1, p_2; q) = \left(q^2\right)^{\frac{d-4}{2}} \frac{d^{d-2}\Omega}{(2\pi)^{d-2}\, 2^{d-1}} dy_{12}\delta\,(1 - y_{12})$$
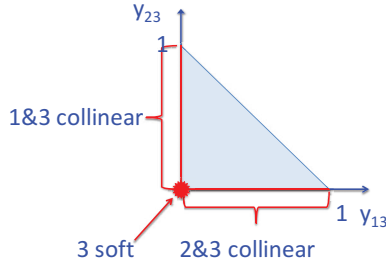
Figure 19.1: Region of integration for the real correction

to write the three-body phase space as

$$d\phi_3\,(p_1, p_2, p_3; q) \;=\; \left(q^2\right)^{1-\epsilon} \frac{1}{(4\pi)^2} \underbrace{\frac{d^{d-3}\Omega}{(2\pi)^{d-3}}}_{\frac{(4\pi)^\epsilon}{\Gamma(1-\epsilon)}}\, d\phi_2\,(q)\,(y_{12}\,y_{13}\,y_{23})^{-\epsilon}$$

$$\times \delta\,(1 - y_{12} - y_{13} - y_{23})\,dy_{12}\,dy_{13}\,dy_{23}. \qquad (19.6.56)$$

Then

$$H_R\,(s) = \frac{C_F\alpha_s}{2\pi}\,\frac{1}{\Gamma(1-\epsilon)}\left(\frac{4\pi\mu^2}{s}\right)^\epsilon H^{(0)}\,(s)$$

$$\times \int dy_{12}\,dy_{13}\,dy_{23}\,\delta\,(1 - y_{12} - y_{13} - y_{23})\,(y_{12}\,y_{13}\,y_{23})^{-\epsilon} \qquad (19.6.57)$$

$$\times \left[(1-\epsilon)\left(\frac{y_{23}}{y_{13}} + \frac{y_{13}}{y_{23}}\right) + 2\left(\frac{y_{12}}{y_{13}y_{23}} - \epsilon\right)\right].$$

The region of integration is shown in Fig. 19.1. The integrand is singular at $y_{13} = 0$ or $y_{23} = 0$. The singularities are regularized by the $(y_{13}y_{23})^{-\epsilon}$ factor in the phase space measure.

The phase-space integral in $H_R\,(s)$ (equation (19.6.57)) can be computed easily (see exercise) and it is equal to

$$\frac{2}{\epsilon^2} + \frac{3}{\epsilon} + \frac{19}{2} - \pi^2 + O\,(\epsilon). \qquad (19.6.58)$$

We find that the sum of the real and virtual corrections is finite,

$$\frac{H_R\,(s) + H_V\,(s)}{H^{(0)}\,(s)} = \frac{C_F\alpha_s}{2\pi}\frac{3}{2} + O\,(\epsilon) = \frac{\alpha_s}{\pi} + O\,(\epsilon). \qquad (19.6.59)$$

Thus we see that σ_{tot}, a totally inclusive quantity is infrared finite (i.e. infrared safe) at one loop.

The natural question at this point is whether there exist other (less inclusive) infrared-safe quantities?

Exercise 19.4

In the lectures we have seen that the 3-point Green's function $I^{(3)}(p_1, p_2)$ can be expressed–up to a "fairly simple" rational polynomial–in terms of the two-point function $I^{(2)}(p_1 + p_2)$. Why was this relation so simple? In this exercise we will derive this relation $I^{(3)}(p_1, p_2) = P(d)I^{(2)}(p_1, p_2)$ ($P(d)$ is a rational polynomial in d) from so called integration-by-parts (IBP) identities. We do this without computing any integrals explicitly. In dimensional regularization the following identities hold (generalization of Gauss' law):

$$\int \frac{d^d k}{(2\pi)^d} \frac{\partial}{\partial k^\mu} k^\mu I(k, p, m, \ldots) = 0,$$

$$\int \frac{d^d k}{(2\pi)^d} \frac{\partial}{\partial k^\mu} p^\mu I(k, p, m, \ldots) = 0.$$

By computing the derivatives and replacing the new scalar products in the numerator by inverse propagators, such as $k \cdot p = 1/2\left(k^2 + p^2 - (k-p)^2\right)$, we obtain a (homogeneous, linear) system of equations by means of which more complicated integrals can be expressed in terms of simpler ones [4]

- *Evaluate the equations*

$$\int \frac{d^d k}{(2\pi)^d} \frac{\partial}{\partial k^\mu} k^\mu \frac{1}{k^2 (k - p_1)^2 (k - p_{12})^2} = 0,$$

$$\int \frac{d^d k}{(2\pi)^d} \frac{\partial}{\partial k^\mu} p^\mu \frac{1}{k^2 (k - p_1)^2 (k - p_{12})^2} = 0$$

($p_{12} = p_1 + p_2$, $p_1^2 = p_2^2 = 0$, $g^\mu_\mu = d$) in order to reduce the three-point function to two-point functions; the propagators of the two-point functions might acquire higher exponents.

---

[4]This method of computing integrals has the advantage that it is easily automated. The systems of equations can however become large.

- *Find two equations that reduce the (two) two-point functions with one squared propagator each down to the so-called "master integral"*

$$I^{(2)}(p_1 + p_2) = \int \frac{d^d k}{(2\pi)^d} \frac{1}{k^2 (k - p_{12})^2} \, .$$

- *Check the relation using the integrals evaluated explicitly in the main text.*

Exercise 19.5

Show that the d-dimensional three-particle phase space for $q \to p_1 + p_2 + p_3$ can be expressed in terms of the Lorentz-invariants $s_{ij} = (p_i + p_j)^2$ as

$$
\begin{aligned}
d\phi_3 \; &= \; \frac{d^{d-1}p_1}{2E_1(2\pi)^{d-1}} \frac{d^{d-1}p_2}{2E_2(2\pi)^{d-1}} \frac{d^{d-1}p_3}{2E_3(2\pi)^{d-1}} (2\pi)^d \, \delta^d(q - p_1 - p_2 - p_3) \\
&= (2\pi)^{3-2d} \, 2^{-1-d} \, (q^2)^{\frac{2-d}{2}} \, d^{d-2}\Omega d^{d-3}\Omega \\
&\quad \times (s_{12}s_{13}s_{23})^{\frac{d-4}{2}} \; ds_{12} \, ds_{13} \, ds_{23} \, \delta\left(q^2 - s_{12} - s_{13} - s_{23}\right) \, .
\end{aligned}
$$

Hints:

- *The d-dimensional volume measure in spherical coordinates is given by*

$$
\begin{aligned}
d^{d+1}p \; &= \; E \, dE \, d^d \, p_E = E \, dE \, E^{d-1} d^d\Omega \\
d^d\Omega \; &= \; (\sin\theta_1)^{d-1} d\theta_1 d^{d-1}\Omega \, .
\end{aligned}
$$

- *Show that*

$$\sin^2\theta_1 \; = \; \frac{1}{4} \frac{s_{12} \, s_{13} \, s_{23}}{q^2 \, E_1^2 \, E_2^2} \, ,$$

where θ_1 is the angle between p_1 and p_2.

Exercise 19.6
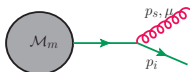
Let $y_{ij} = \frac{s_{ij}}{q^2}$. Using the previous exercise, compute the real correction to the process $e^+ e^- \to q\bar{q}$:

$$
\begin{aligned}
H_R(s) \; &= \; \frac{C_F \alpha_S}{2\pi} \frac{1}{\Gamma(1-\epsilon)} \left(\frac{4\pi\mu^2}{s}\right)^\epsilon H^{(0)}(s) \\
&\quad \times \int dy_{12} \, dy_{13} \, dy_{23} \, \delta\left(1 - y_{12} - y_{13} - y_{23}\right) (y_{12} \, y_{13} \, y_{23})^{-\epsilon} \\
&\quad \times \left[(1-\epsilon)\left(\frac{y_{23}}{y_{13}} + \frac{y_{13}}{y_{23}}\right) + 2\left(\frac{y_{12}}{y_{13} \, y_{23}} - \epsilon\right)\right] \, .
\end{aligned}
$$

Hint: *Transform the triangular integration region into the unit square and evaluate the B (Euler β) functions.*

19.7   Origin of the singular behaviour

A natural question is if we can construct the approximate cross section universally, i.e. independently of the process and observable. Our presentation above suggests the affirmative answer. To understand how, we have to study the origin of the singular behaviour in the squared matrix element (SME). This singularity arises from propagator factors that diverge

$$\propto \frac{1}{(p_i + p_s)^2} = \frac{1}{2\,p_i \cdot p_s} = \frac{1}{2E_i E_s (1 - \cos\theta)} \simeq \frac{1}{E_i E_s \theta^2}$$

In the collinear limit of two external momenta, characterized by $\theta \to 0$, the matrix element behaves as $\mathcal{M}_{m+1} \simeq \mathcal{M}_m/\theta$ + less singular terms (a factor of θ appears in the numerator factors). In the soft limit $E_s \to 0$ the leading singular behaviour is $\mathcal{M}_{m+1} \simeq \mathcal{M}_m/E_s$ + less singular terms. The phase space of the radiated gluon in these limits is approximated as

$$\frac{d^3 p_s}{2E_s} = \frac{1}{2} E_s \, dE_s \, d\cos\theta \, d\phi \simeq \frac{1}{4} E_s \, dE_s \, d\theta^2 \, d\phi \, .$$

Therefore in the cross section we find logarithmic singularities both in the soft and the collinear limits: $\frac{dE_s}{E_s}$ or $\frac{d\theta^2}{\theta^2}$. These are called the infrared singular limits. In dimensional regularization the logarithmic singularities appear as poles:

$$\int dy_{13} \, y_{13}^{-1-\epsilon} = -\frac{1}{\epsilon}.$$

Thus, the singular behaviour arises at kinematically degenerate phase space configurations, which at the NLO accuracy means that one cannot distinguish the following configurations: (i) a single hard parton, (ii) the single parton splitting into two nearly collinear partons, (iii) the single parton emitting a soft gluon (on-shell gluon with very small energy). Then an answer to the question posed at the end of the previous section is given by the Kinoshita-Lee-Nauenberg (KLN) theorem:

In massless, renormalized field theory in four dimensions, transition rates

*are infrared safe if summation over kinematically degenerate initial and final
states is carried out.*

For the $e^+e^- \to$ hadrons process, the initial state is free of infrared
singularities that can emerge only off coloured particles (partons). Typical
infrared-safe quantities are (i) event shape variables and (ii) jet cross sections.

19.7.1   Event shapes

Thrust, thrust major/minor, C- and D-parameters, oblateness, sphericity,
aplanarity, jet masses, jet-broadening, energy-energy correlation, differential
jet rates are examples of event shape variables. The value of an event shape
does not change if a final-state particle further splits into two collinear
particles, or emits a soft gluon, hence it is (qualitatively) infrared safe. As
as example we consider the thrust T, which is defined by

$$T = \max_{\vec{n}} \frac{\sum_{i=1}^{m} |\vec{p}_i \cdot \vec{n}|}{\sum_{i=1}^{m} |\vec{p}_i|}, \tag{19.7.60}$$

where $\vec{n}$ is a three-vector (the direction of the thrust axis) such that T is
maximal. The particle three-momenta $\vec{p}_i$ are defined in the e^+e^- centre-of-
mass frame. T is infrared safe because neither $p_i \to 0$, nor replacing p_i
with $zp_i + (1 - z)p_i$ change the value of T. At LO accuracy it is possible to
perform the phase space integrations and we find the differential distribution
in T:

$$\frac{1}{\sigma} \frac{d\sigma}{dT} = C_F \frac{\alpha_s}{2\pi} \left[\frac{2(3T^2 - 3T + 2)}{T(1-T)} \ln\left(\frac{2T-1}{1-T}\right) - 3(3T-2)\frac{2-T}{1-T} \right]. \tag{19.7.61}$$

We see that the perturbative prediction for the thrust distribution is singu-
lar at $T = 1$. In addition to the linear divergence in $1 - T$ there is logarithmic
divergence, as well. The latter is characteristic to event shape distribu-
tions. In perturbation theory at nth order logarithms of $1 - T$ in the form
$\alpha_s^n \ln^m(1/(1-T))$, $m \leq 2n-1$ appear in the differential distributions of event
shapes, like (19.7.61). These spoil the convergence of the perturbation series
and call for resummation if we want to make reliable predictions near the
edge of the phase space, for large values of T, where most of the data occur
and the best experimental statistics are available. Resummations of leading
(LL, $m = 2n - 1$) and next-to-leading (NLL, $m = 2n - 2$), next-to-next-to-
leading logarithms[5] are available for many event shape variables (for some,

---

[5]The nomenclature in the literature is different as the resummation is performed
for a different formula than the differential distribution.

like thrust even NNNLL is known), but the discussion of this technique is beyond the scope of these lectures.

Exercise 19.7

The thrust variable T is used to characterize final states in $e^+e^- \rightarrow$ hadrons. For m particles in the final state it is defined by Eq. (19.7.60). The momenta are taken in the centre of mass system.

- *Verify that T is infrared and collinear safe.*

- *What is the range of values that T can take if*

    (*a*) *there are only two particles in the final state, or*

    (*b*) *there are three particles in the final state, or*

    (*c*) $m \rightarrow \infty$ *and all $\vec{p}_i$ are distributed spherically.*

Exercise 19.8

Compute the thrust distribution at LO accuracy. Hints:

- *Write the squared matrix elements for three partons in the final state using scaled energy variables $x_i = 2E_i/\sqrt{s} = 1 - y_{jk}$ (i, j, $k = 1, 2, 3$, with $i \neq j \neq k$).*

- *Convince yourself that the value of thrust is $T = \max\{x_1, x_2, x_3\}$.*

- *Find the region of integration in terms of x_1 and x_2.*

- *Find the region where $T = x_1$, x_2 and x_3 and integrate the fully differential cross section with the $\delta(T - T(x_1, x_2))$ function.*

19.7.2 Jet algorithms

Jets are sprays of energetic, on-shell, nearly collinear hadrons. The number of jets does not change if a final-state particle further splits into two collinear particles, or emits a soft gluon, hence it is again qualitatively infrared safe. In order to quantify the jet-like structure of the final states jet algorithms have been invented. These have a long history with rather slow convergence. The reason is that the experimental and theoretical requirements posed to a jet algorithm are rather different. Experimentally we need cones that include almost all hadron tracks at cheap computational price. Theoretically the

important requirements are *infrared safety*, so that perturbation theory can be employed to make predictions and *resummability*, so that we can make predictions in those region of the phase space where most of the data appear.[6]

For many years experimenters at hadron colliders preferred cone jet algorithms (according to the 'Snowmass accord') [Berger, 1992]. These start from a cone seed (centre of the cone) in pseudorapidity (η) and azimuthal-angle (ϕ) plane: (η_c, ϕ_c). We define a distance of a hadron track i from the seed by $d_{ic} = \sqrt{(\eta_i - \eta^c)^2 + (\phi_i - \phi^c)^2}$. A track belongs to the cone if $d_{ic} < R$, with a predefined value for R (usually between 0.5 and 0.8). However, it turned out that (i) this is an infrared unsafe definition and (ii) there is a problem how to treat overlapping cones, so the cone jet definition has been abandoned.

Theoreticians prefer iterative jet algorithms, consisting of the following steps. (i) First we define a *distance d_{ij} between two momenta* (of partons or hadron tracks) and a *rule to combine two momenta*, p_i and p_j into $p_{(ij)}$. (ii) Then we select a *value for resolution*, d_{cut} and consider all pairs of momenta. If the minimum of $\{d_{ij}\}$ is smaller than d_{cut}, then we combine the momenta p_i and p_j and start the algorithm again. If the minimum is larger than d_{cut}, then the remaining momenta (after the combinations) are considered the *momenta of the jets*, and the algorithm stops. The drawback of this algorithm is that it becomes very expensive computationally for many particles in the final state. This is not an issue in perturbative QCD computations because according to our basic assumption there are only few partons, but a major problem for the final states in the detectors where hundreds of hadrons may appear in a single event.

At the experiments of LEP theory won and the Durham (or k_{T})-algorithm was used. It was invented so that resummation of large logarithmic contributions could be achieved [Catani et al., 1991]. The distance measure is $d_{ij} = 2\frac{\min(E_i^2, E_j^2)}{s} R_{ir}$, where $R_{ij} = 1 - \cos\theta_{ij}$ and the recombination scheme is simple addition of the four momenta, $p_{(ij)}^\mu = p_i^\mu + p_j^\mu$. The resolution parameter $y_{\text{cut}} = d_{\text{cut}}/s$ can take values in $(0, 1]$. The perturbative QCD prediction contains logarithmically enhanced terms of the form $\alpha_s^n \ln^m(1/y_{\text{cut}})$, at any order. Such terms have to be resummed if we want to use small value of y_{cut} where we find the bulk of the data (see Figure 17.58). Predictions are available with leading ($m = 2n$) and next-to-leading ($2n - 1$) logarithms (LL and NLL) summed up to all orders [Catani et al., 1991].

Figure 17.58 shows the fixed order LO and NLO predictions, as well as

---

[6]Recently jet identification is considered pattern recognition and deep-learning techniques are being developed to identify jets, which is however beyond our scope.

predictions where NLO and NLL are matched. The curve at NLO accuracy gives a good description of the data measured by the ALEPH collaboration [Barate et al., 1998], but only for $y_{cut} > 0.01$. As $\alpha_s \ln^2(100) = 2.5$, for smaller values of y_{cut} resummation is indispensable. However, the resummed prediction is not expected to give a good description at large y_{cut} because in the resummation formula only the collinear approximation of the matrix element is used. Matching the two predictions gives a remarkably good description of the data over the whole phase space.

At hadron colliders the k_T-algorithm needs modifications. First, instead of energy, the boost-invariant measure of hardness, transverse momentum is used to define the distance between tracks, $d_{ij} = \min(p_{Ti}^2, p_{Tj}^2)\frac{R_{ij}^2}{R^2}$ where $R_{ij}^2 = (y_i - y_j)^2 + (\phi_i - \phi_j)^2$ (distance in rapidity–azimuthal-angle plane), R is a small positive real number, and we need a distance from the beam $d_{iB} = p_{Ti}^2$, too. Also, the algorithm needs modification because either d_{ij} or d_{iB} can be the smallest distance. If a d_{ij} is the smallest value, then i and j are merged, while if the smallest is a d_{iB}, then momentum p_i becomes a jet momentum and is removed from the tracks to be clustered. We then call jet candidates with transverse momentum larger than a predefined value, $p_{Ti} > E_R$ resolved jets. The merging rule changes as well. In the usual merging we add transverse momenta, $p_{T(ij)} = p_{Ti} + p_{Tj}$ and we add rapidities y and azimuthal angles ϕ weighted, $y_{(ij)} = (w_i y_i + w_j y_j)/(w_i + w_j)$ and $\phi_{(ij)} = (w_i \phi_i + w_j \phi_j)/(w_i + w_j)$. The weight can be $w_i = p_{Ti}, p_{Ti}^2, E_{Ti}$, or E_{Ti}^2. Such a merging is boost invariant along the direction of the beam. The parameter R plays a similar role as d_{cut} in electron-positron annihilation or the cone radius R in the cone algorithms: the smaller R, the narrower the jet. Popular values in the experimental analyses are $R = 0.4 - 0.7$.

The iterative k_T-algorithm is infrared safe and resummation of large logarithmic contributions of the form $\alpha_s^n \ln^{2n}$ and $\alpha_s^n \ln^{2n-1}$ is possible, which is a clear advantage from the theoretical point of view. The logarithms are those of $1/R$ and/or Q/E_R, Q being the hard process scale. By taking E_R sufficiently large in hadron-hadron collisions, we avoid such leading contributions from initial-state showering and the underlying event (collisions not belonging to the hard parton-parton scattering), so these terms are determined by the time-like showering of final-state partons (when the virtuality of the parent parton is always positive). Particles within angular separation R tend to combine and particles separated by larger distance than R from all other particles become jets. The algorithm assigns a clustering sequence to particles within jets, so we can look at jet substructure.

Nevertheless, at the TEVATRON experiments the k_T-algorithm did not

become a standard for several reasons. The jets have irregular, often weird shapes as seen on Fig. 17.59 (left) because soft particles tend to cluster first (even arbitrary soft particles can form jets). As a result there is a non-linear dependence on soft particles, energy calibration and estimating acceptance corrections are more difficult. The underlying event correction depends on the area of the jet (in $\eta - \phi$ plane). It was also very expensive computationally, so experimenters had a clear preference of cone algorithms. The breakthrough occurred with Refs. [Cacciari and Salam, 2006, Cacciari et al., 2008] where variants of the k_{T}-algorithm and an improved, fast implementation was introduced. The distance formula was modified to $d_{ij} = \min(p_{\mathrm{T}i}^{2n}, p_{\mathrm{T}j}^{2n})\frac{R_{ij}^2}{R^2}$ ($n = -1, 0, 1$). Infrared safety is independent of n, as well as NLL resummation of large logarithms. It was found that with $n = -1$ (called anti-k_{T}-algorithm) particles close in angle cluster first, which results in regular cone-like shapes as seen on Fig. 17.59 (right) without using stable cones. As a result it became the standard jet algorithm at the LHC experiments. Yet, one should keep in mind that there is no 'perfect' jet algorithm. For instance, the anti-k_{T} one does not provide useful information on jet substructure. It is important to remember that *in perturbative QCD theoretical prediction can be made only with infrared-safe jet functions, but among those the goal of the study may help decide which algorithms to use.*

Analytically, measures of "jettyness" or event shapes are represented by "jet functions", $J(\{p_i\})$, where $\{p_i^\mu\}_{i=1}^n$ is the set of momenta of final state particles. Thrust is an example of the jet function J_m. In perturbation theory the requirement of infrared safety can be formulated as conditions for the jet functions. For instance, at NLO accuracy, the jet function J_m of an m-jet measure (m is the number of jets) must obey:

$$J_m^{(m)}(p_1 \ldots p_m) \to 0 \quad \text{if any} \quad p_i \cdot p_j \to 0$$
$$J_m^{(m+1)}(p_1 \ldots p_{m+1}) \to 0 \quad \text{if} \quad p_i \cdot p_j \quad \text{and} \quad p_k \cdot p_l \to 0 \quad (i \neq k)$$
$$(19.7.62)$$

(for an m-jet measure we need m well separated momenta). Furthermore,

$$J_m^{(m+1)}(p_1, \ldots, p_j = \lambda q, \ldots, p_{m+1}) \to J_m^{(m)}(p_1, \ldots, p_{m+1}) \quad (19.7.63)$$

if $\lambda \to 0$, and q^μ is a fixed vector,

$$J_m^{(m+1)}(p_1, \ldots, p_i, \ldots, p_j, \ldots, p_{m+1}) \to J_m^{(m)}(p_1, \ldots, p, \ldots, p_{m+1}) \quad (19.7.64)$$

if $p_i^\mu \to z p^\mu$, $p_j^\mu \to (1-z) p^\mu$. In the first case in the new jet function $J_m^{(m)}(p_1, \ldots, p_{m+1})$ we have omitted the soft momentum p_j^μ, while in the

second case the two collinear momenta p_i^μ and p_j^μ are replaced by a single momentum p^μ denoting the collinear direction. The cross section is the phase space integral of the squared matrix element weighted by the jet function, for instance

$$\sigma = \frac{1}{2s} \int d\phi_n \, |\mathcal{M}_n|^2 \, J_m^{(n)} (p_1, \dots p_n) \,.$$

In our case of electron-positron annihilation into partons, for an arbitrary jet function $J^{(n)}$ we have the leading-order term

$$H^{(0)}(s, J) = N_c \, e^2 \left(\sum_q e_q^2 \right) \frac{d-2}{d-1} \int d\phi_2 \, (p_1, p_2; q) \, J^{(2)} (p_1, p_2) \,,$$

the virtual correction

$$H_V (s, J) = \frac{C_F \alpha_s}{2\pi} \frac{1}{\Gamma(1-\epsilon)} \left(\frac{4\pi\mu^2}{s} \right)^\epsilon \left(-\frac{2}{\epsilon^2} - \frac{3}{\epsilon} - 8 + \pi^2 + O(\epsilon) \right)$$
$$\times H^{(0)} \left(s, J^{(2)} \right) \,,$$

and the real correction

$$H_R (s, J) = \frac{C_F \alpha_s}{2\pi} \frac{1}{\Gamma(1-\epsilon)} \left(\frac{4\pi\mu^2}{s} \right)^\epsilon H^{(0)} (s)$$
$$\times \int dy_{12} \, dy_{13} \, dy_{23} \, \delta (1 - y_{12} - y_{13} - y_{23}) (y_{12} \, y_{13} \, y_{23})^{-\epsilon}$$
$$\times \left[(1 - \epsilon) \left(\frac{y_{23}}{y_{13}} + \frac{y_{13}}{y_{23}} \right) + 2 \left(\frac{y_{12}}{y_{13} \, y_{23}} - \epsilon \right) \right] J^{(3)} (p_1, p_2, p_3) \,.$$

For the total cross section $J^{(n)} = 1$ and cancellation of infrared poles takes place as in Eq. (19.6.59). For thrust $T^{(2)} (p_1, p_2) = 1$ (by momentum conservation the two outgoing quarks are back-to-back, this direction defines the thrust axis event-by event), and

$$T^{(3)} (p_1, p_2, p_3) \leq 1 \,.$$
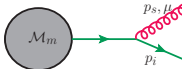
In general, we cannot integrate $H_R (s, J)$ analytically because of the presence of the jet function $J^{(3)}$. Therefore, we do not know how to combine H_V and H_R. To find the solution, we have to understand the structure of infrared singularities in $|\mathcal{M}_n|^2$.

Exercise 19.9
Generalize the requirements for the jet function for a computation at NLO accuracy as given in Eqs. (19.7.62)–(19.7.64) to NNLO accuracy.

19.8   Factorization of $|\mathcal{M}_n|^2$ in the soft limit

The soft limit is defined by $p_s^\mu = \lambda\, q^\mu$, with $\lambda \in \mathbb{R}^+$ (positive real number) and $\lambda \to 0$ for q^μ fixed. In this limit the emission of the soft gluon from (internal) propagators is infrared finite. If we consider the emission of a soft gluon off an external quark (assumed to be massless here) we find
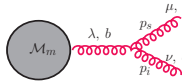
$$\propto \mathcal{M}_m T_i^s\, g_s\, \bar{u}(p_i, s_i)\gamma^\mu\, \frac{\slashed{p}_i + \slashed{p}_s}{s_{is}}$$

$$\overset{p_s \to 0}{\simeq} T_i^s\, g_s\, \frac{1}{s_{is}}\, \bar{u}\,(p_i, s_i)\,\gamma^\mu \slashed{p}_i = T_i^s\, g_s\, \frac{p_i^\mu}{p_i \cdot p_s}\bar{u}\,(p_i, s_i)\,,$$

where T_i^s is the colour charge operator of the soft gluon s, g_s is the strong coupling, $\bar{u}(p_i, s_i)$ is the Dirac adjoint spinor for the outgoing quark labelled with i and $s_{is} = (p_i + p_s)^2 = 2p_i \cdot p_s$. In taking the limit, we used the anti-commutation relation (18.2.2) to write $\gamma^\mu \slashed{p}_i = -\slashed{p}_i\gamma^\mu + 2p_i^\mu$ and the Dirac equation of the massless bi-spinor, $\bar{u}(p_i)\slashed{p}_i = 0$. The factor $\frac{p_i^\mu}{p_i \cdot p_s}$ is the "square root" of the eikonal factor $S_{ik}\,(s) = \frac{2s_{ik}}{s_{is}s_{ks}}$.

The emission of a soft gluon off an external gluon (in light-cone gauge) is given by

$$\propto \mathcal{M}_m \varepsilon^\mu\,(p_s, n)\, \frac{1}{s_{is}}\, d^{\lambda\lambda'}\,(p_i + p_s, n)$$

$$\times \Gamma^{asb}_{\nu\mu\lambda'}\,(-p_i, -p_s, p_i + p_s)\,\varepsilon^\nu\,(p_i, n)$$

where in the three-gluon vertex in the limit becomes

$$V_{\nu\mu\lambda}(-p_i, -p_s, p_i + p_s) =$$
$$= -(p_i + 2p_s)_\nu\, g_{\mu\lambda} + (2p_i + p_s)_\mu\, g_{\nu\lambda} - (p_i - p_s)_\lambda\, g_{\mu\nu}$$
$$= 2p_{i\mu}\, g_{\lambda\nu} + \big[-(p_i + p_s)_\lambda\, g_{\mu\nu} - p_{i\nu}\, g_{\mu\lambda}\big]$$
$$+ \big[p_{s\mu}\, g_{\nu\lambda} + 2p_{s\,\lambda}\, g_{\mu\nu} - 2p_{s\nu}\, g_{\mu\lambda}\big]$$
$$\overset{p_s \to 0}{\simeq} 2p_{i\mu}\, g_{\nu\lambda} - \big[(p_i + p_s)_\lambda\, g_{\mu\nu} + p_{i\nu}\, g_{\mu\lambda}\big]\,.$$

We use $d^{\lambda\lambda'}(p_i + p_s, n)(p_i + p_s)_\lambda = 0$ and $\varepsilon^\nu(p_i, n)p_{i\nu} = 0$, thus

$$\frac{1}{s_{is}}d^{\lambda\lambda'}(p_i + p_s, n)\Gamma^{asb}_{\nu\mu\lambda'}(-p_i, -p_s, p_i + p_s)\varepsilon^\nu(p_i, n) \overset{p_s \to 0}{\simeq}$$

$$T^s_b g_s \frac{p_{i\mu}}{p_i \cdot p_s}\left(d^{\lambda\lambda'}(p_i, n)g_{\lambda'\nu}\varepsilon^\nu(p_i, n)\right) = T^s_b g_s \frac{p_{i\mu}}{p_i \cdot p_s}(-\varepsilon^\lambda(p_i, n)).$$

These two results can be unified and formalized by

$$\hat{S}_s \langle c_s|\, \mathcal{M}_{m+1}(p_s, \ldots)\rangle = g_s\epsilon^\mu(p_s)\,\boldsymbol{J}_\mu(s)|\mathcal{M}_m(\ldots)\rangle$$

where c_s is the colour index of the soft gluon s, $\hat{S}_s$ is an operator which takes the soft limit and keeps the leading singular term in $1/\lambda$, and $\boldsymbol{J}_\mu(s)$ is given by

$$\boldsymbol{J}_\mu(s) = \sum_{k=1}^m \boldsymbol{T}^s_k \frac{p_{k\mu}}{p_k \cdot p_s}.$$

The soft gluon can be emitted from any of the external legs, therefore the sum in the previous formula runs over all external partons. A soft quark leads to an integrable singularity because the fermion propagator is less singular than that of the gluon. Colour conservation implies that the current $\boldsymbol{J}_\mu(s)$ is conserved,

$$p^\mu_s \boldsymbol{J}_\mu(s)|\mathcal{M}_m\rangle = \sum_{k=1}^m \boldsymbol{T}^s_k|\mathcal{M}_m\rangle = \quad \quad = 0.$$

Then the soft limit of $\left\langle \mathcal{M}^{(0)}_m\middle|\,\mathcal{M}^{(0)}_m\right\rangle$ is as follows:

$$\hat{S}_s\,|\mathcal{M}_{m+1}(p_s, \ldots)|^2 = 4\pi\alpha_s\mu^{2\epsilon}$$

$$\times \sum_{i=1}^m \sum_{k=1}^m \underbrace{\epsilon_\mu(s)\epsilon^*_\nu(s)\frac{p^\mu_i p^\nu_k}{p_i \cdot p_s\, p_k \cdot p_s}}_{d_{\mu\nu}(p_s, n)}\langle \mathcal{M}_m|\boldsymbol{T}_i \cdot \boldsymbol{T}_k|\mathcal{M}_m\rangle$$

$$= -8\pi\alpha_s\mu^{2\epsilon}\sum_{i,k=1}^m \frac{1}{2}S_{ik}(s)\left|\mathcal{M}^{(0)}_{m(i,k)}\right|^2 + \text{gauge terms}$$

$$\propto \quad \quad + \ldots\ldots \tag{19.8.65}$$

The gauge terms give zero contribution on on-shell matrix elements due to gauge invariance.

19.9 Factorization in the collinear limit

The collinear limit of momenta p_i and p_r is defined by the Sudakov parametrization:

$$p_i^\mu = z_i p^\mu + k_{iT}^\mu - \frac{k_{iT}^2}{z_i}\frac{n^\mu}{2\,p\cdot n}, \qquad p_r^\mu = z_r p^\mu + k_{rT}^\mu - \frac{k_{rT}^2}{z_r}\frac{n^\mu}{2\,p\cdot n}$$

where $k_{iT}^\mu + k_{rT}^\mu = 0$ and $z_i + z_r = 1$. The momentum p^μ is the collinear direction and

$$p^2 = p_i^2 = p_r^2 = n^2 = 0, \qquad k_{iT}\cdot p = k_{rT}\cdot n = 0,$$

In the collinear limit k_{iT}^μ, $k_{rT}^\mu \to 0$ and $s_{ir} = -\frac{k_{rT}^2}{z_i z_r}$. We now state the following theorem

> *In a physical gauge, the leading collinear singularities are due to the collinear splitting of an external parton.*

This means that we need to compute in the collinear limit. There are three cases:

f_{ir}	$\to$	$f_i + f_r$
q	$\to$	$q + g$
g	$\to$	$q + \bar{q}$
g	$\to$	$g + g$

We compute explicitly the first case and leave the second and third ones as exercise. For the case of a quark splitting into a quark and a gluon we have

$$= C_F g_s^2 \mu^{2\epsilon} \frac{\not{p}_i + \not{p}_r}{s_{ir}} \gamma^\mu \not{p}_i \gamma^\nu d_{\mu\nu}(p_r, n) \frac{\not{p}_i + \not{p}_r}{s_{ir}}$$

$$= C_F\, 4\pi\alpha_s \mu^{2\epsilon} \frac{\not{p}_i + \not{p}_r}{s_{ir}} \left(-\gamma^\mu \not{p}_i \gamma_\mu + \frac{\not{p}_r \not{p}_i \not{n} + \not{n} \not{p}_i \not{p}_r}{p_r \cdot n}\right) \frac{\not{p}_i + \not{p}_r}{s_{ir}}.$$

Using
$$(19.9.66)$$

$$-\gamma^\mu \not{p}_i \gamma_\mu = (d-2)\not{p}_i, \quad \not{p}_i \not{p}_i = p_i^2\, \mathbb{1}, \quad \not{p}_i \not{p}_r \not{p}_i = s_{ir} \not{p}_i - p_i^2 \not{p}_r = s_{ir} \not{p}_i,$$

we find

$$\left(\not{p}_i + \not{p}_r\right)\left(-\gamma^\mu \not{p}_i \gamma_\mu\right)\left(\not{p}_i + \not{p}_r\right) = (d-2)\, s_{ir}\not{p}_r,$$

$$\not{p}_r \not{p}_i \not{n} = -\not{p}_i \not{p}_r \not{n} + s_{ir}\not{n} = \not{p}_i \not{n}\not{p}_r - 2\not{p}_i p_r \cdot n + s_{ir}\not{n} =$$
$$= -\not{n}\not{p}_i\not{p}_r + 2 p_i\cdot n\not{p}_r - 2\not{p}_i p_r\cdot n + s_{ir}\not{n}.$$

Then

$$\left(\not{p}_i + \not{p}_r\right)\left(\not{p}_r\not{p}_i\not{n} + \not{n}\not{p}_i\not{p}_r\right)\left(\not{p}_i + \not{p}_r\right) =$$

$$= 2\left(\not{p}_i + \not{p}_r\right)\left(p_i\cdot n\,\not{p}_r - p_r\cdot n\,\not{p}_i + p_i\cdot p_r\,\not{n}\right)\left(\not{p}_i + \not{p}_r\right)$$

$$= 2\Big[p_i\cdot n\,s_{ir}\not{p}_i - p_r\cdot n\,s_{ir}\not{p}_r$$

$$+ p_i\cdot p_r\left(2\,(p_i + p_r)\cdot n\left(\not{p}_i + \not{p}_r\right) - (p_i + p_r)^2\,\not{n}\right)\Big]$$

$$= s_{ir}\left[4p_i\cdot n\,\not{p}_i + 2p_i\cdot n\,\not{p}_r + 2p_r\cdot n\,\not{p}_i - s_{ir}\not{n}\right].$$

Substituting these results and then the Sudakov parametrization of the momenta into Eq. (19.9.66) we obtain

$$\overset{p_i\|p_r}{\simeq} \frac{1}{s_{ir}}\,C_F\,4\pi\alpha_s\mu^{2\epsilon}\left[2\,(1-\epsilon)\,z_r + 4\frac{z_i^2}{z_r} + 2z_i + 2z_i + O\,(k_T)\right]\not{p}$$

$$= \frac{1}{s_{ir}}\,C_F\,8\pi\alpha_s\mu^{2\epsilon}\left[2\underbrace{\frac{z_i}{z_r} + (1-\epsilon)\,z_r}_{\frac{1+z_i^2}{1-z_i}-\epsilon(1-z_i)}\right]\not{p}$$

Similarly to the soft case we can define an operator $\hat{C}_{ir}$ which takes the collinear limit and keeps the leading singular ($O(1/k_T^2)$) terms:

$$\hat{C}_{ir}\left|\mathcal{M}_{m+1}^{(0)}\right|^2 = 8\pi\alpha_s\mu^{2\epsilon}\frac{1}{s_{ir}}\left\langle\mathcal{M}_m^{(0)}\,(p,\ldots)\right|\hat{P}_{qg}^{(0)}\,(z_i, z_r, k_T; \epsilon)\left|\mathcal{M}_m^{(0)}\,(p,\ldots)\right\rangle.$$

$$(19.9.67)$$

The kernel $\hat{P}_{qg}$, called Altarelli-Parisi splitting kernel for the process $q \rightarrow q + g$. It is diagonal in the spin-state of the parent (splitting) parton:

$$\langle s|\,\hat{P}_{qg}\,|s'\rangle = C_F\left[2\frac{z_i}{z_r} + (1-\epsilon)\,z_r\right]\delta_{ss'}. \qquad (19.9.68)$$

Similar calculations give the splitting kernels for the gluon splitting processes, which display azimuthal correlations of the parent parton

$$\langle\mu|\,\hat{P}_{q\bar{q}}^{(0)}\,(z_i, z_r, k_T; \epsilon)\,|\nu\rangle = T_R\left[-g^{\mu\nu} + 4z_iz_r\frac{k_T^\mu k_T^\nu}{k_T^2}\right], \quad (19.9.69)$$

$$\langle\mu|\,\hat{P}_{gg}^{(0)}\,(z_i, z_r, k_T; \epsilon)\,|\nu\rangle =$$

$$= 2C_A\left[-g^{\mu\nu}\left(\frac{z_i}{z_r} + \frac{z_r}{z_i}\right) - 2\,(1-\epsilon)\,z_iz_r\frac{k_T^\mu k_T^\nu}{k_T^2}\right]. \quad (19.9.70)$$

The soft and collinear limits overlap when the soft gluon is also collinear to its parent parton:

$$
\hat{C}_{jr}\,\hat{S}_r\,\left|\mathcal{M}^{(0)}_{m+1}\,(p_r,\ldots)\right|^2 = -8\pi\alpha_s\mu^{2\epsilon}\sum_{k\neq j}\frac{2z_j}{s_{jr}\,z_r}\left|\mathcal{M}^{(0)}_{m(j,k)}\,(\ldots)\right|^2
$$

$$
= 8\pi\alpha_s\mu^{2\epsilon}\,T_j^2\,\frac{2}{s_{jr}}\frac{z_j}{z_r}\left|\mathcal{M}^{(0)}_m\right|^2. \qquad (19.9.71)
$$

The notation for the splitting kernels in these lectures is different from the usual notation in the literature. Usually, $\hat{P}^{(0)}_{ij}\,(z,k_T;\epsilon)$ denotes the splitting kernel for the process $f_i(p) \rightarrow f_j(zp) + f_k((1-z)p)$, which does not lead to confusion for $1 \rightarrow 2$ splittings because the momentum fraction of parton j determines that of parton k as their sum has to be one, $z_j + z_k = 1$. For splittings involving more partons, it is more appropriate to introduce as many momentum fractions z_i as the number of offspring partons, with the constraint $\sum_i z_i = 1$, and use the flavour indices to denote the offspring partons in the order of the momentum fractions in the argument. For $1 \rightarrow 2$ splittings this means the use of $\hat{P}^{(0)}_{ir}\,(z_i,z_r,k_T;\epsilon)$ for the splitting process $f_k(p) \rightarrow f_i(z_ip) + f_r(z_rp)$. The flavour of the parent parton f_k is determined uniquely by the flavour summation rules, $q + g = q$, $q + \bar{q} = g + g = g$. These flavour summation rules are unique also for $1 \rightarrow 3$ splittings.

Exercise 19.10
Compute the Altarelli-Parisi-splitting kernel $\hat{P}_{qg}(z)$ for the process $q \rightarrow qg$ from the collinear limit of the matrix element for the process $e^+e^- \rightarrow q\bar{q}g$:

$$
\left|M_3(e^+e^- \rightarrow q\bar{q}g)\right|^2 = 8\pi\alpha_s\mu^{2\epsilon}\left|M_2(e^+e^- \rightarrow q\bar{q})\right|^2
$$

$$
\times\frac{1}{s}\left((1-\epsilon)\left(\frac{y_{23}}{y_{13}} + \frac{y_{13}}{y_{23}}\right) + 2\left(\frac{y_{12}}{y_{13}y_{23}} - \epsilon\right)\right).
$$

Exercise 19.11
The Altarelli-Parisi splitting kernel $\hat{P}_{q\bar{q}}(z)$ for the process $g \rightarrow q_i\bar{q}_r$ is

defined by the following collinear limit:

$$\langle \mathcal{M}^{(0)}_{n+1}(p_i, p_r, \ldots) | \mathcal{M}^{(0)}_{n+1}(p_i, p_r, \ldots)\rangle \overset{p_i \| p_r}{\simeq}$$

$$\frac{1}{s_{ir}} 8\pi\alpha_s\mu^{2\epsilon} \langle \mathcal{M}^{(0)}_n(p, \ldots) | \hat{P}^{(0)}_{q\bar{q}}(z, k_{\mathrm{T}}) | \mathcal{M}^{(0)}_n(p, \ldots)\rangle$$

$$= \frac{1}{s_{ir}} 8\pi\alpha_s\mu^{2\epsilon} \langle \mathcal{M}^{(0)}_n(p, \ldots) | \mu\rangle \langle \mu | \hat{P}^{(0)}_{q\bar{q}}(z, k_{\mathrm{T}}) | \nu\rangle \langle \nu | \mathcal{M}^{(0)}_n(p, \ldots)\rangle$$

Compute $\langle \mu | \hat{P}^{(0)}_{q\bar{q}}(z, k_{\mathrm{T}}) | \nu\rangle$ *in leading order in* k_{T}.

Exercise 19.12
Derive the flavour summation rules for $1 \to 3$ splittings.

Exercise 19.13
Compute the soft limit of Eq. (19.9.67) *and the collinear limit of Eq.* (19.8.65).

19.9.1 Regularization of real corrections by subtraction

The cross section at NLO accuracy is a sum of two terms, the LO prediction and the corrections at one order higher in the strong coupling,

$$\sigma_{\mathrm{NLO}} = \sigma^{\mathrm{LO}} + \sigma^{\mathrm{NLO}},$$

where σ^{LO} is the integral of the fully differential Born cross section over the available phase space defined by the jet function, while σ^{NLO} is the sum of the real and virtual corrections:

$$\sigma^{\mathrm{LO}} = \int_m d\sigma^B \, J_m(\{p\}_m),$$

$$\sigma^{\mathrm{NLO}} = \int_{m+1} d\sigma^R \, J_m(\{p\}_{m+1}) + \int_m d\sigma^V \, J_m(\{p\}_m).$$

Both contributions to σ^{NLO} are divergent in four dimensions, but their sum is finite for infrared-safe jet functions.

The factorization of the squared matrix elements in the soft and collinear limits allows for a method independent of the processes and observables to regularize the real corrections in their singular limits. The essence of

the method is to devise an approximate cross section $d\sigma^A$ that matches the singular behaviour of the real cross section $d\sigma^R$ in all kinematically degenerate regions of the phase space when one parton becomes soft or two partons become collinear. Then we subtract this approximate cross section from the real one and the difference can be integrated in four dimensions, similarly to

$$\int_0^1 dx \left(\frac{f(x)}{x^{1-\epsilon}} - \frac{f(0)}{x^{1-\epsilon}} \right) < \infty \qquad (19.9.72)$$

for arbitrary ϵ (in particular when $\epsilon = 0$) provided the limit $\lim_{x\to 0} f(x) < \infty$. Next, we integrate $d\sigma^A$ over the phase space of the unresolved parton and we add it to $d\sigma^V$. In the example of Eq. (19.9.72) this step corresponds to computing the integral

$$\int_0^1 dx \frac{f(0)}{x^{1-\epsilon}} = f(0) \frac{1}{\epsilon} \; .$$

The integrated subtraction term cancels the explicit poles in the virtual correction and the sum can also be integrated in four dimensions.

The key for this procedure is a proper mapping of the $(m+1)$-parton phase space to the m-parton one which respects the limits, thus the approximate cross section is defined with the m-parton jet function. After such a mapping the phase space of the $(m + 1)$ partons in the final state can be written in the form

$$\phi_{m+1}((\{p\}_{m+1})) \to \phi_m(\{\tilde{p}\}_m)\phi_1 \qquad (19.9.73)$$

where ϕ_1 is related to the phase space measure of the unresolved parton. As a result we integrate $d\sigma^A$ with the jet function J_m of m final state momenta. This way we can rewrite the NLO correction as a sum of two finite terms,

$$\sigma^{\mathrm{NLO}} = \int_{m+1} \left[d\sigma^R \, J_m(\{p\}_{m+1}) - d\sigma^A \, J_m(\{\tilde{p}\}_m) \right]_{\epsilon=0}$$
$$+ \int_m \left[d\sigma^V + \int_1 d\sigma^A \right]_{\epsilon=0} J_m(\{p\}_m) \, . \qquad (19.9.74)$$

The definition of the approximate cross section is not unique and the best choice may depend on further requirements, which we do not discuss here. We also skip the precise definition of the momenta $\tilde{p}^\mu$ which are obtained by mapping the $(m + 1)$-particle phase space onto an m-particle phase space times a one-particle phase space. A widely used general subtraction scheme that can be used also for processes including massive partons with smooth massless limits is presented in Ref. [Catani et al., 2002] where these definitions are given explicitly. This method uses the factorization of the squared

matrix element in the soft and collinear limits. The challenge posed by the overlapping singularity in the soft-collinear limit is solved by a smooth interpolation between these singular regions.

The factorization properties of Eqs. (19.8.65) and (19.9.67) play other very important roles in pQCD. The numerical implementation of the squared matrix element is a process prone to errors. Testing the factorization in the kinematically degenerate phase space regions serves a good check of the implementation. The computation is even more difficult for the virtual corrections. Similar factorization holds for those, which more recently has been utilized to find the virtual corrections ("collinear bootstrap"). The factorized form of the squared matrix element can be used in resumming logarithmically enhanced terms at all orders, or in devising a parton shower algorithm for modelling events (see Sect. 21.3). The splitting kernels that appear in the collinear factorization have a role in the evolution equations of the parton distribution functions (see Sect. 20.7).

The state of the art in making precision predictions assaults on the one hand the full automation of computations at NLO, and on the other the realm of next-to-next-to-leading order (NNLO) corrections. The automation of computing jet cross sections at NLO accuracy has been accomplished and several programs are available with the aim to facilitate automated solutions for computing jet cross sections at NLO accuracy:

- aMC@NLO (http://amcatnlo.web.cern.ch),
- BlackHat/Sherpa (https://blackhat.hepforge.org),
- FeynArts/FormCalc/LoopTools (http://www.feynarts.de),
- GoSam (https://gosam.hepforge.org),
- HELAC-NLO (http://helac-phegas.web.cern.ch),
- MadGolem
  (http://www.thphys.uni-heidelberg.de/~lopez/madgolem-corner.html).

There is also the `MadGraph5_aMC@NLO` computer program that provides full automation of computing QCD jet cross sections at NLO accuracy (https://launchpad.net/mg5amcnlo).

In the NNLO case the infrared singularity structure is much more involved than in the case of NLO computations due to complicated overlapping single and double unresolved configurations. Several subtraction methods have been proposed for the regularization of the infrared divergences. There is intense research to find a general one that can be automated. To provide an impression about the importance of NNLO corrections, we present QCD predictions at various accuracies (LO, NLO and NNLO) for the thrust

distribution computed with $\alpha_s = 0.118$ and at a centre-of-mass energy of $\sqrt{s} = 91.2$ GeV in Fig. 17.60. For all calculations the uncertainty band reflects the uncertainty due to the variation of the renormalization scale around the default scale $\mu = \sqrt{s}$ by factors of two in both directions. We find that even the prediction at NNLO accuracy differs significantly from the (hadron-level) data measured by the ALEPH collaboration at LEP. In Figure 17.60 (right) we show the effect of NNNLL resummation matched to the NNLO prediction, which gives nice agreement between data and theory except for small values of $\tau = 1 - T$. The difference is most likely due to hadronization corrections that we do not discuss in this book.

Chapter 20

Deeply inelastic lepton-proton scattering

MOTTO:

If you want to learn about nature, to appreciate nature, it is necessary to understand the language that she speaks in.

(Richard P. Feynman)

20.1 Kinematics

Perturbative QCD stems from the parton model that was developed to understand deeply inelastic lepton-hadron scattering (DIS). The purpose of those experiments was to study the structure of the proton by measuring the kinematics of the scattered lepton. In Fig. 17.61 (left) we show a real event in the H1 experiment at the HERA collider. The value of Q^2, which is the modulus squared of the momentum transfer between the lepton and the proton is $21475\,\text{GeV}^2 >> 1\,\text{GeV}^2$, signifying that the scattering is well in the deeply inelastic region. The parton model interpretation of the event is shown in Fig. 17.61 (right): the lepton is scattered by an angle θ due to the exchange of a virtual photon with one of the constituents of the proton

(a parton).

The measurement is inclusive from the point of view of hadrons (X means any number of hadrons that are not observed separately), thus the process can be described in pQCD.

The DIS kinematics is described by the following variables (using the notation of Fig. 17.61 (right)):

$$\text{centre-of-mass energy}^2 = s = (P + k)^2 \,,$$
$$\text{momentum transfer} = q^\mu = k^\mu - k'^\mu \,,$$
$$|\text{momentum transfer}|^2 = Q^2 = -q^2 = 2MExy \,,$$
$$\text{scaling variable} = x = Q^2/(2P \cdot q) \,,$$
$$\text{energy loss} = \nu = (P \cdot q)/M = E - E' \,,$$
$$\text{relative energy loss} = y = (P \cdot q)/(P \cdot k) = 1 - E'/E \,,$$
$$\text{recoil mass}^2 = W^2 = (P + q)^2 = M^2 + \frac{1 - x}{x} Q^2 \,,$$

As $q^2 < 0$, it is customary to introduce Q^2, the magnitude of q^2. E and E' are the energies of the incoming and outgoing lepton.

20.2 Parametrization of the target structure

The cross section for $e(k) + p(P) \rightarrow e(k') + X$ reads

$$d\sigma = \sum_X \frac{1}{4ME} \int d\phi \, \frac{1}{4} \sum_{\text{spin}} |\mathcal{M}|^2 \,. \qquad (20.2.1)$$

The summation runs over all possible (unobserved) hadronic final states. We factorize the phase space and the squared matrix element into two parts, one for the lepton (denoted by L) and one for the hadrons (denoted H):

$$d\phi = d\phi_L \, d\phi_H \,, \qquad d\phi_L = \frac{d^3 k'}{(2\pi)^3 2E'} \,, \qquad \frac{1}{4} \sum_{\text{spin}} |\mathcal{M}|^2 = \frac{e^4}{Q^4} L^{\mu\nu} H_{\mu\nu} \,.$$

Then the hadron part of the cross section is the dimensionless tensor of Lorentz indices $W_{\mu\nu} = \frac{1}{8\pi} \sum_X \int d\phi_H H_{\mu\nu}$ (the factor of $\frac{1}{8\pi}$ is included here by convention). As it depends on two momenta P^μ and q^μ, the most general

gauge invariant expression for the Lorentz tensor can be written as

$$W_{\mu\nu}(P, q) = \left(-g_{\mu\nu} + \frac{q_\mu q_\nu}{q^2}\right) W_1(x, Q^2)$$
$$+ \left(P_\mu - q_\mu \frac{P \cdot q}{q^2}\right)\left(P_\nu - q_\nu \frac{P \cdot q}{q^2}\right) \frac{W_2(x, Q^2)}{P \cdot q}$$

where the structure functions $W_i(x, Q^2)$ are dimensionless functions of the scaling variable and the momentum transfer.

For the lepton part we express the kinematic relations $E' = (1 - y)E$, $\cos\theta = 1 - \frac{xyM}{(1-y)E}$ to change variables to scaling variable and relative energy loss:

$$\frac{d^3 k'}{(2\pi)^3 2E'} = \frac{d\varphi}{2\pi} \frac{E'}{8\pi^2} dE' \, d\cos\theta = \frac{d\varphi}{2\pi} \frac{yME}{8\pi^2} dy \, dx$$

and compute the trace $L^{\mu\nu} = \frac{1}{2}Tr[\not{k}\gamma^\mu \not{k}'\gamma^\nu] = k^\mu k'^\nu + k^\nu k'^\mu - g^{\mu\nu} k \cdot k'$. Then the differential cross section as a function of x and y is obtained from Eq. (20.2.1) as

$$\frac{d^2\sigma}{dx \, dy} = \frac{4\pi\alpha^2}{y Q^2} \left[y^2 W_1(x, Q^2) + \left(\frac{1-y}{x} - xy\frac{M^2}{Q^2}\right) W_2(x, Q^2) \right],$$

which we rewrite in the scaling limit, defined by $Q^2 \to \infty$ with x fixed, as

$$\frac{d^2\sigma}{dx \, dy} = \frac{4\pi\alpha^2}{y Q^2} \left[(1 + (1 - y)^2) F_1 + \frac{1-y}{x}(F_2 - 2xF_1) \right]. \qquad (20.2.2)$$

The dimensionless functions F_1 and F_2 were first measured by the SLAC-MIT experiment [Miller et al., 1972]. The result of that measurement supplemented by some later ones is shown in Fig. 20.1. The interesting feature is that in the scaling limit F_2 becomes independent of Q^2, $F_2(x, Q^2) \to F_2(x)$ (in fact, the independence starts at quite low values of Q^2).

20.3   DIS in the parton model

Let us now describe the same scattering process by assuming the proton is a bunch of free flying quarks and the lepton exchanges a hard virtual photon with one of those quarks as shown in Fig. 17.61 (right). The struck quark carries a momentum p^μ, which is a fraction of the proton momentum,
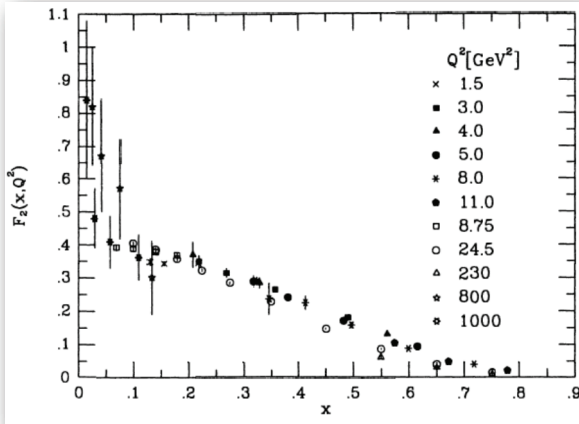
Figure 20.1: Measured value of the F_2 structure function at several different values of Q^2

$p^\mu = \xi P^\mu$, so we consider the process $\ell(k) + q(p) \to \ell(k') + q(p')$. The corresponding cross section is

$$d\hat{\sigma} = \frac{1}{2\hat{s}} \int d\phi_2 \, \frac{1}{4} \sum_{\text{spin}} |\mathcal{M}|^2,$$

with $\hat{s} = (p + k)^2$. The hat refers to partonic quantities (cross section, c.m. energy squared) here and below. The squared matrix element is proportional to the product of the lepton tensor $L^{\mu\nu}$ and a similar quark tensor $Q_{\mu\nu} = \frac{1}{2}Tr[\not{p}\gamma^\mu \not{p}'\gamma^\nu] = p^\mu p'^\nu + p'^\mu p'^\mu - g^{\mu\nu} p \cdot p'$, i.e. $L^{\mu\nu}Q_{\mu\nu} = 2(\hat{s}^2 + \hat{u}^2)$ where $\hat{u} = (p - k')^2 = -2p \cdot k'$. As $y = P \cdot q / P \cdot k = 2p \cdot q / 2p \cdot k = (\hat{s} + \hat{u})/\hat{s}$, momentum conservation $p'_\mu = p_\mu + q_\mu$ implies for the on-shell condition of the scattered quark $0 = p'^2 = (p + q)^2 = 2p \cdot q + q^2 = \hat{s} + \hat{u} - Q^2$. We have $y = Q^2/\hat{s}$ and $\hat{u} = (y - 1)\hat{s}$ so

$$\frac{1}{4} \sum_{\text{spin}} |\mathcal{M}|^2 = \frac{e_q^2 e^4}{Q^4} L^{\mu\nu}Q_{\mu\nu} = 2e_q^2 e^4 \frac{\hat{s}^2}{Q^4}\left(1 + (1 - y)^2\right).$$

Also $Q^2 = 2p \cdot q = 2\xi P \cdot q$, so $p'^2 = Q^2(\xi/x - 1)$. Then the two-particle phase space is

$$d\phi_2 = \frac{d^3 k'}{(2\pi)^3 2E_{k'}} \frac{d^4 p'}{(2\pi)^4} 2\pi\delta_+(p'^2) (2\pi)^4 \delta^4(k + p - k' - p')$$

$$= \frac{d\varphi}{2\pi} \frac{E'}{4\pi} dE' \, d\cos\theta \, \frac{x}{Q^2} \delta(\xi - x),$$

(20.3.3)

or using $E' = \frac{\sqrt{\hat{s}}}{2}(1 - y)$ and $\cos\theta = 1 - \frac{2yx}{\xi(1 - y)}$, we obtain $d\phi_2 = \frac{d\varphi}{(4\pi)^2} \frac{y\hat{s}}{Q^2} \, dy \, dx \, \delta(\xi - x)$. The differential cross section in x and y

$$\frac{d^2\hat{\sigma}}{dx \, dy} = \frac{4\pi\alpha^2}{Q^2} [1 + (1 - y)^2] \frac{1}{2} e_q^2 \delta(\xi - x).$$

(20.3.4)

Comparing Eqs. (20.2.2) and (20.3.4), we find the parton model predictions

$$F_1(x) \propto e_q^2 \delta(\xi - x), \qquad F_2 - 2xF_1 = 0, \quad \text{called Callan-Gross relation.}$$

(20.3.5)

Thus F_2 probes the constituent of the proton with momentum fraction $\xi = x$. However, this prediction for F_2 cannot be correct because $F_2(x)$ is not a δ function as seen from Fig. 20.1, which makes us formulate the naïve parton model in the following way:

> the virtual photon scatters incoherently off the constituents (partons) of the proton;
> the probability that a quark q carries a momentum fraction of the proton between ξ and $\xi + \delta\xi$ is $f_q(\xi)d\xi$.

Exercise 20.1

Compute the contribution to the DIS cross section in Eq. (20.2.2) with the exchange of a transversely polarized photon. Hint: Use Eq. (18.2.3) for the numerator in the propagator of the transversely polarized photon and the Callan-Gross relation in Eq. (20.3.5). Can you identify the result with any of the terms in Eq. (20.2.2)? What is the source of the remainder?

20.4   Measuring the proton structure

With the assumptions of the naïve parton model the Callan-Gross relation predicts

$$F_2(x) = 2xF_1(x) = \sum_q \int_0^1 d\xi \, f_q(\xi) \, x \, e_q^2 \, \delta(x - \xi) = x \sum_q e_q^2 \, f_q(x).$$

(20.4.6)

For example, taking into account four flavours and simplifying the notation by using $f_q(x) \equiv q(x)$, we obtain a prediction for the structure function measured in scattering of charged-lepton off proton (neutral current interaction):

$$F_2^{\text{em}}(x) = x\left[\frac{4}{9}\left(u(x) + \bar{u}(x) + c(x) + \bar{c}(x)\right) + \frac{1}{9}\left(d(x) + \bar{d}(x) + s(x) + \bar{s}(x)\right)\right].$$

Similarly, in charged current interactions the prediction is

$$F_2^{\bar{\nu}}(x) = 2x\left[u(x) + \bar{d}(x) + c(x) + \bar{s}(x)\right] \text{ (with } W^-\text{)},$$

$$F_2^{\nu}(x) = 2x\left[d(x) + \bar{u}(x) + s(x) + \bar{c}(x)\right] \text{ (with } W^+\text{)}.$$

Further information can be obtained if we use different targets. Assuming two flavours and isospin symmetry, the proton structure (with uud valence quarks) is

$$F_2^{\text{p}}(x) = x\left[\frac{4}{9}\left(u_p(x) + \bar{u}_p(x)\right) + \frac{1}{9}\left(d_p(x) + \bar{d}_p(x)\right)\right],$$

(20.4.7)

and that of the neutron (with udd valence quarks) is

$$F_2^{\text{n}}(x) = x\left[\frac{4}{9}\left(u_n(x) + \bar{u}_n(x)\right) + \frac{1}{9}\left(d_n(x) + \bar{d}_n(x)\right)\right]$$

$$= x\left[\frac{1}{9}\left(u_p(x) + \bar{u}_p(x)\right) + \frac{4}{9}\left(d_p(x) + \bar{d}_p(x)\right)\right].$$

(20.4.8)

The measurements are supplemented by sum rules. For instance, as the proton consists of uud valence quarks, we have

$$\int_0^1 dx \, \left(u_p(x) - \bar{u}_p(x)\right) = 2, \quad \int_0^1 dx \, \left(d_p(x) - \bar{d}_p(x)\right) = 1,$$

$$\int_0^1 dx \, \left(s_p(x) - \bar{s}_p(x)\right) = 0.$$

The combination of the measurements and sum rules gives separate information on the quark distributions in the proton $f_q(x)$. The result of such measurements performed by the NMC collaboration [Arneodo et al., 1997] is shown in Fig. 17.62 (left) together with a fit to the data by the CTEQ collaboration [Pumplin et al., 2002]. The parton distributions deduced from the fit are shown in Fig. 17.62 (right).

We can infer the proton momentum from the measurements. The surprising result is that *quarks give only about half of the momentum of the proton*, $\sum_q \int_0^1 dx\, x f_q(x) \simeq 0.5$. By now we know that the other half is carried by gluons, but clearly the naïve parton model is not sufficient to interpret the gluon distribution in the proton. With our experience in perturbative QCD we try to compute radiative corrections to the quark process to see if that helps to find the role of the gluon distribution.

Exercise 20.2
It is not feasible to use a neutron target experimentally. Instead deuteron is used which is the bound state of a proton and a neutron. The corresponding structure function is $F_2^d(x) = \frac{1}{2}(F_2^p(x) + F_2^n(x))$, with F_2^p and F_2^n given in Eqs. (20.4.7) and (20.4.8), respectively. Which combination of the structure function on proton and deuteron targets gives the u- and d-quark distributions?

20.5   Improved parton model: perturbative QCD

Using the relations $dy = dQ^2/\hat{s}$ and $\delta(\xi - x) = \frac{1}{\xi}\delta\left(1 - \frac{x}{\xi}\right)$, we rewrite the differential cross section (20.3.4) in a more usual notation,
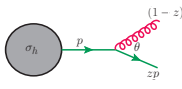
$$\frac{d^2\sigma}{dx\, dQ^2} = \int_0^1 \frac{d\xi}{\xi} \sum_i f_i(\xi) \frac{d^2\hat{\sigma}}{dx\, dQ^2}\left(\frac{x}{\xi}, Q^2\right), \qquad (20.5.9)$$

which gives the cross section as a convolution of a long-distance component (the parton distribution function, PDF) and a short-distance component (the hard scattering cross section). This form of the cross section is the main content of the *factorization theorem*, which we derived heuristically, but

there exists a rigorous though not completely process independent proof, based on QFT.

The factorization formula (20.5.9) raises some questions. Knowing that the quarks do not give the total momentum of the proton, it is natural to include the contribution of gluons in Eq. (20.5.9). However, we do not yet know the corresponding hard scattering cross section. We also do not know how we can apply perturbation theory. Furthermore, the scaling was exact in the parton model. Is it so in QCD? There is a common answer to these questions: DIS in perturbative QCD.

To develop perturbative QCD for DIS, let us revisit the infrared singularities once more. Let us denote the hard scattering cross section for some final state by σ_h. Then the cross section in the collinear approximation for the same final state with an extra gluon of relative transverse momentum $k_T = E\theta$, carrying momentum fraction $(1-z)$ is
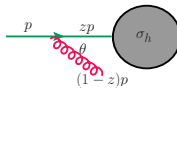
$$\propto \sigma_{h+g} \simeq \sigma_h 2 C_F \frac{\alpha_s}{\pi} \frac{dE}{E} \frac{d\theta}{\theta} = \sigma_h C_F \frac{\alpha_s}{\pi} \frac{dz}{1-z} \frac{dk_T^2}{k_T^2} .$$

Integrating over z up to one and over k_T we find soft and collinear divergences. In studying perturbative QCD we found that these infrared singularities in the final state cancel against infrared divergences in the virtual correction for infrared safe quantities:
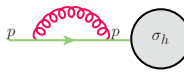
$$\propto \sigma_{h+V} \simeq -\sigma_h C_F \frac{\alpha_s}{\pi} \frac{dz}{1-z} \frac{dk_T^2}{k_T^2} .$$

If there is a coloured parton in the initial state, then the splitting may occur before the hard scattering and the momentum of the parton that enters the hard process is reduced to zp^μ, so

$$\propto \sigma_{h+g}(p) \simeq \sigma_h(zp) 2 C_F \frac{\alpha_s}{\pi} \frac{dE}{E} \frac{d\theta}{\theta}$$

$$= \sigma_h(zp) C_F \frac{\alpha_s}{\pi} \frac{dz}{1-z} \frac{dk_T^2}{k_T^2} .$$

Integrating over z up to one and over k_T we again find soft and collinear divergences. The corresponding ϵ poles multiply $\sigma_h(zp)$, while in the virtual correction the poles multiply $\sigma_h(p)$, irrespective whether the infrared divergence is in the initial or final state:

$$\propto \sigma_{h+V} \simeq -\sigma_h(p) C_F \frac{\alpha_s}{\pi} \frac{dz}{1-z} \frac{dk_T^2}{k_T^2} .$$

The sum of the real and virtual corrections then contains an uncancelled singularity,

$$\sigma_{h+g} + \sigma_{h+V} \simeq C_F \frac{\alpha_s}{\pi} \underbrace{\int_{m_g^2}^{Q^2} \frac{dk_T^2}{k_T^2}}_{\text{infinite if } m_g = 0} \underbrace{\int_0^1 \frac{dz}{1-z} [\sigma_h(zp) - \sigma_h(p)]}_{\text{finite}},$$

where we used a finite gluon mass to regulate the collinear divergence (instead of dimensional regularization) to make manifest that the collinear singularity remains, while the soft one (at $z \to 1$) vanishes in the sum.

This uncancelled collinear singularity in the initial state is a general feature of perturbative QCD computations with incoming coloured partons and its form is universal, so we can find its precise form studying the structure function at NLO accuracy. We know that in the parton model (QCD at LO) the prediction for hard scattering cross section $\hat{F}_2$ is finite:

$$\hat{F}_{2,q}(x) = \frac{d^2\hat{\sigma}}{dx\, dQ^2}\bigg|_{F_2} = e_q^2 x\, \delta(1-x), \quad \hat{F}_{2,g}(x) = \frac{d^2\hat{\sigma}}{dx\, dQ^2}\bigg|_{F_2} = \sum_q e_q^2\, x \cdot 0$$

i.e. it is zero in the gluon channel because the virtual photon does not interact with the gluon directly. At one order higher in α_s we find (the diagrams below show the contributions to each term: one diagram at LO, one loop diagram and two real radiation diagrams at NLO)

$$\hat{F}_{2,q}(x) = \frac{d^2\hat{\sigma}}{dx\, dQ^2}\bigg|_{F_2} = e_q^2 x\left[\delta(1-x) + \frac{\alpha_s}{4\pi}\left(P^{qq}(x)\ln\frac{Q^2}{m_g^2} + C_2^q(x)\right)\right],$$
$$(20.5.10)$$
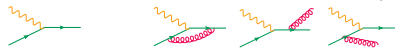
and (only one real radiation diagram with gluon splitting in the initial state contributes)

$$\hat{F}_{2,g}(x) = \frac{d^2\hat{\sigma}}{dx\, dQ^2}\bigg|_{F_2} = \sum_q e_q^2 x\left[0 + \frac{\alpha_s}{4\pi}\left(P^{gq}(x)\ln\frac{Q^2}{m_q^2} + C_2^g(x)\right)\right],$$
$$(20.5.11)$$

where $P^{ij}(x)$ is the Altarelli-Parisi splitting function for $i \to j + k$ (regularized at $x = 1$), while $C_2(x)$ is the remaining finite term, called coefficient

function. The space-like splitting function $P^{ji}(x)$ is obtained from the time-like splitting kernel $\hat{P}_{jk}$ in four dimensions through the following steps: (i) crossing the kernel for time-like splitting into space-like splitting:

$$\hat{P}^{(0),\bar{i}k}(x, k_\mathrm{T}) = -(-1)^{2s(i)+2s(j)} \, x \, \hat{P}^{(0)}_{jk}\left(\frac{1}{x}, k_\mathrm{T}; \epsilon = 0\right) \qquad (20.5.12)$$

where $\bar{i}$ is the antiparticle of parton i, $s(i)$ denotes the spin of parton i; (ii) averaging over the spin states of parton i to obtain $\langle \hat{P}^{(0),\bar{i}k}(x, k_\mathrm{T})\rangle$; (iii) relabelling superscripts $\langle \hat{P}^{(0),\bar{i}k}(x, k_\mathrm{T})\rangle \rightarrow P^{j\bar{i}}(x)$ and (iv) adding the contribution from the one-loop diagram (see exercise). The flavours satisfy the flavour summation rule $f_i = f_j + f_k$. We see that at NLO the prediction for $\hat{F}_2$ does not contain ultraviolet divergences. The final state infrared divergences also cancel, but an un-cancelled singularity remains in the initial state, regularized with a small mass (m_g or m_q) here.

The hard scattering function is not measurable, only the structure function is physical:

$$F_{2,q}(x, Q^2) = x \sum_i e_{q_i}^2 \left[f_{q_i}^{(0)}(x) \right.$$

$$\left. + \frac{\alpha_\mathrm{s}}{2\pi} \int_0^1 \frac{d\xi}{\xi} f_{q_i}^{(0)}(\xi) \left(P^{qq}\left(\frac{x}{\xi}\right) \ln \frac{Q^2}{m_g^2} + C_2^q\left(\frac{x}{\xi}\right) \right) \right].$$

However, this function appears divergent if the regulator is removed, $m_g \rightarrow 0$. While $C_2(x)$ depends on the process under investigation, the divergence does not because it is multiplied with universal splitting functions.

Exercise 20.3
Compute the coefficient $C_2^g(x)$ in Eq. (20.5.11).

20.6   Factorization in DIS

If the remaining divergences are universal (and they are because do not depend on the hard scattering), we can absorb the singularity into the parton

distribution functions. For instance, defining

$$
f_q(x, \mu_F) = f_q^{(0)}(x) + \frac{\alpha_s}{2\pi} \int_0^1 \frac{d\xi}{\xi} \left\{ f_q^{(0)}(\xi) \left[P^{qq}\left(\frac{x}{\xi}\right) \ln \frac{\mu_F^2}{m_g^2} + K^{qq}\left(\frac{x}{\xi}\right) \right] \right\},
$$
$$(20.6.13)$$

the structure function becomes (recall that the strong coupling depends on another scale, the renormalization scale μ_R)

$$
F_{2,q}(x, Q^2) = x \sum_i e_{q_i}^2 \left[f_i(x, \mu_F) \right.
$$
$$
\left. + \frac{\alpha_s(\mu_R)}{2\pi} \int_0^1 \frac{d\xi}{\xi} f_i(\xi, \mu_F) \left(P^{qq}\left(\frac{x}{\xi}\right) \ln \frac{Q^2}{\mu_F^2} + (C_2^q - K^{qq})\left(\frac{x}{\xi}\right) \right) \right]
$$
$$(20.6.14)$$

where the summation runs over the light quark flavours.[1] The long distance physics is factored into the parton distribution functions that depend on the *factorization scale* μ_F. The short distance physics is factored into the hard scattering cross section that depends on both the factorization and the renormalization scales. Both scales are arbitrary, unphysical scales. The term K^{ij} defines the *factorization scheme*. It is not unique, finite terms can be shifted between the short and long distance parts, but it is important that it must be chosen the same in all computations (the $\overline{MS}$ scheme is the standard where $K^{ij} = 0$).

Defining the convolution in x-space,

$$
(f \otimes g)(x) \equiv \int_0^1 dy \int_0^1 dz f(y) g(z) \delta(x - yz),
$$

we see that the structure function is 'factorized' in the form of a convolution,

$$
F_{2,q}(x, Q^2) = x \sum_i e_{q_i}^2 \left(f_i(\mu_F) \otimes \hat{F}_{2,i}(\mu_R, t) \right)(x), \qquad t = \ln \frac{Q^2}{\mu_F^2}.
$$

---

[1]Depending on what we consider light quark in the colliding proton, we speak about four (u, d, c and s quarks) or five flavour number scheme (the b quark also considered in addition to the lighter ones).

Exercise 20.4

The regularization of the splitting function at $x = 1$ is achieved by the +-prescription defined by

$$\int_0^1 dx [g(x)]_+ f(x) = \int_0^1 dx g(x) (f(x) - f(1))$$

for any smooth test function $f(x)$. The contribution of the loop corrections has the same kinematics as the LO one, so it has to be proportional to $\delta(1 - x)$. Thus the complete regularized splitting function has the form

$$P^{qq}(x) = C_F \left[\frac{1 + x^2}{(1 - x)_+} + K\delta(1 - x) \right].$$

We can obtain the parton distribution for a 'quark in a quark' from Eq. (20.6.13) by the substitution $f_q^{(0)}(x) \rightarrow \delta(1 - x)$

$$f_q(x, \mu_F) = \delta(1 - x) + \frac{\alpha_s}{2\pi} P^{qq}(x) \ln \frac{\mu_F^2}{m_g^2}.$$

Integration over x gives the number of quarks in a quark that has to be one, independently of μ_F. Thus we have the condition $\int_0^1 dx P^{qq}(x) = 0$. Compute the regularized splitting function.

20.7 DGLAP equations

We can compute the short-distance component of the factorized structure function of Eq. (20.6.14) in QCD perturbation theory. It depends on the renormalization scale, but recall that it has to satisfy the renormalization group equation.

We cannot compute the parton distribution functions in perturbation theory, so it seems that this is the end of the story: perturbative QCD appears non-predictive for processes with hadrons in the initial state. However, the arguments that lead to the renormalization group equation come to the rescue. While the right hand side of Eq. (20.6.14) depends on both renormalization and factorization scales, the measurable quantity F_2 does not, which can be expressed by the renormalization group equation. Of course, this statement has to be understood perturbatively, namely at any order in PT, the right

hand side of the renormalization group equation is not exactly zero, but may contain terms that are higher order in perturbation theory. Only infinite order is expected to give exact independence of the scales. The renormalization group equation gives the missing piece of information needed to make the theory predictive.

To write the renormalization group equation, we introduce Mellin transforms defined by $f(N) \equiv \int_0^1 dx\, x^{N-1} f(x)$, which turns a convolution into a real product:

$$\int_0^1 dx\, x^{N-1} \int_0^1 dy \int_0^1 dz\, \delta(x - yz) f(y) g(z) =$$
$$= \int_0^1 dy \int_0^1 dz\, (yz)^{N-1} f(y)\, g(z) = f(N) g(N) .$$

So $F_{2,q}(N, Q^2) = x \sum_i e_{q_i}^2 f_i(N, \mu_F) \hat{F}_{2,i}(N, \mu_R, t)$ is independent of μ_F, expressed as

$$\mu_F \frac{dF_2}{d\mu_F} = 0 \left(= O(\alpha_s^{n+1}) \text{ in PT at } O(\alpha_s^n) \right).$$

Let us explore the consequences of this renormalization group equation. For simplicity, we assume the existence of only one quark flavour, $F_{2,q}(N, Q^2) = x\, e_{q_i}^2\, f_q(N, \mu_F)\, \hat{F}_{2,i}(N, \mu_R, t)$. Then the renormalization group equation reads

$$\hat{F}_{2,q}(N, t) \frac{df_q}{d\mu_F}(N, \mu_F) + f_q(N, \mu_F) \frac{d\hat{F}_{2,q}}{d\mu_F}(N, t) = 0 .$$

Dividing with $f_q\, \hat{F}_{2,q}$, it turns into

$$\mu_F \frac{d \ln f_q}{d\mu_F}(N, \mu_F) = -\mu_F \frac{d \ln \hat{F}_{2,q}}{d\mu_F}(N, t) \equiv -\gamma_{qq}(N), \qquad (20.7.15)$$

where $\gamma_{qq}(N)$ is called the anomalous dimension because it acts as a factor $\mu_F^{-\gamma_{qq}(N)}$ in the dimensionless function $f_q(N, \mu_F)$. Taking the Mellin moment of Eq. (20.6.13) and then its derivative with respect to μ_F, we obtain that the anomalous dimension is

$$\gamma_{qq}(N) = -\mu_F \frac{d \ln f_q}{d\mu_F}(N, \mu_F) = -\frac{\alpha_s(\mu_R)}{\pi} P^{qq}(N) + O(\alpha_s^2), \qquad (20.7.16)$$

thus it is the Mellin transform of the splitting function, which can be computed in PT. Equation (20.7.15) implies that *the scale dependence of the*

parton distribution functions can be predicted in PT. This together with the universality of parton distribution functions makes perturbative QCD predictive: *we can measure the parton distribution functions in one process at a certain scale and then use it in another process at another scale to make predictions.*

How shall we choose the renormalization and factorization scales? If we want to avoid large logarithms that spoil the convergence of the perturbative series, the scales should be chosen near the characteristic physical scale of the process Q, e.g. $\mu_R^2 = \mu_F^2 = Q^2$. Then the renormalization group equation becomes

$$Q^2 \frac{d \ln f_q}{dQ^2}(N, Q^2) = -\frac{1}{2} \gamma_{qq}\left(N, \alpha_s(Q^2)\right), \qquad (20.7.17)$$

which is the Mellin transform of

$$Q^2 \frac{df_q}{dQ^2}(x, Q^2) = \frac{\alpha_s(Q^2)}{2\pi}\left((P^{qq} \otimes f_q(Q^2))\right)(x). \qquad (20.7.18)$$

Our discussion was highly simplified by considering only one quark flavour and neglecting the mixing of partons. If we make the full computation we obtain the celebrated formula

$$Q^2 \frac{df_i}{dQ^2}(x, Q^2) = \frac{\alpha_s(Q^2)}{2\pi} \sum_j \left(P^{ij} \otimes f_j(Q^2)\right)(x), \qquad (20.7.19)$$

called DGLAP equation, named after Yuri Dokshitzer [Dokshitzer, 1977], Vladimir Gribov, Lev Lipatov [Gribov and Lipatov, 1972] and Guido Altarelli, Giorgio Parisi [Altarelli and Parisi, 1977].

Let us now solve the (simplified) DGLAP equation in Mellin space, Eq. (20.7.17). It is a simple first order differential equation whose solution is

$$f_q(N, Q^2) = f_q(N, Q_0^2) \exp\left[-\int_{t_0}^t dt \, \gamma_{qq}\left(N, \alpha_s(\Lambda^2 e^t)\right)\right].$$

Let us recall the one-loop formula in Eq. (19.3.20), $\alpha_s(Q^2) = \frac{1}{b_0 t}$, $t = \ln \frac{Q^2}{\Lambda^2}$ and introduce the abbreviation $d_{qq}(N) = -\frac{\gamma_{qq}(N)}{2\pi b_0} \leq 0$. Then

$$f_q(N, Q^2) = f_q(N, Q_0^2) \exp\left[d_{qq}(N) \int_{t_0}^t \frac{dt}{t}\right], \qquad (20.7.20)$$

or

$$f_q(N, Q^2) = f_q(N, Q_0^2) \left(\frac{t}{t_0}\right)^{d_{qq}(N)}, \qquad (20.7.21)$$

called *scaling violation*.

As $\gamma_{qq}(1) = 0$, the number of valence q-quark in the proton, given by the integral $\int_0^1 dx\, f_q(x, Q^2)$, is independent of Q^2. Higher moments vanish more rapidly, therefore the average x decreases as Q^2 increases. Thus we predict that $f_q(x, Q^2)$ increases at small x and decreases at large x. This prediction is seen to be valid from the measurements shown in Fig. 20.2.

Exercise 20.5
Compute the anomalous dimension $\gamma_{qq}(x)$ using Eq. (20.7.16).
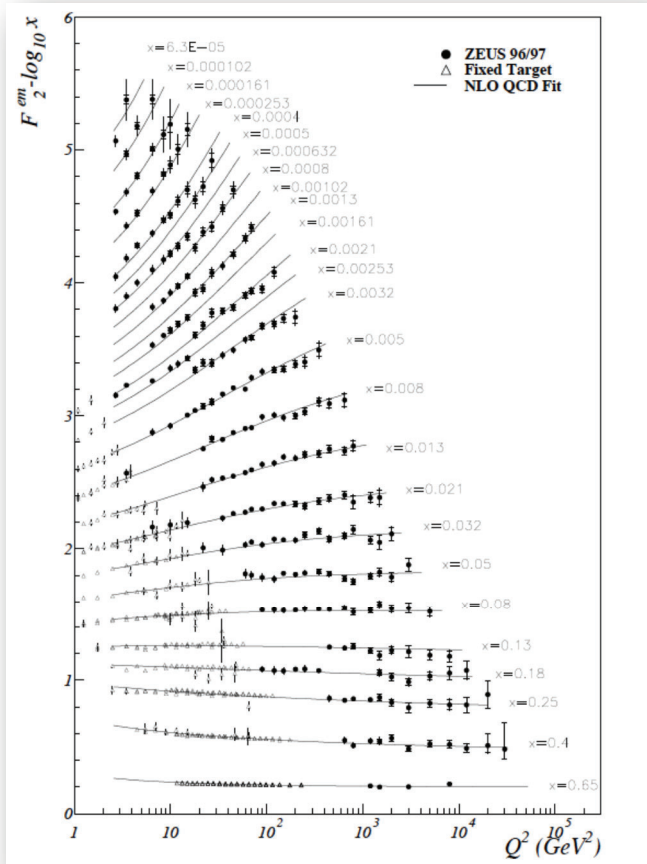
Figure 20.2: Measurement of the F_2 structure function at different Q^2 as a function of x,

Chapter 21

Hadron collisions

21.1   Factorization theorem

While electron-positron annihilation and DIS played very important roles in establishing perturbative QCD for understanding high-energy scattering experiments, presently and in the mid-term future the experiments at the energy frontier can be found at the LHC. Thus we are most interested in the theoretical tools needed to understand high-energy proton-proton collisions.

Fortunately, the tools we have developed so far can be generalized straightforwardly to hadron collisions. The most general form of the factorization theorem includes convolution with two parton distribution functions, one for each colliding parton, the hard scattering cross section, and possibly a convolution with a fragmentation function (FF) of a parton into an identified hadron in the final state. Thus, the differential cross section for a hypothetical inclusive process $pp \rightarrow Z + \pi + X$, in which we identify a Z

boson and a pion only, has the form

$$
d\sigma_{pp \to Z+\pi+X}(s, x, \alpha_s, \mu_R, \mu_F) =
$$

$$
= \sum_{i,j,k} \int_0^1 dx_1 f_{i/p}(x_1, \alpha_s, \mu_F) \int_0^1 dx_2 f_{j/p}(x_2, \alpha_s, \mu_F)
$$

$$
\times \int_x^1 \frac{dz}{z} d\hat{\sigma}_{ij \to Z+k+X}(\hat{s}, z, \alpha_s(\mu_R), \mu_R, \mu_F) D_{\pi/k}\left(\frac{x}{z}, \hat{s}\right)
\qquad (21.1.1)
$$

$$
+ O\left(\frac{\Lambda}{Q}\right)^P .
$$

In the factorization formula Eq. (21.1.1) s denotes the total centre-of-mass energy squared, x/z is the longitudinal momentum fraction of the pion in the parton k, μ_R and μ_F are the renormalization and factorization scales, $f_{i/p}(x)$ is the parton distribution function for parton i in the proton with momentum fraction x, $d\hat{\sigma}_{ij \to Z+k+X}(\hat{s})$ is the hard scattering cross section for the partonic process, $D_{\pi/k}(x)$ is the fragmentation function for the process parton $k \to \pi$. The last term shows that power-suppressed contributions at high Q^2 are neglected ($p > 1$). Substituting the parton distribution functions and fragmentation functions with δ functions (in momentum and flavour) we obtain the cross section formulae in DIS and electron-positron annihilation.

The parton distribution functions and fragmentation functions constitute the long-distance, non-perturbative components of the cross section that cannot be computed in perturbative QCD, only extracted from measurements. Thus, it is a natural question whether or not the factorization theorem is predictive. The answer is a clear yes for the following reasons.

We can compute the hard scattering cross section in perturbation theory, which involves (i) renormalization of ultraviolet divergences (order by order in perturbation theory), (ii) cancellation of infrared ones for infrared safe observables using a subtraction method, (iii) absorbing initial state collinear divergences into renormalization of parton distribution functions (and possibly uncancelled final state ones into that of the fragmentation function). The non-perturbative components are universal, so can be measured in one process and used to make predictions in another one. Furthermore, the evolution of these with Q^2 can be predicted in perturbation theory by the DGLAP equations as shown in Fig. 17.63.

In summary, we are prepared to make predictions for any high-energy scattering process. The theoretical framework for such predictions relies on QCD perturbation theory and the factorization theorem. In perturbation theory we can compute the hard scattering cross section and the evolution

of the parton distribution functions. There are universal elements, such as the parton distribution functions and fragmentation functions, as well as the subtraction method for computing radiative corrections. These principles are well understood and reasonably simple, though the actual implementations are cumbersome and their improvements are subjects of active research.

21.2   Are we happy?

At this point theorists can make precision predictions for distributions of infrared safe observables. The main bottleneck to make such predictions is the algebraic complexity of computing amplitudes and the analytic complexity of evaluating loop integrals. The state of the art considers the computation of NLO corrections a solved problem with automated implementations for processes up to about five partons in the final state (at tree level). The exact number depends on the process being considered because the numerical integrations become too expensive eventually. Nevertheless, all processes listed in the 'Les Houches wishlist (2011)' are known by now. Furthermore, there is also a computer code to compute seven-jet production in electron-positron annihilation [Becker et al., 2012].

For experimenters the situation is less satisfactory. While predictions in perturbative QCD are based on a solid theoretical ground, those lack important features. While perturbative QCD gives predictions for final states with few partons, the experiments detect hadrons. A tool that can simulate real events with hadrons at correct rates would be much more handy. To finish these lectures we look into modelling events in a qualitative way. A more detailed description can be found for example in Ref. [Skands, 2012].

21.3   Modelling events

Figure 17.64 shows our view of a proton-proton scattering event at high energy. The three parallel lines ending in discs from both sides represent the two incoming protons. At high energies these protons consist of (almost) free-flying partons, two of which (one from each) collide at high centre-of-mass energy and produce the hard scattering, with perturbatively computable cross section. This is where signatures of new physics may appear. The hard scattering cross section is process dependent. We have discussed how it can be computed from first principles, from Feynman diagrams and rules. The precision of the predictions can be improved systematically in perturbation theory by computing the effect of radiative quantum corrections.

Before collision the colliding partons may emit other partons nearly collinear with the beam. These collinear emissions in the initial state give rise to divergences that can be factored into the renormalized parton distribution functions. After collision few energetic partons appear that may emit less energetic partons and each develops showers of partons. Emissions into almost the same direction as the original parton occur with enhanced probability (due to the collinear divergence) as well as emissions of soft gluons. This is represented in Figure 17.64 by red quark and gluon lines. Both factorization and parton showering can be described from first principles based upon known physics of QCD and are universal, meaning that these are independent of the process and observable. We have seen how factorization works, but have not discussed how parton showers are modelled with shower Monte Carlo (SMC) programs [Sjostrand et al., 2006, Corcella et al., 2001]. We mentioned marginally how the large logarithms emerging in the final state splittings can be resummed. Such resummations give improved prediction for the cross section (as seen in Fig. 17.60), but does not simulate events.

Parton showers still only give a description of events in terms of quarks and gluons, whereas detectors detect only hadrons. We do not know how to compute hadronization, the transition from quarks and gluons to hadrons, from first principles. Yet the idea of local parton-hadron duality (see, e.g. Ref. [Dokshitzer et al., 1991]) provides some sort of theoretical understanding. It states that

after accounting for all gluon and quark production down to scales $\simeq \Lambda_{\mathrm{QCD}}$, the transition from partons to hadrons is essentially local in phase space, i.e. there is no rearrangement of energy and momentum.

Thus the directions and momenta of hadrons will be closely related to those of the partons and the hadron multiplicity will reflect the parton multiplicity, too. This is illustrated by the green lines with dots.

In addition to the energetic partons in the initial state, there are also low-energy ones that may collide, which is energy and process dependent. This low-energy physics is described in models of underlying event, which are also part of modern shower Monte Carlo programs. The underlying event produces low-energy partons. Also at the end of the shower low-energy partons emerge. As QCD confines partons, these partons turn into hadrons before detection, a process called hadronization. We do not have a theory of hadronization based on first principles. Instead, shower Monte Carlo programs include models that describe hadronization in a process independent way. These models contain parameters that are fixed experimentally.

21.4   Conclusions

In the last three chapters we discussed the theoretical basis of interpreting the results of high-energy collider experiments. We discussed how perturbative QCD can be made predictive and also the main uncertainties in the predictions. We used the following key ingredients in this tour:

(i) gauge invariance that allows us to write down the Lagrangian and which predicts many important features of the theory;

(ii) renormalization that cancels ultraviolet divergences systematically order-by-order in perturbation theory and introduces a dimension-ful scale into even the scaleless Lagrangian of massless QCD, leading to scaling violations of one-scale observables that would be scale independent in the classical theory;

(iii) asymptotic freedom at high energies emerging from the quantum structure of the theory and the non-abelian nature of the gauge group;

(iv) need for infrared safety, emerging from asymptotic freedom, to ensure that the infrared divergences, associated with unresolved parton emission, cancel between real and virtual contributions, allowing the perturbative calculation of jet cross sections, without a detailed understanding of the mechanism by which partons become jets;

(v) factorization that makes possible to use perturbative QCD to calculate the interactions of hadrons, since all the non-perturbative physics gets factorized, into parton distribution functions;

(vi) evolution and universality of parton distribution functions that allows us to extract those measuring cross sections in one process, like DIS, and then used to predict the cross sections for any other process. Again, this factorization introduces a scale dependence into the parton model so that the structure functions of DIS, and other one-scale observables become scale dependent.

These features make perturbative QCD predictive, without forcing us to solve the theory at all possible scales: unknown or not calculated high and low-energy effects can be renormalized, factorized and cancelled away.

In the last chapter we study the sector of the standard model with broken symmetry. The photon appears here, which is massless like the gluon. However, the photon does not carry colour charge and does not have self interaction, it only mediates the electromagnetic interaction between fermions.

As the coupling of electromagnetism is much weaker than the strong coupling, the processes with photon radiation can be approximated quite well already at the lowest order in perturbation theory. Therefore in our introductory textbook we are satisfied with predictions at Born level, although the precision of experiments require the inclusion of at least the first radiative corrections.

Chapter 22

Electroweak sector of the standard model

MOTTO:

And as they drifted up, their minds sang with the ecstatic knowledge that either what they were doing was completely and utterly and totally impossible or that physics had a lot of catching up to do.

(Douglas Adams: So Long, and Thanks for All the Fish)

22.1 Weinberg mixing

The underlying gauge group of the broken part of the standard model is

$$G = SU(2)_{\mathrm{L}} \otimes U(1)_Y .$$

Here L stands for left (and later R for right) polarized particle currents and Y is the hypercharge. The field content in one family (we consider the first

one here) is

$$\psi_1 = \begin{pmatrix} u \\ d \end{pmatrix}_L \qquad \psi_2 = u_R, \qquad \psi_3 = d_R \qquad \text{quarks}$$

$$\psi_1 = \begin{pmatrix} v_e \\ e^- \end{pmatrix}_L \qquad \psi_2 = 0, \qquad \psi_3 = e_R^- \qquad \text{leptons}$$

where for each flavour $f = u, d, v, e$ and

$$f_{L/R} \equiv f_{\mp} = \frac{1}{2}(1 \mp \gamma_5) f .$$

One could imagine $\psi_2 = v_R$, but such leptons have not been observed and thus not considered members of the standard model particles. There are three families of each field ψ_i. For a matrix $U \in G$ the following transformation rules hold

$$U\psi_1(x) = e^{i\boldsymbol{T} \cdot \boldsymbol{\alpha}(x)} e^{i y_1 \beta(x)} \psi_1(x) \text{ where } \boldsymbol{T} = \frac{1}{2}(\tau_1, \tau_2, \tau_3) \text{ and}$$

$$U\psi_j(x) = \qquad e^{i y_j \beta(x)} \psi_j(x), \quad j = 2, 3 .$$

Here τ_a represent the Pauli matrices, while $\boldsymbol{\alpha} = (\alpha_1, \alpha_2, \alpha_3)$ and β are real numbers. The number y_j denotes the eigenvalue of the U(1) generator $Y/2$, called weak hypercharge, for field ψ_j (the factor $\frac{1}{2}$ is included to maintain the traditional $Y = B + S$, baryon number + strangeness definition for the first three quarks). The Lagrangian for one family (family replication is implicitly understood) is

$$\mathcal{L} = \sum_{j=1}^{3} i\bar{\psi}_j(x) \not{D}^{(j)} \psi_j(x), \tag{22.1.1}$$

with $D_\mu^{(j)} = \partial_\mu + \delta_{j1} i g \, \boldsymbol{T} \cdot \boldsymbol{W}_\mu + i g' \, y_j B_\mu$. The Lagrangian in Eq. (22.1.1) is invariant under the gauge transformation of the ψ_j fields, provided the four gauge fields introduced in the covariant derivative transform according to the rules

$$B_\mu \xrightarrow{G} B'_\mu(x) = B_\mu(x) - \frac{1}{g'} \partial_\mu \beta(x) \tag{22.1.2}$$

$$\boldsymbol{T} \cdot \boldsymbol{W}_\mu(x) \xrightarrow{G} \boldsymbol{T} \cdot \boldsymbol{W}'_\mu(x) = U(x) \boldsymbol{T} \cdot \boldsymbol{W}_\mu(x) U^\dagger(x) + \frac{i}{g} \left[\partial_\mu U(x) \right] U^\dagger(x) \tag{22.1.3}$$

where $U(x) = \exp[i\mathbf{T} \cdot \boldsymbol{\alpha}(x)]$. The gauge invariant kinetic term for these vector fields is

$$\mathcal{L}_{B,W} = -\frac{1}{4} B_{\mu\nu} B^{\mu\nu} - \frac{1}{4} \mathbf{W}_{\mu\nu} \cdot \mathbf{W}^{\mu\nu},$$

with $B_{\mu\nu} = \partial_\mu B_\nu - \partial_\nu B_\mu \equiv \partial_{[\mu} B_{\nu]}$ and $\mathbf{W}_{\mu\nu} = \partial_{[\mu} \mathbf{W}_{\nu]} - g \, \mathbf{W}_\mu \times \mathbf{W}_\nu$. $B_{\mu\nu}$ is invariant under G transformations, while $\mathbf{T} \cdot \mathbf{W}_{\mu\nu}$ transforms covariantly:

$$\mathbf{T} \cdot \mathbf{W}_{\mu\nu} \overset{G}{\to} U(x) \mathbf{T} \cdot \mathbf{W}_{\mu\nu} U^\dagger(x).$$

In quantum field theory the mass of a particle is the position of the pole in the inverse two-point function in momentum space.[1] Gauge symmetry forbids such mass terms for gauge bosons. In case of the Dirac Lagrangian the fermion propagator $\Delta_j(q) = i\frac{q}{q^2 + i\varepsilon}$ depends only on the momentum q, i.e. does not contain mass. Thus, the mass of the fermion is zero. An extra term proportional to $i\bar{\psi}\psi$ would lead to a pole-position different from zero. However, fermion masses must also be absent because

$$m\,\bar{\psi}\psi = m\,\bar{\psi}_L\psi_R + m\,\bar{\psi}_R\psi_L,$$

but the ψ_L, ψ_R fields transform differently under G. Thus the G-invariant Lagrangian describes massless fields in contradiction to observation (for instance $m_W \simeq 80\,\text{GeV}$, $m_e \simeq 511\,\text{keV}$ in natural units). We return to the problem of masses in the following sections.

The gauge invariant $\mathcal{L}_\psi$ contains interactions of the fermion fields with gauge bosons:

$$-g\,\bar{\psi}_1 \mathbf{T} \cdot \mathbf{W} \psi_1 - g' \sum_j y_j \, \bar{\psi}_j \, \slashed{B} \, \psi_j$$

where

$$\mathbf{T} \cdot \mathbf{W}_\mu = \frac{1}{2} \begin{bmatrix} W_\mu^3 & W_\mu^1 - iW_\mu^2 \\ W_\mu^1 + iW_\mu^2 & -W_\mu^3 \end{bmatrix}.$$

The off-diagonal terms lead to charged-current interactions

$$\mathcal{L}_{CC} = -\frac{g}{2\sqrt{2}} \left(W_\mu^\dagger [\bar{u}\gamma^\mu (1 - \gamma_5) d + \bar{\nu}\gamma^\mu (1 - \gamma_5) e] + \text{h.c.} \right),$$

with the stepping operators

$$W_\mu = \frac{1}{\sqrt{2}} \left(W_\mu^1 + iW_\mu^2 \right), \qquad W_\mu^\dagger = \frac{1}{\sqrt{2}} \left(W_\mu^1 - iW_\mu^2 \right),$$

---

[1]This is the pole mass definition that differs from the renormalized mass discussed earlier. The two definitions are related in perturbation theory.

and the letters u, d, e, v stand for the spinor of the relevant particle. The diagonal terms lead to neutral-current interactions

$$\mathcal{L}_{NC} = - \sum_j \bar{\psi}_j \left(g\, T^3 W^3 + g'\, y_j B \right) \psi_j \,. \tag{22.1.4}$$

We would like to identify the fields W_μ^3 and B_μ with the observed fields Z_μ and A_μ (the latter denoting the electromagnetic field), but both W_μ^3 and B_μ are massless, therefore an arbitrary combination of them is possible:

$$\begin{bmatrix} W_\mu^3 \\ B_\mu \end{bmatrix} = \begin{bmatrix} \cos\theta_W & \sin\theta_W \\ -\sin\theta_W & \cos\theta_W \end{bmatrix} \begin{bmatrix} Z_\mu \\ A_\mu \end{bmatrix}.$$

The angle θ_W is called Weinberg (or weak mixing) angle. Equation (22.1.4) becomes then

$$\mathcal{L}_{NC} = - \sum_j \bar{\psi}_j \Bigg[A \left(g\, T^3 \sin\theta_W + g'\, y_j \cos\theta_W \right)$$
$$+ Z \left(g T^3 \cos\theta_W - g' y_j \sin\theta_W \right) \Bigg] \psi_j$$
$$\equiv \mathcal{L}_{QED} + \mathcal{L}_{NC}^{(Z)} \,.$$

The term with A_μ should give QED and for this we require

$$g \sin\theta_W = g' \cos\theta_W = e \qquad \text{and} \qquad Q = \frac{Y}{2} + T^3 \tag{22.1.5}$$

where Q is the electromagnetic charge operator, with

$$Q_1 = \begin{bmatrix} Q_{u/v} & 0 \\ 0 & Q_{d/e} \end{bmatrix} \qquad Q_2 = Q_{u/v} \qquad Q_3 = Q_{d/e}.$$

In order to have the correct electromagnetic charge, the hypercharge of the different species has to be

$$y_1 = Q_{u/v} - \frac{1}{2} = Q_{d/e} + \frac{1}{2} \qquad y_2 = Q_{u/v} \qquad y_3 = Q_{d/e}. \tag{22.1.6}$$

A possible right handed neutrino v_R would have both $Q_{v_R} = 0$ and $y_{v_R} = 0$ and thus it would not couple to anything (sterile neutrino). The existence of such neutrino cannot be excluded, but since it does not interact with any other particle of the model, we have no possibility to detect it in collider

experiments and for this reason we exclude it from the standard model. We finally obtain

$$\mathcal{L}_{QED} = -e\, A_\mu J^\mu_{EM}, \qquad \mathcal{L}^{(Z)}_{NC} = \frac{-e}{\sin\theta_W \cos\theta_W} Z_\mu J^\mu_Z,$$

$$J^\mu_{EM} = \sum_j Q_j\, \bar{\psi}_j \gamma^\mu \psi_j,$$

$$J^\mu_Z = \sum_j \left(T_3 - \sin^2\theta_W Q_j\right) \bar{\psi}_j \gamma^\mu \psi_j \equiv J^\mu_3 - \sin^2\theta_W J^\mu_{EM}.$$

In terms of the usual fermion fields

$$\mathcal{L}^{(Z)}_{NC} = \frac{-e}{\sin\theta_W \cos\theta_W} Z_\mu \sum_f \bar{f}\gamma^\mu \left(v_f - a_f\gamma_5\right) f, \qquad f = u, d \text{ or } \nu, e,$$

where the axial coupling is $a_f = T^f_3$ and the vector coupling is $v_f = T^f_3 - 2Q_f \sin^2\theta_W$. We leave it as an exercise to compute the cubic and quartic self-interactions among gauge bosons.

Exercise 22.1

The part of the standard model Lagrangian that determines the interaction between fermions and electroweak gauge bosons is given by

$$\mathcal{L} = \sum_{\psi_L} \bar{\psi}_L \gamma^\mu \left(i\partial_\mu + g\frac{1}{2}\vec{\tau}\cdot\vec{W}_\mu + g'yB_\mu\right)\psi_L + \sum_{\psi_R} \bar{\psi}_R \gamma^\mu \left(i\partial_\mu + g'yB_\mu\right)\psi_R.$$

The fields $\vec{W}_\mu$ and B_μ denote the gauge fields of the weak isospin and the hypercharges. The photon field A_μ and the Z boson field Z_μ can be written as linear combinations of these fields:

$$A_\mu = B_\mu \cos\theta_W + W^3_\mu \sin\theta_W$$

$$Z_\mu = -B_\mu \sin\theta_W + W^3_\mu \cos\theta_W .$$

The relations of the various couplings are given by Eq. (22.1.5)

$$e = g \sin\theta_W = g' \cos\theta_W .$$

Show that one obtains the QED Lagrangian by substituting the photon and the Z boson fields for the W^3 and the B fields in the Lagrangian density above.

22.2   U(1) Brout-Englert-Higgs mechanism

Our gauge symmetric Lagrangian is renormalizable, but the symmetry forbids masses, which contradicts reality. There is a way out: it is possible to get non-symmetric result from an invariant Lagrangian. Let us consider a Lagrangian $\mathcal{L}$ that

  (a) is invariant under transformations of a continuous symmetry group G,

  (b) has a degenerate set of states with minimal energy, which transform under G as the members of a given multiplet.

The system arbitrarily selects one of these states as the ground state of itself, we say in these cases that *the symmetry is spontaneously broken*. The simplest example in field theory is the $G = U(1)$ Brout-Englert-Higgs (BEH) model. We consider the spontaneous symmetry breaking (SSB) of such a model and move later on to the case of standard model.

Let us assume a Lagrangian $\mathcal{L}$ of a complex scalar field ϕ which is symmetric under global $U(1)$ transformations

$$\mathcal{L} = \partial_\mu \phi^* \partial^\mu \phi - V(\phi)$$

where

$$V(\phi) = \mu^2 \phi^* \phi + \lambda (\phi^* \phi)^2$$

is the potential. $\mathcal{L}$ is invariant under global

Figure 22.1: The Mexican hat potential

$$\phi \rightarrow \phi' = e^{-i e \theta} \phi$$

phase transformations. The potential is bounded from below if $\lambda > 0$, which leaves two options

  (1) If $\mu^2 > 0$, then V has a single minimum at $|\phi| = 0$ (a quadratic function, rotationally symmetric around the V axis over the ϕ_1–ϕ_2 plane with minimum at zero).

  (2) If $\mu^2 < 0$, V is still rotationally symmetric, but has an infinite number of degenerate states with minimum energy at $|\phi_0| = \sqrt{\frac{-\mu^2}{2\lambda}} \equiv \frac{v}{\sqrt{2}}$ (often called Mexican hat potential, see Fig. 22.1). The value of the potential at $\phi_0 = \frac{v}{\sqrt{2}} e^{i\theta}$ is $V(\phi_0) = -\frac{\lambda}{4} v^4 < V(0) = 0$.

If we choose for example $\theta = 0$ as the ground state for the spontaneously broken theory, and we parameterize the field around it as

$$\phi(x) = \frac{1}{\sqrt{2}}[v + \phi_1(x) + i\phi_2(x)], \quad \text{with} \quad \phi_1, \phi_2 \text{ real functions,}$$

then the potential contains the following terms:

$$\phi^*\phi = \frac{1}{2}v^2 + v\phi_1 + \frac{1}{2}\phi_1^2 + \frac{1}{2}\phi_2^2$$

$$(\phi^*\phi)^2 = \frac{1}{4}v^4 + v^3\phi_1 + v^2\phi_1^2 + \frac{1}{2}\left(v^2 + 2v\phi_1\right)\left(\phi_1^2 + \phi_2^2\right) + \frac{1}{4}\left(\phi_1^2 + \phi_2^2\right)^2$$

$$= \frac{1}{4}v^4 + v^3\phi_1 + \frac{3}{2}v^2\phi_1^2 + v\phi_1^3 + \frac{1}{2}v^2\phi_2^2 + v\phi_1\phi_2^2 + \frac{1}{4}\left(\phi_1^2 + \phi_2^2\right)^2.$$

Consequently

$$V(\phi) = V(\phi_0) + v\underbrace{\left(\mu^2 + \lambda v^2\right)}_{=\,0}\phi_1 + \frac{1}{2}\left(\mu^2 + 3\lambda v^2\right)\phi_1^2$$

$$+ \frac{1}{2}\underbrace{\left(\mu^2 + \lambda v^2\right)}_{=\,0}\phi_2^2 + \lambda v\phi_1\left(\phi_1^2 + \phi_2^2\right) + \frac{\lambda}{4}\left(\phi_1^2 + \phi_2^2\right)^2.$$

From the last equation we can read off that the mass of ϕ_2 vanishes, $m_{\phi_2}^2 = 0$, which is a realization of Goldstone's general theorem:

> *If a Lagrangian $\mathcal{L}$ is invariant under a continuous symmetry group G but the vacuum is only invariant under a subgroup $H \subset G$, then there exist as many massless spin-0 particles (Goldstone bosons) as broken generators.*

In the $U(1)$ case there is one broken generator. The corresponding Goldstone boson is ϕ_2 that describes excitations around the flat direction in the potential.

We are more interested in the case when the symmetry is local. Then the gauge-invariant Lagrangian is

$$\mathcal{L} = \left(D_\mu\phi\right)^*\left(D^\mu\phi\right) - V(\phi) - \frac{1}{4}F_{\mu\nu}F^{\mu\nu},$$

with $D_\mu[A] = \partial_\mu - ieA_\mu$. We parameterize $\phi(x)$ around the ground state as

$$\phi(x) = \frac{1}{\sqrt{2}}[v + h(x)]\,e^{i\frac{\xi(x)}{v}}.$$

The exponential factor is a phase that can be rotated (gauged) away by exploiting the gauge invariance of $\mathcal{L}$. In this gauge we use the transformed fields

$$\phi'(x) = e^{-i\frac{\xi(x)}{v}}\phi(x) = \frac{1}{\sqrt{2}}[v + h(x)]$$

$$A'_\mu(x) = A_\mu(x) - \frac{1}{ev}\partial_\mu\xi(x).$$

In terms of the transformed fields (we drop the prime $'$ to ease the notation) the Lagrangian becomes

$$\mathcal{L} = \frac{1}{2}(\partial_\mu h)(\partial^\mu h) + \frac{1}{2}e^2v^2A^2 + e^2vh(x)A^2 + \frac{1}{2}e^2h^2A^2 - \frac{1}{4}F_{\mu\nu}F^{\mu\nu}$$
$$- V\left(\frac{v}{\sqrt{2}}\right) - \lambda v^2h^2(x) - \lambda vh^3(x) - \frac{\lambda}{4}h^4(x),$$

from which we conclude the following spectrum: a scalar Higgs particle h with mass $m_h = \sqrt{2\lambda v^2}$, cubic and quartic self interactions, and a massive $U(1)$ field A_μ with mass $m_A = ev$. The massive vector field has three components A_i ($i = 1, 2, 3$) and as $A^2 = A_0^2 - \sum_{i=1}^{3}A_i^2$ and A_0 is unphysical due to gauge fixing, the mass terms for the A_i field components have the correct (negative) sign in the Lagrangian. The excitations of this gauge field interact with the Higgs particle (third and fourth terms). We could identify the $U(1)$ symmetry with that of QED, but then the vacuum would be electrically charged, which contradicts to our observations.

22.3 Brout-Englert-Higgs mechanism in the standard model

In the electroweak part of the standard model the covariant derivative acting on the BEH field is given by

$$D_\mu^{(\phi)} = \partial_\mu + ig\,\boldsymbol{T} \cdot \boldsymbol{W}_\mu + ig'\,y_\phi B_\mu.$$

We introduce a new $SU(2)$-doublet

$$\phi = \begin{bmatrix} \phi^+ \\ \phi^0 \end{bmatrix} = \frac{1}{\sqrt{2}}\begin{bmatrix} \phi_1 + i\phi_2 \\ \phi_3 + i\phi_4 \end{bmatrix}.$$

Choosing $y_\phi = \frac{1}{2}$, the upper component has electric charge +1 and the lower component is electrically neutral. After SSB of $SU(2)_L \times U(1)_Y$ into $U(1)_Q$

the field becomes

$$\phi = \frac{1}{\sqrt{2}}\, e^{i\boldsymbol{T}\cdot\boldsymbol{\xi}(x)/v} \begin{bmatrix} 0 \\ v + h(x) \end{bmatrix}.$$

This ground state is electrically neutral, and so it does not couple to the photon, which consequently remains massless as shown below. Eliminating the unitary phase (in other words "choosing unitary gauge"), the scalar kinetic term becomes

$$\frac{1}{2}\left((\partial_\mu h)\,(\partial^\mu h) + \left|(ig\,\boldsymbol{T}\cdot\boldsymbol{W}_\mu + ig'\,y_\phi B_\mu)\begin{bmatrix} 0 \\ v+h \end{bmatrix}\right|^2\right)$$

(the terms containing a single derivative of the h field cancel). Furthermore, using $y_\phi = \frac{1}{2}$,

$$\frac{1}{2}\left|(ig\,\boldsymbol{T}\cdot\boldsymbol{W}_\mu + ig'\,y_\phi B_\mu)\begin{bmatrix} 0 \\ v \end{bmatrix}\right|^2 = \frac{1}{2}\left|\frac{v}{2}\left(\sqrt{2}g\,W_\mu^\dagger, g'\,B_\mu - g\,W_\mu^3\right)\right|^2$$

$$= \frac{v^2}{4}\left\{g^2\,W_\mu^\dagger W^\mu\right.$$

$$\left. + \frac{1}{2}\underbrace{[g'\,(A\cos\theta_W - Z\sin\theta_W) - g\,(A\sin\theta_W + Z\cos\theta_W)]^2}_{=[-Z(g'\sin\theta_W + g\cos\theta_W)]^2 = Z_\mu Z^\mu\,\frac{g^2}{\cos^2\theta_W}}\right\}.$$

We rewrite the quadratic terms in the braces as

$$M_W^2\,W_\mu^\dagger W^\mu + \frac{1}{2}M_Z^2 Z_\mu Z^\mu$$

with

$$M_W = \frac{v\,g}{2} \quad\text{and}\quad M_Z = \frac{v\,g}{2\cos\theta_W} = \frac{M_W}{\cos\theta_W}. \tag{22.3.7}$$

Thus we find that *SSB predicts* the masses of the vector bosons (note that the A_μ field of QED is massless), with a non-trivial relation between M_W and M_Z:

$$\frac{M_W}{M_Z} = \cos\theta_W = \frac{g}{\sqrt{g^2 + g'^2}}.$$

The vector boson propagator is that of a massive vector field (with three components propagating),

$$\alpha \underset{M_V}{\overset{p}{\wwave}} \beta \quad = -\mathrm{i}\frac{g^{\alpha\beta} - \frac{p^{\alpha}p^{\beta}}{M_V^2}}{p^2 - M_V^2 + \mathrm{i}M_V\Gamma_V}, \text{ where } V = W^{\pm},\, Z.$$

Low energy experimental facts (for example decay width of $\mu^- \rightarrow e^- \bar{\nu}_e \nu_\mu$, $n \rightarrow p\,e^- \bar{\nu}_e$ or $p \rightarrow n\,e^+ \nu_e$, $\Lambda \rightarrow p\,e^- \bar{\nu}_e$, helicity suppression of $\pi^- \rightarrow e^- \bar{\nu}_e$) can be nicely described by the four-fermion interaction term

$$\mathcal{H}_I = \frac{G_F}{\sqrt{2}} J^\mu J_\mu, \tag{22.3.8}$$

introduced by Enrico Fermi, where $G_F = 1.16637 \cdot 10^{-5}\,\mathrm{GeV}^{-2}$ is Fermi's constant and

$$J_\alpha = \bar{u}\gamma_\alpha\,(1 - \gamma_5)\,[d\cos\theta_C + s\sin\theta_C] + \bar{\nu}_e\gamma_\alpha\,(1 - \gamma_5)\,e + \bar{\nu}_\mu\gamma_\alpha\,(1 - \gamma_5)\,\mu,$$

with $\sin\theta_C \simeq 0.22$ (θ_C is called Cabibbo's angle as this mixing of the quark fields was introduced by Nicola Cabibbo).

In the low energy limit, the propagator of the massive gauge bosons becomes

$$\alpha \underset{M_V}{\overset{p}{\wwave}} \beta \quad \underset{|p| \ll M_V}{\longrightarrow} \quad +\mathrm{i}\frac{g^{\alpha\beta}}{M_V^2},$$

and from the electroweak theory we can recover the $V - A$ model of weak interactions (recall Table 4.1) with

$$\frac{G_F}{\sqrt{2}} = \frac{g^2}{8\,M_W^2} = \frac{1}{2\,v^2}. \tag{22.3.9}$$

As a result we deduce *the vacuum expectation value of the BEH field in terms of the Fermi constant, known precisely from low-energy experiments*, $v = \left(\sqrt{2}\,G_F\right)^{-\frac{1}{2}} \simeq 246\,\mathrm{GeV}$.

We can also predict the value of M_W as a function of $\sin\theta_W$. Rearranging Eq. (22.3.9) and substituting $e = g\sin\theta_W$, we obtain

$$M_W = \frac{1}{\sin\theta_W}\sqrt{\frac{\pi\alpha}{\sqrt{2}\,G_F}}$$

where the fine structure α is not to be confused with the index α above. Using the Feynman rules of the electroweak theory, from the tree-level diagrams of Fig. 22.2,
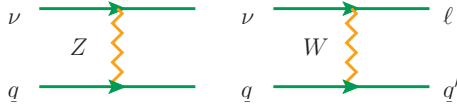
Figure 22.2: Neutral and charged current neutrino scattering at tree level

we can deduce the following predictions for neutral and charged current neutrino scattering:

$$\sigma\,(v\,q \to v\,q) \equiv \sigma_{\mathrm{NC}}\,(s) \propto \frac{8\pi\,g^4}{3\,M_Z^4\,\cos^4\theta_{\mathrm{W}}}\,s\,\left(a_q^2 + a_q v_q + v_q^2\right),$$

$$\sigma\,(v\,q \to l\,q') \equiv \sigma_{\mathrm{CC}}\,(s) \propto \frac{8\pi\,g^4}{4\,M_W^4}\,s\,.$$

$$(22.3.10)$$

(a_q and v_q denote the axial-vector and vector couplings of quark q). The ratio of the two cross sections depends only on $\sin\theta_{\mathrm{W}}$ (at LO accuracy):

$$\frac{\sigma_{\mathrm{NC}}}{\sigma_{\mathrm{CC}}} = \left(\frac{M_W}{M_Z\cos\theta_{\mathrm{W}}}\right)^4 \underbrace{\frac{4}{3}\left(a_q^2 + a_q v_q + v_q^2\right)}_{f(\sin\theta_{\mathrm{W}})}.$$

Fitting this prediction to the measured value of the ratio one finds $\sin^2\theta_{\mathrm{W}} = 0.231$. Then with $\alpha(M_Z) \simeq 1/128$, obtained from the measured value $\alpha(\simeq 0) \simeq 1/137$ by running the coupling, we can predict the values of the gauge boson masses (at lowest order in perturbation theory),

	SM prediction at LO	measured
$\frac{M_W c^2}{\mathrm{GeV}}$	80.23	80.385
$\frac{M_Z c^2}{\mathrm{GeV}}$	91.49	91.188

We close this section with recording the complete Lagrangian in the

Higgs sector:

$$\mathcal{L}_h = \frac{1}{2}\partial_\mu h\,\partial^\mu h - \frac{1}{2}M_h^2 h^2 - \frac{M_h^2}{2\,\mathrm{v}}h^3 - \frac{M_h^2}{8\,\mathrm{v}^2}h^4$$
$$+ \left(M_W^2 W_\mu^+ W^{-\mu} + \frac{1}{2}M_Z^2 Z_\mu Z^\mu\right)\left(1 + 2\frac{h(x)}{\mathrm{v}} + \frac{h^2(x)}{\mathrm{v}^2}\right).$$

where $M_h = \sqrt{-2\mu^2} = \sqrt{2\lambda}\,\mathrm{v}$. The Higgs boson was observed at the LHC by the ATLAS and CMS experiments. Its mass was measured to be approximately $125.1\,\mathrm{GeV}/c^2$, so $\lambda \simeq 0.13$. The Lagrangian also contains cubic and quartic Higgs self interactions as well as vector boson-Higgs interactions, proportional to M_V^2. In order to prove that the standard model Higgs boson was found the experiments have measured these couplings and showed that these are consistent with the standard model predictions.

Exercise 22.2
In addition to explaining the mass of vector bosons, there is another puzzle that the existence of the Higgs boson can explain. In the standard model scattering of the electroweak vector bosons W^+ and W^- is possible via exchange of a photon or a Z boson both in the s and t-channels, as well as through four-point interaction. Compute the cross section for longitudinally polarized vector bosons assuming these processes at LO accuracy using the Feynman rules in Sect. 22.7. What can you observe as the total centre-of-mass energy of the colliding vector bosons grow, $\sqrt{s} \to \infty$?

With SSB, the colliding vector bosons can also interact through an off-shell Higgs boson. Compute the contribution of these diagrams to the cross section. How does the cross section now behave at large s?

Exercise 22.3
Compute the decay width of muon decay, $\mu^- \to e^-\bar{\nu}_e\nu_\mu$ (i) in the four-fermion interaction theory of Fermi, (see Eq. (22.3.8)), (ii) in the standard model (the necessary Feynman rules can be found in Sect. 22.7).

Exercise 22.4
Compute the cross sections in Eq. (22.3.10)

22.4   GIM (Glashow, Iliopoulos, Maiani) mechanism

From the success of the low-energy interaction term in Eq. (22.3.8) we conclude that the $SU(2)_L$ partner of the u quark should be

$$d_c = d \cos \theta_C + s \sin \theta_C$$

instead of d quark only as seen in Eq. (22.1.1). However, if we use the field d_c in $\mathcal{L}_{NC}^{(Z)}$ instead of d, we have

$$\mathcal{L}_{NC}^{(Z)} \propto \cos \theta_C \, \sin \theta_C \, Z_\mu \left[\bar{d} \gamma^\mu \left(v_d - a_d \gamma_5 \right) s + \bar{s} \gamma^\mu \left(v_d - a_d \gamma_5 \right) d \right]$$
$$+ \cos^2 \theta_C \, Z_\mu \bar{d} \gamma^\mu \left(v_d - a_d \gamma_5 \right) d + \cdots,$$

which gives flavour-changing neutral currents (FCNC) in the first two terms with similar strength as $Zd\bar{d}$ itself (third term), in contradiction to experimental facts. For instance, $K_L = [d\bar{s}]$ decays via neutral current into $\mu\bar{\mu}$, while $K^+ = [u\bar{s}]$ decays via charged current into $\nu_\mu \bar{\mu}$ according to the following diagrams:
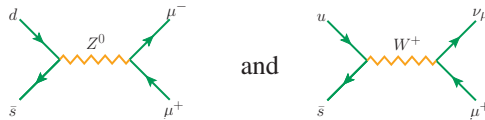
The ratio of their decay width is

$$\frac{\Gamma \left(K_L \to \mu^+ \mu^- \right)}{\Gamma \left(K^+ \to \mu^+ \nu_\mu \right)} = 2.8 \cdot 10^{-9},$$

meaning that the neutral-current process is much suppressed. The solution of Sheldon Lee Glashow, John Iliopoulos and Luciano Maiani (GIM) to the problem is the following: in addition to u, d, s quarks there should exist a c quark, and two quark doublets $\begin{pmatrix} u \\ d_c \end{pmatrix}$ and $\begin{pmatrix} c \\ s_c \end{pmatrix}$ where

$$\begin{bmatrix} d_c \\ s_c \end{bmatrix} = \begin{bmatrix} \cos \theta_C & \sin \theta_C \\ -\sin \theta_C & \cos \theta_C \end{bmatrix} \begin{bmatrix} d \\ s \end{bmatrix} \equiv V \begin{bmatrix} d \\ s \end{bmatrix}.$$

Obviously, $V^\dagger V = V V^\dagger = 1$ from which

$$\bar{d}_c d_c + \bar{s}_c s_c = \bar{d}d + \bar{s}s,$$

which means that writing the Lagrangian in terms of the rotated fields is equivalent to writing it using the original ones. In the latter case flavour changing neutral currents do not appear, so these must be absent also when we write the Lagrangian in terms of the rotated field. This prediction of the charm, based on the absence of FCNC (in 1970) was confirmed by the discovery of the particle J/ψ, a $c\bar{c}$ bound state (in 1974). The problem comes back at one loop if the c quark is too heavy, $m_c \gg 1\,\text{GeV}$. The two diagrams
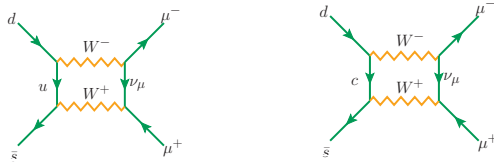
cancel because both are proportional to $\cos\theta_C \sin\theta_C$, but with different signs. This cancellation is incomplete if the second diagram is suppressed by m_c in the propagator $\frac{1}{p^2 - m_c^2}$, which happens when $m_c \gg 1\,\text{GeV}$, suggesting that the mass of the c quark should be around 1 GeV.

22.5   Fermion masses

We already discussed that explicit mass terms in the fermion sector would break $SU(2)\times U(1)$ invariance. However, we can introduce a gauge-invariant fermion-scalar couplings

$$
\mathcal{L}_Y = c_d \underbrace{\left(\bar{u}, \bar{d}\right)_{\text{L}} \begin{pmatrix} \phi^{(+)} \\ \phi^{(0)} \end{pmatrix}}_{\equiv \bar{\psi}_{\text{L}} \cdot \phi} d_{\text{R}} + c_u \left(\bar{u}, \bar{d}\right)_{\text{L}} \begin{pmatrix} \phi^{(0)*} \\ -\phi^{(+)*} \end{pmatrix} u_{\text{R}}
$$

$$
\text{(22.5.11)}
$$

$$
+ c_e \left(\bar{v}_e, \bar{e}\right)_{\text{L}} \begin{pmatrix} \phi^{(+)} \\ \phi^{(0)} \end{pmatrix} e_{\text{R}} + \text{h.c.},
$$

where the hermitian conjugate terms are abbreviated. For the leptons it is of the form $\bar{e}_{\text{R}} \left(\phi^{(-)}, \bar{\phi}^{(0)}\right) \begin{bmatrix} v_e \\ e \end{bmatrix}_{\text{L}}$ and these are similar for quarks (see exercise). The terms in $\mathcal{L}_Y$ are called Yukawa terms and the couplings c_d, c_u, c_e are called Yukawa couplings. An infinitesimal transformation is given by:

$$
\delta\bar{\psi}_{\text{L}} = \bar{\psi}_{\text{L}} \left(-\mathrm{i}\,\boldsymbol{T} \cdot \boldsymbol{\epsilon} - \mathrm{i}\,y_{\text{L}}\epsilon\right), \qquad \delta\phi = \left(\mathrm{i}\,\boldsymbol{T} \cdot \boldsymbol{\epsilon} + \frac{i}{2}\epsilon\right)\phi,
$$

so

$$\delta \left(\bar{\psi}_{\mathrm{L}} \cdot \phi \right) = \left[-i \, \boldsymbol{T} \cdot \boldsymbol{\epsilon} + i \, \boldsymbol{T} \cdot \boldsymbol{\epsilon} - i \, y_{\mathrm{L}} \epsilon + \frac{i}{2} \epsilon \right] \left(\bar{\psi}_{\mathrm{L}} \cdot \phi \right)$$

$$= -i \left(y_{\mathrm{L}} - \frac{1}{2} \right) \epsilon \left(\bar{\psi}_{\mathrm{L}} \cdot \phi \right)$$

where $y_{\mathrm{L}} = y_1 = y_3 + \frac{1}{2}$ (from Eq. (22.1.6)). Thus,

$$\left. \begin{array}{c} \delta \left(\bar{\psi}_{\mathrm{L}} \cdot \phi \right) = -i \, y_3 \epsilon \left(\bar{\psi}_{\mathrm{L}} \cdot \phi \right) \\ \delta \, d_{\mathrm{R}} = i \, y_3 \epsilon \, d_{\mathrm{R}} \end{array} \right\} \Rightarrow \delta \left[\left(\bar{\psi}_{\mathrm{L}} \cdot \phi \right) d_{\mathrm{R}} \right] = 0.$$

It is left as an exercise to check the gauge invariance of the second term, proportional to c_u. In a unitary gauge

$$\phi(x) = \frac{1}{\sqrt{2}} \begin{pmatrix} 0 \\ v + h(x) \end{pmatrix},$$

from which

$$\mathcal{L}_Y = \frac{1}{\sqrt{2}} (v + h(x)) \left[c_d \, \bar{d}_{\mathrm{L}} d_{\mathrm{R}} + c_u \, \bar{u}_{\mathrm{L}} u_{\mathrm{R}} + c_e \, \bar{e}_{\mathrm{L}} e_{\mathrm{R}} \right] + \text{h.c.}$$

We see that there are mass terms with $m_i = -\frac{c_i v}{\sqrt{2}}$ where $i = d, u, e$:

$$\mathcal{L}_Y = - \left(1 + \frac{h(x)}{v} \right) \left[m_d \, \bar{d}d + m_u \, \bar{u}u + m_e \, \bar{e}e \right].$$

The standard model predicts that *the coupling to the Higgs boson of the fermions is proportional to the fermion masses.* This prediction awaits experimental confirmation. The first direct measurements of Higgs-fermion couplings with large uncertainties are appearing at the time of writing this book.

Exercise 22.5

Let us define a conjugate field $\tilde{\phi}$ to the Higgs field ϕ by $\tilde{\phi} = i\tau_2 \phi^*$, where τ_2 is the second Pauli matrix, so $\tilde{\phi} = \begin{pmatrix} \phi^{(0)*} \\ -\phi^{(+)*} \end{pmatrix}$. Check that the infinitesimal transformation of $\tilde{\phi}$ under $SU(2)_L \times U(1)_Y$ is $\delta\tilde{\phi} = \left(i \, \boldsymbol{T} \cdot \boldsymbol{\epsilon} - \frac{i}{2}\epsilon \right) \tilde{\phi}$. Prove that the second term in Eq. (22.5.11) is invariant under $SU(2)_L \times U(1)_Y$, i.e. $\delta \left[\left(\bar{\psi}_L \cdot \tilde{\phi} \right) u_R \right] = 0$.

22.6 Flavour mixing

We have seen how the BEH mechanism, in addition to the gauge boson masses, generates masses for the fermions if there is one family. However, in the standard model there are three families. Let us explore if there are additional consequences of the BEH mechanism in this case. The most general Yukawa terms are

$$
\mathcal{L}_Y = \sum_{j,k} \left\{ \left(\bar{u}'_j, \bar{d}'_j \right)_L \left[c^{(d)}_{jk} \left(\begin{array}{c} \phi^{(+)} \\ \phi^{(0)} \end{array} \right) d'_{kR} + c^{(u)}_{jk} \left(\begin{array}{c} \phi^{(0)*} \\ -\phi^{(+)*} \end{array} \right) u'_{kR} \right] \right.
$$

$$
\left. + \left(\bar{v}'_j, \bar{l}' \right)_L c^{(l)}_{jk} \left(\begin{array}{c} \phi^{(+)} \\ \phi^{(0)} \end{array} \right) l'_{kR} \right\} + \text{h.c.} \qquad (22.6.12)
$$

where the fermion doublets are weak eigenstates and the couplings $c^{(i)}_{jk}$ are arbitrary elements of 3×3 matrices (in flavour space). After spontaneous symmetry breaking the Lagrangian becomes

$$
\mathcal{L}_Y = - \left(1 + \frac{h(x)}{\mathsf{v}} \right) \left\{ \bar{d}'_L \underline{M}'_d d'_R + \bar{u}'_L \underline{M}'_u u'_R + \bar{l}'_L \underline{M}'_l l'_R + \text{h.c.} \right\},
$$

where d', u' and l' are vectors in flavour space. The mass matrices are given by

$$
\left(M'_d \right)_{ij} = -c^{(d)}_{ij} \frac{\mathsf{v}}{\sqrt{2}}, \qquad \left(M'_u \right)_{ij} = -c^{(u)}_{ij} \frac{\mathsf{v}}{\sqrt{2}}, \qquad \left(M'_l \right)_{ij} = -c^{(l)}_{ij} \frac{\mathsf{v}}{\sqrt{2}}.
$$

Their diagonalization determines the mass eigenstates. If none of the fermion masses are zero (actually they are positive), $\underline{M}'$ is invertible. Furthermore, the flavour space is finite dimensional. Then $\underline{M}$ can be decomposed as

$$
\underline{M}' = \underline{H} \cdot \underline{U}
$$

where $\underline{U}\,\underline{U}^\dagger = \mathbb{1}$, $\underline{H} = \underline{H}^\dagger$ and $\underline{H}$ is positive definite. (A general $n \times n$ complex matrix has $2n^2$ independent real components, while both a unitary and a hermitian matrix has n^2 independent real components.) The hermitian matrix $\underline{H}$ can thus be diagonalized (its diagonal form is denoted by $\underline{M}$):

$$
\underline{M}' = \underline{S}^\dagger \underline{M}\, \underline{S}\, \underline{U},
$$

with $\underline{S}\,\underline{S}^\dagger = \mathbb{1}$ and $\underline{M}$ has positive diagonal entries:

$$
\begin{aligned}
\underline{M}_d &= \text{diag}\left(m_d, m_s, m_b \right), \\
\underline{M}_u &= \text{diag}\left(m_u, m_c, m_t \right), \\
\underline{M}_l &= \text{diag}\left(m_e, m_\mu, m_\tau \right).
\end{aligned}
$$

The mass eigenstates are

$$d_L = \underline{S}_d\, d'_L, \qquad u_L = \underline{S}_u u'_L, \qquad l_L = \underline{S}_l\, l'_L,$$
$$d_R = \underline{S}_d\, \underline{U}_d\, d'_R, \quad u_R = \underline{S}_u\, \underline{U}_u\, u'_R, \quad l_R = \underline{S}_l\, \underline{U}_l\, l'_R$$

and the Lagrangian becomes

$$\mathcal{L}_Y = -\left(1 + \frac{h(x)}{\mathsf{v}}\right)\left(\bar{d}\underline{M}_d\, d + \bar{u}\underline{M}_u\, u + \bar{l}\underline{M}_l\, l\right).$$

The matrices $\underline{S}$ and $\underline{S}\,\underline{U}$ are unitary. Thus

$$\bar{\psi}'_L \cdot \psi'_L = \bar{\psi}_L \cdot \psi_L \qquad \bar{\psi}'_R \cdot \psi'_R = \bar{\psi}_R \cdot \psi_R$$

where $\psi = d, u$ or l. Therefore, the absence of flavour changing neutral currents is preserved (this goes under the name of generalized GIM-mechanism). For charged currents

$$\bar{u}'_L d'_L = \bar{u}_L \underline{S}_u\, \underline{S}^\dagger_d d_L \equiv \bar{u}_L \underline{V}\, d_L,$$

where $\underline{V} = \underline{S}_u\, \underline{S}^\dagger_d$ is the Cabibbo-Kobayashi-Maskawa (CKM) matrix[2] that couples u-type quarks with d-type quarks. Although, $\underline{V}\,\underline{V}^\dagger = \mathbb{1}$, $\underline{V}$ is different from the identity matrix because $\underline{S}_u \neq \underline{S}_d$. The CKM matrix appears in $\mathcal{L}_{CC}$ when written in terms of mass eigenstates instead of weak eigenstates:

$$\mathcal{L}_{CC} = \frac{g}{2\sqrt{2}} W^+_\mu \left[\sum_{ij} \bar{u}_i \gamma^\mu (1 - \gamma_5)\, \underline{V}_{ij}\, d_j + \sum_\ell \bar{\nu}_\ell \gamma^\mu (1 - \gamma_5)\, \ell \right] + \text{h.c.}.$$

The presence of the CKM matrix in the charged current interactions is a non-trivial prediction of the standard model even if the values of the matrix elements are unknown parameters.

In the standard model $m_\nu = 0$, thus we can rotate away $\underline{V}$ in the lepton sector by redefining the phases of neutrino flavours such that $\underline{S}_\nu = \underline{S}_\ell$. This is ruled out by the observed masses for neutrinos seen via neutrino oscillations, which we discuss in the next section.

The CKM matrix is a unitary 3×3 matrix. A general unitary matrix has 9 independent parameters: three real rotational angles (as for a general orthogonal matrix) and six complex phases. We can choose the phases of the six quarks freely, thus can absorb all but one (five) complex phases of

---

[2]Named after Nicola Cabibbo, Makoto Kobayashi, and Toshihide Maskawa.

the CKM matrix into the definition of the quark wave functions, which is reflected by the usual parametrization of the CKM matrix:

$$
\begin{aligned}
\underline{V} &= \begin{pmatrix} V_{ud} & V_{us} & V_{ub} \\ V_{cd} & V_{cs} & V_{cb} \\ V_{td} & V_{ts} & V_{tb} \end{pmatrix} \\
&= \begin{pmatrix} 1 & 0 & 0 \\ 0 & c_{23} & s_{23} \\ 0 & -s_{23} & c_{23} \end{pmatrix} \begin{pmatrix} c_{13} & 0 & s_{13}e^{i\delta} \\ 0 & 1 & 0 \\ -s_{13}e^{i\delta} & 0 & c_{13} \end{pmatrix} \begin{pmatrix} c_{12} & s_{12} & 0 \\ -s_{12} & c_{12} & 0 \\ 0 & 0 & 1 \end{pmatrix}
\end{aligned}
$$
(22.6.13)

where $c_{ij} = \cos\theta_{ij}$, $s_{ij} = \sin\theta_{ij}$ and $\delta \neq 0$ is the remaining phase. At the time of writing this book the experimental status of the CKM matrix is the following:

$$
|\underline{V}| =
\begin{pmatrix} 0.97446 \pm 0.00010 & 0.22452 \pm 0.00044 & (3.65 \pm 0.12) \cdot 10^{-3} \\ 0.22438 \pm 0.00044 & 0.97359^{+0.00010}_{-0.00011} & (42.14 \pm 0.76) \cdot 10^{-3} \\ (8.96^{+0.24}_{-0.33}) \cdot 10^{-3} & (41.33 \pm 0.74) \cdot 10^{-3} & 0.999105 \pm 0.000032 \end{pmatrix}.
$$
(22.6.14)

The one remaining phase is the signal of CP-violation, thus CP-violation is predicted in the standard model with three families. The observed CP-violation in the decay of kaons and B-mesons is in agreement with the prediction of the standard model, thus the inventors of the three-family CKM matrix, Makoto Kobayashi and Toshihide Maskawa were awarded the Nobel prize in physics in 2008. (The two-family version was invented by Nicola Cabibbo, hence the latter 'C', but that matrix is real, thus does not predict CP-violation.)

Exercise 22.6
Prove that the CKM-matrix is real if there are only two families.

22.7 Parameters and Feynman rules of the standard model

The predictive power of the standard model is strong because we can compute the probability of many elementary particle processes with high precision. However, in these computations we need the values of the input parameters of the standard model that have to be extracted from measured data. Therefore, it might be useful to collect the parameters of the standard model, even if they are partially correlated.

In the gauge and scalar sector there are five parameters: the three gauge couplings, g_s, g and g', the vacuum expectation value v of the BEH field and the mass of the Higgs particle M_H. All other parameters can be expressed as functions of these five:

$$M_W = \frac{1}{2} g v, \quad M_Z = \frac{1}{2}\sqrt{g^2 + g'^2}\, v, \quad \lambda = \frac{M_H^2}{2v^2}, \quad \tan\theta_W = \frac{g'}{g},$$

and $g \sin\theta_W = g' \cos\theta_W = e$. In practice we had better choose parameters that can be measured most precisely. These are Fermi's constant G_F, the electromagnetic coupling α_{em} and the mass of the Z^0 boson, M_Z. The relations

$$G_F = \frac{1}{\sqrt{2}v^2}, \quad \text{and} \quad \alpha_{em} = \frac{g^2 g'^2}{4\pi(g^2 + g'^2)}$$

imply that

$$v^2 = \frac{1}{\sqrt{2}G_F},$$

$$g^2 = 2\sqrt{2}\, M_Z^2\, G_F \left(1 + \sqrt{1 - \frac{4\pi\alpha_{em}}{\sqrt{2}M_Z^2\, G_F}}\right),$$

$$g'^2 = 2\sqrt{2}\, M_Z^2\, G_F \left(1 - \sqrt{1 - \frac{4\pi\alpha_{em}}{\sqrt{2}M_Z^2\, G_F}}\right)$$

in the range $\tan\theta_W < 1$.

In the fermion sector the input parameters are the Higgs-Yukawa couplings. It is not simple to count the independent ones among them. Therefore, assuming n fermion families, we consider the $3n$ fermion masses[3] and

---

[3]Two quarks and one charged lepton are massive in each family – the neutrinos are massless in the standard model.

the $(n-1)^2$ independent elements of the CKM-matrix as input parameters. Thus for $n = 3$ the number of input parameters is $5 + 3 \cdot 3 + 2^2 = 18$. We have neglected the Θ coupling that characterizes the QCD vacuum as the experimental upper bound is very small.

Feynman rules

We list the Feynman rules of electroweak interactions in unitary gauge, using the notation of Sect. 18.4:[4]

- Cubic gauge field interactions $V_{1,\alpha} V_{2,\beta} V_{3,\gamma}$ (with all-incoming kinematics, $p^\mu + q^\mu + r^\mu = 0$): $\Gamma_{\alpha,\beta,\gamma}(p,q,r) = ieC V_{\alpha,\beta,\gamma}(p,q,r)$ where $V_{\alpha,\beta,\gamma}(p,q,r) = (p-q)_\gamma\, g_{\alpha\beta} + (q-r)_\alpha\, g_{\beta\gamma} + (r-p)_\beta\, g_{\alpha\gamma}$ is the same function as in QCD, while C depends on the type of the gauge boson participating in the interaction:

$V_1 V_2 V_3$	C
$\gamma W^+ W^-$	1
$Z W^+ W^-$	$\dfrac{\cos\theta_W}{\sin\theta_W}$

- Quartic gauge field interactions $V_{1,\alpha} V_{2,\beta} V_{3,\gamma} V_{4,\delta}$: $\Gamma_{\alpha,\beta,\gamma,\delta} = ie^2 C\left[2g_{\alpha\beta}g_{\gamma\delta} - g_{\alpha\gamma}g_{\beta\delta} - g_{\alpha\delta}g_{\beta\gamma}\right]$, C again depends on the type of the gauge boson participating in the interaction:

$V_1 V_2 V_3 V_4$	C
$W^+ W^+ W^- W^-$	$\dfrac{1}{(\sin\theta_W)^2}$
$W^+ W^- Z Z$	$-\left(\dfrac{\cos\theta_W}{\sin\theta_W}\right)^2$
$W^+ W^- \gamma Z$	$-\dfrac{\cos\theta_W}{\sin\theta_W}$
$W^+ W^- \gamma\gamma$	-1

[4]We focus on the interaction vertices only as the propagators of the various fields were already presented earlier, those of the photon and charged leptons in the section on QED, those of the massless scalar and quarks among the QCD Feynman rules and those of the massive gauge bosons in Sect. 22.2. Finally, the denominator in the propagator of a massive scalar is the same as for the massive gauge boson, while its numerator coincides with that for the massless scalar. Some authors use opposite sign convention for the massive gauge bosons as we do (e.g. Ref. [Denner, 1993]). As a result, their vertices have opposite signs if odd number of massive gauge bosons are involved, which does not influence values of observable quantities.

- Cubic Higgs interaction: ieC where

$$C = -\frac{3M_H^2}{2\sin\theta_W M_W} \ .$$

- Quartic Higgs interactions: $ie^2 C$ where

$$C = -\frac{3M_H^2}{4(\sin\theta_W)^2 M_W^2} \ .$$

- Cubic gauge field-Higgs interactions $V_{1,\alpha}V_{2,\beta}H$: $ieg_{\alpha\beta}C$ where C depends on the type of the gauge boson participating in the interaction:

$V_1 V_2 H$	C
$W^+ W^- H$	$\dfrac{M_W}{\sin\theta_W}$
ZZH	$\dfrac{M_W}{\sin\theta_W(\cos\theta_W)^2}$

- Quartic gauge field-Higgs interactions $V_\alpha V_\beta HH$: $ie^2 g_{\alpha\beta}C$ where C depends on the type of the gauge boson participating in the interaction:

$V_1 V_2 HH$	C
$W^+ W^+ HH$	$\dfrac{1}{2(\sin\theta_W)^2}$
$ZZHH$	$\dfrac{1}{2(\cos\theta_W \sin\theta_W)^2}$

- Gauge field-fermion interactions $V_\alpha \bar{f}_i f_j$: $-ie\gamma_\alpha(C^- P_- + C^+ P_+)$ where $C^\pm$ depend on the type of the gauge boson participating in the interaction, the flavour f of fermions and family number i and j:

$V\bar{f}_i f_j$	C^+	C^-
$\gamma \bar{f}_i f_j$	$e_f \delta_{ij}$	$e_f \delta_{ij}$
$Z \bar{f}_i f_j$	$g_f^+ \delta_{ij}$	$g_f^- \delta_{ij}$
$W^+ \bar{u}_i d_j$	0	$\dfrac{1}{\sqrt{2}\sin\theta_W}V_{ij}$
$W^- \bar{d}_j u_i$	0	$\dfrac{1}{\sqrt{2}\sin\theta_W}V_{ij}^\dagger$
$W^+ \bar{\nu}_i \ell_j$	0	$\dfrac{1}{\sqrt{2}\sin\theta_W}\delta_{ij}$
$W^- \bar{\ell}_j \nu_i$	0	$\dfrac{1}{\sqrt{2}\sin\theta_W}\delta_{ij}$

where

$$g_f^+ = -\frac{\sin\theta_W}{\cos\theta_W}e_f, \qquad g_f^- = \frac{T_f^3 - \sin\theta_W^2 e_f}{\sin\theta_W \cos\theta_W}.$$

- Higgs-fermion interaction $H\bar{f}_i f_j$: ieC where

$$C = -\delta_{ij}\frac{1}{2\sin\theta_W}\frac{m_{f,i}}{M_W}.$$

The relations between the vector, axial-vector couplings of the Z boson and the $g_f^\pm$ couplings read as

$$\frac{v_f}{2\sin\theta_W\cos\theta_W} = \frac{1}{2}\left(g_f^- + g_f^+\right) = \frac{T_f^3 - 2(\sin\theta_W)^2 e_f}{2\sin\theta_W\cos\theta_W},$$

$$\frac{a_f}{2\sin\theta_W\cos\theta_W} = \frac{1}{2}\left(g_f^- - g_f^+\right) = \frac{T_f^3}{2\sin\theta_W\cos\theta_W}.$$

22.8 Neutrino mixing and oscillation

If neutrinos also have masses, $m_\nu \neq 0$, then a mixing matrix , similar to the CKM matrix, appears also in the charged currents of leptons. Such a matrix is called Pontecorvo-Maki-Nakagawa-Sakata (PMNS) matrix.[5] According to the standard notation, instead of $\underline{S}_\nu$ used in conjunction of the BEH field, we write

$$|\nu_m\rangle = \sum_f U_{fm}|\nu_f\rangle, \qquad |\nu_f\rangle = \sum_m U_{fm}^*|\nu_m\rangle \qquad (22.8.15)$$

where $|\nu_m\rangle$ denotes the mass eigenstates ($m = 1, 2, 3$), while $|\nu_f\rangle$ corresponds to the flavour eigenstates ($f = e, \mu, \tau$). The kets are vectors in the space of free neutrinos. For anti-neutrinos the mixing reads as

$$|\bar{\nu}_m\rangle = \sum_f U_{fm}^*|\bar{\nu}_f\rangle, \qquad |\bar{\nu}_f\rangle = \sum_m U_{fm}|\bar{\nu}_m\rangle. \qquad (22.8.16)$$

The PMNS matrix is a unitary (3×3) matrix. In the general case it has nine independent parameters: three real rotations (just like in a (3×3) orthogonal matrix) and six complex phases. If the neutrinos are Dirac

---

[5]Named after pioneering researchers Bruno Pontecorvo, Ziro Maki, Masami Nakagawa and Soichi Sakata.

fermions, then five phases can be absorbed into the state vectors of charged leptons, as for quarks, so only one phase remains. In such cases the usual parametrization of the PMNS matrix is the same as for the CKM matrix in (Eq. (22.6.13)), $\underline{U} = \underline{V}$, with $c_{fm} = \cos\theta_{fm}$, $s_{fm} = \sin\theta_{fm}$ and $\delta \neq 0$, is the CP-violating phase. In case of Majorana neutrinos ($\nu \equiv \bar{\nu}$), $\underline{U} = \underline{V}\underline{P}$ where $\underline{P} = \mathrm{diag}\left(1, e^{\mathrm{i}\frac{\alpha_{21}}{2}}, e^{\mathrm{i}\frac{\alpha_{31}}{2}}, \ldots, e^{\mathrm{i}\frac{\alpha_{n-1}}{2}}\right)$, ($n$ is the number of Majorana neutrinos that can be different from 3). We do not know the physical origin of the PMNS matrix. According to experimental observations charged leptons do not mix, but neutrinos may mix. If they do so, then the matrix $\underline{S}_\nu = \underline{U}_{\text{PMNS}}$ is an analogue of the CKM matrix. In charged currents flavour eigenstates participate (those are created and annihilated). In high-energy scattering experiments of particles the masses of neutrinos are negligible. Our measurements are by far not sufficiently precise to measure any effect of neutrino masses.

Neutrinos are stable particles due to their small masses and weak interactions with other particles. Thus, they exist in asymptotically free states. Moreover, according to observations and depending on the question we raise, we can use a macroscopic, point-like particle approach in describing their motion. For instance, we can measure the speed of electrons directly using time-of-flight measurements and thus their masses if we know their energies. Therefore, it depends on the question which description is the most convenient: (i) classical, (ii) quantum mechanical, (iii) or quantum field theoretical. As a matter of fact, neutrinos show classical, quantum and relativistic features, similarly to electrons.

A characteristic quantum phenomenon is the double-slit interference with particles. For example, even single photons or electrons produce the characteristic interference lines if we let sufficiently many pass (one by one) through the two slits. These "characteristic" interference lines are those that are also produced by a plane wave of light. Such light is the classical manifestation of an ensemble of plane wave photons.

Similar quantum mechanical phenomenon is the oscillation of neutrinos, which is *interference in flavour space*. If neutrinos have different masses, then their phases change differently as they travel the distance L between the source and the detector. As a result flavour interference occurs, called *neutrino oscillation*. We do not measure L, the time T needed to travel the distance L, the energy E and momentum p of each individual neutrino, but we measure their average values in a neutrino beam. Thus, we use the plane wave approximation as for classical (beam of) light, $|\nu_m(\vec{x}, t)\rangle =$

$e^{-i\phi_m(\vec{x},t)}|\nu_m(0,0)\rangle$ where the phase is $\phi_m(\vec{x},t) = (E_m t - \vec{p}_m \cdot \vec{x})/\hbar$.[6] We assume that the neutrinos move along the x-axis inertially and we use the abbreviation $|\vec{p}_m| \equiv p_m$. According to the dispersion relation $E_m^2 = p_m^2 c^2 + m_m^2 c^4$. If $m_1 \neq m_2$, then the neutrinos travelling in time T a distance L will arrive with different phase,

$$\hbar\Delta\phi_{12} = (E_1 T - p_1 L) - (E_2 T - p_2 L) = \Delta E T - \Delta p L$$

$$= \frac{\Delta E^2}{E_1 + E_2} T - \frac{\Delta p^2}{p_1 + p_2} L = \frac{L}{2}\left(\frac{\Delta E^2}{\langle E \rangle}\frac{T}{L} - \frac{\Delta p^2}{\langle p \rangle}\right). \qquad (22.8.17)$$

The speed of the neutrinos in the laboratory frame V is $v = L/T$ and $p = \gamma m v = E v/c^2$ ($\gamma(v) = (1 - v^2/c^2)^{-1/2}$). Thus $E/T = pc^2/L$. This ratio is Lorentz-invariant because in a frame V' moving with speed u in V,

$$E' = \gamma(u)(E - up) = \gamma(u)E(1 - uv/c^2),$$

$$T' = \gamma(u)(T - uL/c^2) = \gamma(u)T(1 - uv/c^2),$$

which means that $E/T = E'/T'$. As a result, in all inertial reference frames $T/L = E/(pc^2)$.

In real experiments it is easier to measure L (instead of T) so we write the phase difference as

$$\Delta\phi_{12} = \frac{L}{2\hbar}\left(\frac{\Delta E^2}{\langle E \rangle}\frac{\langle E \rangle}{\langle pc^2 \rangle} - \frac{\Delta p^2}{\langle p \rangle}\right) = \frac{L}{2\hbar c^2}\left(\frac{\Delta(E^2 - pc^2)}{\langle p \rangle}\right) = \frac{\Delta m_{12}^2 c^4}{2\hbar c^2 \langle p \rangle}L. \qquad (22.8.18)$$

Such a phase difference can lead to a change of neutrino flavour. The probability of the change $\nu_f \to \nu_{f'}$ is

$$P(\nu_f \to \nu_{f'}) = |\langle \nu_{f'}|\nu_f(t)\rangle|^2 = \left|\sum_{m,n} U_{f'm}U_{fn}^* e^{-i\phi_n}\langle \nu_m|\nu_n\rangle\right|^2$$

$$= \left|\sum_m U_{f'm}U_{fm}^* e^{-i\phi_m}\right|^2. \qquad (22.8.19)$$

In order to compute the sum, let us first consider the simplified case of two

---

[6]In this section–as opposed to the rest of the book–we use SI instead of natural units so $\hbar$ and c appears explicitly.

summands ($\Delta\phi = \phi_1 - \phi_2$):

$$(u_1 e^{i\phi_1} + u_2 e^{i\phi_2})(u_1^* e^{-i\phi_1} + u_2^* e^{-i\phi_2}) = |u_1|^2 + |u_2|^2 + u_1 u_2^* e^{i\Delta\phi} + u_1^* u_2 e^{-i\Delta\phi}$$

$$= |u_1|^2 + |u_2|^2 + 2\mathrm{Re}(u_1 u_2^*)\cos(\Delta\phi) - 2\mathrm{Im}(u_1 u_2^*)\sin(\Delta\phi)$$

$$= |u_1 + u_2|^2 - 4\mathrm{Re}(u_1 u_2^*)\sin^2\left(-\frac{\Delta\phi}{2}\right) + 2\mathrm{Im}(u_1 u_2^*)\sin(-\Delta\phi).$$

$$(22.8.20)$$

Generalization to $n \geq 2$ leads to the usual form of neutrino oscillation probability,

$$P(\nu_f \to \nu_{f'}) = \delta_{f'f} - 4\sum_n \sum_{m>n} \mathrm{Re}(U_{fm}^* U_{f'm} U_{fn} U_{f'n}^*)\sin^2\left(\frac{\Delta\phi_{mn}}{2}\right)$$

$$+ 2\sum_n \sum_{m>n} \mathrm{Im}(U_{fm}^* U_{f'm} U_{fn} U_{f'n}^*)\sin(\Delta\phi_{mn}).$$

$$(22.8.21)$$

For Dirac neutrinos, if the complex phase in the PMNS matrix vanishes, $\delta = 0$ (no CP-violation in the neutrino sector), then the PMNS matrix is real and the last term vanishes in Eq. (22.8.21). In this case the only source of neutrino oscillation is the second term, in which the square of the sinus is periodic in π. Therefore, it is useful to rewrite its argument as

$$\frac{\Delta\phi_{mn}}{2} = \pi\frac{L}{L_{mn}^{(r)}}$$

where

$$L_{mn}^{(r)} = \frac{2hc^2\langle p\rangle}{\Delta m_{mn}^2 c^4} = \frac{2hc\langle E\rangle}{\Delta m_{mn}^2 c^4}\frac{\langle p\rangle c}{\langle E\rangle}$$

is the characteristic length of oscillation. In oscillation experiments one can usually measure the energy of the neutrinos and they travel with the speed of light in vacuum. (Their energy is more than 1 MeV, while their masses are smaller than 1 eV.) So it is more convenient to use the second form, in which $\langle p\rangle c/\langle E\rangle \simeq 1$ so it is natural to drop it.

We obtain another form if we substitute $L_{mn}^{(r)}$ expressed as a function of the neutrino energy,

$$\frac{\Delta\phi_{mn}}{2} = \frac{\pi}{2}\frac{\Delta m_{mn}^2 c^4}{hc\langle E\rangle}L.$$
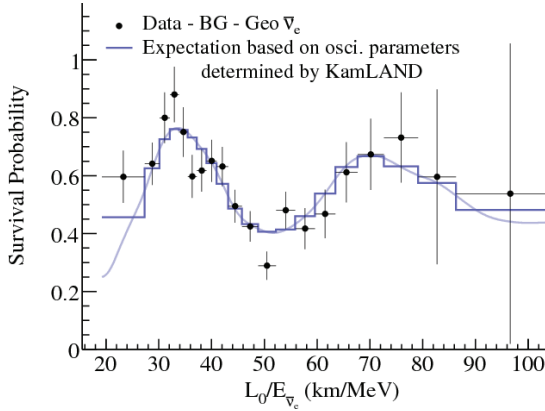
Figure 22.3: Results of the KamLAND experiment compared to the theory of neutrino oscillation (solid line).

As $hc \simeq 1.24 \cdot 10^{-9}$ eV km, and $\pi/2.48 \simeq 1.27$, then

$$\frac{\Delta\phi_{mn}}{2} = \frac{\pi}{2}\frac{\Delta m_{mn}^2 c^4}{hc\langle E\rangle}L \simeq 1.27\frac{\Delta m_{mn}^2 c^4}{\text{eV}^2}\frac{\text{GeV}}{\langle E\rangle}\frac{L}{\text{km}},$$

while the oscillation length is

$$L^{(r)} = 2.48\,\text{km}\frac{\langle E \text{ or } pc\rangle}{\text{GeV}}\frac{\text{eV}^2}{\Delta m^2 c^4} = 2.48\,\text{m}\frac{\langle E \text{ or } pc\rangle}{\text{MeV}}\frac{\text{eV}^2}{\Delta m^2 c^4}.$$

Finally, using natural units, we obtain

$$\frac{\Delta\phi_{mn}}{2} = \frac{\Delta m_{mn}^2}{4\langle E \text{ or } p\rangle}L.$$

Neutrinos can show interference in flavour space because they remain coherent over long distances due to their weak interactions. Thus, the plane-wave approximation can be applied. The experiments are performed with neutrino beams. Oscillation experiments confirm our formula for neutrino oscillation (see Fig. 22.3) within the uncertainty of the data. Neutrino oscillation was observed in the following experiments:[7]

---

[7]The 2015 Nobel prize in physics was awarded to Profs. Takaaki Kajita and Arthur B. McDonald for the discovery of neutrino oscillations.

- the difference between the observed and expected rates of atmospheric neutrinos in the high-statistics data of the Super-Kamiokande experiment;

- reduced event numbers as compared to expectations in radio-chemical neutrino experiments (Chlorine, Galley/GNO, SAGE) and number of observed events depending on time and energy at Super-Kamiokande, SNO and Borexino;

- decrease of muon neutrinos and increase of electron neutrinos in far-detector experiments (MINOS, T2K: Tokai to Kamioka, NOνA);

- disappearance of electron anti-neutrinos in not too far and close detector experiments (Daya Bay, Chooz, RENO)

- change of spectra of electron anti-neutrinos in far detector experiment (KamLAND).

All these experimental observations prove that neutrinos have masses and the lepton flavour number is not conserved, which calls clearly for *explanation beyond the standard model*.

In the near future the most important tasks in the neutrino sector from the experimental side is to measure the mass of the neutrinos and the parameters of the PMNS mixing matrix. At present we have (sometimes contradictory) experimental information only for the sum of the neutrino masses. From cosmological observations the current conservative upper bound is $\sum_{i=1}^{3} m_i \leq 0.23$ eV. From oscillation experiments we know two squared mass differences, δm^2 and Δm^2, with the latter being about thirty times larger than the former. We conclude that there are two mass eigenstates of approximately equal masses (one of which can even vanish), while the third one has much different mass. However, we do not know if the very different mass is much bigger than the other two, called *normal hierarchy* (NH), or much smaller than the other two, called *inverse hierarchy* (IH).

The further parameters of neutrino oscillation are the mixing angles θ_{ij} and the complex phase δ of the PMNS matrix. In the oscillation formula $\sin^2 \theta_{ij}$ appears, therefore those are measured directly.

The PMNS matrix, obtained from a global fit of the parameters to data, (at 99 % confidence level) [Esteban et al., 2017] is the following:

$$|\underline{U}| = \begin{pmatrix} 0.800 - 0.844 & 0.515 - 0.581 & 0.139 - 0.155 \\ 0.229 - 0.516 & 0.438 - 0.699 & 0.614 - 0.790 \\ 0.249 - 0.528 & 0.462 - 0.713 & 0.595 - 0.776 \end{pmatrix}.$$

Compare these numbers with the precision of the parameters of the CKM matrix in (Eq. (22.6.14)). From the experimental point of view the main difficulty is to improve the precision of the parameters. From the theoretical point of view the challenge is to understand the origin of the PMNS matrix (or in popular terms "to understand the origin of neutrino masses") and why it is so different from the CKM matrix. We do not know the answer to these theoretical questions, but we can state with certainty that in order to answer them, we have to go beyond the standard model of particle interactions.

22.9 Anomaly cancellation

Our final topic is a key feature of the SM, which is generally expected from any QFT model of particle physics beyond the standard model. We do not present all details of the computations, but those that are needed to understand the concept of anomaly cancellation. The rest is left for exercise.

Let us consider a theory with both vector and axial-vector interactions, such as the standard model. W^μ is a gauge field. The current $J_\mu \propto \bar\psi \gamma_\mu \psi$ is a classically conserved vector current, $\partial^\mu J_\mu = 0$. The amplitude for the process
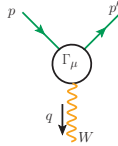
is proportional to $W_\mu \Gamma^\mu$, where $\Gamma^\mu = \langle p' | J^\mu | p \rangle$. The matrix element of the divergence of the current is

$$\langle p' | \partial^\mu J_\mu | p \rangle = (p' - p)^\mu \langle p' | J_\mu | p \rangle = \langle p' | q^\mu J_\mu | p \rangle = 0.$$

Thus $q^\mu J_\mu = 0$, which is the form of the vector Ward identity.

$J_\mu^5 = \bar\psi \gamma_\mu \gamma_5 \psi$ is a classical axial current for which

$$i\gamma_\mu \partial^\mu \psi = m\psi \implies -\gamma_\mu \partial^\mu \psi = i\, m\psi$$

$$-i\partial_\mu \bar\psi \gamma^\mu = m\bar\psi \implies \partial^\mu \bar\psi \gamma_\mu = i\, m\bar\psi .$$

We multiply the first equation with $\bar\psi \gamma^5$ from left and the second one with $\gamma^5 \psi$ from right and add the two equations. Using the anti-commutation relation $\{\gamma^5, \gamma^\mu\} = 0$, we obtain

$$\partial^\mu J_\mu^5 = 2i\, m\bar\psi \gamma_5 \psi \equiv 2m\, J_5 ,$$

which vanishes if $m = 0$, implying conserved axial current at tree level. The Feynman diagrams that contribute to Γ_μ and Γ_μ^5 at higher orders are
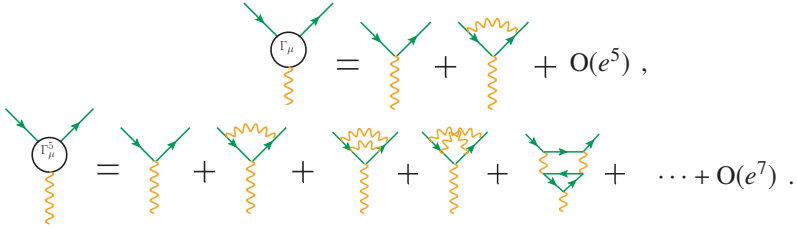
The last diagram[8] which contributes to Γ_μ^5 violates the conservation of the axial current. We define

$$T_{\kappa\lambda\mu}(p_1, p_2) = S_{\kappa\lambda\mu}(p_1, p_2) + S_{\lambda\kappa\mu}(p_2, p_1)$$

where
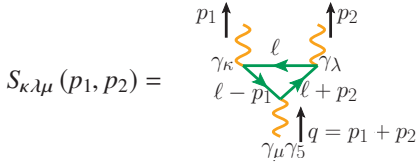
$$S_{\kappa\lambda\mu}(p_1, p_2) =$$

and we expect the following Ward identities

$$\begin{aligned}
\text{axial:} && q^\mu T_{\kappa\lambda\mu} &= 0, \\
\text{vector:} && p_1^\kappa T_{\kappa\lambda\mu} &= 0, \\
\text{vector:} && p_2^\kappa T_{\kappa\lambda\mu} &= 0.
\end{aligned}$$

$S_{\kappa\lambda\mu}$ is given by (omitting coupling factors)

$$S_{\kappa\lambda\mu}(p_1, p_2) \propto -(-i)^3$$

$$\times \int \frac{d^4\ell}{(2\pi)^4} \text{Tr}\left(\gamma_\mu\gamma_5 \frac{i}{\slashed{\ell} - \slashed{p}_1 - m} \gamma_\kappa \frac{i}{\slashed{\ell} - m} \gamma_\lambda \frac{i}{\slashed{\ell} + \slashed{p}_2 - m} \right)\Bigg|_{m=0}$$

$$= -\int \frac{d^4\ell}{(2\pi)^4} \frac{\text{Tr}\left[\gamma_\mu\gamma_5 \left(\slashed{\ell} - \slashed{p}_1\right) \gamma_\kappa \slashed{\ell} \gamma_\lambda \left(\slashed{\ell} + \slashed{p}_2\right) \right]}{(\ell - p_1)^2 (\ell + p_2)^2 \ell^2}.$$

---

[8]This diagram represents two diagrams: itself and another with one of the fermion arrows reversed.

Using

$$q^\mu \gamma_\mu \gamma_5 = \left[\ell + \not{p}_2 - \left(\ell - \not{p}_1 \right) \right] \gamma_5 = \left(\ell + \not{p}_2 \right) \gamma_5 + \gamma_5 \left(\ell - \not{p}_1 \right)$$

and $\not{p}\not{p} = p^2 \mathbb{1}$, we find

$$q^\mu S_{\kappa\lambda\mu} (p_1, p_2) = - \int \frac{d^4\ell}{(2\pi)^4} \, \mathrm{Tr} \left[\gamma_5 \frac{\left(\ell - \not{p}_1 \right) \gamma_\kappa \ell \gamma_\lambda}{(\ell - p_1)^2 \, \ell^2} + \gamma_5 \frac{\gamma_\kappa \ell \gamma_\lambda \left(\ell + \not{p}_2 \right)}{(\ell + p_2)^2 \, \ell^2} \right].$$

We now shift ℓ by p_1: $\ell \rightarrow \ell + p_1$ in the first term and use $\gamma_\lambda \gamma_5 = -\gamma_5 \gamma_\lambda$ to obtain

$$q^\mu S_{\kappa\lambda\mu} (p_1, p_2) = \int \frac{d^4\ell}{(2\pi)^4} \mathrm{Tr} \left[\gamma_5 \frac{\gamma_\lambda \ell \gamma_\kappa \left(\ell + \not{p}_1 \right)}{\ell^2 \, (\ell + p_1)^2} - \gamma_5 \frac{\gamma_\kappa \ell \gamma_\lambda \left(\ell + \not{p}_2 \right)}{\ell^2 \, (\ell + p_2)^2} \right]$$

$$= -q^\mu S_{\lambda\kappa\mu} .$$

Thus

$$q^\mu T_{\kappa\lambda\mu} (p_1, p_2) = 0$$

provided the shift is allowed. However, the integral is divergent, so the shift may be forbidden. For instance, with a cut-off regularization the momentum shift leads to a finite term which is different from zero. Use of dimensional regularization looks better as then the momentum shift is allowed. Nevertheless, the ambiguity remains also in this case, but disguised in a different form: in $d \neq 4$ dimensions γ_5 is ambiguous (γ_5 is intrinsically 4-dimensional). The 't Hooft-Veltman prescription says for $\gamma_5 = i\gamma_0\gamma_1\gamma_2\gamma_3$ in $d \neq 4$ dimensions

$$\{\gamma_\mu, \gamma_5\} = 0 \qquad \text{for} \quad \mu = 0, 1, 2, 3$$
$$[\gamma_\mu, \gamma_5] = 0 \qquad \text{for other values of } \mu.$$

We now recompute $q^\mu S_{\kappa\lambda\mu} (p_1, p_2)$ with this prescription. Let $\ell_\mu = \tilde{\ell}_\mu + \hat{\ell}_\mu$ where $\tilde{\ell}_\mu$ has $\mu = 0, 1, 2, 3$ components and $\hat{\ell}_\mu$ has components in the other $d - 4$ dimensions. With $p_i^\mu = \tilde{p}_i^\mu$ (external momenta kept in $d = 4$) and

$$q^\mu \gamma_\mu \gamma_5 = \left(\ell + \not{p}_2 \right) \gamma_5 + \gamma_5 \left(\ell - \not{p}_1 \right) - 2\gamma_5 \hat{\ell} = \left(\ell + \not{p}_1 \right) \gamma_5 + \gamma_5 \left(\ell - \not{p}_2 \right) - 2\gamma_5 \hat{\ell},$$

we find

$$q^\mu T_{\kappa\lambda\mu} (p_1 + p_2) \propto 2 \int \frac{d^d\ell}{(2\pi)^d} \, \mathrm{Tr} \left[2\gamma_5 \hat{\ell} \frac{\ell - \not{p}_1}{(\ell - p_1)^2} \gamma_\kappa \frac{\ell}{\ell^2} \gamma_\lambda \frac{\ell + \not{p}_2}{(\ell + p_2)^2} \right],$$

which has 5 terms. The only one that does not vanish, after integrations gives

$$4\,(-4\mathrm{i})\,\epsilon_{\alpha\beta\kappa\lambda}\,p_1^\alpha\,p_2^\beta \int \frac{\mathrm{d}^d\ell}{(2\pi)^d}\frac{\ell^2}{\ell^2\,(\ell-p_1)^2\,(\ell+p_2)^2} =$$

$$= -16\mathrm{i}\,\epsilon_{\alpha\beta\kappa\lambda}\,p_1^\alpha\,p_2^\beta\,\frac{d-4}{d}I^{(2)}(p_1+p_2)$$

$$= \frac{1}{2\pi^2}\,\epsilon_{\alpha\beta\kappa\lambda}\,p_1^\kappa\,p_2^\lambda + O(\epsilon).$$

Dimensional regularization respects the vector Ward identities, but the axial-vector Ward identity is violated at one loop. *There is no regularization which respects both vector and axial-vector Ward identities simultaneously.* We prefer to keep the vector Ward identities, which is an expression of insisting on gauge invariance. The axial-vector Ward identity is then violated, which is called *axial anomaly*. It is supported by the observed decay rate $\Gamma\left(\pi^0 \to \gamma\gamma\right) = (7.7 \pm 0.6)$ eV. The chiral symmetry forbids $\pi^0 \to \gamma\gamma$ at tree level, but the anomaly triangle diagrams predict

$$\Gamma\left(\pi^0 \to \gamma\gamma\right) = \left(\frac{N_c}{3}\right)^2 \frac{\alpha^2 m_\pi^2}{64\pi^3 f_\pi} = 7.73\ \text{eV},$$

hence the *anomaly is physical* and can be measured. According to the Adler-Bardeen theorem

axial anomaly receives only 1-loop contributions.

A gauge anomaly destroys the renormalizability of a quantum field theory. $G = SU(2)_\mathrm{L} \times U(1)_Y$ is chiral, so axial anomalies are present and dangerous; they should exactly cancel. In $SU(2)_\mathrm{L} \times U(1)_Y$ the triangle diagrams also contain the generators of the gauge group and the total anomaly is proportional to the trace of

$$T^{a_1}T^{a_2}T^c + T^{a_2}T^{a_1}T^c = \{T^{a_1}, T^{a_2}\}\,T^c$$

for a given fermion in the loop (T^c is the generator at the vertex with $\gamma_\mu\gamma_5$). The generators are $T^a = \frac{\tau_a}{2}$ or y_a with anti-commutation relations

$$\{\tau_i, \tau_j\} = 2\delta_{ij}, \quad \{y_i, y_j\} = 2y_i\,y_j.$$

Then

$$\mathrm{Tr}\left(\{T^{a_1}, T^{a_2}\}\,\tau_c\right) \propto \mathrm{Tr}\left(\tau_c\right) = 0$$

for both $T^a = \frac{\tau_a}{2}$ and y_a, while

$$\text{Tr}\left(\{T^{a_1}, T^{a_2}\}\, y_c\right) \propto \delta^{a_1 a_2}\, Q_c,$$

or

$$\text{Tr}\left(\{y^{a_1}, y^{a_2}\}\, y_c\right) \propto Q_c \qquad \left(\text{Tr}\,(y_c) = \text{Tr}\,(Q_c) \propto Q_c\right)$$

Based on these considerations the total contribution in a family is proportional to $Q_e + Q_\nu + N_c\,(Q_u + Q_d) = -1 + 0 + 3\left(\frac{2}{3} - \frac{1}{3}\right) = 0$ for left-handed members. For right-handed members $Q_\nu = 0$ is absent from the sum. Consequently, the axial anomaly cancels in the standard model. Any theory beyond the standard model should also have this cancellation if we want a renormalizable model.

Chapter 23

Outlook

In the theoretical part of this book we emphasized that QCD radiative corrections play an essential role in understanding the structure of the theory, interpreting data and finding signatures of new physics that cannot be explained by the standard model. The theory of radiative corrections in the electroweak part of the standard model is equally important though the effects are usually less pronounced. As a result, electroweak corrections have also been computed to many processes that play important role in particle phenomenology. These computations are technically challenging and the resulting corrections are usually much smaller than those of QCD, simply due to the large difference in the size of the couplings. Nevertheless, in certain kinematic regions as well as for interpreting the non-hadronic final states at the LEP experiments, taking such corrections into account is crucial.

As the LHC collides hadrons, the strong interaction has a role in every single interaction. As a thumb rule, we can state that the effect of first order electroweak corrections is similar to that of the second order QCD corrections. Thus in a computation at NNLO QCD accuracy ($O(\alpha_s^2)$ relative correction) the first order electroweak corrections ($O(\alpha)$ relative correction) should also be taken into account. Such computations are hampered by the mixed QCD and electroweak corrections at $O(\alpha_s\alpha)$ relative accuracy.

We put more emphasis on the computation of QCD corrections because their role of quantum corrections is qualitatively different in QCD than in the electroweak theory. In general QCD predictions at LO accuracy provide only an order of magnitude estimate due to the strong dependence on the unphysical scales. The NLO corrections are crucial in order to decrease the dependence on these scales. In order to estimate the accuracy of the scale

dependence one needs to know the NNLO corrections. As opposed to this, the electroweak theory gives a fairly good description of data already at LO accuracy (see for instance the predictions for the masses of vector bosons in Sect. 22.2). This description is improved by usually very little if we take into account the radiative corrections.

The relative importance of quantum corrections changes in collisions at energies larger than that of the LHC. Asymptotic freedom makes QCD corrections relatively smaller. The electroweak corrections may even increase due to increasing logarithmic contributions $\log M_V/s$ if s increases, which has the same numerical effect as decreasing M_V. In future experiments it will be interesting to see if any sign of restoration of the electroweak symmetry can be observed. In the symmetric phase the electroweak vector bosons are massless, just like the gluon. Then the electroweak theory will become similar to QCD, but with an important difference. In QCD Λ_{QCD} is a cut-off, below which perturbation theory cannot be applied (we use hadronization models). For the electroweak theory at large energies the perturbation theory works both below and above the electroweak scale v, but the techniques may change. At present there is very little known about what we should expect at future colliders in this respect.

There are many exciting developments and several big unanswered questions in the current research of particle physics. Among the big questions we mentioned the origin of neutrino masses. It is also an established experimental fact that most of the energy density in the universe is in a form that is different from the baryonic matter and electromagnetic radiation, whose physics we can test in the laboratory. The research to uncover the nature of dark matter and dark energy is flourishing at the time of writing this book. Another big question is our very existence, namely that the standard model predicts equal amount a matter and anti-matter, which is clearly not the case in the universe. The mechanism of breaking this symmetry is unknown. At present we do not even know whether the answer to these questions may come from colliders, or some other fields like cosmology or neutrino experiments.

There are also long standing as well as recently emerging anomalies in particle physics. The significance of these anomalies have not reached the discovery level of "five sigma", yet they are quite pronounced with deviations from standard model predictions in the 3–4 sigma range. Among the prominent ones we mentioned the long standing difference between the measured and computed value of the anomalous muon magnetic moment. Another interesting deviation concerns also the muon, which being the massive brother of the electron, can build muonic atoms if it is captured by a proton. Due to the much larger mass the average distance of the muon to

the proton is much smaller than that of the electron in the ordinary hydrogen atom. Thus it is more sensitive to the electric charge distribution inside the proton. The radius of the proton measured in muonic atoms differs from the radius measured in ordinary hydrogen.

Between writing and publishing this book several anomalies have been observed by the LHCb experiment at the LHC. These concern a fundamental assumption of the standard model that is known as *flavour universality* in the lepton sector. The second and third particle families assumed to be exact copies of the first one with only one exception, namely the particle masses. Therefore the standard model predicts that processes with identical initial state and with only difference in the final state in the type of leptons, such as $B^0 \rightarrow K^{*0}\mu^+\mu^-$ and $B^0 \rightarrow K^{*0}e^+e^-$) should occur with approximately equal probability. Quantitatively it means that the standard model predicts

$$R_{K^{*0}} = \frac{\mathcal{B}(B^0 \rightarrow K^{*0}\mu^+\mu^-)}{\mathcal{B}(B^0 \rightarrow K^{*0}e^+e^-)} \simeq 1 \qquad (23.0.1)$$

for the ratio of the branching fractions (the exact value depends on the value of the invariant mass squared q^2 of the charged lepton pair). Modern particle detectors can identify the leptons in the final state with high accuracy so such ratios can be measured fairly well. The results published by the LHCb collaboration [Aaij et al., 2017]

$$R_{K^{*0}} = \begin{cases} 0.66^{+0.11}_{-0.07}(\text{stat}) \pm 0.03(\text{syst}) \text{ for } 0.045 < q^2 < 1.1 \, \text{GeV}^2/c^4 \\[2mm] 0.69^{+0.11}_{-0.07}(\text{stat}) \pm 0.05(\text{syst}) \text{ for } 1.1 < q^2 < 6.0 \, \text{GeV}^2/c^4 \end{cases}$$
$$(23.0.2)$$

seem to suggest violation of the principle of flavour universality. The observations currently show deviations from the standard model predictions at about three sigma and await confirmation by other experiments. If deviations with more than five sigma significance are confirmed, these will constitute discoveries that will require non-trivial extension of the standard model, similarly to the impact of the discovery of parity violation on the extension of the Fermi theory.

In recent years particle physics has started to employ new techniques inspired by developments in information technology. The particle detector prepares a three-dimensional image of the final state measuring the direction, energy and momentum of particle flow and the bend of particle tracks by magnetic field. The purpose of data analysis is to find out the hard scattering process from this information. This is a typical pattern recognition problem. Engineering of pattern recognition has undergone tremendous development

in this millennium, facilitated by the immense increase of computing power, appearance of algorithms using neural networks and deep learning. Presently it is a field of constant change and emerging new ideas, and thus beyond the scope of this book.

While the items mentioned in this section are very exciting developments in particle physics, we have deliberately not discussed those in detail, as they are neither properly confirmed, nor fully established with scientific methods yet. So instead of going into the details, let us close our book with several quotes.

There is a theory which states that if ever anyone discovers exactly what the Universe is for and why it is here, it will instantly disappear and be replaced by something even more bizarre and inexplicable.

There is another theory which states that this has already happened.

(Douglas Adams)

Why God Particle? Two reasons. One, the publisher wouldn't let us call it the Goddamn Particle, though that might be a more appropriate title, given its villainous nature and the expense it is causing. The title ended up offending two groups: (1) those who believe in god and (2) those who do not.

(Leon Lederman)

We need something new. We can't predict what that will be or when we will find it because if we knew that, we would have found it already!

(Stephen Hawking)

"Would you tell me, please, which way I ought to go from here?"
"That depends a good deal on where you want to get to," said the Cat.
"I don't much care where–" said Alice.
"Then it doesn't matter which way you go," said the Cat
"–so long as I get SOMEWHERE," Alice added as an explanation.
"Oh, you're sure to do that," said the Cat, "if you only walk long enough."

(Lewis Carroll)

Bibliography

[Aaboud et al., 2017] Aaboud, M. et al. (2017). Measurement of the Higgs boson coupling properties in the $H \rightarrow ZZ^* \rightarrow 4\ell$ decay channel at $\sqrt{s} = 13$ TeV with the ATLAS detector.

[Aad et al., 2010] Aad, G. et al. (2010). Observation of a centrality-dependent dijet asymmetry in lead-lead collisions at $\sqrt{s_{NN}} = 2.77$ TeV with the ATLAS detector at the LHC. *Phys. Rev. Lett.*, 105:252303.

[Aad et al., 2012] Aad, G. et al. (2012). Observation of a new particle in the search for the Standard Model Higgs boson with the ATLAS detector at the LHC. *Phys.Lett.*, B716:1–29.

[Aad et al., 2015] Aad, G. et al. (2015). Combined measurement of the Higgs boson mass in pp collisions at $\sqrt{s} = 7$ and 8 TeV with the ATLAS and CMS experiments. *Phys. Rev. Lett.*, 114:191803.

[Aad et al., 2016] Aad, G. et al. (2016). Measurements of the Higgs boson production and decay rates and constraints on its couplings from a combined ATLAS and CMS analysis of the LHC pp collision data at $\sqrt{s} = 7$ and 8 TeV. *JHEP*, 08:045.

[Aaij et al., 2017] Aaij, R. et al. (2017). Test of lepton universality with $B^0 \rightarrow K^{*0}\ell^+\ell^-$ decays. *JHEP*, 08:055.

[Aamodt et al., 2010] Aamodt, K. et al. (2010). Elliptic flow of charged particles in Pb-Pb collisions at 2.76 TeV. *Phys. Rev. Lett.*, 105:252302.

[Abbiendi et al., 2012] Abbiendi, G. et al. (2012). Search for charged Higgs bosons in e^+e^- collisions at $\sqrt{s} = 189 - 209$ GeV. *Eur. Phys. J.*, C72:2076.

[Abbott, 1981] Abbott, L. (1981). The background field method beyond one loop. *Nucl.Phys.*, B185:189.

[Adams et al., 2003] Adams, J. et al. (2003). Evidence from d + Au measurements for final state suppression of high p(T) hadrons in Au+Au collisions at RHIC. *Phys. Rev. Lett.*, 91:072304.

[Adler et al., 2003] Adler, S. S. et al. (2003). Suppressed π^0 production at large transverse momentum in central Au+ Au collisions at S(NN)**1/2 = 200 GeV. *Phys. Rev. Lett.*, 91:072301.

[Agostinelli et al., 2003] Agostinelli, S. et al. (2003). GEANT4: A simulation toolkit. *Nucl. Instrum. Meth.*, A506:250–303.

[Altarelli and Parisi, 1977] Altarelli, G. and Parisi, G. (1977). Asymptotic freedom in parton language. *Nucl.Phys.*, B126:298.

[An et al., 2017] An, F. P. et al. (2017). Measurement of electron antineutrino oscillation based on 1230 days of operation of the Daya Bay experiment. *Phys. Rev.*, D95(7):072006.

[Arneodo et al., 1997] Arneodo, M. et al. (1997). Measurement of the proton and deuteron structure functions, F2(p) and F2(d), and of the ratio sigma-L / sigma-T. *Nucl.Phys.*, B483:3–43.

[ATLAS, 2017] ATLAS, c. (2017). Measurements of Higgs boson properties in the diphoton decay channel with 36.1 fb^{-1} pp collision data at the center-of-mass energy of 13 TeV with the ATLAS detector.

[Aubert et al., 1974] Aubert, J. et al. (1974). Experimental observation of a heavy particle J. *Phys.Rev.Lett.*, 33:1404–1406.

[Augustin et al., 1974] Augustin, J. et al. (1974). Discovery of a narrow resonance in e+ e- annihilation. *Phys.Rev.Lett.*, 33:1406–1408.

[Barate et al., 1998] Barate, R. et al. (1998). Studies of quantum chromodynamics with the ALEPH detector. *Phys.Rept.*, 294:1–165.

[Barate et al., 2003] Barate, R. et al. (2003). Search for the standard model Higgs boson at LEP. *Phys.Lett.*, B565:61–75.

[Bazavov et al., 2018] Bazavov, A. et al. (2018). Up-, down-, strange-, charm-, and bottom-quark masses from four-flavor lattice QCD.

[Becker et al., 2012] Becker, S., Goetz, D., Reuschle, C., Schwan, C., and Weinzierl, S. (2012). NLO results for five, six and seven jets in electron-positron annihilation. *Phys.Rev.Lett.*, 108:032005.

[Berger, 1992] Berger, E. L. (1992). Research directions for the decade. Proceedings, 1990, Summer Study on High-Energy Physics, Snowmass, USA, June 25 - July 13, 1990.

[Beringer et al., 2012] Beringer, J. et al. (2012). Review of particle physics (RPP). *Phys.Rev.*, D86:010001.

[Bezrukov and Shaposhnikov, 2008] Bezrukov, F. L. and Shaposhnikov, M. (2008). The Standard Model Higgs boson as the inflaton. *Phys. Lett.*, B659:703–706.

[Bityukov and Krasnikov, 2000] Bityukov, S. and Krasnikov, N. (2000). On the observability of a signal above background. *Nucl.Instrum.Meth.*, A452:518–524.

[Branchina et al., 2014] Branchina, V., Messina, E., and Platania, A. (2014). Top mass determination, Higgs inflation, and vacuum stability. *JHEP*, 09:182.

[Busza et al., 2018] Busza, W., Rajagopal, K., and van der Schee, W. (2018). Heavy ion collisions: The big picture and the big questions.

[Cacciari and Salam, 2006] Cacciari, M. and Salam, G. P. (2006). Dispelling the N^3 myth for the k_t jet-finder. *Phys.Lett.*, B641:57–61.

[Cacciari et al., 2008] Cacciari, M., Salam, G. P., and Soyez, G. (2008). The anti-k(t) jet clustering algorithm. *JHEP*, 0804:063.

[Catani et al., 2002] Catani, S., Dittmaier, S., Seymour, M. H., and Trocsanyi, Z. (2002). The dipole formalism for next-to-leading order QCD calculations with massive partons. *Nucl.Phys.*, B627:189–265.

[Catani et al., 1991] Catani, S., Dokshitzer, Y. L., Olsson, M., Turnock, G., and Webber, B. (1991). New clustering algorithm for multi - jet cross-sections in e+ e- annihilation. *Phys.Lett.*, B269:432–438.

[Chatrchyan et al., 2012a] Chatrchyan, S. et al. (2012a). Jet momentum dependence of jet quenching in PbPb collisions at $\sqrt{s_{NN}}$ = 2.76 TeV. *Phys. Lett.*, B712:176–197.

[Chatrchyan et al., 2012b] Chatrchyan, S. et al. (2012b). Observation of a new boson at a mass of 125 GeV with the CMS experiment at the LHC. *Phys.Lett.*, B716:30–61.

[Chatrchyan et al., 2013] Chatrchyan, S. et al. (2013). Observation of a new boson with mass near 125 GeV in pp collisions at $\sqrt{s}$ = 7 and 8 TeV. *JHEP*, 1306:081.

[Cohen et al., 1998] Cohen, A. G., De Rujula, A., and Glashow, S. (1998). A matter – antimatter universe? *Astrophys.J.*, 495:539–549.

[Collins et al., 1989] Collins, P., Martin, A. D., and Squires, E. (1989). Particle physics and cosmology.

[Corcella et al., 2001] Corcella, G., Knowles, I., Marchesini, G., Moretti, S., Odagiri, K., et al. (2001). HERWIG 6: An event generator for hadron emission reactions with interfering gluons (including supersymmetric processes). *JHEP*, 0101:010.

[Cousins and Highland, 1992] Cousins, R. D. and Highland, V. L. (1992). Incorporating systematic uncertainties into an upper limit. *Nucl.Instrum.Meth.*, A320:331–335.

[Cowan et al., 2011] Cowan, G., Cranmer, K., Gross, E., and Vitells, O. (2011). Asymptotic formulae for likelihood-based tests of new physics. *Eur. Phys. J.*, C71:1554. [Erratum: Eur. Phys. J.C73,2501(2013)].

[Denner, 1993] Denner, A. (1993). Techniques for calculation of electroweak radiative corrections at the one loop level and results for W physics at LEP-200. *Fortsch. Phys.*, 41:307–420.

[Dirac, 1931] Dirac, P. A. (1931). Quantized singularities in the electromagnetic field. *Proc.Roy.Soc.Lond.*, A133:60–72.

[Dokshitzer, 1977] Dokshitzer, Y. L. (1977). Calculation of the structure functions for deep inelastic scattering and e+ e- annihilation by perturbation theory in quantum chromodynamics. *Sov.Phys.JETP*, 46:641–653.

[Dokshitzer et al., 1991] Dokshitzer, Y. L., Khoze, V. A., Mueller, A. H., and Troyan, S. I. (1991). Basics of perturbative QCD.

[Durr et al., 2008] Durr, S., Fodor, Z., Frison, J., Hoelbling, C., Hoffmann, R., et al. (2008). Ab-Initio determination of light hadron masses. *Science*, 322:1224–1227.

[Ellis, 1988] Ellis, R. K. (1988). An introduction to the QCD parton model.

[Esteban et al., 2017] Esteban, I., Gonzalez-Garcia, M. C., Maltoni, M., Martinez-Soler, I., and Schwetz, T. (2017). Updated fit to three neutrino mixing: Exploring the accelerator-reactor complementarity. *JHEP*, 01:087.

[Gehrmann-De Ridder et al., 2007] Gehrmann-De Ridder, A., Gehrmann, T., Glover, E., and Heinrich, G. (2007). NNLO corrections to event shapes in e+ e- annihilation. *JHEP*, 0712:094.

[Glashow et al., 1970] Glashow, S., Iliopoulos, J., and Maiani, L. (1970). Weak interactions with lepton-hadron symmetry. *Phys.Rev.*, D2:1285–1292.

[Gribov and Lipatov, 1972] Gribov, V. and Lipatov, L. (1972). Deep inelastic e p scattering in perturbation theory. *Sov.J.Nucl.Phys.*, 15:438–450.

[Halzen and Martin, 1984] Halzen, F. and Martin, A. D. (1984). Quarks and leptons: An introductory course in modern particle physics.

[Horvath, 2003] Horvath, D. (2003). Search for charged Higgs bosons with the OPAL detector at LEP. *Nucl. Phys.*, A721:C453–C456.

[James and Roos, 1975] James, F. and Roos, M. (1975). Minuit: A system for function minimization and analysis of the parameter errors and correlations. *Comput.Phys.Commun.*, 10:343–367.

[Klein and Roodman, 2005] Klein, J. and Roodman, A. (2005). Blind analysis in nuclear and particle physics. *Ann.Rev.Nucl.Part.Sci.*, 55:141–163.

[Lee and Wick, 1974] Lee, T. D. and Wick, G. C. (1974). Vacuum stability and vacuum excitation in a spin 0 field theory. *Phys. Rev.*, D9:2291–2316.

[Leo, 1987] Leo, W. (1987). Techniques for nuclear and particle physics experiments: a how to approach.

[Mangano and Parke, 1991] Mangano, M. L. and Parke, S. J. (1991). Multiparton amplitudes in gauge theories. *Phys.Rept.*, 200:301–367.

[Martin, 1997] Martin, S. P. (1997). A supersymmetry primer. pages 1–98. [Adv. Ser. Direct. High Energy Phys.18,1(1998)].

[Miller et al., 1972] Miller, G., Bloom, E. D., Buschhorn, G., Coward, D., DeStaebler, H., et al. (1972). Inelastic electron-proton scattering at large momentum transfers. *Phys.Rev.*, D5:528.

[Mohr et al., 2016] Mohr, P. J., Newell, D. B., and Taylor, B. N. (2016). CODATA recommended values of the fundamental physical constants: 2014. *Rev. Mod. Phys.*, 88(3):035009.

[Nagy and Trocsanyi, 1999] Nagy, Z. and Trocsanyi, Z. (1999). Multijet rates in e+ e- annihilation: Perturbation theory versus LEP data. *Nucl.Phys.Proc.Suppl.*, 74:44–48.

[Patrignani et al., 2016] Patrignani, C. et al. (2016). Review of particle physics. *Chin. Phys.*, C40(10):100001.

[Perkins, 1982] Perkins, D. (1982). Introduction to high energy physics.

[Prosper and Lyons, 2011] Prosper, H. B. and Lyons, L. (2011). Proceedings of the PHYSTAT 2011 Workshop on statistical issues related to discovery claims in search experiments and unfolding, CERN, Geneva, Switzerland, 17-20 January 2011.

[Pumplin et al., 2002] Pumplin, J., Stump, D., Huston, J., Lai, H., Nadolsky, P. M., et al. (2002). New generation of parton distributions with uncertainties from global QCD analysis. *JHEP*, 0207:012.

[Ryder, 1996] Ryder, L. (1996). Quantum field theory.

[Schael et al., 2013] Schael, S. et al. (2013). Electroweak measurements in electron-positron collisions at W-boson-pair energies at LEP. *Phys.Rept.*, 532:119–244.

[Shaposhnikov and Wetterich, 2010] Shaposhnikov, M. and Wetterich, C. (2010). Asymptotic safety of gravity and the Higgs boson mass. *Phys. Lett.*, B683:196–200.

[Sirunyan et al., 2017] Sirunyan, A. M. et al. (2017). Measurements of properties of the Higgs boson decaying into the four-lepton final state in pp collisions at $\sqrt{s}$ = 13 TeV. *JHEP*, 11:047.

[Sjostrand et al., 2006] Sjostrand, T., Mrenna, S., and Skands, P. Z. (2006). PYTHIA 6.4 physics and manual. *JHEP*, 0605:026.

[Skands, 2012] Skands, P. (2012). Introduction to QCD. *arXiv.org*, 1207.2389:1–85.

[Turner and Wilczek, 1982] Turner, M. S. and Wilczek, F. (1982). Might our vacuum be metastable? *Nature*, 298:633–634.

[Weinzierl, 2009] Weinzierl, S. (2009). Event shapes and jet rates in electron-positron annihilation at NNLO. *JHEP*, 0906:041.

[Woithe et al., 2017] Woithe, J., Wiener, G. J., and Van der Veken, F. F. (2017). Let's have a coffee with the Standard Model of particle physics! *Phys. Educ.*, 52(3):034001.

Index

Bold-face page numbers indicate sections dedicated to the given entry, whereas page numbers in normal type point to textual references. In order to maintain an alphabetic order, Greek symbols and numbers in entries are spelled out in Latin (e.g. "τ-lepton" is listed as "Tau-lepton" or "3-jet events" as "Three-jet events").